General Disclaimer

One or more of the Following Statements may affect this Document

- This document has been reproduced from the best copy furnished by the organizational source. It is being released in the interest of making available as much information as possible.

- This document may contain data, which exceeds the sheet parameters. It was furnished in this condition by the organizational source and is the best copy available.

- This document may contain tone-on-tone or color graphs, charts and/or pictures, which have been reproduced in black and white.

- This document is paginated as submitted by the original source.

- Portions of this document are not fully legible due to the historical nature of some of the material. However, it is the best reproduction available from the original submission.

Produced by the NASA Center for Aerospace Information (CASI)

(NASA-CR-165397) COOLED VARIABLE NOZZLE RADIAL TURBINE FOR ROTOR CRAFT APPLICATIONS (Teledyne CAE) 205 p HC A10/MF A01 CSCL 21E
N82-29323
Unclas
G3/07 28455

NASA CR-165397
TELEDYNE CAE

Report No. 1756

COOLED VARIABLE NOZZLE RADIAL TURBINE FOR ROTOR-CRAFT APPLICATIONS

BY C. ROGO AND M.R. HOLBROOK

JUL 1982
RECEIVED
NASA STI FACILITY
ACCESS DEPT.

TELEDYNE CAE

PREPARED FOR

NATIONAL AERONAUTICS AND SPACE ADMINISTRATION

NASA LEWIS RESEARCH CENTER
CONTRACT NAS 3-22005

NASA CR-165397
TELEDYNE CAE

Report No. 1759

Copy No.

COOLED VARIABLE NOZZLE RADIAL TURBINE FOR ROTOR-CRAFT APPLICATIONS

BY C. ROGO AND M.R. HOLBROOK

TELEDYNE CAE

PREPARED FOR

NATIONAL AERONAUTICS AND SPACE ADMINISTRATION

NASA LEWIS RESEARCH CENTER
CONTRACT NAS 3-22005

1. Report No.
165397

2. Government Accession No.

3. Recipient's Catalog No.

4. Title and Subtitle
COOLED VARIABLE NOZZLE RADIAL TURBINE
FOR ROTOR-CRAFT APPLICATIONS

5. Report Date
MARCH 1981

6. Performing Organization Code
03104

7. Author(s)
C. Rogo and M.R. Holbrook

8. Performing Organization Report No.
1759

9. Performing Organization Name and Address
Teledyne CAE
1330 Laskey Road
Toledo, Ohio

10. Work Unit No.

11. Contract or Grant No.
NAS-3-22005

12. Sponsoring Agency Name and Address
U.S. Army Research & Technology Laboratories (AVRADCOM)
Propulsion Laboratory, Lewis Research Center
Cleveland, Ohio 44135

13. Type of Report and Period Covered
Contractor Report

14. Sponsoring Agency Code
1L162209AH76

15. Supplementary Notes
Project Manager, Kestutis C. Civinskas, U.S. Army Research & Technology Laboratories (AVRADCOM), Propulsion Laboratory, Lewis Research Center, Cleveland, Ohio

16. Abstract

A study has been conducted on an advanced, small 2.27 kb/sec (5 lbs/sec), high temperature, variable area radial turbine for a rotor craft application. Performance analyses were performed for various variable capacity cycles including both single-shaft and free-turbine engine configurations to define an optimum engine design configuration. Parametric optimizations were made on cooled and uncooled rotor configurations. A detailed structural and heat transfer analysis was conducted to provide a 4000-hour life HP turbine with material properties of the 1988 time frame. Two variable area nozzle concepts, i.e., a pivoted vane and a moveable sidewall geometry were analyzed. Cooling and variable geometry penalties were included in the cycle analysis. The study resulted in selection of a variable geometry free-turbine engine configuration with a design 1477K (2200°F) inlet temperature and a compressor pressure ratio of 16:1. An uncooled HP radial turbine rotor with a moveable sidewall nozzle showed the highest performance potential for a time weighted duty cycle.

17. Key Words (Suggested by Author(s))
Radial Flow
Turbines
Turboshafts
Rotor-craft Aircraft
Helicopter Engines

18. Distribution Statement
Unclassified
STAR Category 07

19. Security Classif. (of this report)
UNCLASSIFIED

20. Security Classif. (of this page)
UNCLASSIFIED

21. No. of Pages
191

22. Price*

PRECEDING PAGE BLANK NOT FILMED

FOREWORD

The work described herein has been conducted by Teledyne CAE in accordance with the terms of Contract No. NAS-3-22005 issued by NASA-Lewis Research Center. This program is in support of the U.S. Army Research & Technology Laboratories effort to demonstrate a significant improvement in component performance of small gas turbine engines for future rotorcraft.

PRECEDING PAGE BLANK NOT FILMED

TABLE OF CONTENTS

TABLE OF CONTENTS

LIST OF ILLUSTRATIONS

LIST OF ILLUSTRATIONS

LIST OF ILLUSTRATIONS

LIST OF ILLUSTRATIONS

LIST OF ILLUSTRATIONS

LIST OF ILLUSTRATIONS

LIST OF ILLUSTRATIONS

LIST OF TABLES

SECTION 1.0

SUMMARY

An advanced single stage high pressure radial inflow turbine with a variable geometry nozzle has been designed for a rotorcraft application in the early 1990 time frame. Free-turbine and single-shaft engine cycle studies were conducted to establish performance trade-offs and design boundary conditions. Two variable nozzle geometry concepts, i.e. a pivoted vane and moveable sidewall geometry, were investigated. The results of the design study are summarized below.

1. The engine cycle study resulted in the selection of a variable geometry free-turbine engine, uncooled turbine rotor configuration with a design 1477 K (2200°F) inlet temperature and a compressor pressure ratio of 16:1. A time weighted duty cycle optimization determined the design power rating for best fuel consumption to be at 78% flow and 82% power. The specific power and specific fuel consumption were respectively, ESHP/W = 317.3 kw-sec/kg (193 hp-sec/lb) and ESFC = 0.251 kg/hr-kw (0.413 lbs/hr-hp).

2. Concept evaluations have shown the moveable sidewall nozzle to have performance advantages over the pivoted vane nozzle. Higher pivoted losses at off design were attributable to increased vane leading edge incidences, vane loadings, and free vortex loss changes due to variable stagger settings required to change power (flow). Off-design incidences on the rotor were less severe over most of the flow range with the sidewall concept. Rotor losses are affected by a combination of rotor reaction changes and tip incidences. The conclusions drawn are based on the test data and correlation models at hand. However, data available on the moveable sidewall concept is minimal, and a test progrm plan is outlined for a parallel conparison and evaluation of the two nozzle concepts tested with the same rotor.

3. Parametric aerodynamic geometry studies resulted in a 15 vaned nozzle and a 13 bladed rotor. The design exit swirl from the exducer was determined to be 10 degrees against rotation based on an optimum selection from the off-design characteristics. An optimum nozzle exit angle of 1.344 rad. (77°) was selected. The estimated turbine design efficiency with variable nozzle throat area and nozzle cooling is 87 percent.

4. Vibrational analysis showed potential resonance problems with 15 vanes and the design was modified to 14 vanes. Aerodynamic loading and boundary layer analysis showed no aerodynamic penalties were incurred. The nozzle vanes have internal impingement and pin fin cooling using compressor discharge bleed coolant. Nozzle vane coolant is ejected at the trailing edge with minimum cycle penalty.

5. The life limiting points on the rotor occurred as stress rupture on the blade near the rotor backface and at the exducer hub at the exit. The blading of the configuration is, however, predicted to meet required 4000 hour stress rupture life based on the use of a commercial rapid solidification (CRS) powder metal rotor with directionally recrystallized (DR) blade tips.

6. The LCF limiting area on the rotor is in the disk bore. Cyclic life is predicted to be greater than 10,000 cycles and in excess of the 5,000 cycle goal. Burst margin of the rotor was estimated to be 40% over maximum speed.

SECTION 2.0

INTRODUCTION

Turbomachinery component performance has progressively improved over the years as the need for fuel-conservative light weight compact engines has evolved. The U.S. Army Aviation Material Laboratories (USAAVLABS) Propulsion Division, formed in early 1963, has been a continual sponsor of efforts to demonstrate significant improvement in component performance of small, 0.9 - 2.3 kg/sec (2-5 lbs/sec) airflow, gas turbine engines for future Army rotorcraft. High-performance components, along with improved high temperature materials, have made possible ever higher specific work extraction, lower fuel consumption, and smaller engines. Specific fuel consumption alone has been reduced by nearly one half in turboshaft engines since first installed in helicopters in the early 1950's, as discussed in Reference 1.

These improvements both in the "small" componentry (Reference 2) and simple cycle optimizations eventually reach a state of diminishing returns and consequently a number of alternate gas turbine cycles have been studied for future rotorcraft suitability. The simple cycle gas turbine aircraft engine is configured for optimum performance at a single design point. The selected optimization point relates to a requirement for flow capacity at maximum power or a specified cruise condition at which the majority of operating time will be accumulated for the intended mission. Compressor and turbine components are usually matched for best efficiency at the given design point. If an intermediate power cruise condition is selected for component optimization, all other operating conditions from idle (typically 60-70 percent speed) to maximum power (overspeed) represent off-design conditions for which the flow and efficiency match between components will be degraded.

A single-shaft engine with an output gearbox and clutch arrangement varies power by varying gas generator speed, flow, and pressure ratio. Transient response is limited due to the time required to accelerate the gas generator. Another response limitation is the necessity for output shaft clutch engagement at relatively low gas generator speed with added inertia over the remainder of the acceleration. A fixed geometry gas generator with variable nozzle and free power turbine can be used to maintain gas generator speed at near maximum for improved shaft power transient response. Near constant operation of the gas generator at high output, however, limits the minimum attainable specific fuel consumption which tends to increase operating costs for a specific mission range.

With an all variable capacity gas turbine engine concept, the gas generator and power turbine are maintained efficiently at or near design rotational speed and power output is modulated by variation of engine flow level at constant cycle pressure ratio. Operation at an optimum cycle pressure ratio and turbine inlet temperature over the helicopter mission spectrum maintains a minimum SFC and maximizes range capability.

The U.S. Army Research and Technology Lab (AVRADCOM; Ft. Eustis, VA) has recently undertaken a study (Reference 3), based on available industry component technology data, to determine the most efficient turboshaft engine cycle type for military rotorcraft applications. Various simple, regenerative, and variable flow capacity cycles (VCC) were investigated. This study showed that the engine performance of the VCC was difficult to assess due to lack of data on variable geometry component performance in the higher cycle pressure ratio range of interest. A need was established for demonstrated hardware data on advanced variable geometry components including the variable capacity radial turbine. It was recommended that variable capacity cycle research and development resources be concentrated on determination and reduction of compromises in base component performance due to variable geometry.

The current investigation is the first phase of a program concerned with the optimization, design and test/development of an advanced variable geometry radial turbine. Concepts were studied for cooled and uncooled turbines for a rotorcraft application using material technology of 1988. The work scope covers a six task effort consisting of:

Task I - Concept Evaluations - Evaluation of two variable nozzle area and rotor cooling concepts for a maximum 1644°K (2500°F) temperature with a turbine specific work of 407 kJ/kg to 698 kJ/kg(175-300 Btu/lb) and a maximum flow of 2.3 kg/sec (5.0 lbs/sec). Cycle analysis was conducted for single shaft/free-turbine, variable, and simple cycles to define design requirements.

Task II - Preliminary Design Definition - Aeromechanical parametric studies to define the turbine geometry.

Task III - Aerodynamic Design - Detailed aerodynamic design to define design and off-design performance and blading geometry.

Task IV - Heat-Transfer/Mechanical Design Analysis - Three-dimensional thermal and mechanical analysis of the rotor and definition of the minimum life points of the stator and rotor.

Task V - Test Program Plan - Plan a follow-on program consisting of completion of detailed design, preparation of fabrication drawings, fabrication, and aerodynamic testing of the turbine.

Task VI - Reports.

SECTION 3.0

CONCEPT EVALUATIONS (TASK I)

The objectives of the Task I effort were to:

1. Select two or more nozzle area variation concepts for subsequent detailed evaluation.
2. Select two or more rotor cooling concepts and one uncooled rotor concept for further analysis.

At the end of the Task II effort, one variable nozzle concept and one rotor concept was to be selected for detailed Task III and IV design study.

Analysis Assumptions

The assumptions and requirements for conducting the concept evaluation were stipulated as follows:

1. The turbine was considered to be either the sole turbine or the high pressure turbine of a variable flow capacity engine for a rotorcraft application.
2. The turbine specific work was required to be between 407 kJ/kg (175 Btu/lb) and 698 kJ/kg (300 Btu/lb).
3. The average turbine inlet gas temperature was to be:

   a. Maximum allowable for an uncooled rotor.
   b. 1644K (2500°F) for a cooled rotor configuration.

4. The turbine airflow was specified as 2.27 kg/sec (5.0 lbs/sec) at maximum engine power.
5. Both the uncooled and cooled rotors were based on projected 1988 metal technology.
6. Turbine operation was to be at constant speed and constant pressure ratio over a range of flow corresponding to 50% to 100% of engine maximum power.
7. The turbine was designed for a 4000 hour life based on the following mission cycle:

Percent Rated Power	Percent Time
100	20
60	50
55	20
35	5
IDLE	5

Minimization of overall aerodynamic losses was the basis for the selection of the best nozzle adjusting mechanism. The maximization of turbine efficiency and the selection of work extraction dictated whether the rotor required cooling or no cooling. In order to direct the selection of the nozzle adjusting mechanism, and a selection between a cooled and an uncooled rotor, a cycle analysis and applications study was conducted during the Task I effort. The cycle optimization study consisted of evaluations of compressor and turbine configurations and the associated realistic component performances to meet the required objectives.

Compressor pressure ratio was varied as a function of the turbine inlet temperature and component efficiencies were selected consistent with the geometry necessary to achieve the desired pressure ratios.

In order to determine realistic cooling flows and their penalty assessment, three different nozzle cooling concepts were studied. Also, six different configurations were rated for rotor cooling. Cooling flow rates were determined on the basis of structural capability of the material selected and the type of cooling geometry.

3.1 NOZZLE VARIABLE AREA CONCEPTS

There are a multitude of methods to vary the area of the nozzle of a radial turbine. It is particularly important, however, to hold aerodynamic losses to a minimum while preserving mechanical integrity and reliability. A key to this accomplishment is the operating mechanism. With these two requirements as primary considerations, two systems were selected to meet the desired objectives, based on Teledyne CAE experience. These two selected systems were a pivoted vane concept and an actuated sidewall nozzle concept. These concepts were evaluated as to their vane tip clearance, incidence, aerodynamic penalties, mechanical complexity, weight, size and relative cost. The performance penalties associated with actuation of the variable geometry were also determined as a function of percentage of maximum power flow. On an overall basis, the actuated sidewall concept was shown to have a slight advantage over the pivoted vane concept. Because of the uniqueness and the desirable characteristics of these mechanisms, both were studied in detail.

ORIGINAL PAGE IS
OF POOR QUALITY

3.1.1 Pivoted Vane Nozzle

Figure 1 depicts the layout of a cooled pivoted nozzle. In this configuration, the compressor housing and the actuator drive housing each have a grooved race entrapping a series of ball bearings. This bearing allows the drive housing to rotate freely over the compressor housing. Radial drive pins are located in the slotted end of each nozzle actuating arm so that rotational movement of the drive housing produces a corresponding rotational movement of the nozzle vanes. The nozzle vane alignment is maintained through adjustment of the linkage arm connected from the actuator to the drive housing. Thermal stress and distortion are minimized in this design by mounting the nozzle drive shaft through a grooved disk. This disk is retained in a grooved slot in the turbine rotor back plate. This allows the back plate to grow thermally while leaving the nozzle assembly stationary.

Pivoting the vanes to produce a change in flow capacity has an aerodynamic penalty of increased incidence losses at off-design conditions. These penalties were evaluated and compared against an actuated nozzle sidewall concept described in Section 3.3.2.

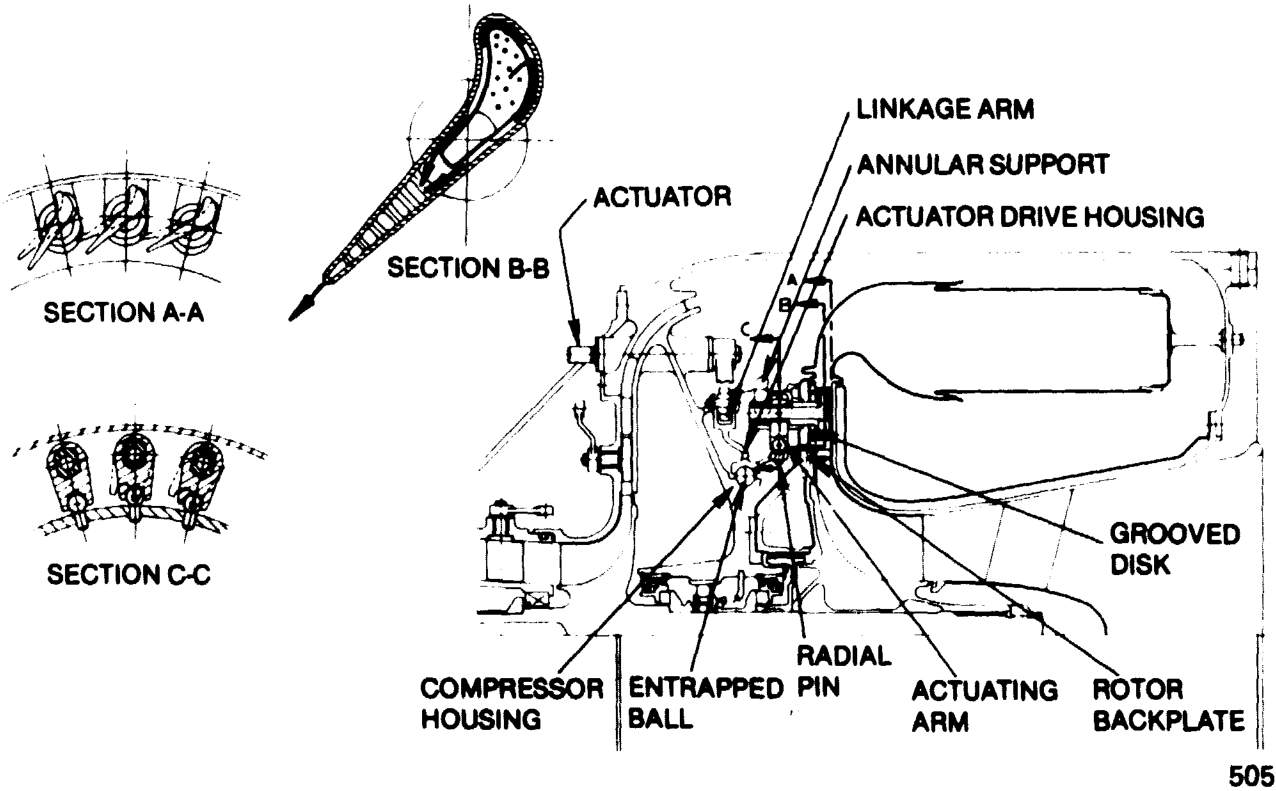

50523

3.1.2 Actuated Sidewall Nozzle

An alternate variable geometry nozzle concept was investigated that varied flow while holding nearly constant rotor and nozzle incidence angles. This concept differs from conventional methods in that the nozzle vanes remain stationary while flow capacity is regulated by moving one of the nozzle sidewalls. This also has the advantage of eliminating the hardware required to rotate the pivoted vanes in unison.

The nozzle vanes are stationary, being cantilever mounted from the vane retainer housing (Figure 2). The nozzle vanes have a fixed setting angle and are cantilever mounted on vane shafts from the vane retainer housing. As the actuated sidewall housing moves to change nozzle width, pockets in the sidewall housing slide over the vanes. A close sliding clearance is maintained between the wetted vane surfaces and the sidewall pockets to minimize loading loss due to leakage around the vane tips at the hub wall. Smooth gas flow into the nozzle is maintained by assembling a section of the front burner section to the actuated sidewall housing. This burner section is provided with a sliding connector to ensure smooth transition with the rest of the burner liner. Flexible elbows are also included to maintain a smooth flowpath in the event the combustor sliding connector malfunctions. The entire assembly is mounted into the compressor housing. The actuated sidewall housing is physically moved by a number of screw-threaded linkage arms to maintain the desired throat area (Figure 3). Alternately, the mechanism can be configured to have the shroud wall as the moveable member.

ORIGINAL PAGE IS
OF POOR QUALITY

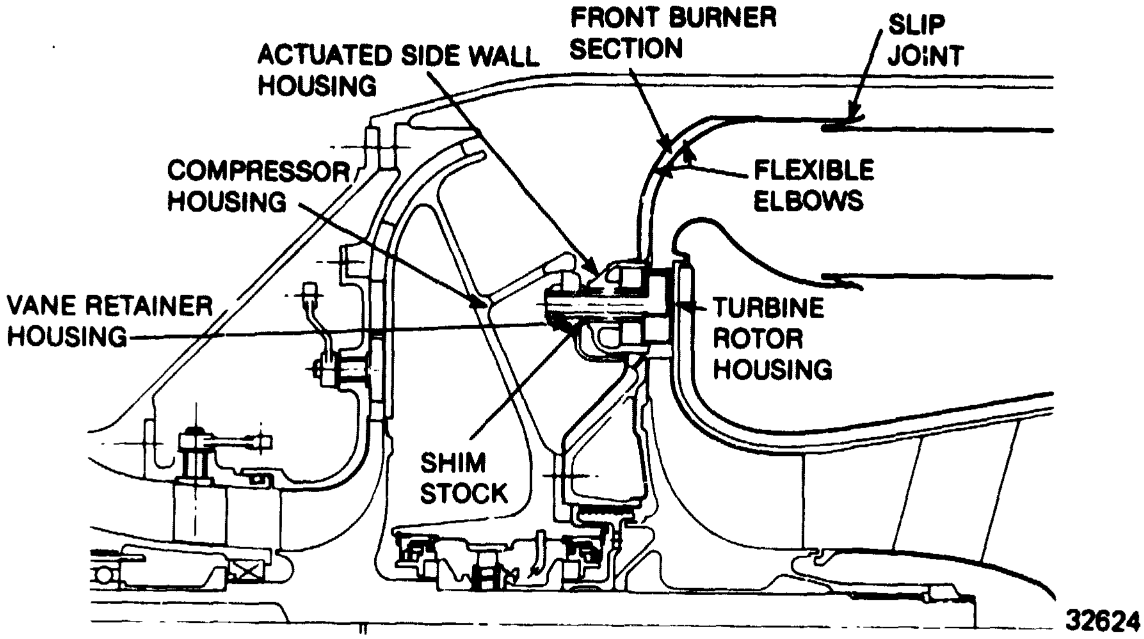

Figure 2. ACTUATED SIDEWALL CONCEPT.

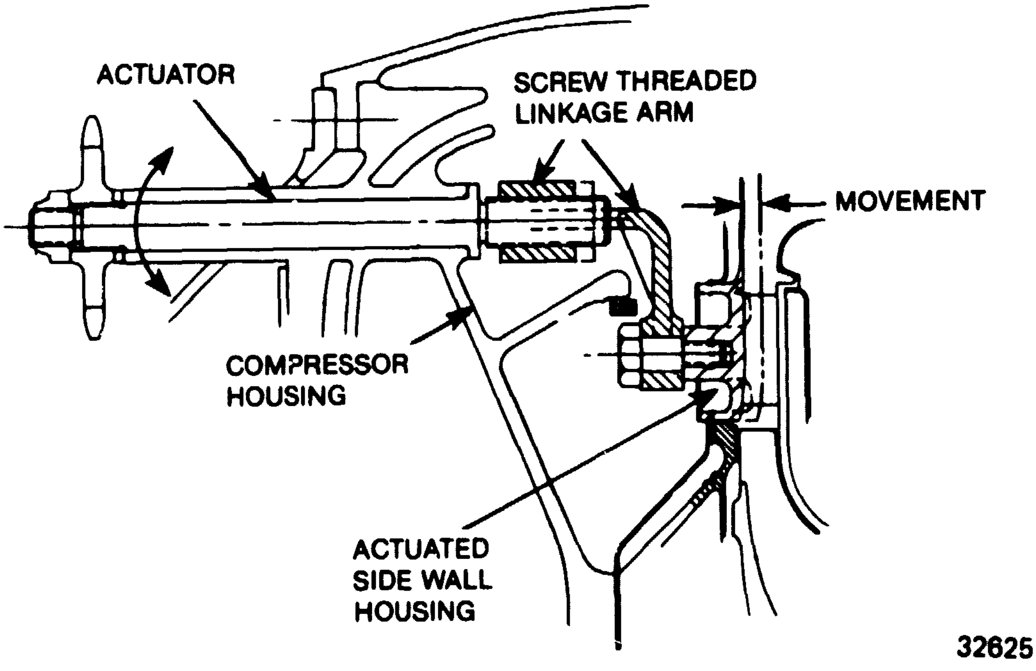

.2 COOLING GEOMETRY CONCEPTS

.2.1 Nozzle Vane And Shroud Cooling

The three nozzle vane cooling configurations shown in igure 4 were evaluated in Task I. Configuration 1 is a geometry ith the leading edge and main body cooled by impingement flow and ne trailing edge cooled by convection enhanced by pin fins. The ooling is ejected in the direction of mainstream flow by slots in ne trailing edge. This cooling flow fills in the trailing edge akes and minimizes the aerodynamic efficiency penalty due to ooling. Configuration 2 is similar to configuration 1 except that he trailing edge pin fins are replaced by splitter plates. onfiguration 3 has the leading edge cooled by an impingement tube nd the pressure and suction sides of the vane are film cooled. lthough the film cooling is ejected in the direction of mainstream low, this geometry results in the highest aerodynamic losses due o destabilizing boundary layer characteristics and high mixing osses. Although many other variations and combinations of these chemes could be generated, the selected three were considered as epresentative of available techniques for performance valuations. The geometries were evaluated on heat transfer, erodynamic, and mechanical bases and rated on a scale from 0 to 5 ith 5 being the best.

The highest total rating denotes the most desirable verall combination of features. Configurations 1 and 2 are oderately complex while configuration 3 is a relatively simple esign. However, configurations 1 and 2 have greatly superior oolant distribution as evidenced by low vane wall thermal radients. Also, with configurations 1 and 2, aerodynamic enalties due to coolant ejection from vane to mainstream are inimized due to wake filling properties with trailing edge treamwise discharge. All three concepts have about the same egree of manufacturing difficulty. Configurations 1 and 2 have he most desirable overall features. Configuration 1, the mpingement and pin fin cooling combination, was selected for urther evaluation due to its highest overall rating.

CONFIGURATION	1 IMPINGEMENT, PIN FINS		2 IMPINGEMENT, SPLITTER PLATES		3 SURFACE FILM EJECTION	
GEOMETRY	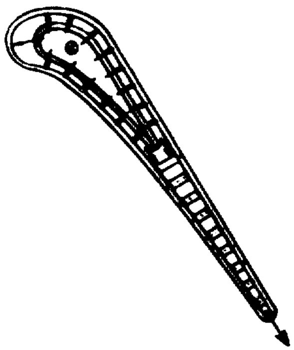		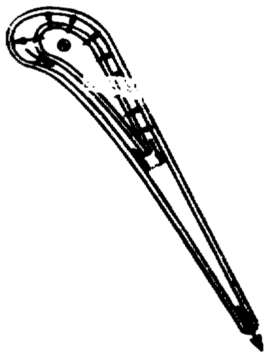		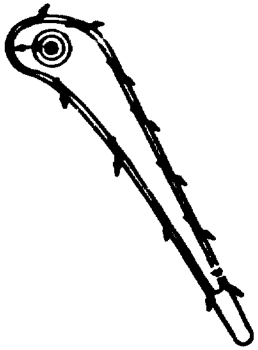	
RATING CONSIDERATION						
COOLING FLOW	4.3%	5	4.3%	5	4.5%	2
SIMPLE SCHEME	MODERATE	3	MODERATE	3	SIMPLE	5
THERMAL GRADIENT	LOW	5	MODERATE	4	HIGH	1
CASTABILITY	FAIR	3	FAIR	3	THIN WALL	2
REQUIRES MACHINING	LINER HOLES	4	LINER HOLES	4	HEADER & VANE	3
COOLING EFF. PENALTY	LOW	5	LOW	4	HIGH	1
TOTAL		25		23		14

50561

Figure 4. NOZZLE VANE COOLING CONCEPT STUDY.

ORIGINAL PAGE IS
OF POOR QUALITY

Figure 5 gives more details on this cooling configuration. Cooling air, supplied by the compressor through hollow vane stems from the nozzle hub sidewall, feeds an impingement liner. The cooling air flows through holes A through Z in the impingement liner and impinges on the inner surface of the nozzle vanes at the leading edge and on the pressure and suction surfaces. The impingement air flows in the chordwise direction in the channel formed by the impingement liner and vane wall. The flow split between the pressure and suction sides is determined by the internal impingement flows and pressure distribution, controlled by impingement hole size and location. Pressure and suction flows join at the end of the impingement liner and flow through a series of pin fin rows, PF1 through PF5, in the trailing edge region. The pin fins are designed to augment heat transfer in the nozzle trailing edge. Cooling flow then discharges into the mainstream flow through a trailing edge slot.

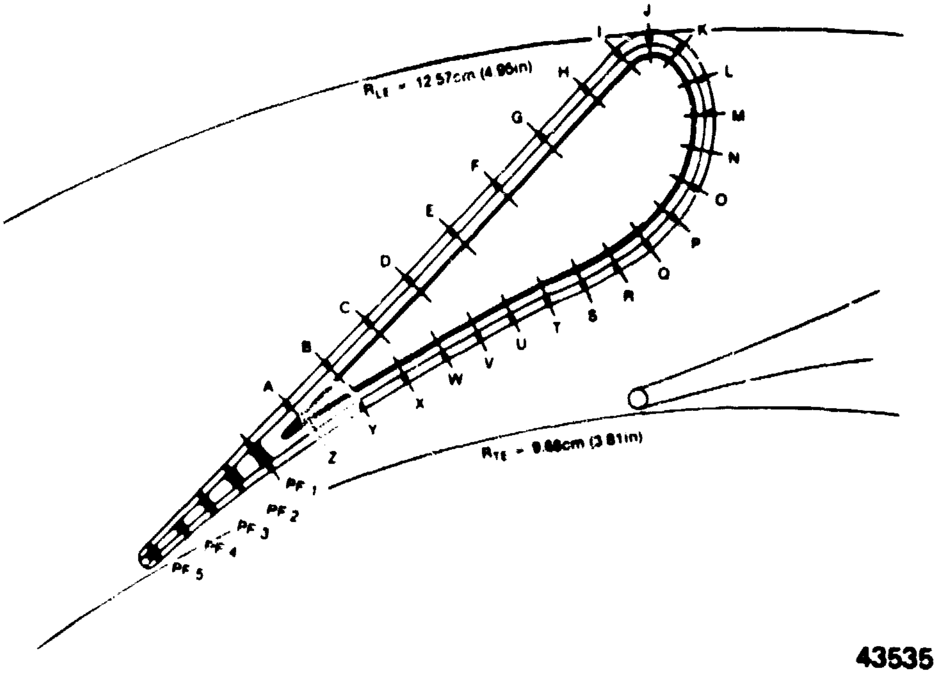

Figure 5. NOZZLE VANE COOLING CONFIGURATION.

ORIGINAL PAGE IS
OF POOR QUALITY

The cooling concept for the turbine inlet nozzle shrouds is a backside impingement configuration. Compressor discharge air flows through impingement plates onto the turbine rotor back plate and turbine rotor housings shown in Figure 6. Shroud cooling air flows inward between the shroud and the impingement plate and is discharged into the mainstream through holes disposed around the circumference at nozzle discharge angle in the shrouds between the nozzle and the rotor leading edge. The nozzle cooling circuits

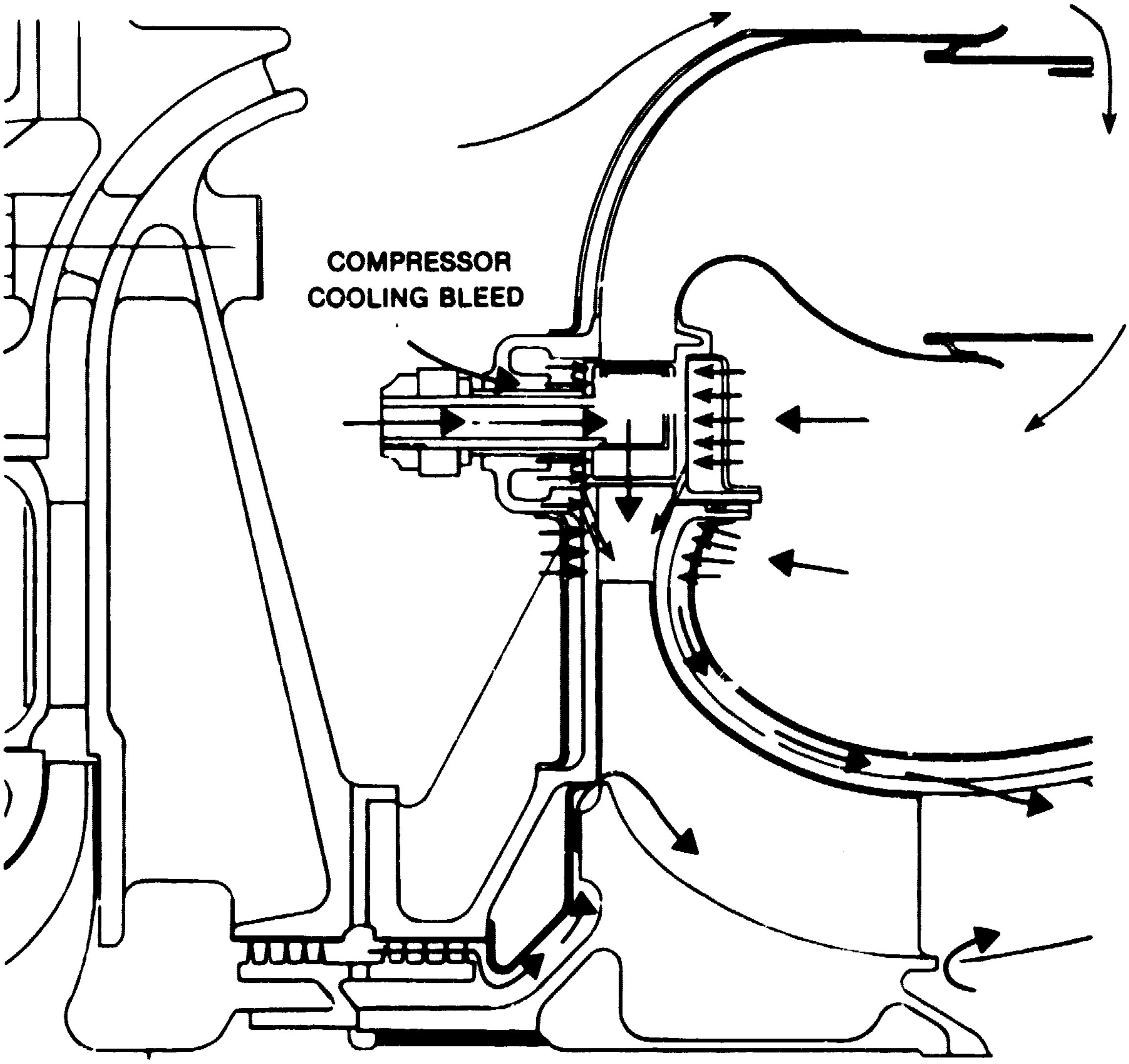

43486

ORIGINAL PAGE IS
OF POOR QUALITY

for the pivoted nozzle concept are shown in Figure 7. The cooling configuration for the actuated sidewall concept, as shown in Figure 6 for a moveable shroud sidewall design, is similar to the pivoted vane scheme with the addition of impingement air into the actuated sidewall housing which is discharged through clearance paths around each vane and buffers vane tip leakage. The complete actuator housing is therefore cooled and mounted stationary to the compressor housing support structure. Air is also circulated to the bearing cavity to maintain proper operating temperatures whereafter it is routed to the rotor backface for rotor hub cooling.

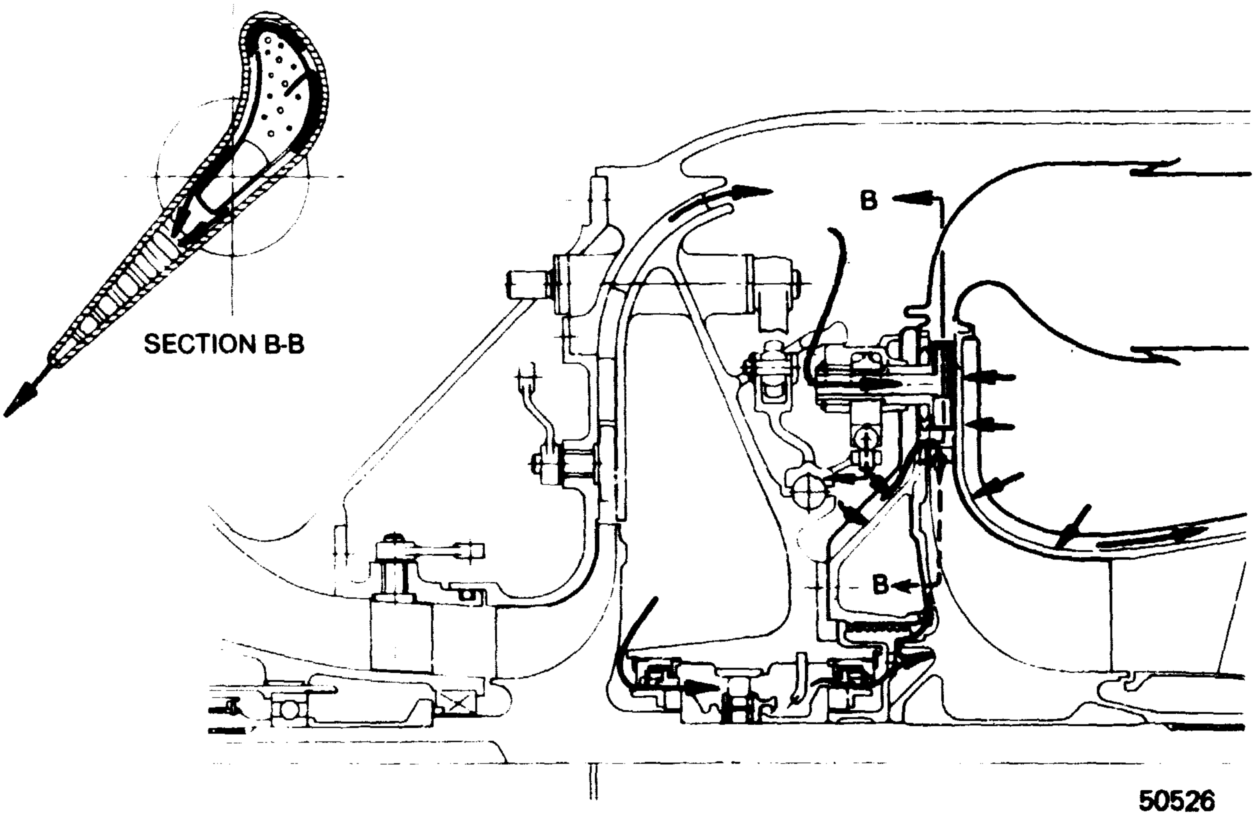

Figure 7. COOLING FLOWS FOR PIVOTED NOZZLE CONCEPT.

3.2.2 Rotor Blade

Cooling a turbine can result in either; 1) an increase in allowable gas temperature with consequent decrease in engine size and higher specific work extraction; or, 2) a decrease in metal temperature and, therefore, an increase in allowable operating stress. The objective of this task was to evaluate rotor cooling concepts by balancing these potential benefits against the penalties incurred by increased complexity and aerodynamic losses.

The following six candidate rotor cooling configurations were evaluated:

1. Two pass suction side film discharge.
2. Two pass suction side variable axial film discharge.
3. Three pass suction side variable axial film discharge.
4. Two pass suction side film discharge with rear entrance
5. Two pass counter-flow suction side film discharge entrance.
6. Two pass axial rib suction side film discharge.

The evaluation was based on the following seven criteria:

1. Cooling flow requirement
2. Simplicity of cooling flowpath
3. Potential for exducer cooling
4. Anticipated local thermal gradient
5. Castability
6. Apparent stress at cooling air entrance
7. Penalty in cooling effectiveness

Figures 8 and 9 are a summary of the candidate cooling designs and the evaluations of heat transfer, aerodynamic, stress, and manufacturing criteria, each rated on a scale of 0 to 5 with 5 being the best. As in the nozzle vane cooling configuration evaluation, the highest total numerical rating denotes the most desirable overall combination of features. As seen from Figures 8 and 9, configurations 1 & 2 rate significantly higher than the remaining four concepts because a simple, castable, cooling scheme makes good use of a small amount of coolant. Configurations 3 through 6 are of nearly equal rank. These configurations are complex castings representing a coolant flowpath that will be difficult to control. As shown in Figure 9, configurations 4 and 5 both contain long, thin entrance cores and provide minimal cooling of the high stress area at the rim front face. Concept 2 was selected for Task II evaluation due to its highest overall rating.

ORIGINAL PAGE IS
OF POOR QUALITY

	1		2		3	
CONFIGURATION	TWO PASS SUCTION SIDE FILM DISCHGE.		TWO PASS SUCTION SIDE FILM DISCHGE.		THREE PASS SUCTION SIDE FILM DISCHGE.	
GEOMETRY	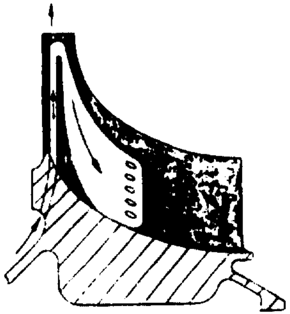		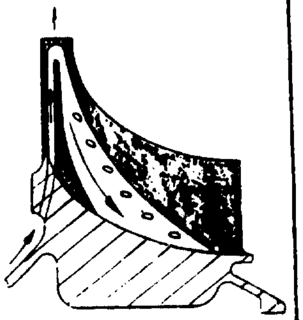		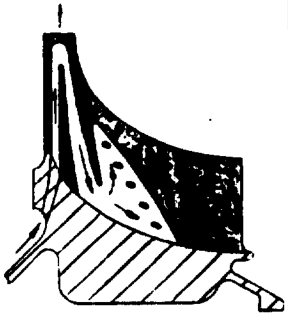	
RATING CONSIDERATION						
COOLING FLOW	2.7%	5	2.7%	5	2.9%	1
SIMPLE SCHEME	GOOD	5	GOOD	5	NO	2
EXDUCER COOLED	NO	2	MODERATE	3	MODERATE	3
BLADE THERMAL GRADIENT	HIGH	2	MODERATE	4	LOW	4
CASTABILITY	GOOD	5	GOOD	4	COMPLEX	2
COOLING ENTRANCE STRESS	MODERATE	2	MODERATE	2	MODERATE	2
COOLING EFF. PENALTY	LOW	4	LOW	4	MODERATE	2
TOTAL		25		27		16

50560

Figure 8. 1644K (2500°F) TURBINE ROTOR COOLING CONCEPT STUDY.

ORIGINAL PAGE IS
OF POOR QUALITY

	4		5		6	
CONFIGURATION	TWO PASS SUCTION SIDE FILM DISCHGE. REAR FACE COOLANT ENTRANCE		TWO PASS CNTR. FL. SUCTION SIDE FILM DISCHGE. REAR FACE COOLANT ENTRANCE		TWO PASS SUCTION SIDE FILM DISCHGE.	
GEOMETRY	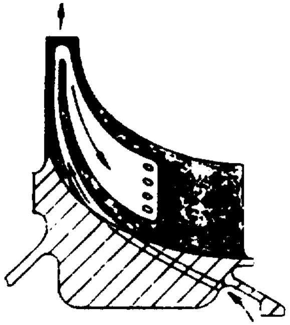		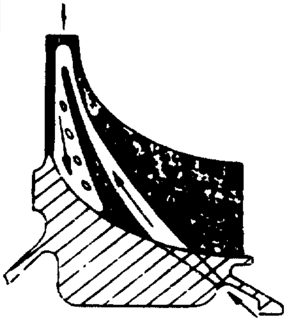		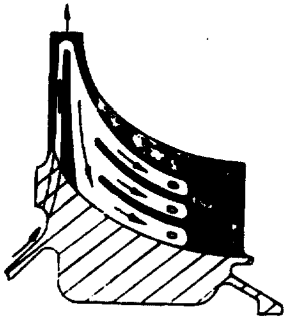	
RATING CONSIDERATION						
COOLING FLOW	2.8%	3	2.8%	3	2.9%	1
SIMPLE SCHEME	FAIR	3	FAIR	3	NO	2
EXDUCER COOLED BLADE	LITTLE	2	SOME	2	YES	4
THERMAL GRADIENT	HIGH	2	HIGH	2	LOW	4
CASTABILITY	DIFFICULT	3	DIFFICULT	3	COMPLEX	2
COOLING ENTRANCE STRESS	LOW	3	LOW	4	MODERATE	2
COOLING EFF. PENALTY	HIGH	1	MODERATE	2	MODERATE	2
TOTAL		17		19		17

50554

Figure 9. 1644K (2500°F) TURBINE ROTOR COOLING CONCEPT STUDY.

3.3 CONFIGURATION SELECTIONS

3.3.1 Compressor Considerations

During the concept evaluation phase, a preliminary compressor design study was conducted to evaluate the feasibility of operation over a 50% flow range at constant speed and pressure ratio. Compressor performance variation with flow was estimated to provide a representative component efficiency schedule for turbine cycle analysis and configuration selection. Single and two-stage centrifugal, and multi-stage axial-centrifugal compressors were evaluated for the range of cycle pressure ratios from 6.0 to 20.0 considered for the specified rotor craft application.

A Teledyne CAE computer code, PRELIM, was used for initial compressor sizing. PRELIM is based on performance prediction logic presented in Reference 4. Compressor polytropic efficiencies are predicted empirically as a function of stage pressure ratio with adjustments for size effects and predicted technology advancement. Corrections are also applied for specific speed and inlet hub-to-tip radius ratio (clearance) effects.

Table I lists the basic objectives for the compressor parametric evaluations. A design point flow equal to 85% of the maximum flow rate (5.0 lb/sec) was selected for compressor evaluation to correspond with part power operation of the turbine components. Turbine optimization at part power maximized overall performance over the 50% flow range of duty cycle operation. During the initial analysis, compressor rotational speed was optimized independent of turbine constraints. After initial consideration, axial-centrifugal compressor combinations were eliminated from the concept evaluation due to insufficient surge-free flow range potential at constant speed. Detailed parametric assumptions for the assessment of centrifugal compressor design point efficiency levels in the PRELIM program are listed in Table II. Variation of compressor design point efficiency with pressure ratio used in the cycle analysis study is given in Figure 10. The efficiency levels shown include decrements for variable geometry and duct loss.

TABLE I

TASK I COMPRESSOR PARAMETRIC OPTIMIZATION

- DESIGN FLOW SIZE (1.93 kg/sec)
- FLOW RANGE CAPABILITY-(2.5 to 5.0 lb/sec) AT DESIGN SPEED
- OVERALL PRESSURE RATIO RANGE - 6:1 to 20:1
  - P/P = 6.0 to 12.0: SINGLE STAGE CENTRIFUGAL
  - P/P = 12.0 to 20.0: DOUBLE STAGE CENTRIFUGAL
    :DOUBLE AXIAL/SINGLE CENTRIFUGAL
- DESIGN SPEED SELECTION - OPTIMUM SPECIFIC SPEED FOR EACH PRESSURE RATIO

TABLE II

TASK I COMPRESSOR DESIGN PARAMETERS

	SINGLE STAGE	FIRST STAGE	SECOND STAGE
INLET AXIAL MACH NO.	0.50	0.60	0.30
INLET HUB-TO-TIP RATIO	0.40	0.50	0.60
INLET AERO. BLOCKAGE, %	2.0	2.0	2.0
EXIT AERO BLOCKAGE, %	10.0	10.0	10.0
RELATIVE VELOCITY RATIO	2.00	1.67	1.67
BACKWARD CURVATURE, rad., deg.	0.611 (35.0)	0.698 (40.0)	0.698 (40.0)
SLIP FACTOR	0.90	0.90	0.90

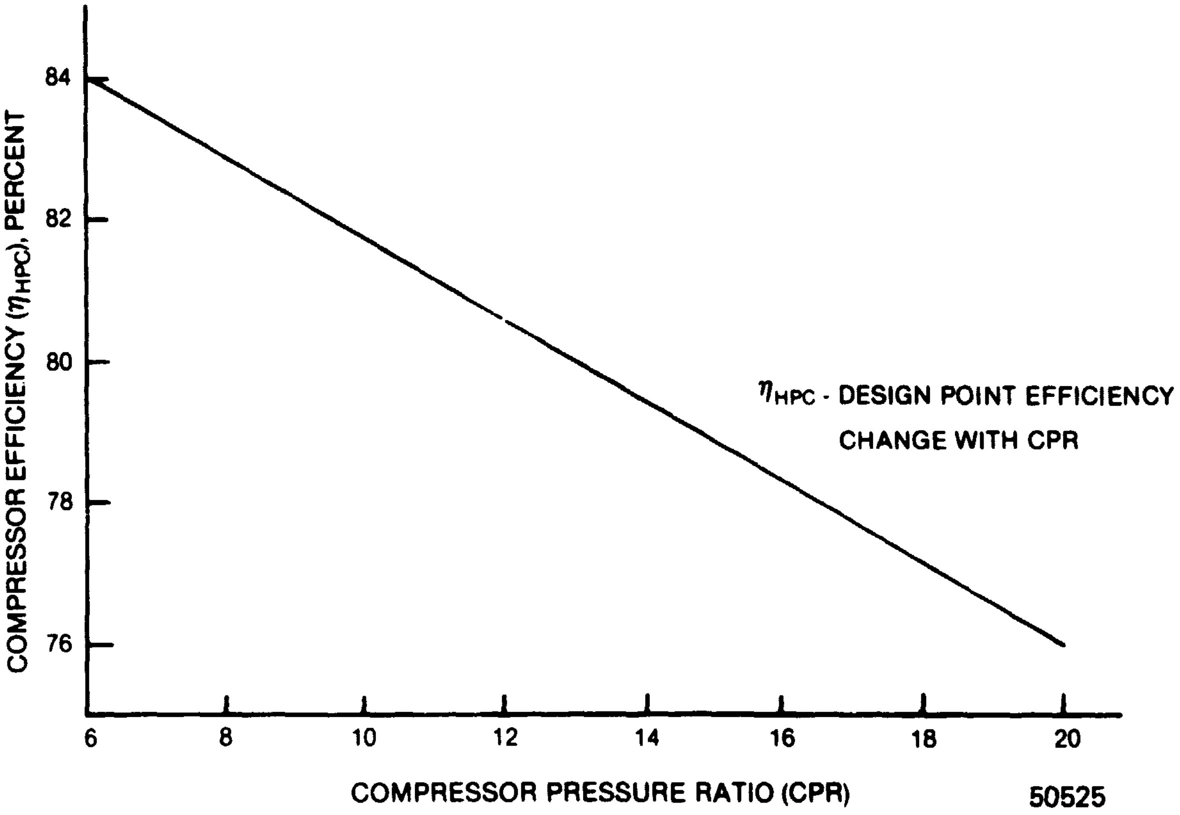

Figure 10. COMPRESSOR DESIGN POINT EFFICIENCY CHANGE WITH COMPRESSOR PRESSURE RATIO.

The single stage range capability of centrifugal stages in the 2.0-2.5 pressure ratio range with variable inlet guide vanes, estimated from Reference 5, is shown in Figure 11. When matched for near-choke operation at design point, a constant pressure ratio flow range of approximately 45% can be achieved for 90° IGV range with 10% minimum surge margin. Addition of a variable area radial diffuser will further extend high speed flow range for higher pressure ratio backward curved centrifugal compressor stages. The effect of variable pivoted-vane radial diffuser on the range of a 4.0-5.0 pressure ratio compressor is illustrated in Figure 12 based on data presented in Reference 6. Again 45 percent constant pressure ratio flow range is possible with 10% minimum surge margin.

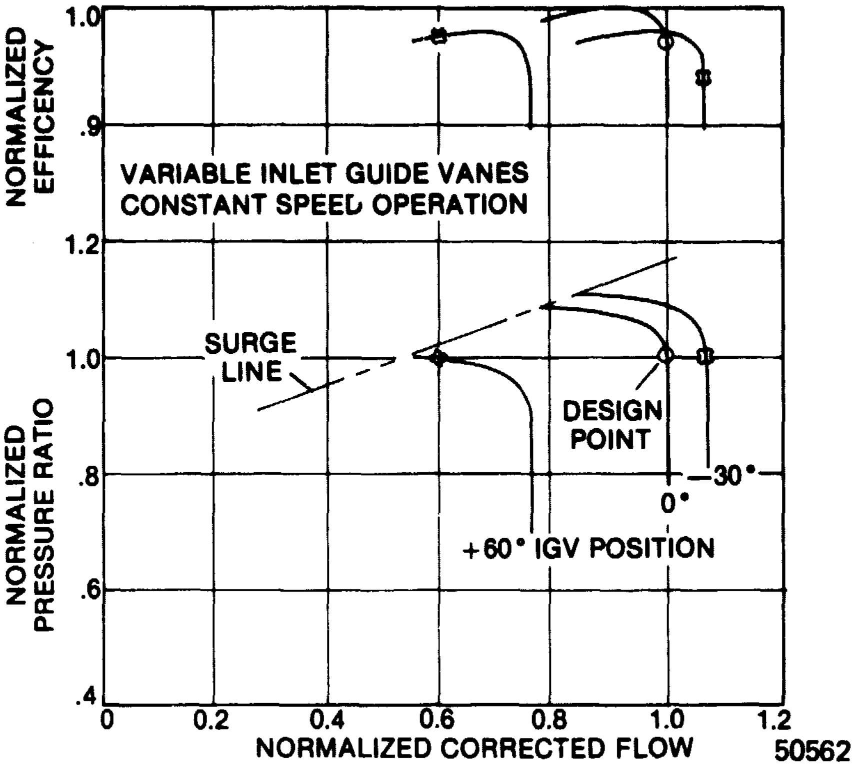

Figure 11. COMPRESSOR RANGE EXTENSION, VARIABLE INLET GUIDE VANES.

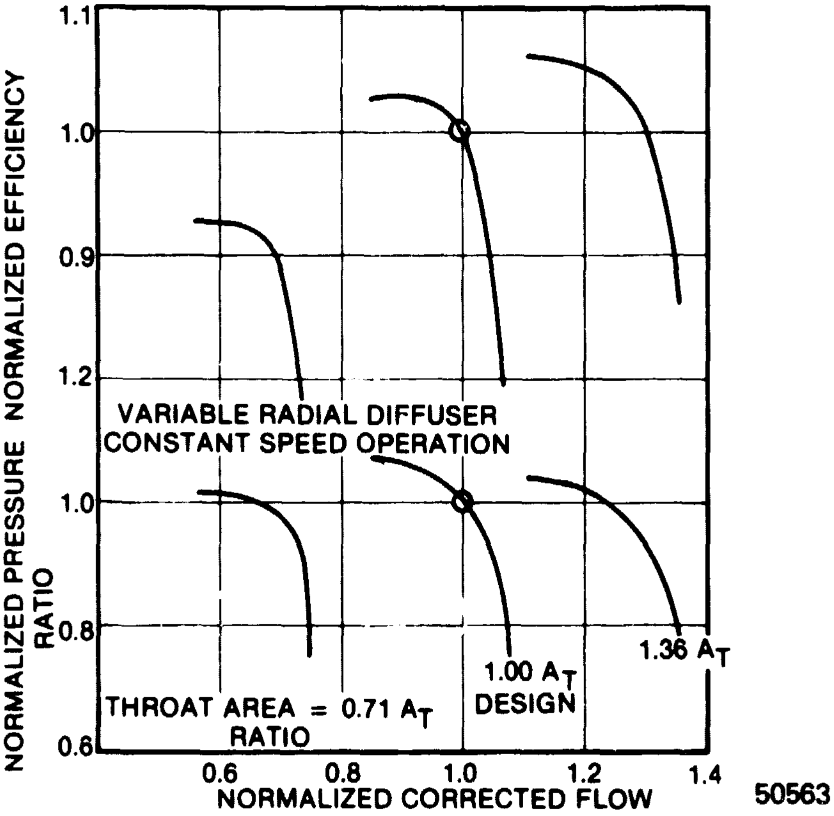

The estimated variation of compressor efficiency with flow rate used for Task I variable capacity cycle analysis and turbine configuration selection is shown in Figure 13. The estimated two-stage compressor map shown in Figure 14, and scaled from Reference 7, was used for simple cycle off-design performance analysis

During the last segment of Task I, the recommended two-stage centrifugal compressor configuration shown in Figure 15 was evaluated at the rotational speed selected for best turbine operation. A design point base compressor adiabatic efficiency level of 0.823 (T-T) is predicted with a cycle pressure ratio of 16.0 for design application in the late 1980's. It is anticipated that fixed leading edge variable inlet guide vanes and variable area radial diffusers will be required to provide stable operation over 50% flow range for this high pressure ratio two-stage gas turbine compressor application. Base compressor efficiency was degraded 4.3 points for cycle analysis to account for guide vane, diffuser vane endwall clearance, and interstage duct losses. A 1.0 point decrement in overall total-to-total efficiency was assessed due to inlet guide vane profile loss at zero stagger design point setting. The assumed penalty for variable radial diffuser geometry was 1.8 point for endwall tip leakage. The two-stage flowpath shown in Figure 15 includes an interstage duct for which a 1.5 point efficiency penalty was assessed.

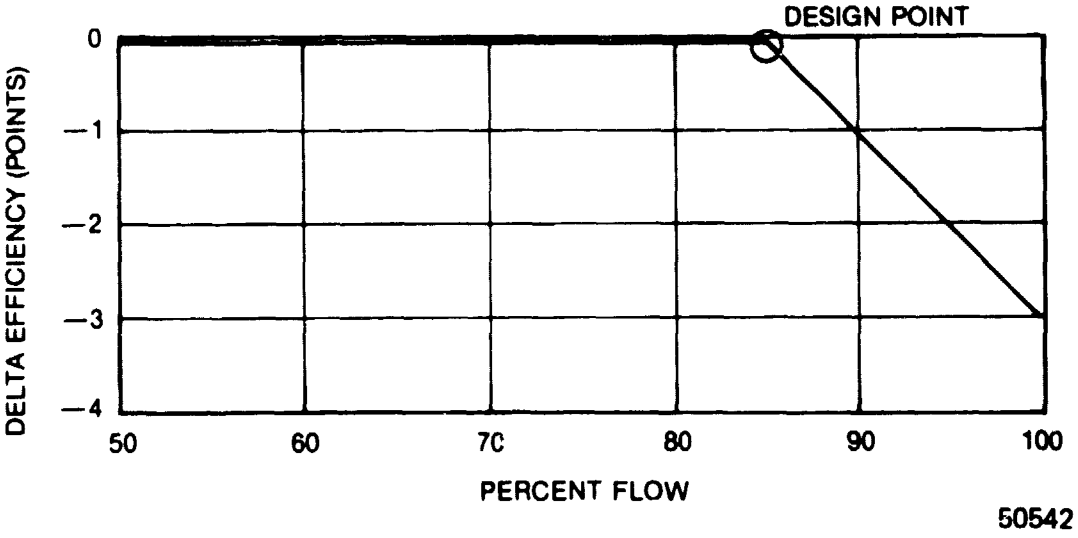

Figure 13. COMPRESSOR EFFICIENCY SCHEDULE, VARIABLE INLET GUIDE VANES.

ORIGINAL PAGE IS
OF POOR QUALITY

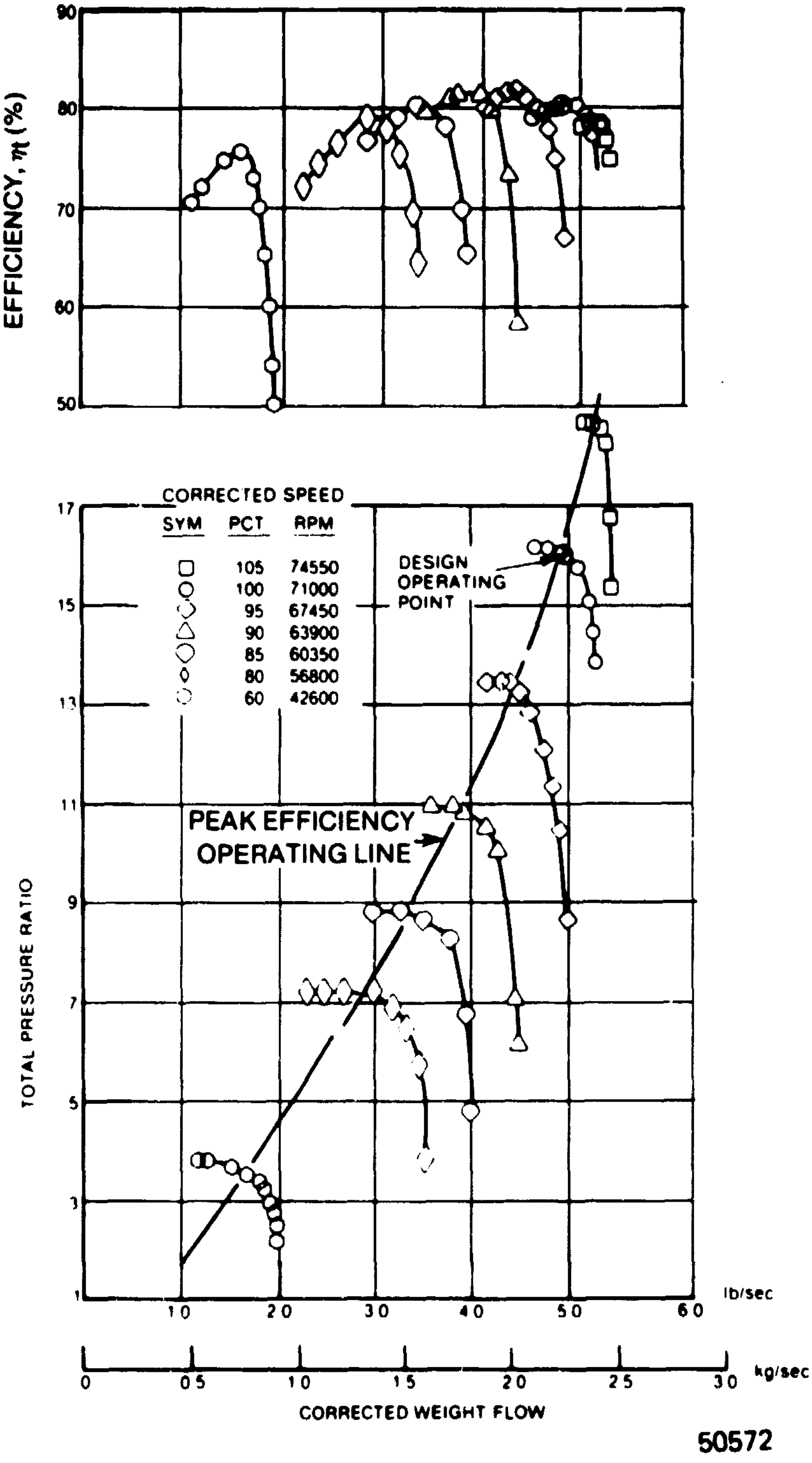

Figure 14. ESTIMATED TWO-STAGE COMPRESSOR MAP.

ORIGINAL PAGE IS
OF POOR QUALITY

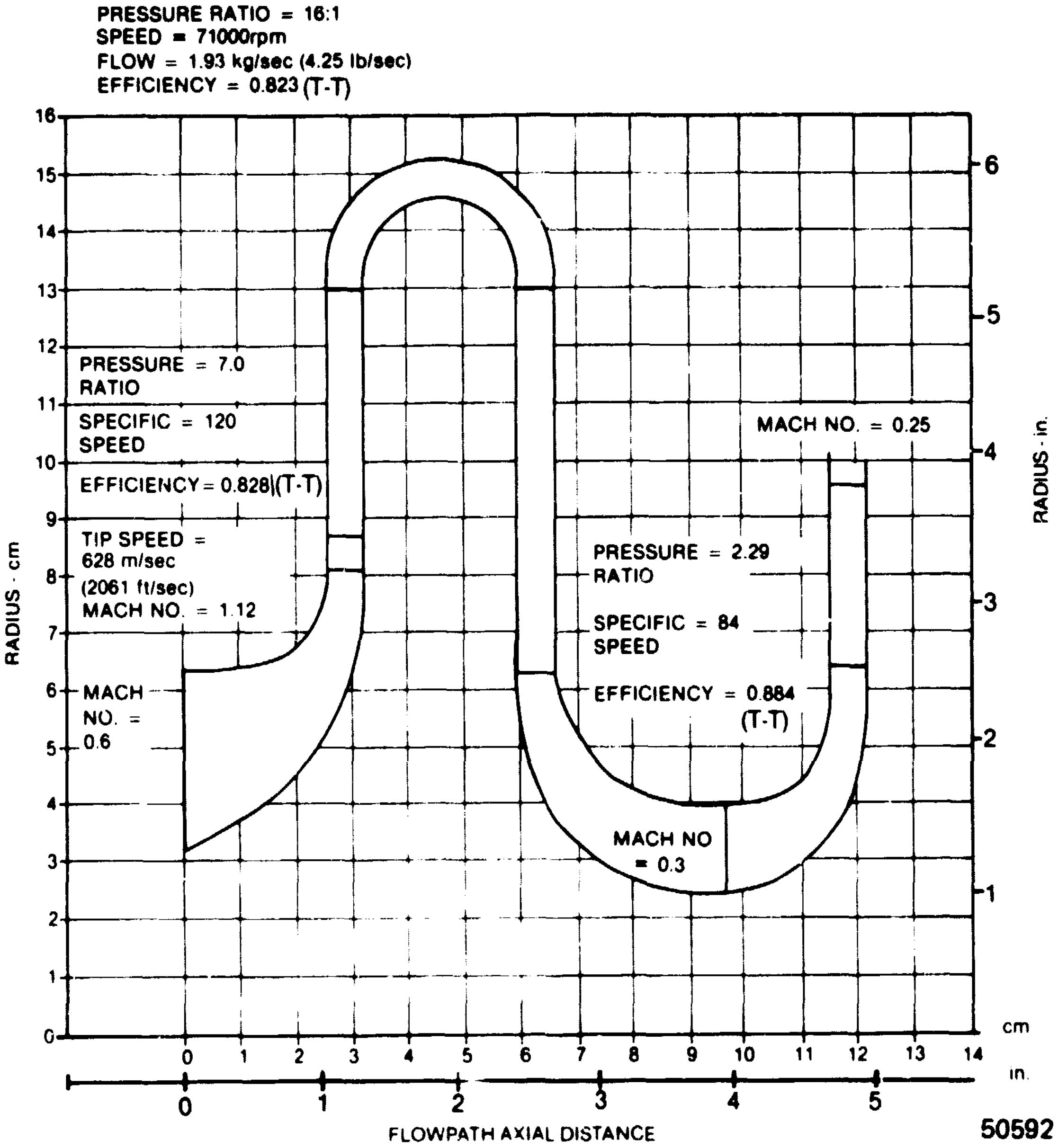

Figure 15. DOUBLE CENTRIFUGAL COMPRESSOR FLOWPATH.

3.3.2 Turbine Concept Analysis

The primary objective of the concept evaluation task was to select a high pressure radial turbine configuration for further refinement in the Task II preliminary design study. Alternative cooled and uncooled turbine rotors, and single-shaft and free-turbine configurations were studied with variations in turbine inlet temperature and cycle pressure ratio. Representative turbine efficiencies were supplied for cycle analysis consistent with 50% flow range and a 1988 design application target. Two turbine inlet nozzle area variation concepts were also evaluated.

Figure 16 shows the level of totally uncooled design point turbine efficiency, based on the previous NASA GATE study results presented in Reference 8, used for initial analysis. The improved level of base turbine efficiency from preliminary specific speed analysis, used for final Task I cycle optimization, is also shown.

Different losses in efficiency were estimated for the respective cooled and uncooled rotor concepts due to the rotor blade cooling. The nozzle assembly shrouds, and the backface of the disk must be cooled for both concepts. In addition, other leakage losses including labyrinth seal leakage flow and cavity purge flow to maintain bearing temperatures must be assigned for a system performance assessment. In the case of a cooled rotor configuration, thicker blading must also be utilized to allow for casting of the geometry. Therefore, cooling loss injection for a high temperature turbine must include all the compromises which must be made aerodynamically and thermodynamically for the construction of the turbine. In addition to the penalties which are incurred due to poorer aerodynamic shapes on the blading, the losses due to cooling injection into the mainstream must also be assessed.

Cooling losses were approximated by a computer program using correlations similar to those of References 9 and 10. The computer code estimates losses of pressure due to a simple momentum mixing model with the cooling flow injected into the mainstream at constant static pressure. Comparisons of this analytical approach to experimental data have shown good agreement for axial turbines. Heat transfer analysis showed that the suction side of the exducer was a critical area for cooling. It was assumed, therefore, that cooling ejection must take place on the suction side of the exducer to provide additional film cooling enhancement. This produces somewhat higher rotor cooling losses as compared to pressure side ejection as used for a lower temperature rotor configuration (Reference 11).

A summary of the cooling flows and leakage distributions assigned for the cycle analysis of the cooled and uncooled configurations is given in Table III with locations identified in Figure 17. A total of 5.0 points loss in efficiency was calculated for the 1644°K (2500°F) cooled rotor turbine system and 1.7 points loss for the uncooled 1477°K (2200°F) turbine system.

An in-house radial turbine meanline analysis computer code, (Radial Flow Turbine Design Point Program), was used to provide the initial uncooled rotor flowpath sizing shown in Figure 18. This program has the capacity of varying selected design parameters to determine their overall effect on total and static efficiencies. The internal loss systems are based on modified internal correlations (References 12, 13 and 14) and the predictions have shown good agreement with test data.

Design point pressure loss components for this configuration, based on the correlations of Reference 13, are given in Table IV. Blade wetted surface friction losses are estimated for both nozzle and rotor based on meridional meanline length, inlet and exit blade angles. Nozzle clearance loss is based on a vane tip gap of 0.0127 cm. (0.005 in.), while rotor clearance loss is based on an assumption of 0.0508 cm. (0.020 in.) rotor shroud face running clearance. The rotor diffusion loss term is associated with the change in absolute critical velocity ratio from inlet tip to rotor exit meanline. Trailing edge loss for both nozzle and rotor accounts for blade exit dump based on nozzle and rotor trailing edge thicknesses of 0.0508 cm. (0.020 in.) and 0.038 cm. (0.015 in.) respectively. Rotor incidence, optimized for design rotor tip relative angle of zero degrees, was included in the analysis. The free-vortex loss relates to friction loss and any sudden contraction or expansion losses in the region between nozzle vane trailing edge and rotor leading edge. In the case of constriction or opening positions of the sidewalls, a pressure loss term was added to the free vortex space corresponding to sudden expansion $\Delta P/P_5 = (1 - A5/A6)^2$ and a full dynamic head loss for a sudden contraction. This loss may be lower in reality but a conservative value was used to account for probable nonuniform incidences and recirculation in the rotor tip region. Disk friction losses were estimated from the relation of Reference 15.

Figure 19 shows the flowpath for the Teledyne CAE Model TS-120 variable nozzle radial turbine which has a demonstrated efficiency of 88% (T-T), Reference 16. Nozzle and rotor losses predicted for this turbine are provided in Table V as a basis for

TABLE III

COOLING FLOWS AND PERFORMANCE PENALTIES FOR COOLED AND UNCOOLED TURBINE CONCEPTS

		% COOLING FLOW/POINTS LOSS IN EFFICIENCY	
COOLING LOCATION (Fig. 17)	COMPONENT	1644°K (2500°F) COOLED ROTOR CONCEPT	1477°K (2200°F) UNCOOLED ROTOR CONCEPT
1	NOZZLE VANE	4.3/0.4	3.0/0.3
2	VANE HUB SHROUD	2.2/0.2	1.1/0.07
3	VANE REAR SHROUD	2.4/0.3	1.1/0.1
4	ROTOR BACKPLATE	1.1/0.1	0.4/0.03
5	VANELESS SPACE & ROTOR SHROUD	0.9/0.1	0.4/0.1
6	ROTOR BACKFACE & SEAL LEAKAGE	1.0/1.0	1.0/1.0
7	REAR BEARING CAVITY PURGE	0.3/0.3	0.1/0.1
8	ROTOR	3.2/2.0	0/0
9	ROTOR GEOMETRY PENALTY	0/0.6	0/0
	TOTAL	14.8/5.0	7.1/1.7

TABLE IV

RADIAL TURBINE DESIGN POINT LOSSES

(Actuated Sidewall Nozzle, Uncooled Rotor)

	NOZZLE ΔP/P (%)	ROTOR ΔP/P (%)
FRICTION	1.7	1.4
CLEARANCE: ACT. SIDEWALL	0.2	3.9
PIV. VANE	0.3	3.9
DIFFUSION	0.0	2.8
TRAILING EDGE	2.0	0.4
INCIDENCE	0.0	0.0
FREE FORTEX & SUDDEN EXPANSION, CONTRACTION	12.2	---
DISK FRICTION	0	2.0

TABLE V

TS-120 TURBINE LOSS COMPONENTS

	NOZZLE Δ P/P (%)	ROTOR Δ P/P (%)
FRICTION	1.5	2.1
CLEARANCE	0.3	4.6
DIFFUSION	0.0	7.1
TRAILING EDGE	2.5	1.3
INCIDENCE	0.0	0.3
FREE VORTEX	7.9	---

comparison with variable nozzle radial turbine loss levels in Table IV. The initial cooled rotor flowpath is shown in Figure 20. Variation of design point efficiency with cycle pressure ratio, input to cycle optimization analysis, is shown in Figure 21.

Off-design efficiency variation with flow for the variable capacity cycle was initially based on selection of a turbine design point at 60% of maximum flow. Subsequent cycle analysis indicated that a minimum duty cycle weighted ESFC would be achieved by optimization of the turbine flowpath for a design point between 70% and 80% of maximum flowrate. Figure 22 shows the off-design schedule of total-to-total efficiency input to initial cycle analyses based on the design point program modeling for an actuated sidewall nozzle configuration. The efficiency schedule was later modified as shown to include the differential effects of nozzle sidewall sudden expansion and contraction at 50% and 100% of maximum flowrate. Variation of the individual loss components with flow is given in Table VI. The total of free vortex and sudden expansion losses for 50% flow exceeds that at design flow by 9.4% while the same total for 100% flow is 4.8% above the design value. The final selection of turbine design point flow was based on minimum specific fuel consumption over the contract duty cycle. The representative radial turbine map shown in Figure 23 was used for simple cycle off-design performance matching.

The meanline flow analysis computer code was used to evaluate design point velocity triangles for actuated sidewall and pivoted vane nozzle concepts. The preliminary velocity diagrams predicted for these nozzle variation configurations are shown in Figures 24 and 25. The flowpath for the preliminary pivoted nozzle configuration is shown in Figure 26. Rotor inlet work factor (V_θ / U_t) was selected to give zero incidence and thus a minimum incidence loss at design point. The design nozzle exit angle was reduced for the pivoted nozzle concept to allow pivoting of the vanes closed for 50% flow without exceeding an exit flow angle of 1.8 rad (80^o). During the latter part of Task I, a Teledyne turbine off-design analysis computer code was used to evaluate efficiency change with flow for the actuated sidewall nozzle configuration. Sudden expansion/contraction loss estimates for the nozzle sidewall step were combined with efficiency losses due to change in rotor velocity diagrams to provide the efficiency/flow schedule shown in Figure 27. It is seen by comparison of Figure 27 with Figure 22 that predictions of turbine efficiency variation with flow for the actuated sidewall nozzle configuration are equivalent for the design point and off-design program analyses. Teledyne CAE test data and analysis presented in Reference 17 were combined as shown in Figure 28 to provide a similar efficiency model for the pivoted vane nozzle configuration. Efficiency curves for the two concepts were compared as shown in Figure 29 to provide

TABLE VI

RADIAL TURBINE OFF-DESIGN LOSSES

	NOZZLE ΔP/P (%)		ROTOR ΔP/P (%)	
	50%	100%	50%	100%
FRICTION	2.7	1.2	0.9	2.8
CLEARANCE	0.3	0.1	3.1	5.7
DIFFUSION	0.0	0.0	1.7	2.6
TRIALING EDGE	2.2	1.8	0.2	1.0
FREE VORTEX SUDDEN EXPANSION, CONTRACTION & INCIDENCE	21.6	17.0	---	---
DISK FRICTION	---	---	2.8	1.4

a basis for selection between the alternate nozzle adjustment methods. The specified duty cycle for the turbine design application includes the following operation schedule:

Percent Rated Power	Percent Time
100	20
60	50
55	20
35	5
IDLE	5

The duty cycle time weighted efficiency for the actuated sidewall nozzle exceeds that for the pivoted vane nozzle by about one (1.0) efficiency point. The actuated nozzle sidewall concept was, therefore, selected for further evaluation in later tasks.

ORIGINAL PAGE IS
OF POOR QUALITY

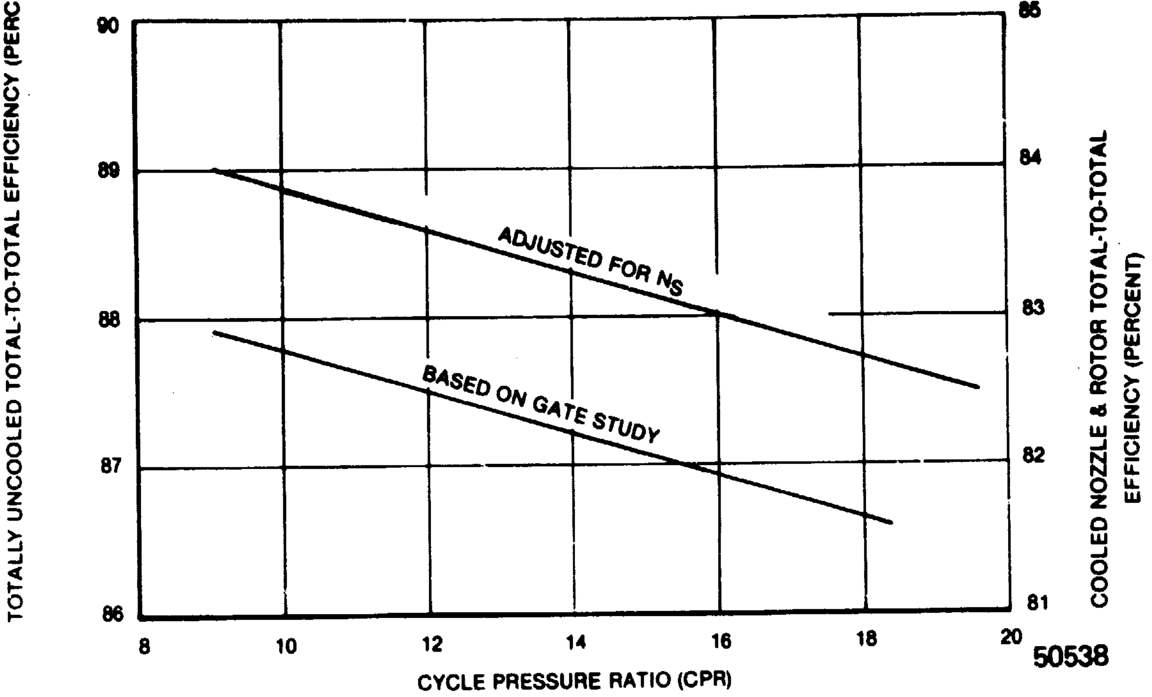

Figure 16. PRELIMINARY TURBINE DESIGN POINT EFFICIENCIES.

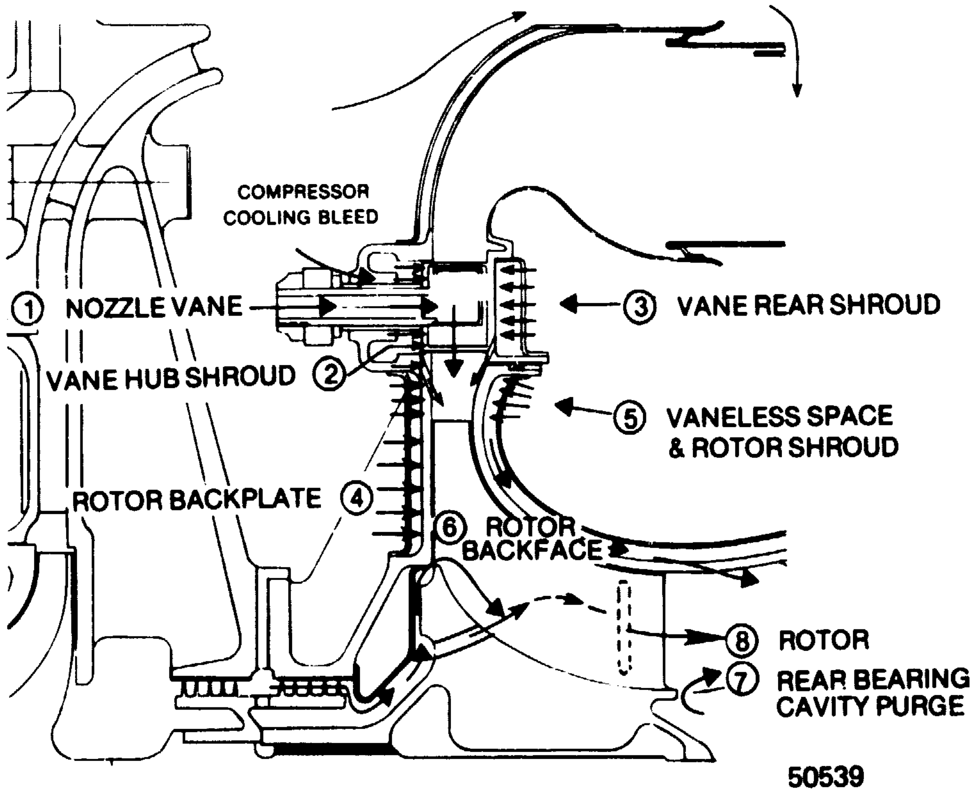

Figure 17. TURBINE COOLING AND LEAKAGE FLOWS.

ORIGINAL PAGE IS OF POOR QUALITY

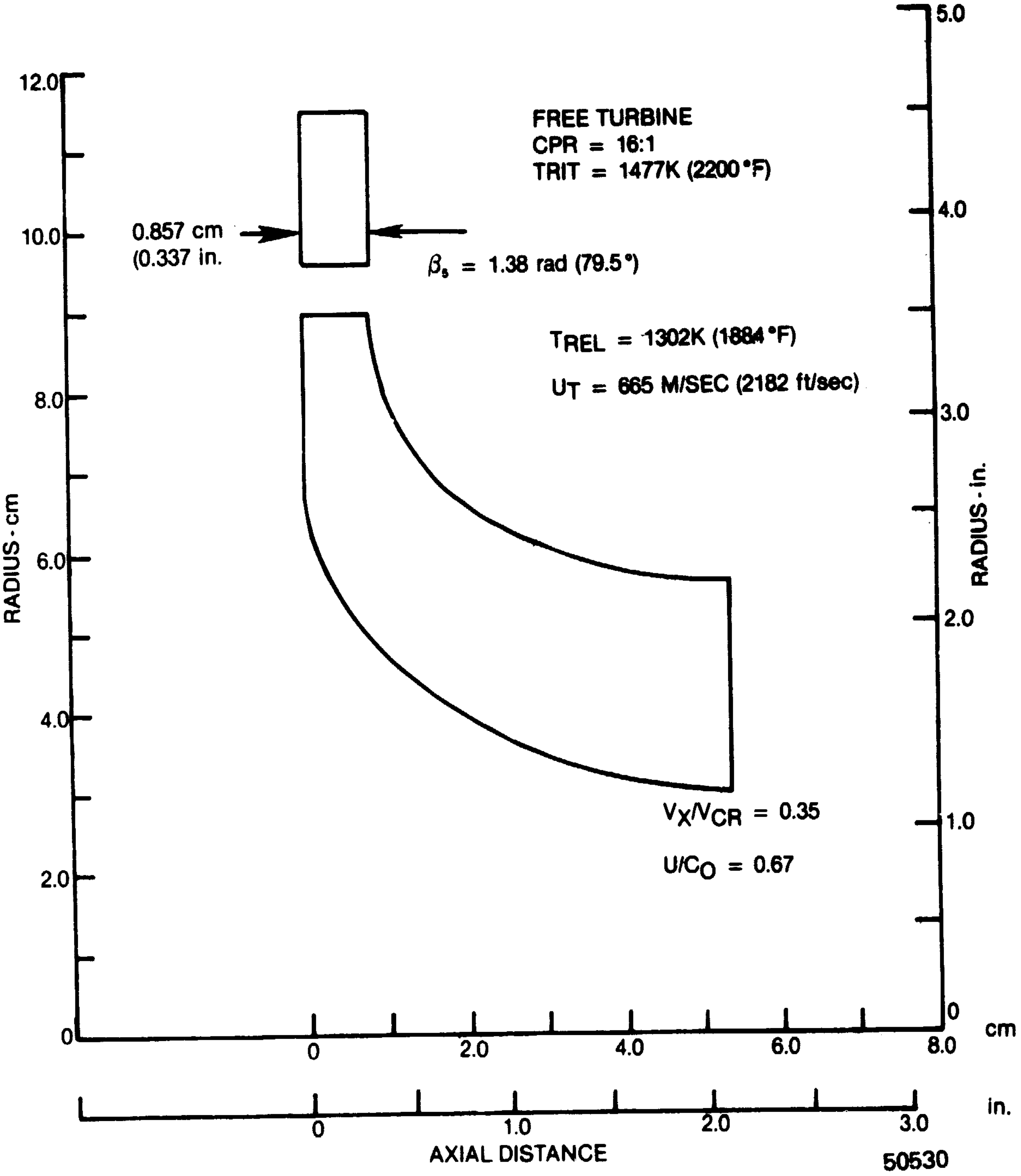

Figure 18. PRELIMINARY, UNCOOLED ROTOR, ACTUATED SIDEWALL TURBINE FLOWPATH.

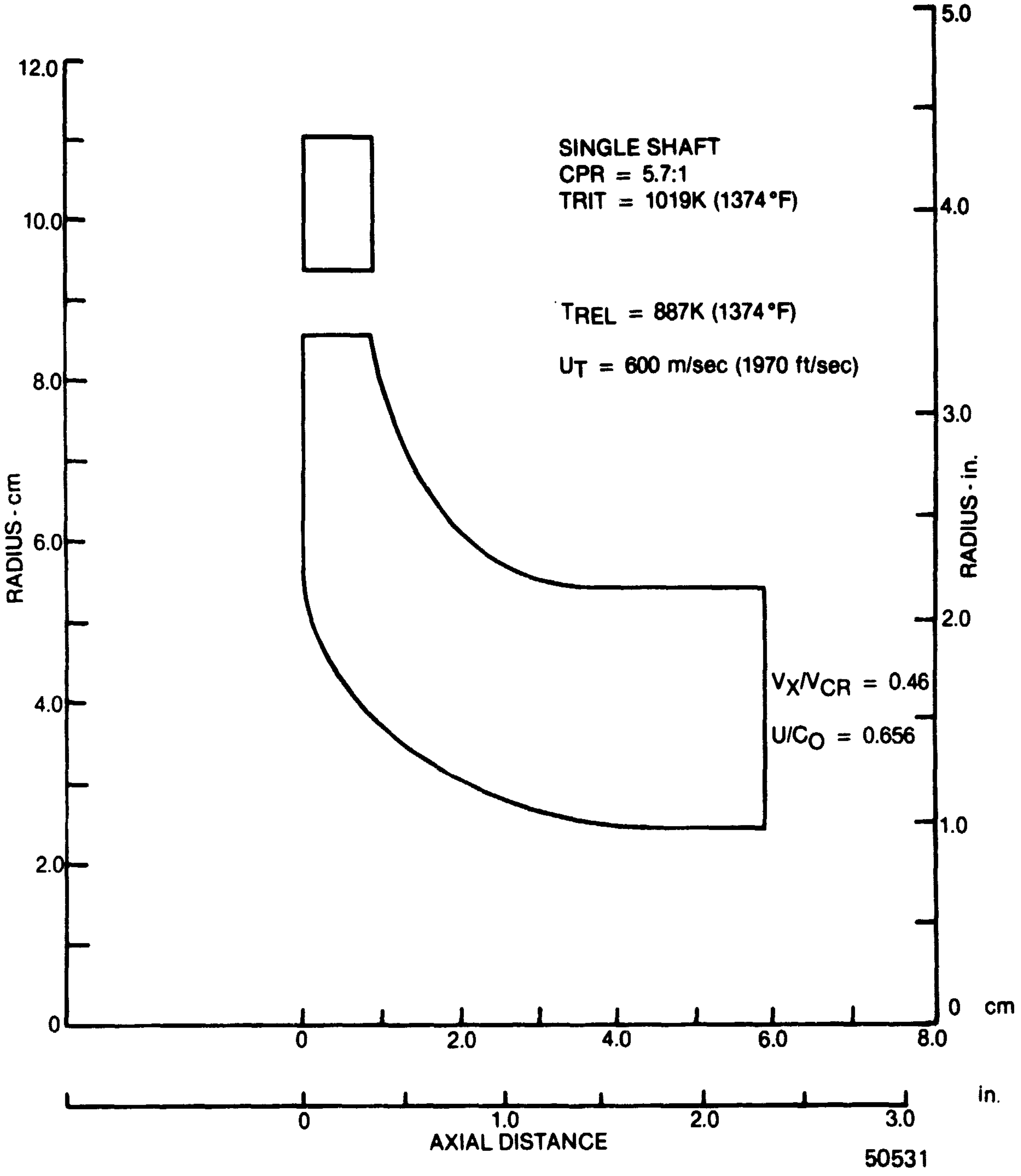

Figure 19. TS-120 RADIAL TURBINE FLOWPATH.

ORIGINAL PAGE IS
OF POOR QUALITY

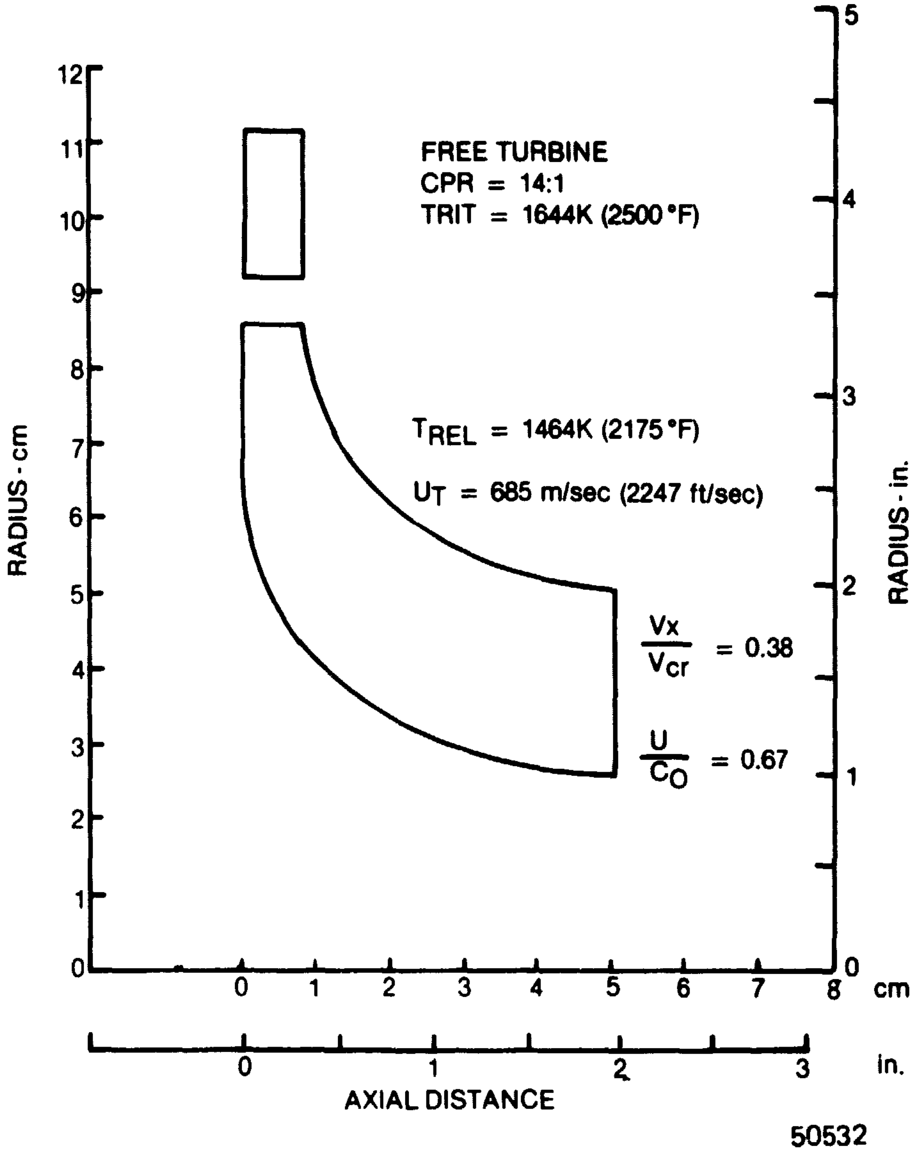

Figure 20. PRELIMINARY COOLED ROTOR TURBINE FLOWPATH.

ORIGINAL PAGE IS
OF POOR QUALITY

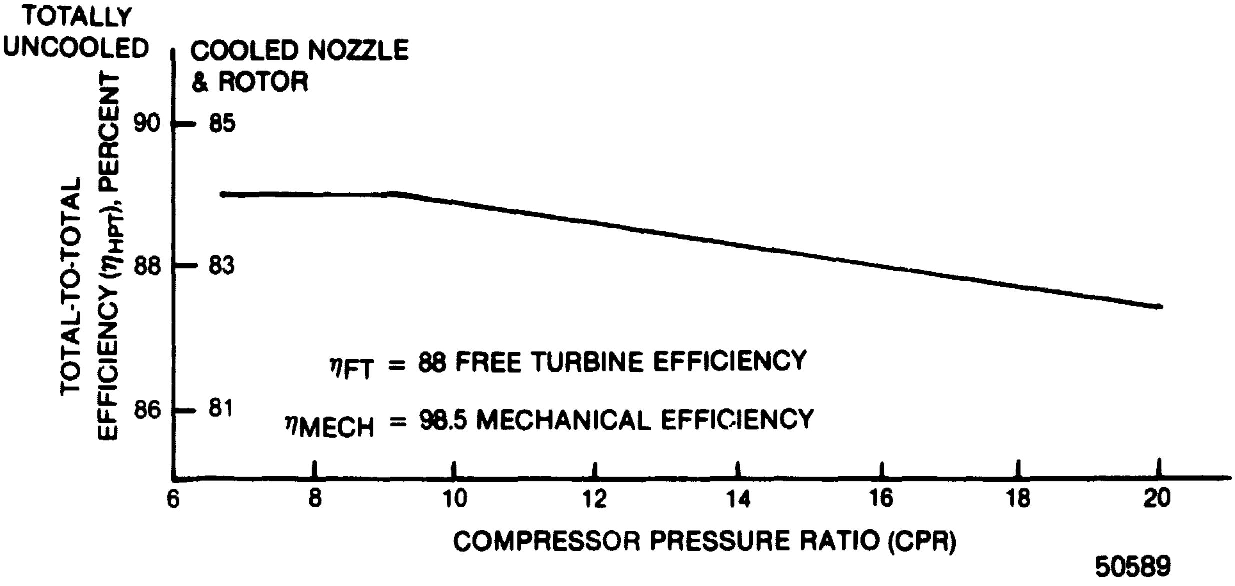

Figure 21. TURBINE DESIGN POINT EFFICIENCY CHANGE WITH CPR.

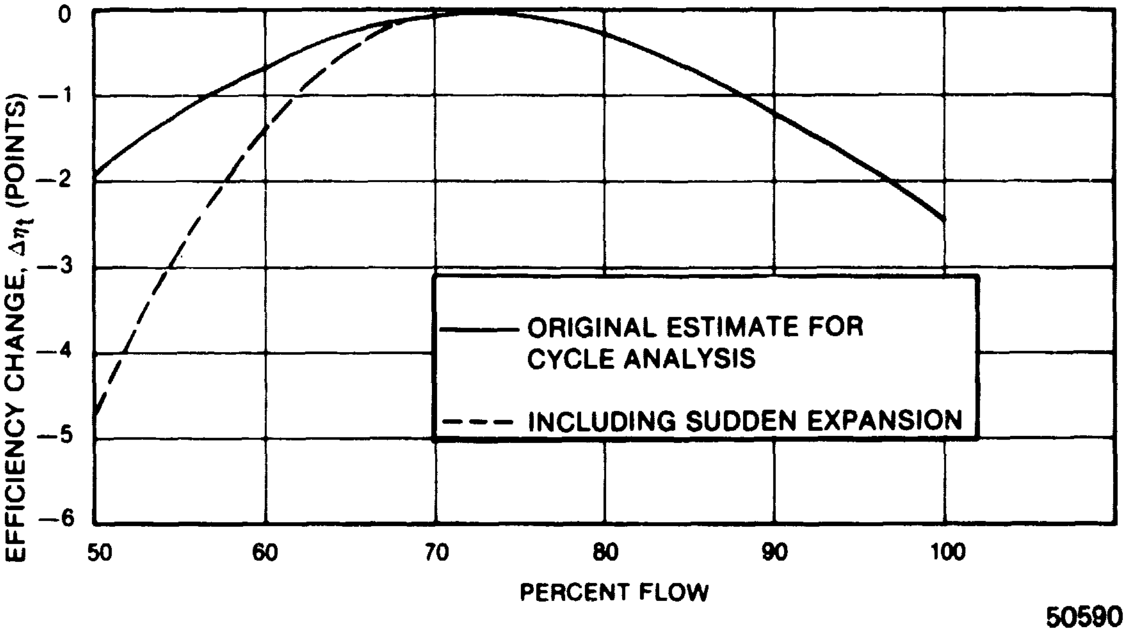

Figure 22. PRELIMINARY TURBINE EFFICIENCY SCHEDULE WITH FLOW.

ORIGINAL PAGE IS
OF POOR QUALITY

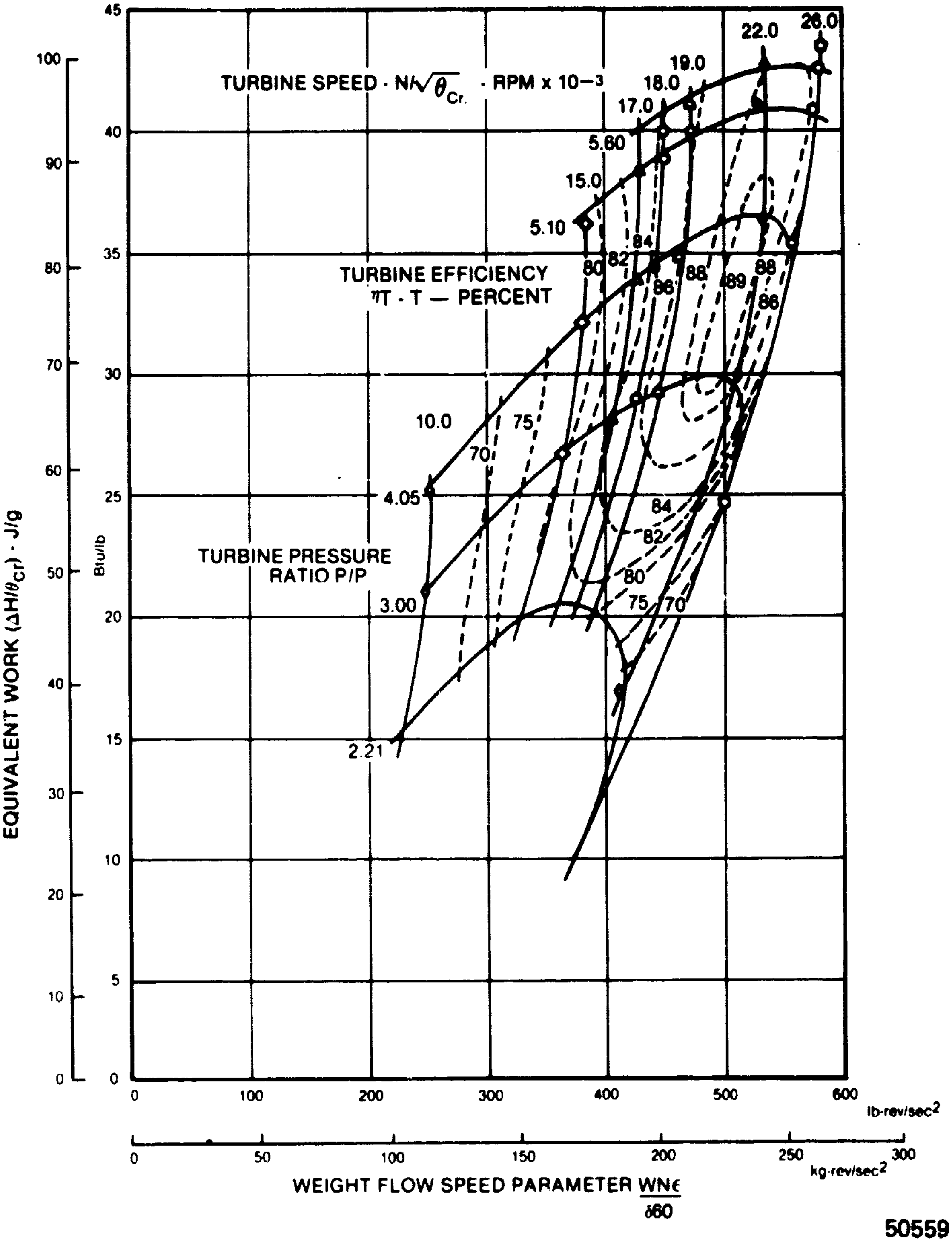

50559

Figure 23. RESEARCH RADIAL TURBINE PERFORMANCE MAP.

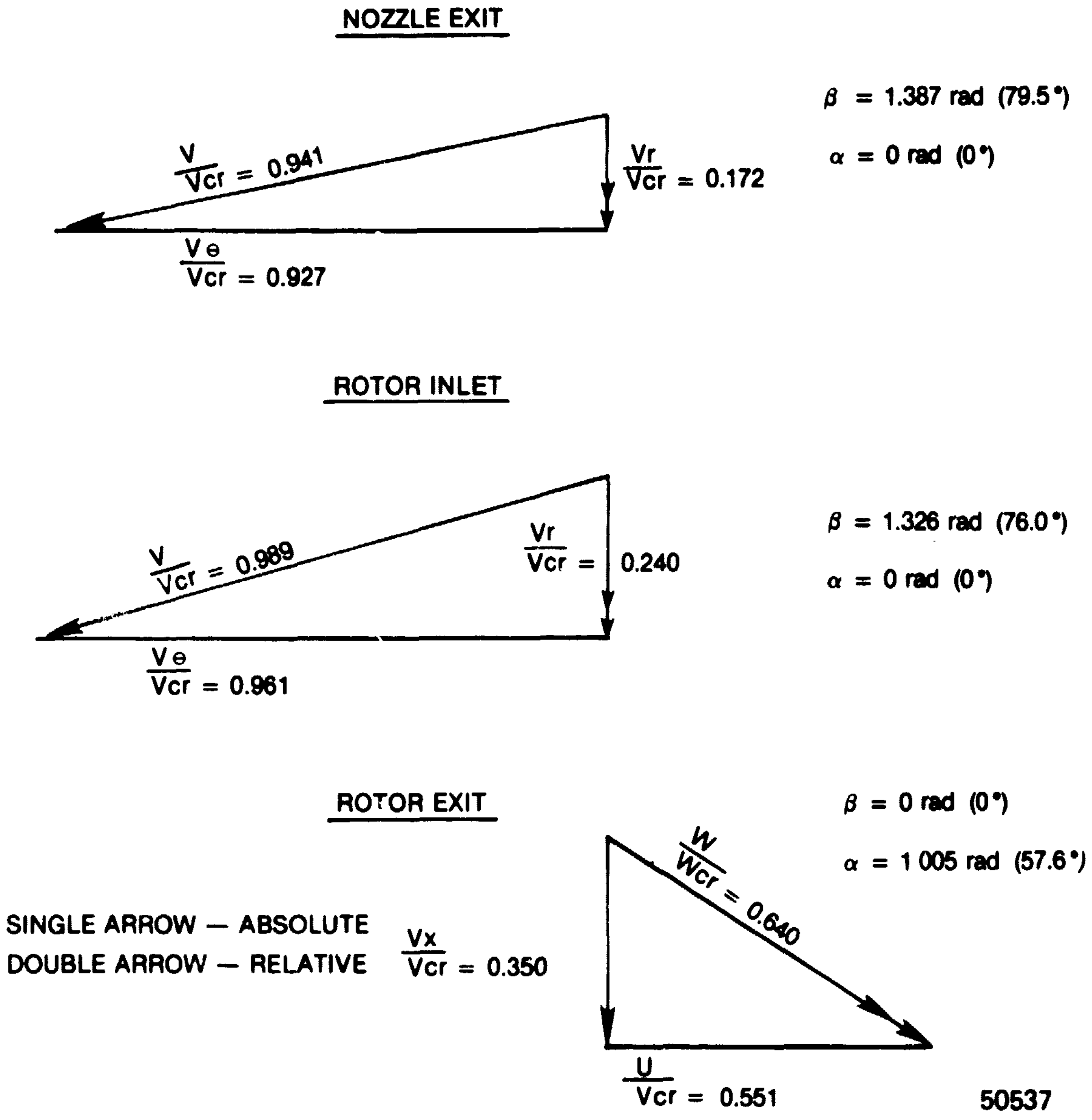

Figure 24. ACTUATED SIDEWALL DESIGN POINT VELOCITY TRIANGLES.

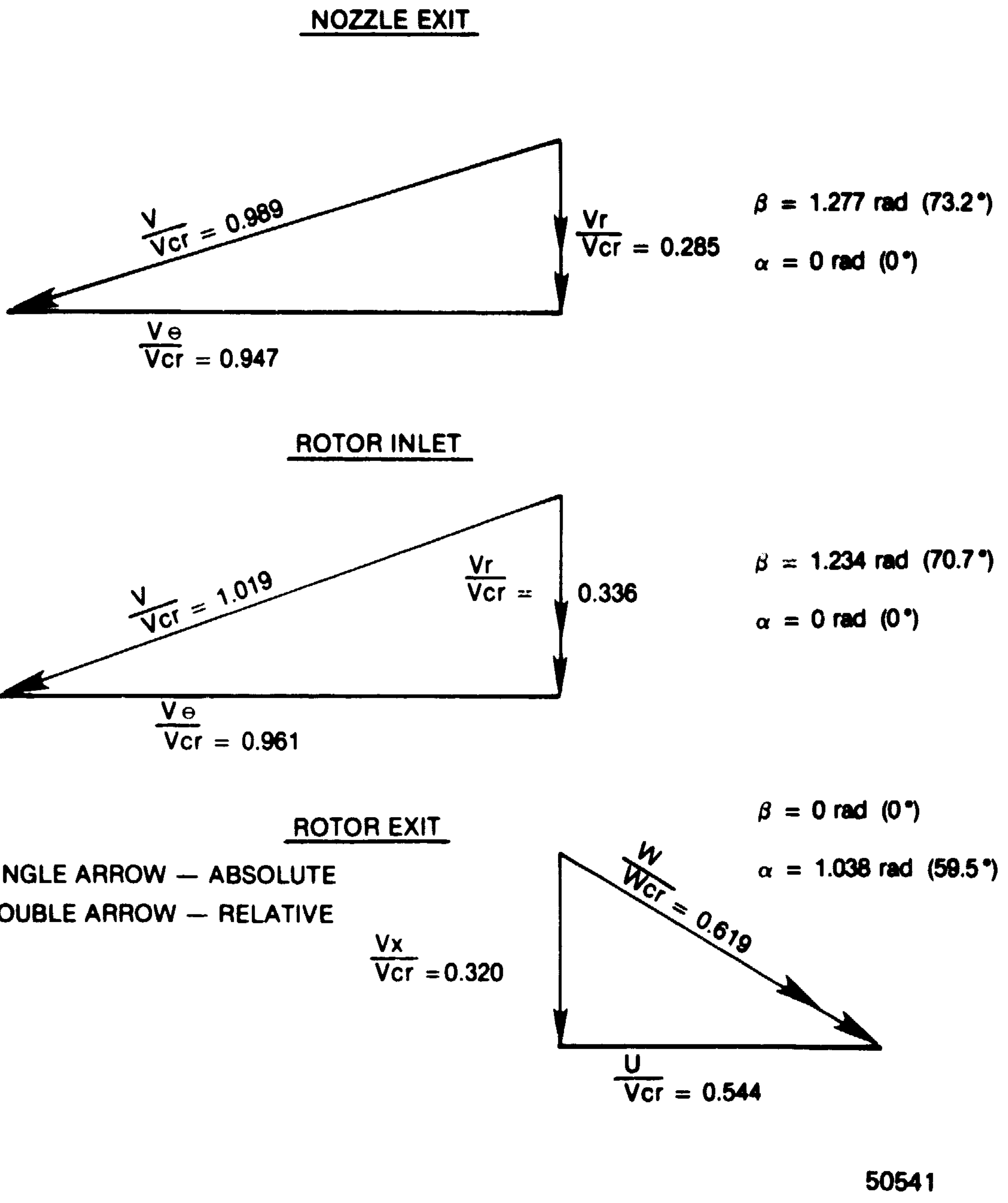

Figure 25. PIVOTED NOZZLE DESIGN POINT VELOCITY TRIANGLES.

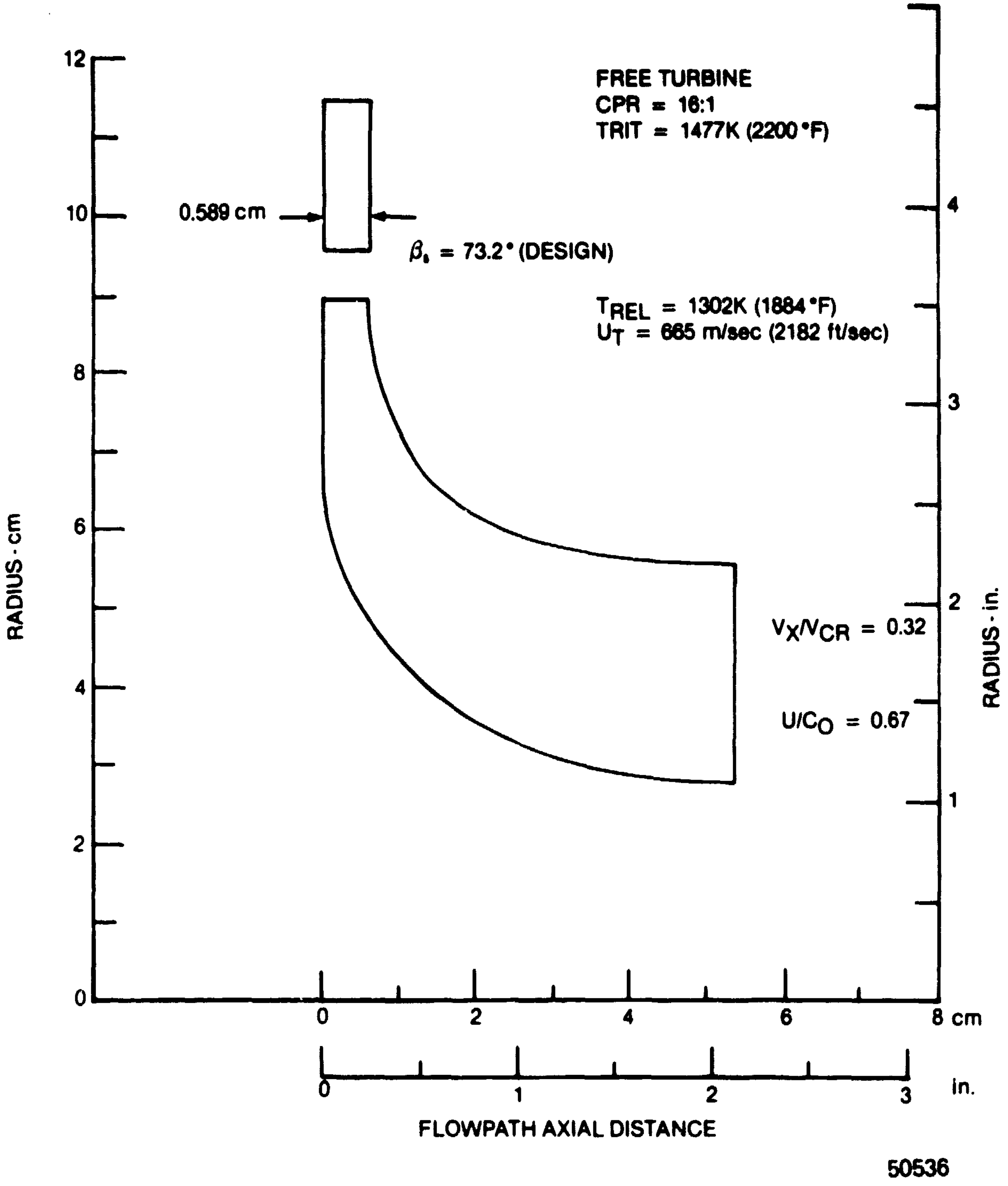

Figure 26. PRELIMINARY PIVOTED NOZZLE TURBINE FLOWPATH.

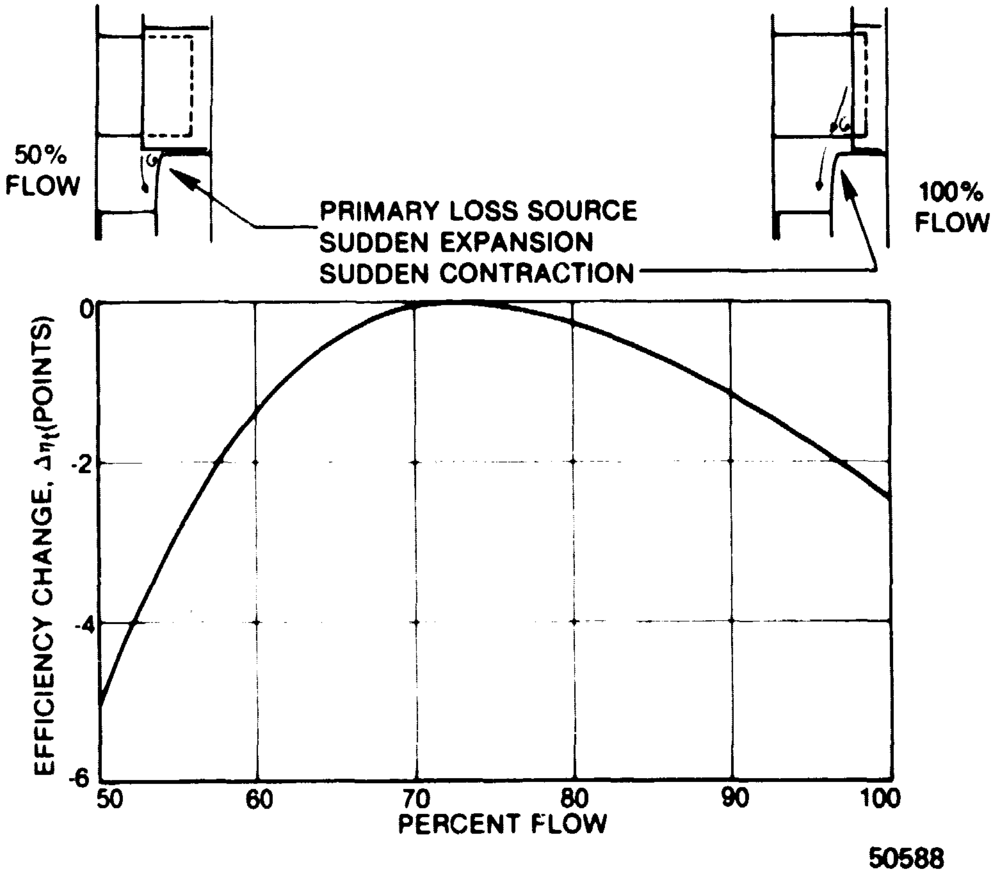

Figure 27. ACTUATED SIDEWALL OFF-DESIGN PERFORMANCE.

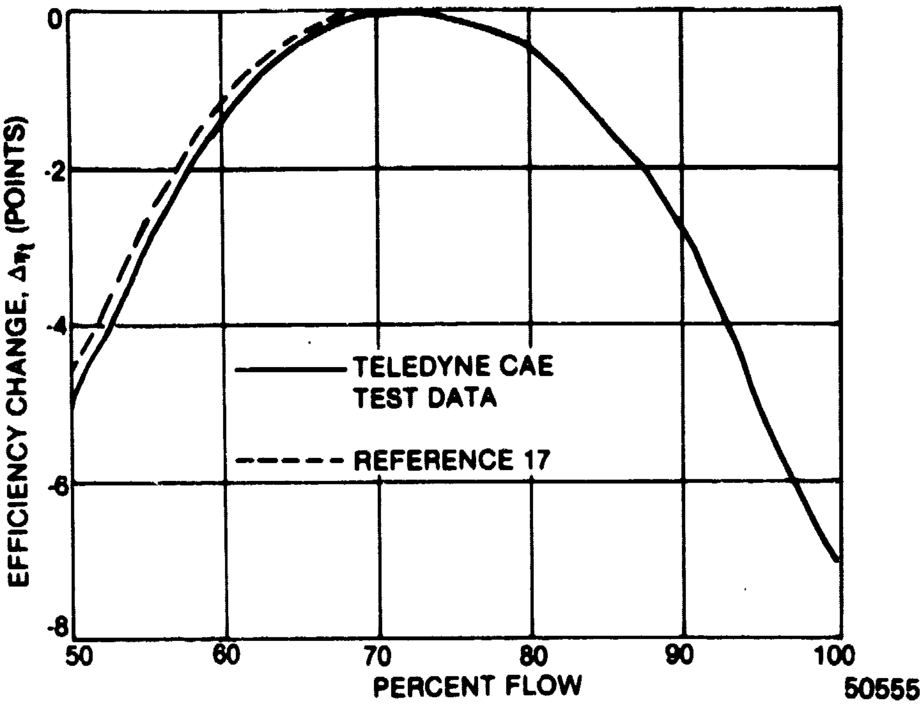

Figure 28. PIVOTED NOZZLE PERFORMANCE.

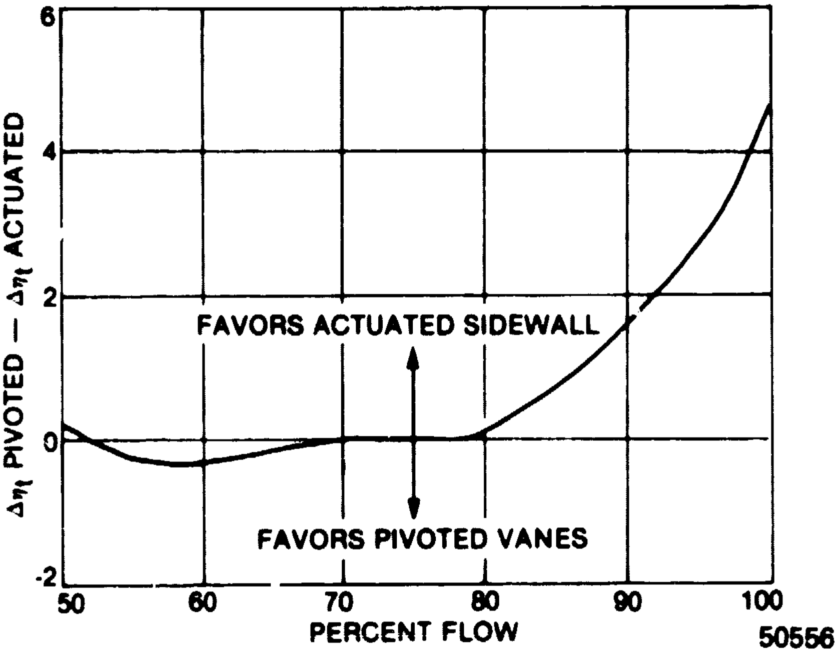

Figure 29. NOZZLE CONCEPT SELECTION.

3.3.3 Cycle Analysis

3.3.3.1 Variable Geometry Cycle Analysis

Cycle analyses were accomplished using a Teledyne CAE performance prediction program, modified for single-shaft and free-turbine engine applications. A helicopter power requirement curve, shown in Figure 30 (Reference 18) was used to relate flight velocity and power level based on the contract duty cycle in order to provide necessary ram inlet conditions input for the performance program.

Compressor design point variation of efficiency with pressure ratio including variable geometry losses is given in Figure 10, Section 3.3.1. The variation of compressor efficiency with flow rate at constant pressure ratio used in the variable capacity cycle studies is shown in Figure 13 of the same section. Turbine design point efficiency variation with compressor pressure ratio assumed for both single-shaft and free-turbine configurations is given in Figure 21, Section 3.3.2. The variable nozzle single-shaft TS-120 turbine produced a design specific work ($\Delta H/\theta_{CR}$) of 43.6 BTU/lb with efficiency in excess of 0.880 (T-T) in the early 1970's, Reference 16. With application of advanced technology the variable nozzle radial turbine should produce a design specific work of 38.3 BTU/lb with 0.880 (T-T) efficiency (for 16:1 CPR application) including the effects of variable geometry and stator cooling and this value was assigned for baseline performance. The initial turbine off-design efficiency schedule with flow rate used for the variable capacity cycle studies is given in Figure 22, Section 3.3.2.

Optimum cycle pressure ratios were determined for the following turbine inlet temperature and cycle combinations at 218.7 km/hr (118 kts) which relates to the initial 60% power design point as shown in Figure 30.

ENGINE	TURBINE INLET TEMP	COOLING
Free-turbine	1644K (2500°F)	Yes
	1533K (2300°F)	No
	1477K (2200°F)	No
	1422K (2100°F)	No
	1311K (1900°F)	No
Single-shaft	1644K (2500°F)	Yes
	1533K (2300°F)	No
	1422K (2100°F)	No
	1311K (1900°F)	No

Other design point cycle assumptions are as follows:

- Inlet pressure loss $\frac{\Delta P}{P} = 0.01$
- Combustor pressure loss $\frac{\Delta P}{P} = 0.03$
- Combustor efficiency $\eta = 0.995$
- Interturbine transition duct loss $\frac{\Delta P}{P} = 0.01$
- Power turbine efficiency including a one point loss for variable geometry $\eta = 0.88$
- Exhaust diffuser loss $\frac{\Delta P}{P} = 0.059$
- Gear box mechanical efficiency $\eta = 0.985$
- Gas generator spool mechanical efficiency $\eta_{MECH} = 0.99$

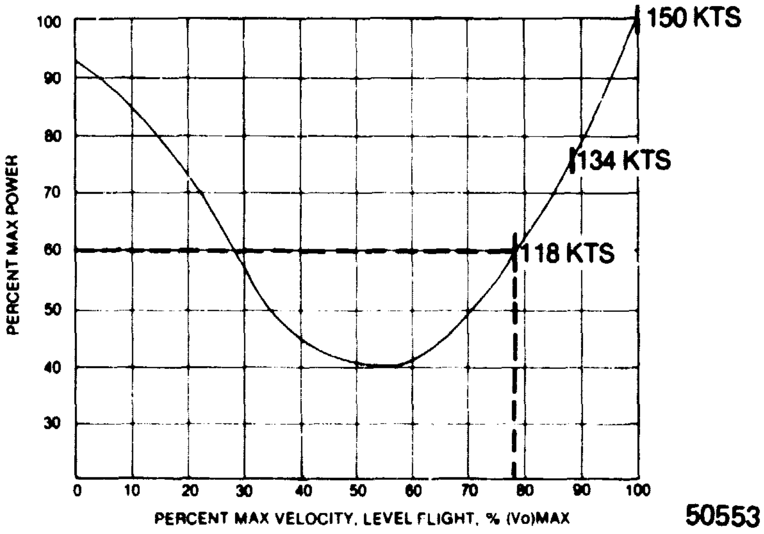

Figure 30. HELICOPTER POWER REQUIRED SCHEDULE.

Figures 31 and 32 show the results of these optimization runs at 60% power for those combinations selected for further analysis. Figure 33 shows the variation of equivalent specific fuel consumption with turbine inlet temperature at constant (60%) power and optimum cycle pressure ratios for the single and free-shaft turbine configurations. Those configurations selected for further consideration based on equivalent specific fuel consumption over the contract power duty cycle are listed in Table VII.

Two free-turbine configurations were chosen for further analysis: with turbine cooling - 1644K (2500°F) turbine inlet temperature and cycle pressure ratio of 14:1; and, without turbine cooling - 1477K (2200°F) turbine inlet temperature and cycle pressure ratio of 16:1. Considering the variation of equivalent specific fuel consumption with percent power, Figure 34 1644K (2500°F) cooled and Figure 35 1477K (2200°F) uncooled, the following revised design points were selected:

(1) Cooled: 1644K (2500°F) TRIT, 78% power (71% flow)

(2) Uncooled: 1477K (2200°F) TRIT, 82% power (78% flow)

Optimization of both turbine and compressor component efficiencies at these design points allows mission time-weighted ESFC to be minimized for cooled and uncooled rotor configurations. Further refinement of the design point selection, off-design ESFC variation analysis could be carried out with minimal impact on design flow selection and ESFC estimates. Engine cycle parameters for these configurations are shown on the final Task I engine flowpath in Figures 36 and 37.

The optimum cycle pressure ratio, 15:1 at 1533K (2300°F) turbine inlet temperature, for the single shaft turbine configuration, resulted in a very high turbine specific work requirement. In order to select a more representative cycle for 1533K (2300°F) turbine inlet temperature within contract work limits, a compressor pressure ratio of 9.0:1 was chosen. Figure 38 depicts the variation of percent flow, equivalent shaft horsepower, equivalent specific horsepower, and equivalent specific fuel consumption for the selected uncooled single-shaft cycle. The single-shaft cooled and uncooled cycles were eliminated late in Task I due to Army preference of a free-turbine front drive configuration for all foreseeable helicopter applications.

3.3.3.2 Simple Cycle Analysis

An all-variable geometry cycle (16:1, free turbine, 1477K (2200°F), 50-100 percent flow at constant speed) was compared to a simple cycle operating over the same power duty mission. The estimated two stage compressor map similar to that used for the variable cycle (scaled from Reference 7) and shown in Figure 39 was used in the simple cycle analysis. Higher base level efficiencies were used due to elimination of variable geometry penalty losses. The maximum flow condition of 2.27 kg/sec (5.0 lb/sec) and a pressure ratio of 16:1 set the compressor design operating conditions at 100 percent speed. The HP radial turbine map, used for matching, was assumed to be a scale of the research turbine performance map shown in Figure 23, Section 3.3.2, and the single stage axial power turbine performance is based on a scale of the test map of Reference 19 (Figure 40).

Initial matching calculations showed that only a very limited compressor surge free operating line (mechanical speeds greater than 85 percent) could be attained with the estimated component performance map data inputs. Broader compressor surge operating characteristics would require more stages and/or compressor variable geometry. To show the simple cycle at its higher potential, a surge free compressor operating line, passing through the peak efficiency islands (Figure 41) was assigned for part power operation. A variable geometry power turbine is then required to obtain the desired engine operating characteristics. The operating line excursions on the HP and LP turbine maps are shown in Figures 42 and 43, respectively.

Figure 44 shows the variation of percent compressor airflow, equivalent shaft horsepower, equivalent specific horsepower, and equivalent specific fuel consumption for the simple cycle, variable power turbine study. The fuel consumption of the simple cycle with variable power turbine is better than the all-variable cycle at maximum power, ESFC = 0.256 kg/hr-kw (0.421 lbs/hr-hp) vs 0.261 kg/hr-kw (0.430 lbs/hr-hp), due to higher base level component efficiencies resulting from lower variable geometry penalties. However, the predicted minimum and part power ESFC for the simple cycle is greater than the all-variable geometry configuration primarily due to a poorer overall thermal efficiency and to differences in component efficiency levels due to matching. The compressor and gas generator (HP) turbine component efficiencies were reduced for guide vane, variable stator losses, and turbine variable geometry for the all-variable cycle. The high pressure and power turbines for the all-variable cycle, however, operate at constant work ($\Delta H/\theta_{cr}$), temperature, analysis. This value includes a degradation of two points in efficiency for variable geometry mechanisms. Since turbine inlet temperature and compressor pressure ratio changes for the simple cycle, both the high pressure and power turbine work and corrected speed vary with power level. A representative performance map with a peak efficiency of 88% was also selected for the simple cycle power turbine. As a result of the matching characteristics, a maximum work requirement of the simple cycle power turbine occurs at or near the limit load capability of the turbine. The result of an operating line excursion from 100 percent shaft power to 58 percent power on the simple cycle power turbine map is a change of 5.5 points of efficiency (Figure 43) due to power turbine inlet temperatures and pressure ratio matching. Although other base component efficiency levels are higher for the simple cycle, the poorer matching characteristics and lower cycle thermal efficiency at part power, with respect to the all-variable cycle, causes the minimum ESFC to be 1.9% greater for the simple cycle. The duty cycle time-weighted ESFC for the simple cycle is 0.280 kg/kw-hr (0.461 lb/hp-hr). This is 7.1% greater than the 0.262 kg/kw-hr (0.430 lb/hp-hr) time-weighted ESFC previously estimated for the all-variable cycle.

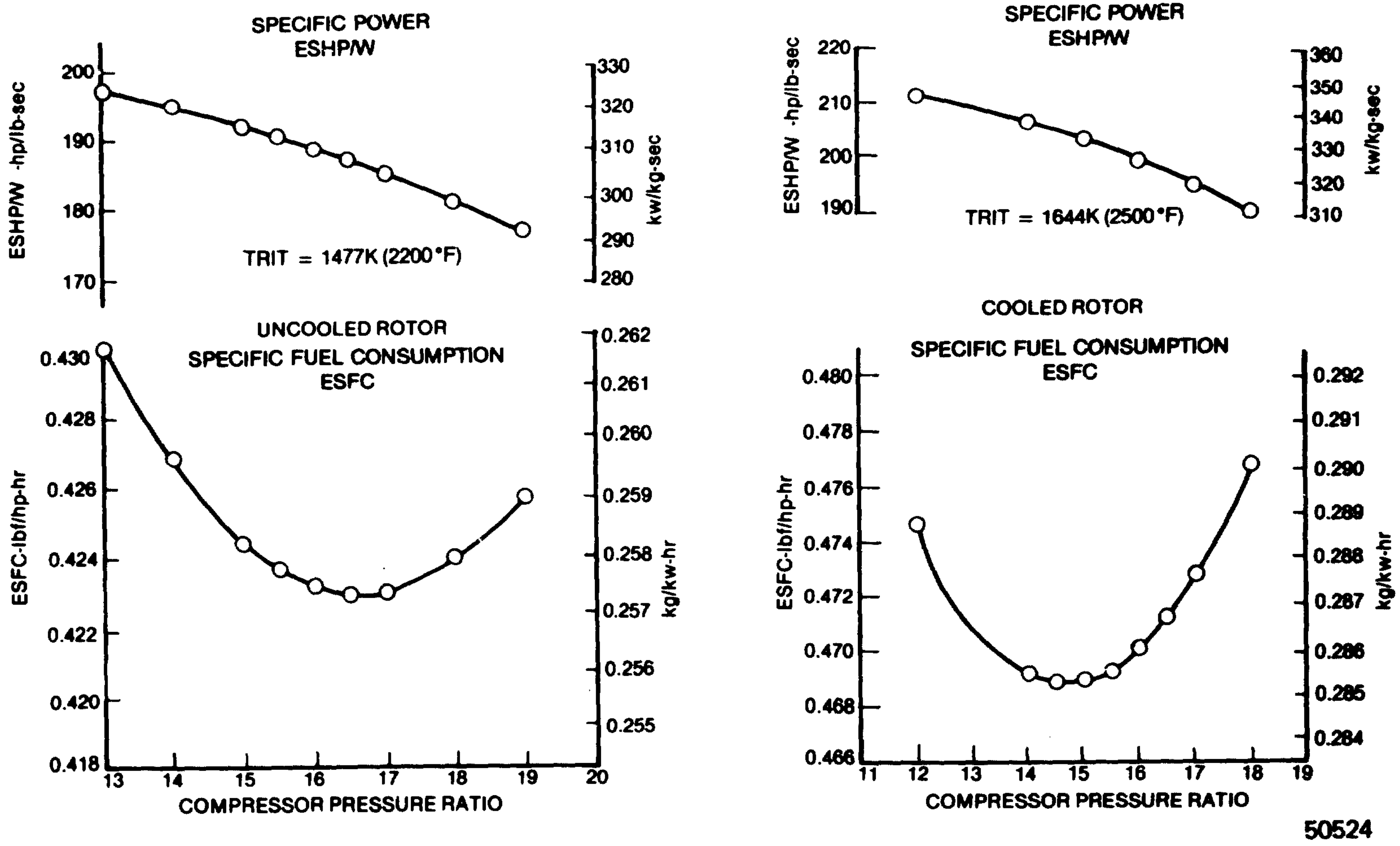

Figure 31. FREE TURBINE CYCLE CPR OPTIMIZATION, 60% POWER DESIGN POINT.

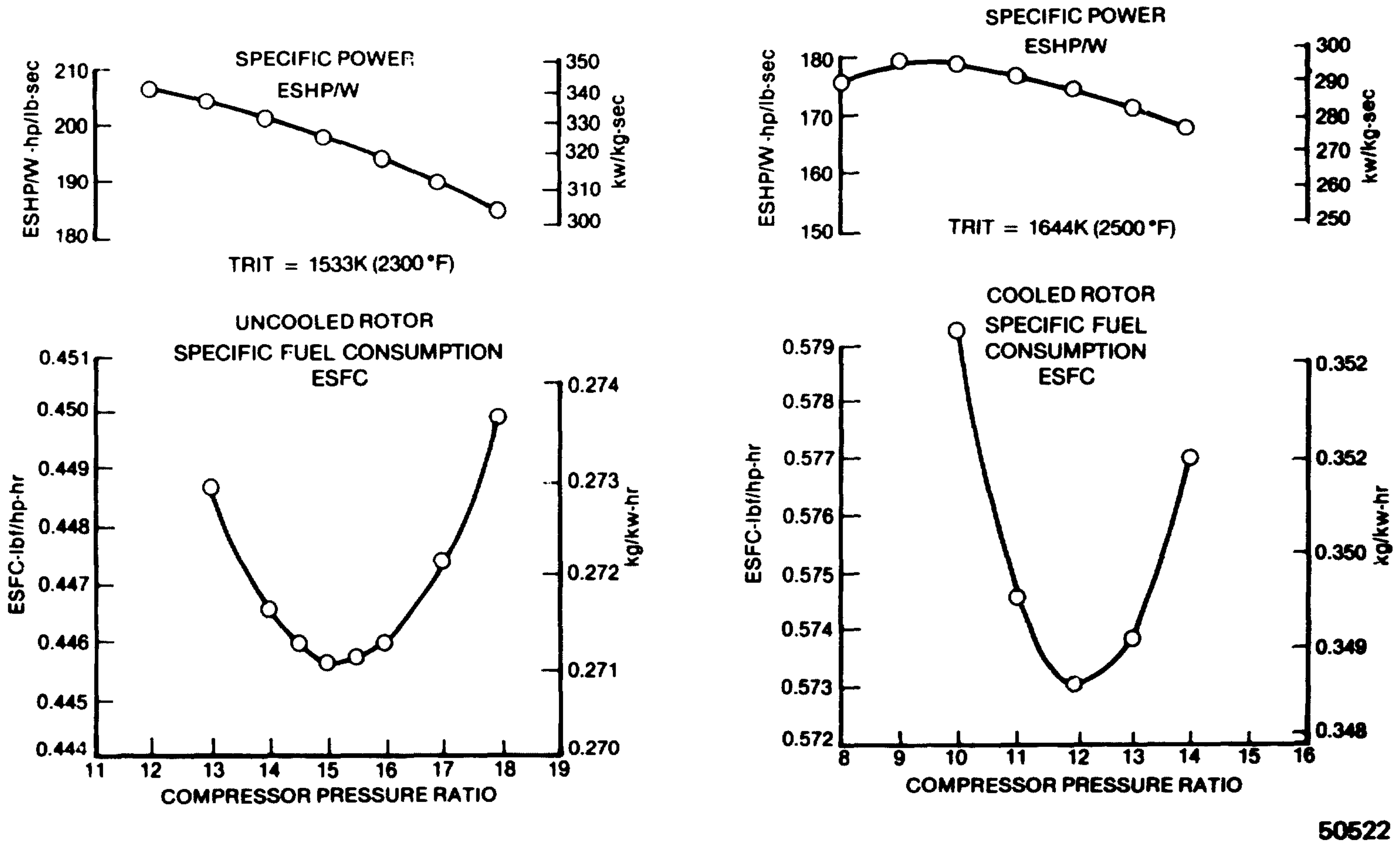

Figure 32. SINGLE-SHAFT CPR OPTIMIZATION, 60% POWER DESIGN POINT.

TABLE VII

DESIGN POINT CYCLE SELECTION RESULTS (60% POWER)

	FREE TURBINE	SINGLE SHAFT
COOLED		
TRIT, K (°F)	1644 (2500)	1644 (2500)
CPR	14:1	12:1
ΔH, J/g (Btu/lb)	469.5 (201.7)	761.2 (327.0)
N (rpm)	75,000	62,000
Trel, K (°F)	1464 (2175)	—
Ut, m/sec (ft/sec)	685 (2247)	—
$f(AN^2) \times 10^{-8}$ m^2rev^2/sec^2 ft^2rev^2/sec^2	0.33 (3.50)	—
ESHP/W, kw-sec/kg (hp-sec/lb)	338.7 (206)	287.7 (175)
ESFC, kg/hr-kw (lb/hr-hp)	0.285 (0.469)	0.349 (0.573)
UNCOOLED		
TRIT, K (°F)	1477 (2200)	1533 (2300)
CPR	16:1	9:1
ΔH, J/g (Btu/lb)	442.3 (190)	657.6 (282.5)
N (rpm)	75,000	62,000
Trel, K (°F)	1302 (1884)	1277 (1840)
Ut, m/sec (ft/sec)	665 (2182)	719 (2359)
$f(AN^2) \times 10^{-8}$ m^2rev^2/sec^2 ft^2rev^2/sec^2	0.32 (3.44)	0.65 (6.96)
ESHP/W kg/hr-kw (lb/hr-hp)	307.4 (187)	356.7 (217)
ESFC, kg/hr-kw (lb/hr-hp)	0.257 (0.423)	0.285 (0.469)

50547

ORIGINAL PAGE IS
OF POOR QUALITY

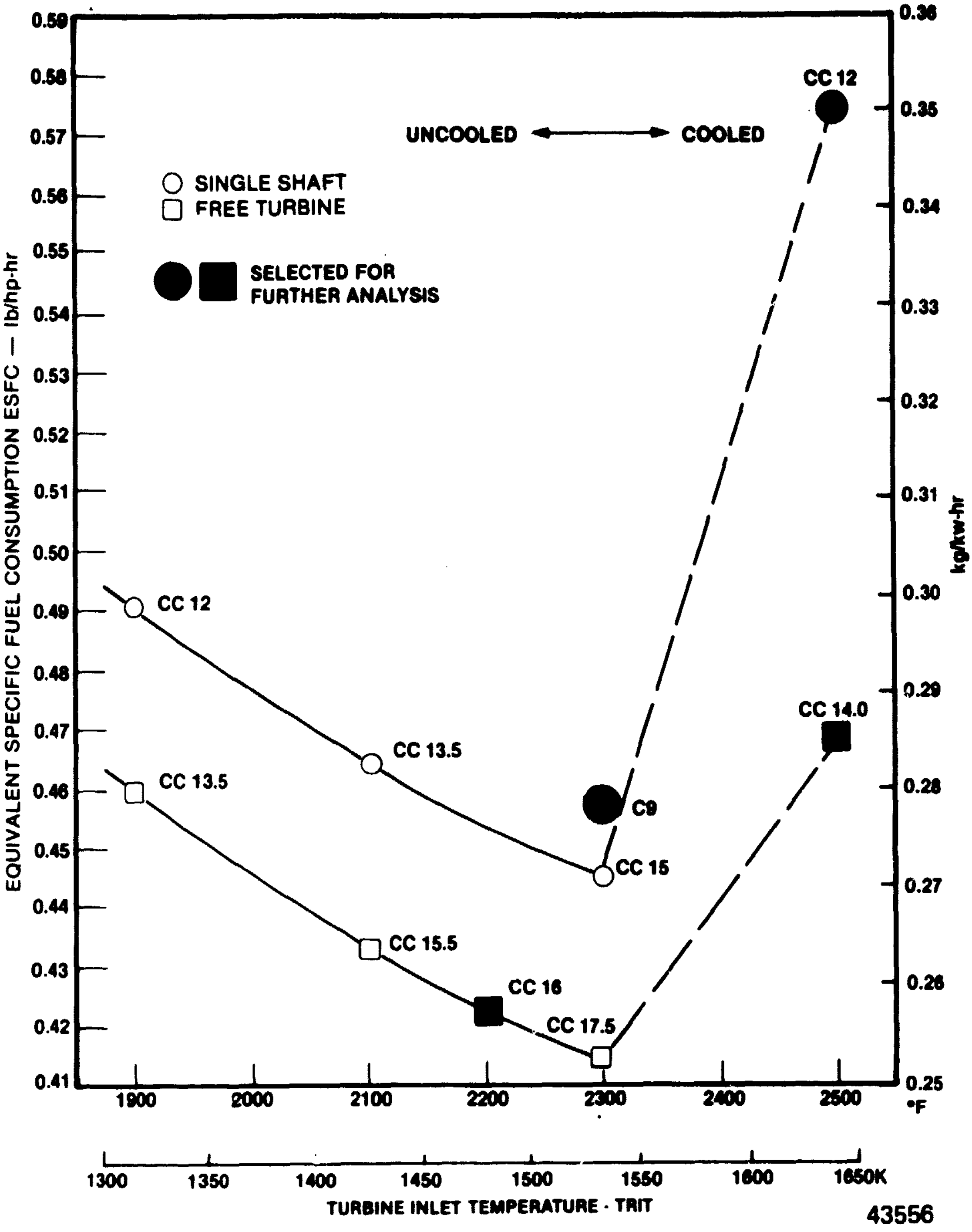

Figure 33. CYCLE OPTIMIZATION SUMMARY, 60% POWER DESIGN POINT.

ORIGINAL PAGE IS
OF POOR QUALITY

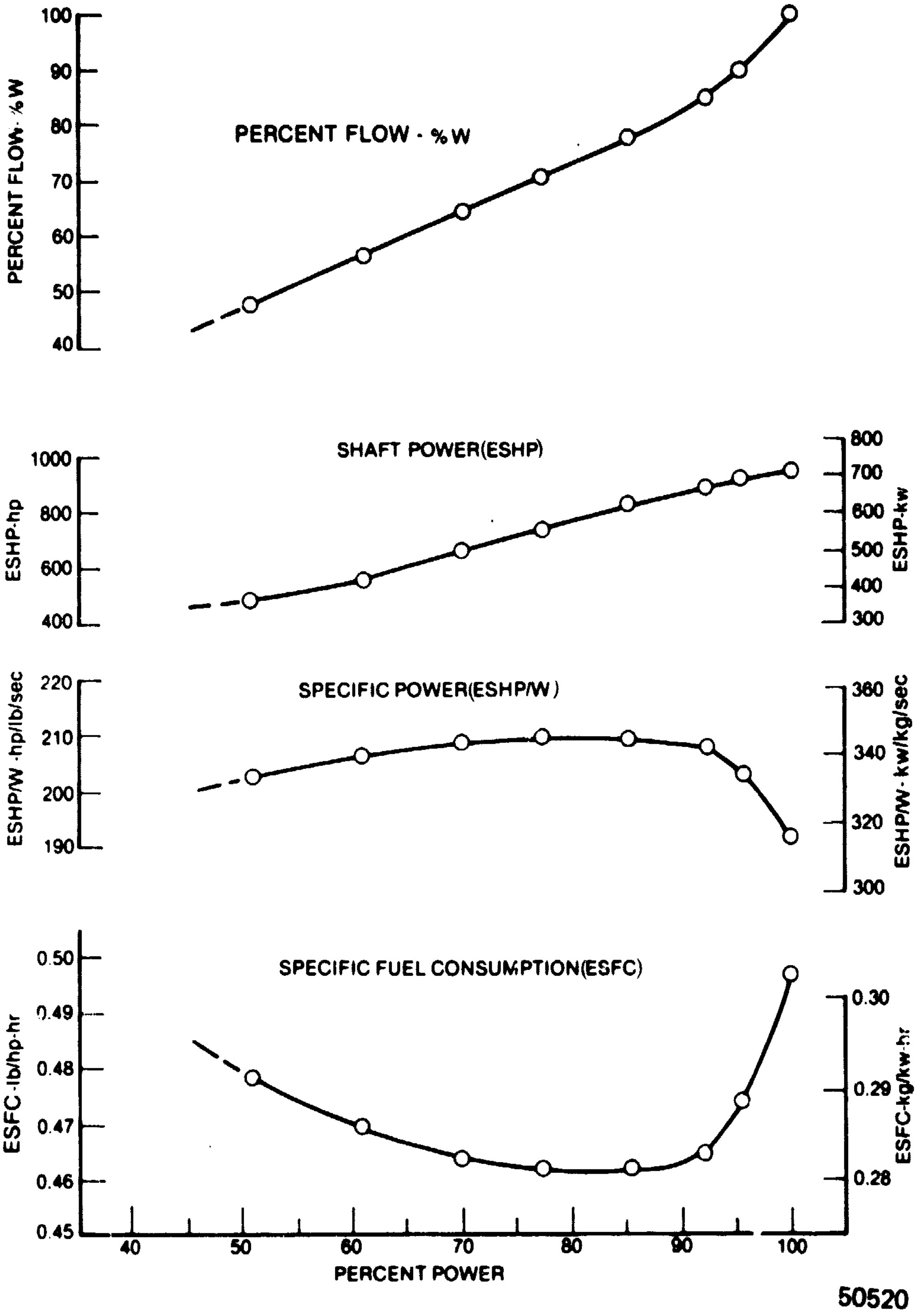

Figure 34. FREE-TURBINE PERFORMANCE, CPR = 14.0, TRIT = 1644K (2500°F), COOLED, S.L., STD. DAY.

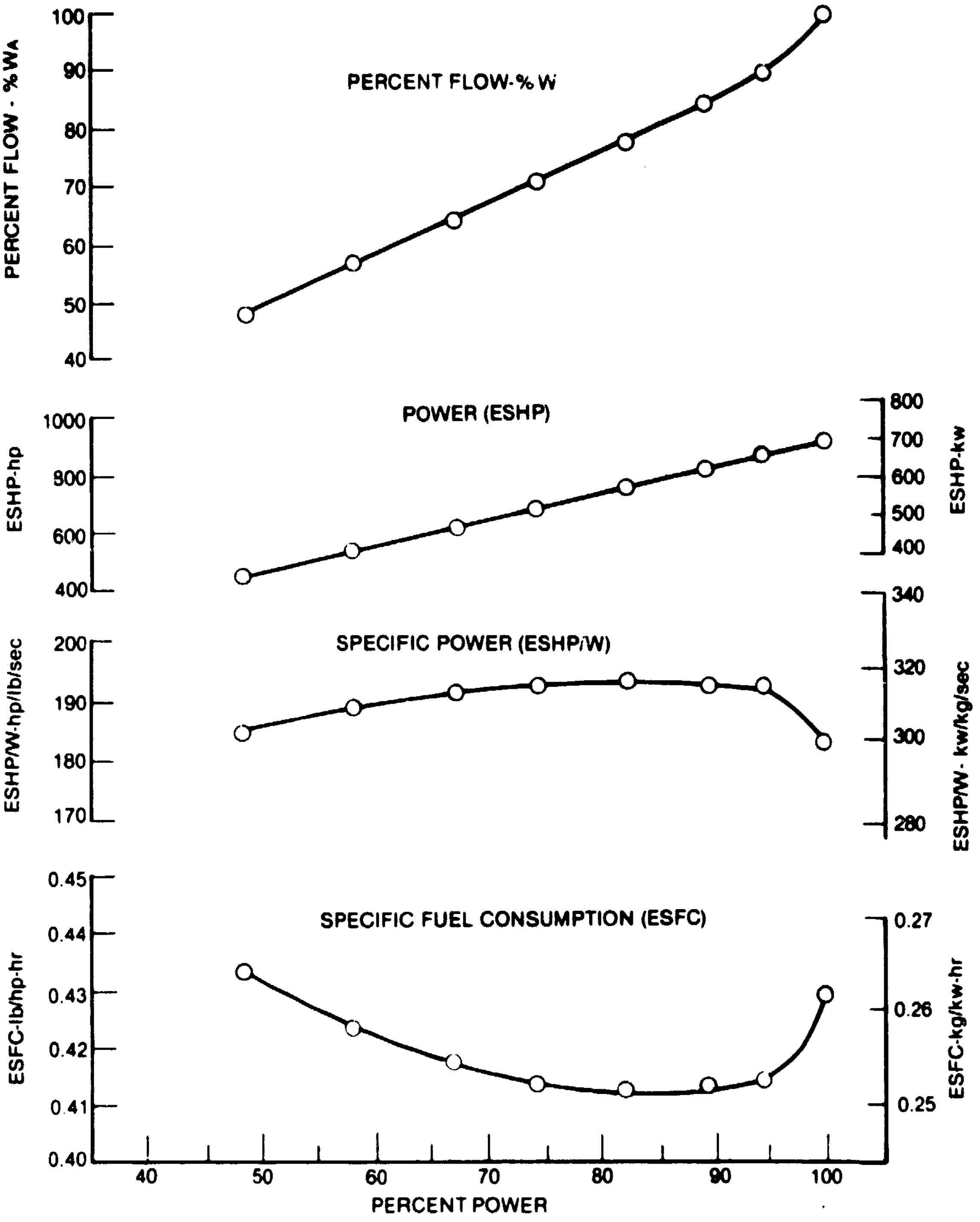

Figure 35. FREE-SHAFT PERFORMANCE, CPR = 16.0, TRIT = 1477K (2200°F), UNCOOLED, S.L., STD. DAY.

ORIGINAL PAGE IS
OF POOR QUALITY

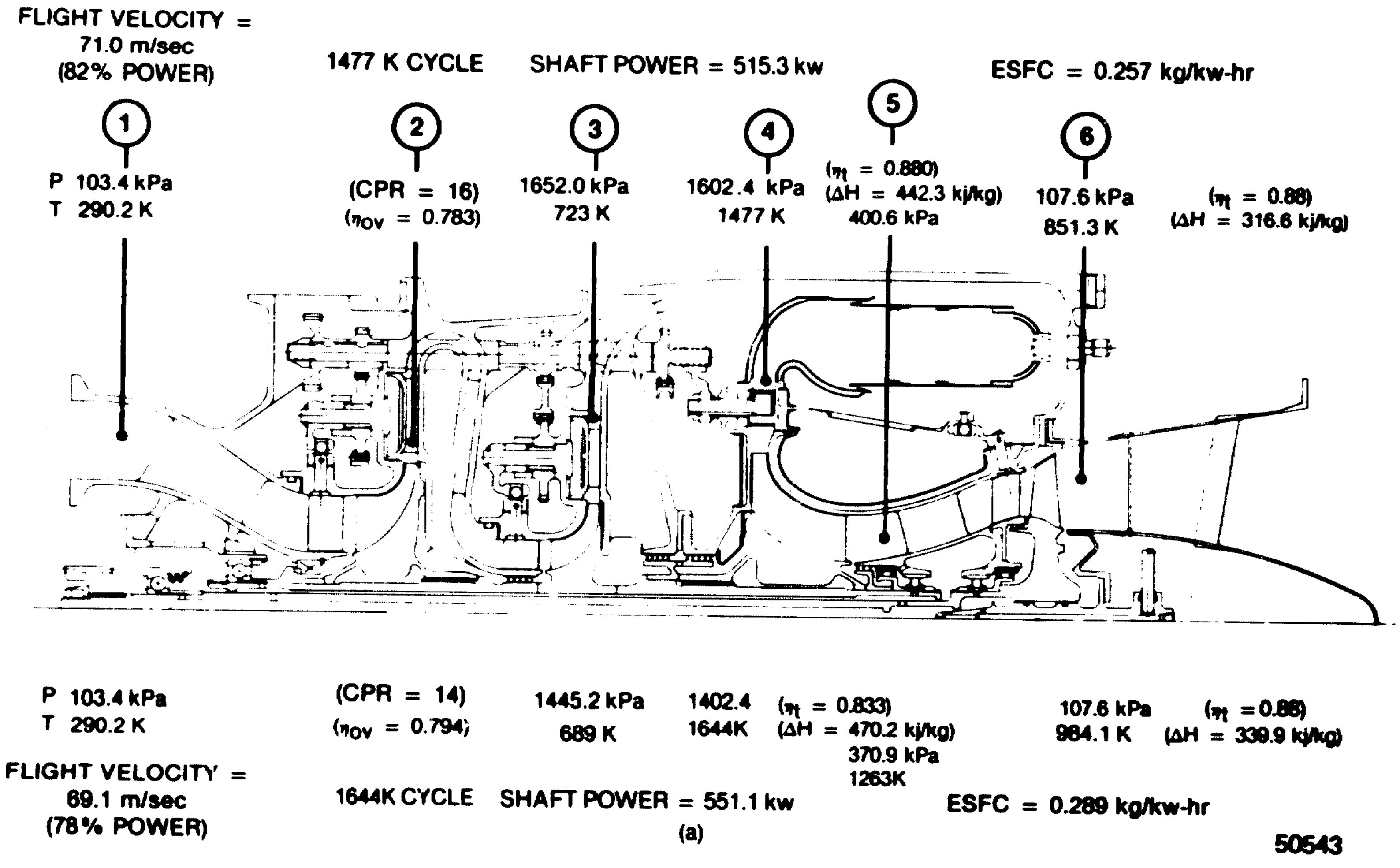

Figure 36. ENGINE CONFIGURATION STUDY RESULTS (SI UNITS).

ORIGINAL PAGE IS
OF POOR QUALITY

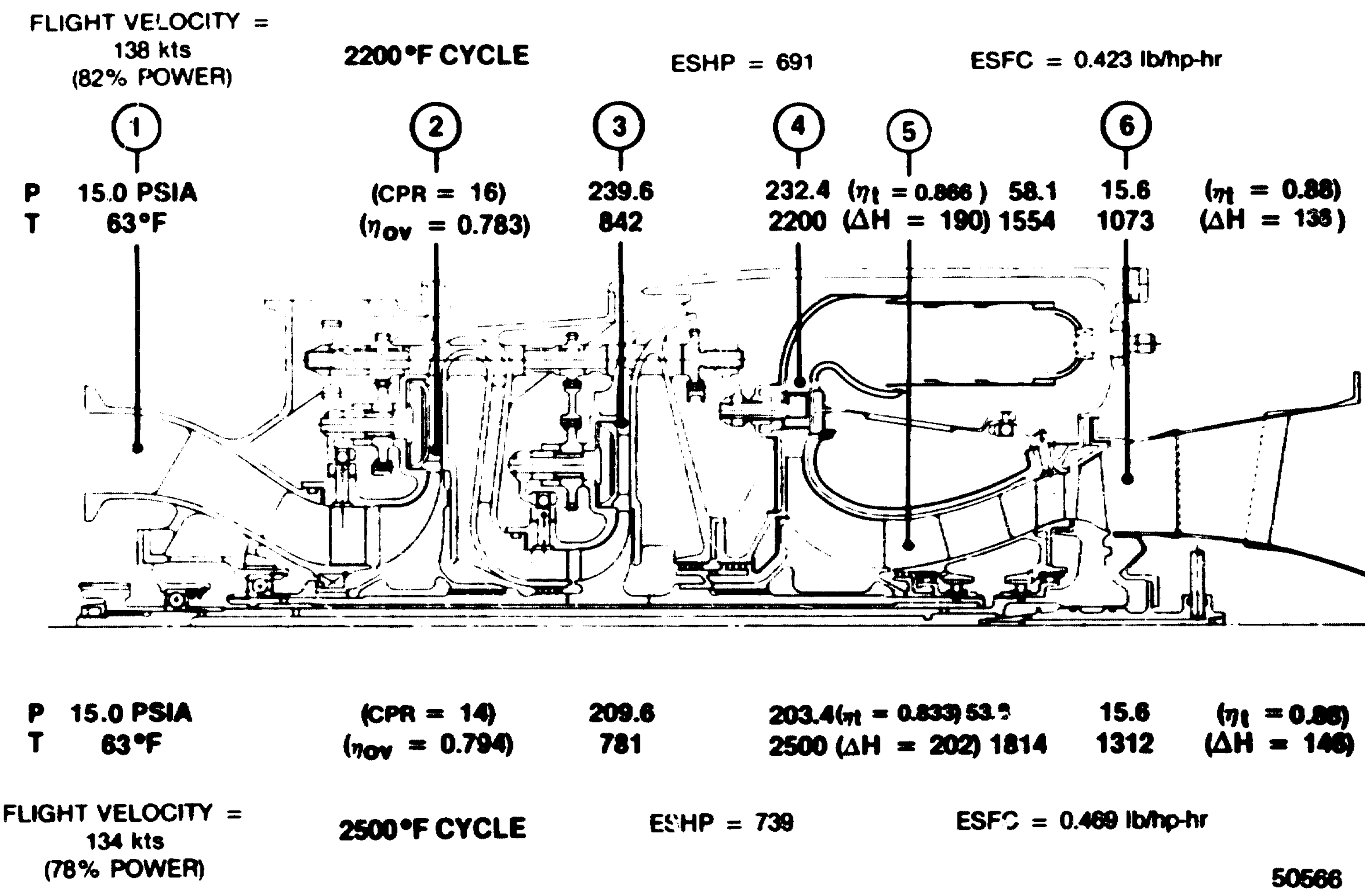

Figure 37. ENGINE CONFIGURATION STUDY RESULTS (CUSTOMARY UNITS).

ORIGINAL PAGE IS
OF POOR QUALITY

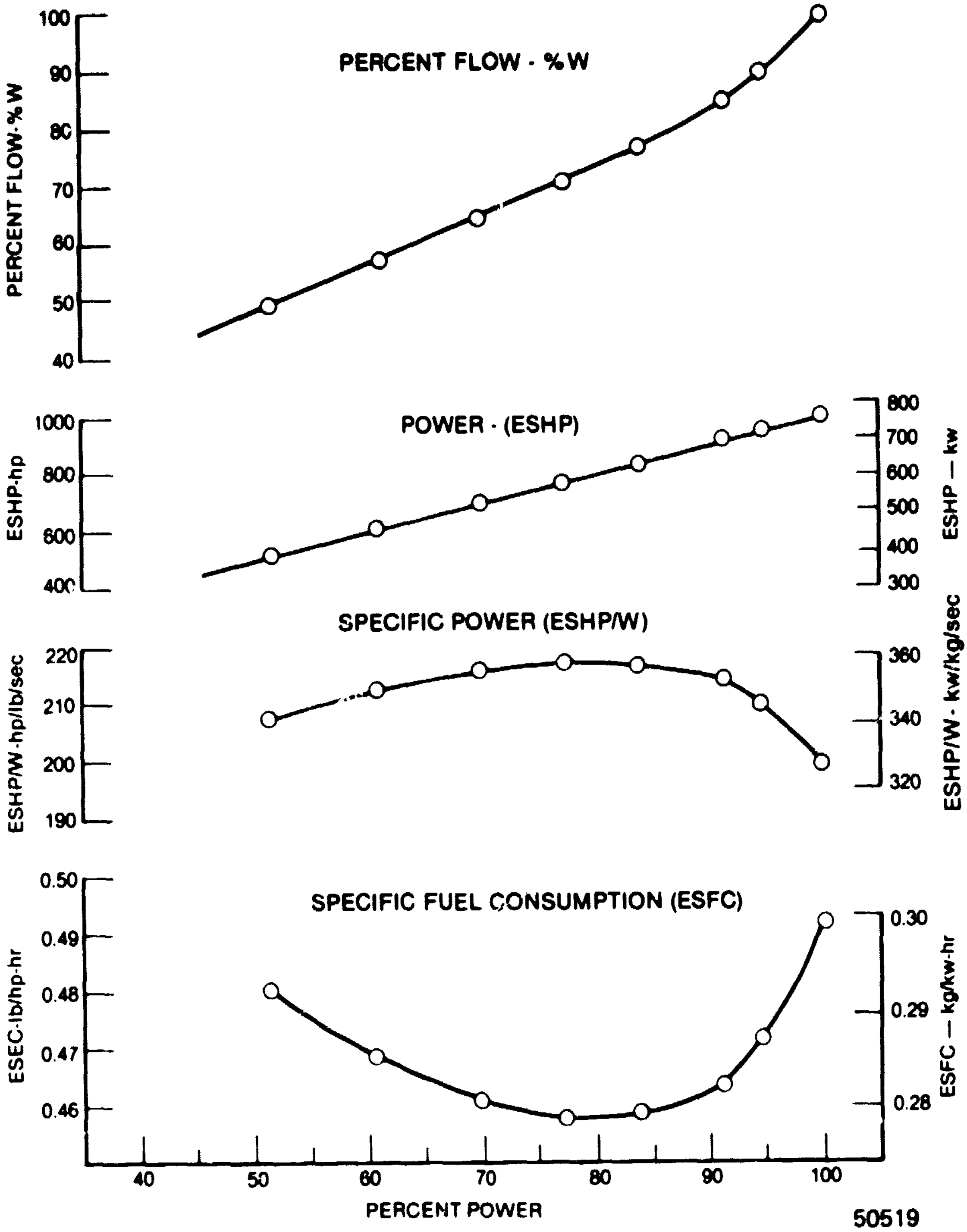

Figure 38. SINGLE-SHAFT PERFORMANCE, CPR = 9.0 TRIT = 1533K, (2300°F), UNCOOLED, S.L., STD. DAY.

ORIGINAL PAGE IS
OF POOR QUALITY

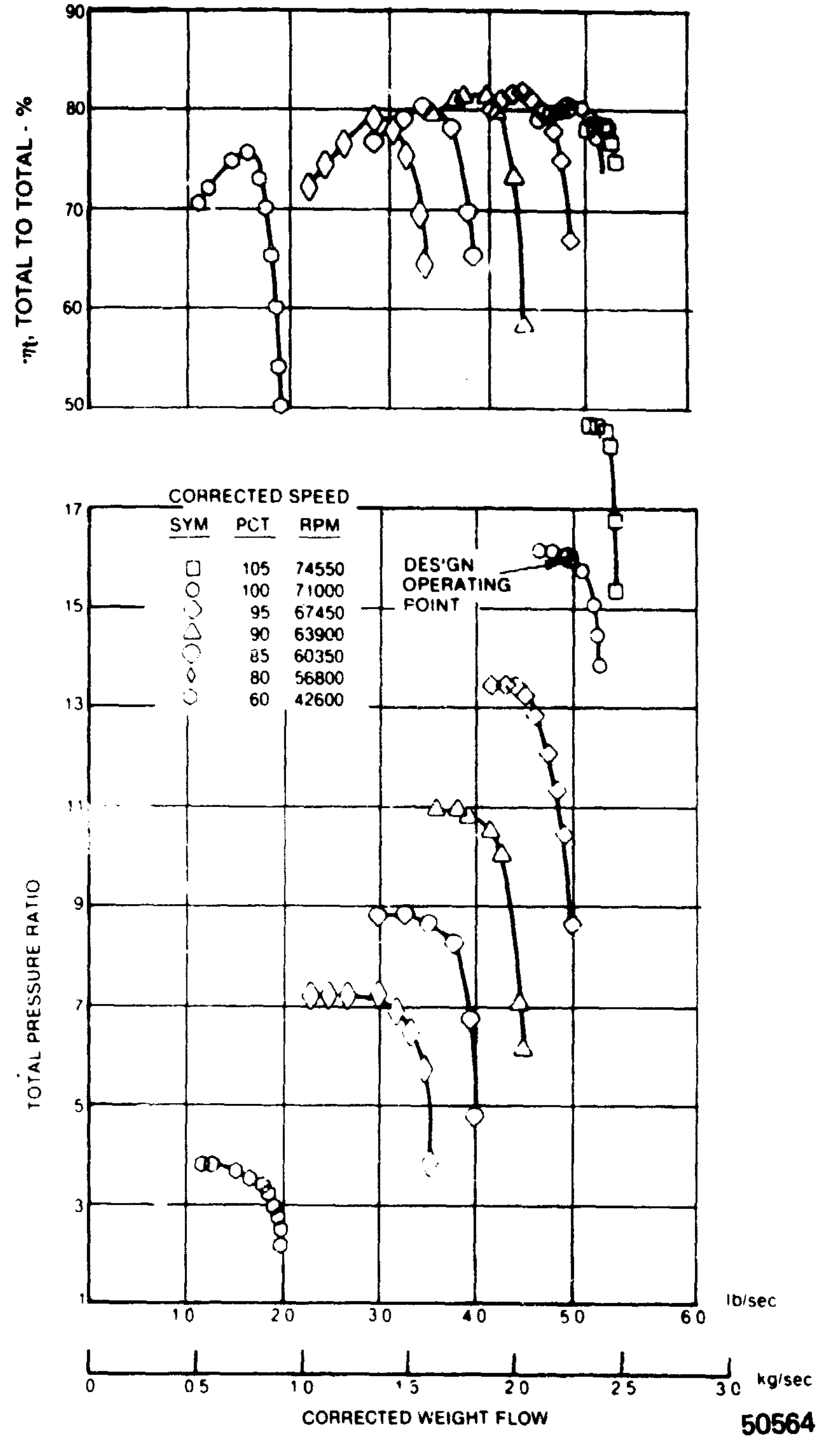

Figure 39. ESTIMATED TWO-STAGE COMPRESSOR MAP FOR SIMPLE CYCLE ANALYSIS.

ORIGINAL PAGE IS
OF POOR QUALITY

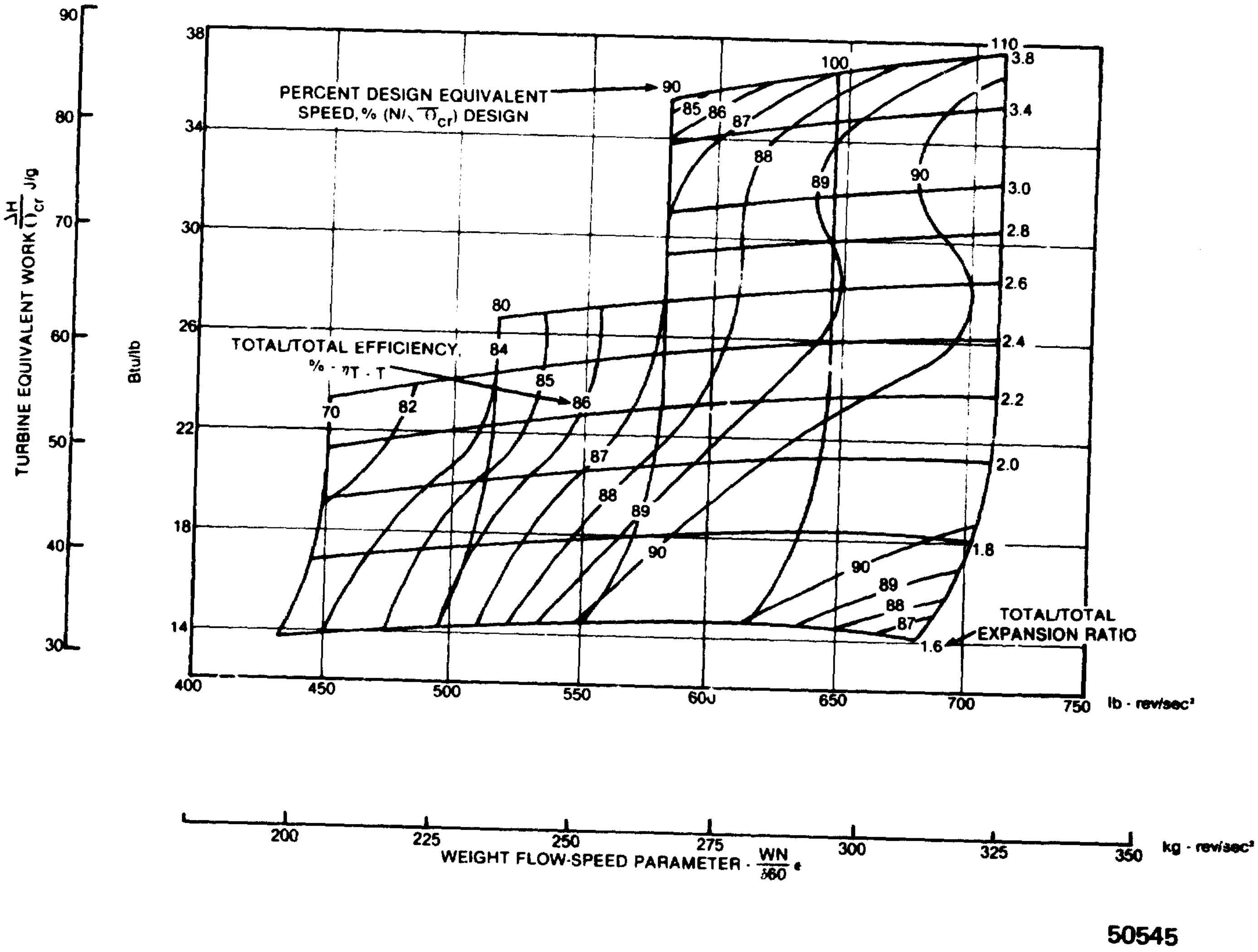

Figure 40. POWER TURBINE PERFORMANCE MAP.

ORIGINAL PAGE IS
OF POOR QUALITY

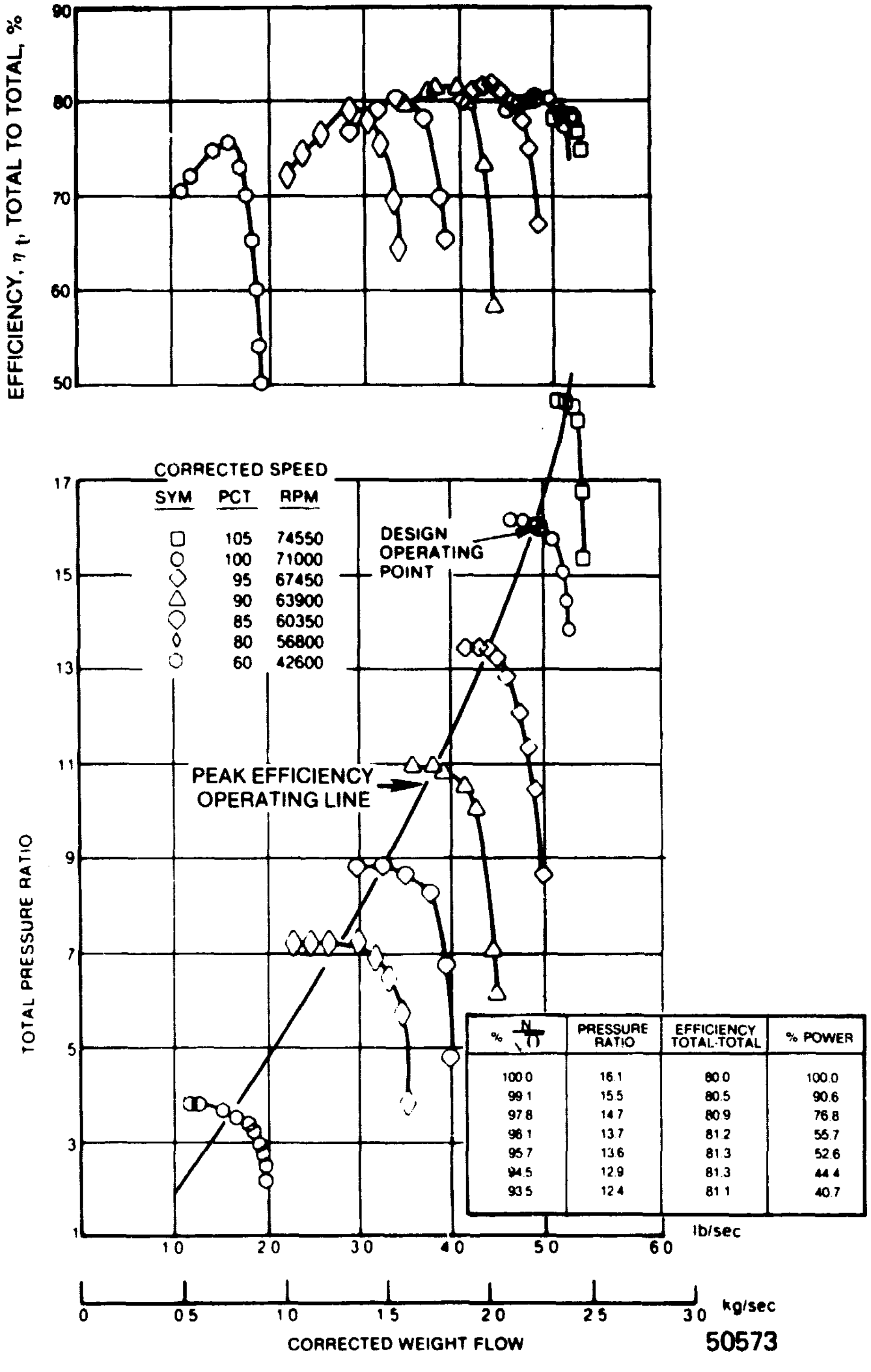

$\% \frac{N}{\sqrt{\theta}}$	PRESSURE RATIO	EFFICIENCY TOTAL-TOTAL	% POWER
100.0	16.1	80.0	100.0
99.1	15.5	80.5	90.6
97.8	14.7	80.9	76.8
96.1	13.7	81.2	56.7
95.7	13.6	81.3	52.6
94.5	12.9	81.3	44.4
93.5	12.4	81.1	40.7

Figure 41. ESTIMATED TWO-STAGE COMPRESSOR MAP - OPERATING LINE SIMPLE CYCLE WITH VARIABLE POWER TURBINE.

ORIGINAL PAGE IS
OF POOR QUALITY

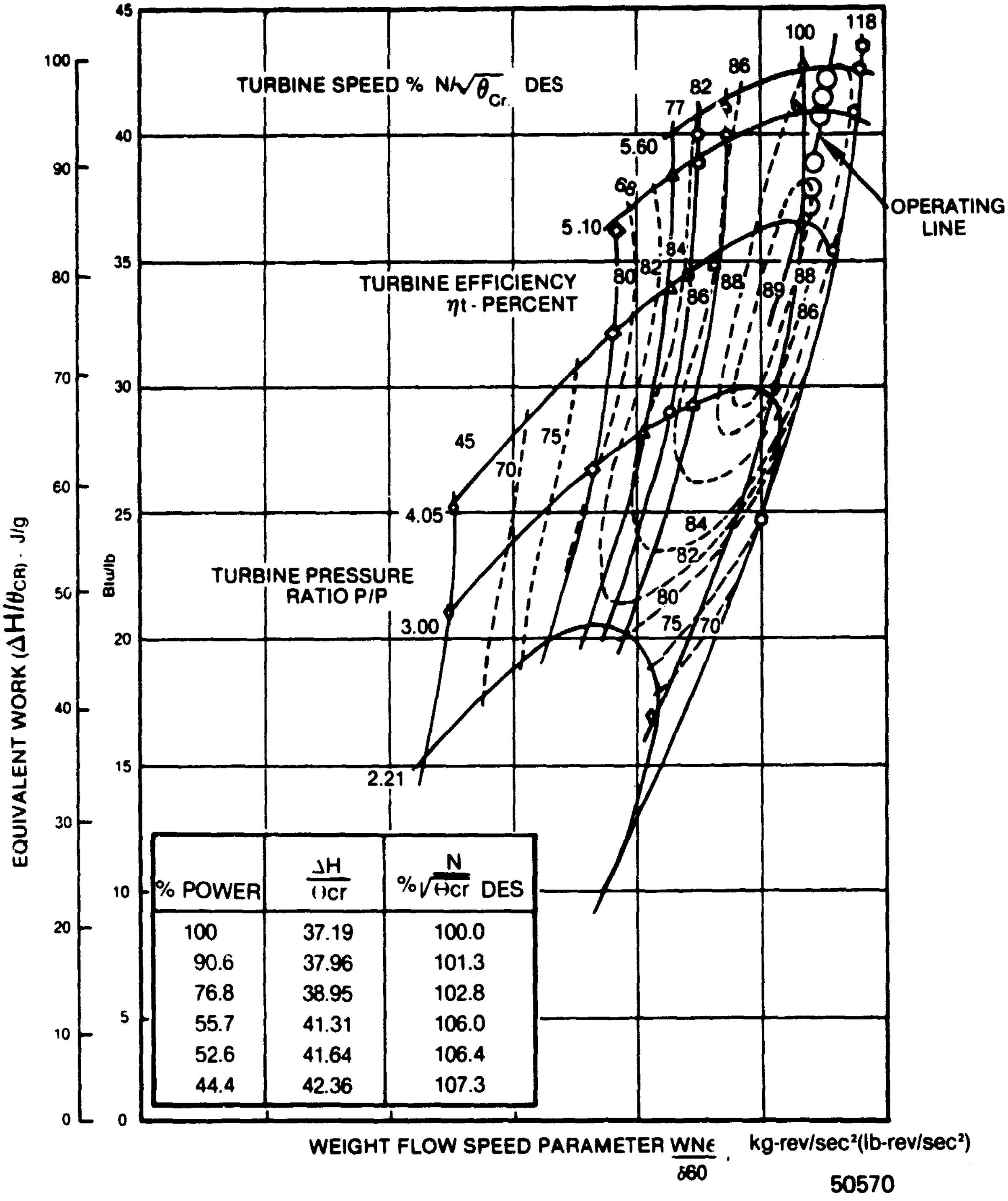

% POWER	$\frac{\Delta H}{\theta cr}$	$\% \frac{N}{\sqrt{\theta cr}}$ DES
100	37.19	100.0
90.6	37.96	101.3
76.8	38.95	102.8
55.7	41.31	106.0
52.6	41.64	106.4
44.4	42.36	107.3

Figure 42. SIMPLE CYCLE WITH VARIABLE POWER TURBINE - HIGH PRESSURE TURBINE OPERATING LINE.

ORIGINAL PAGE IS
OF POOR QUALITY

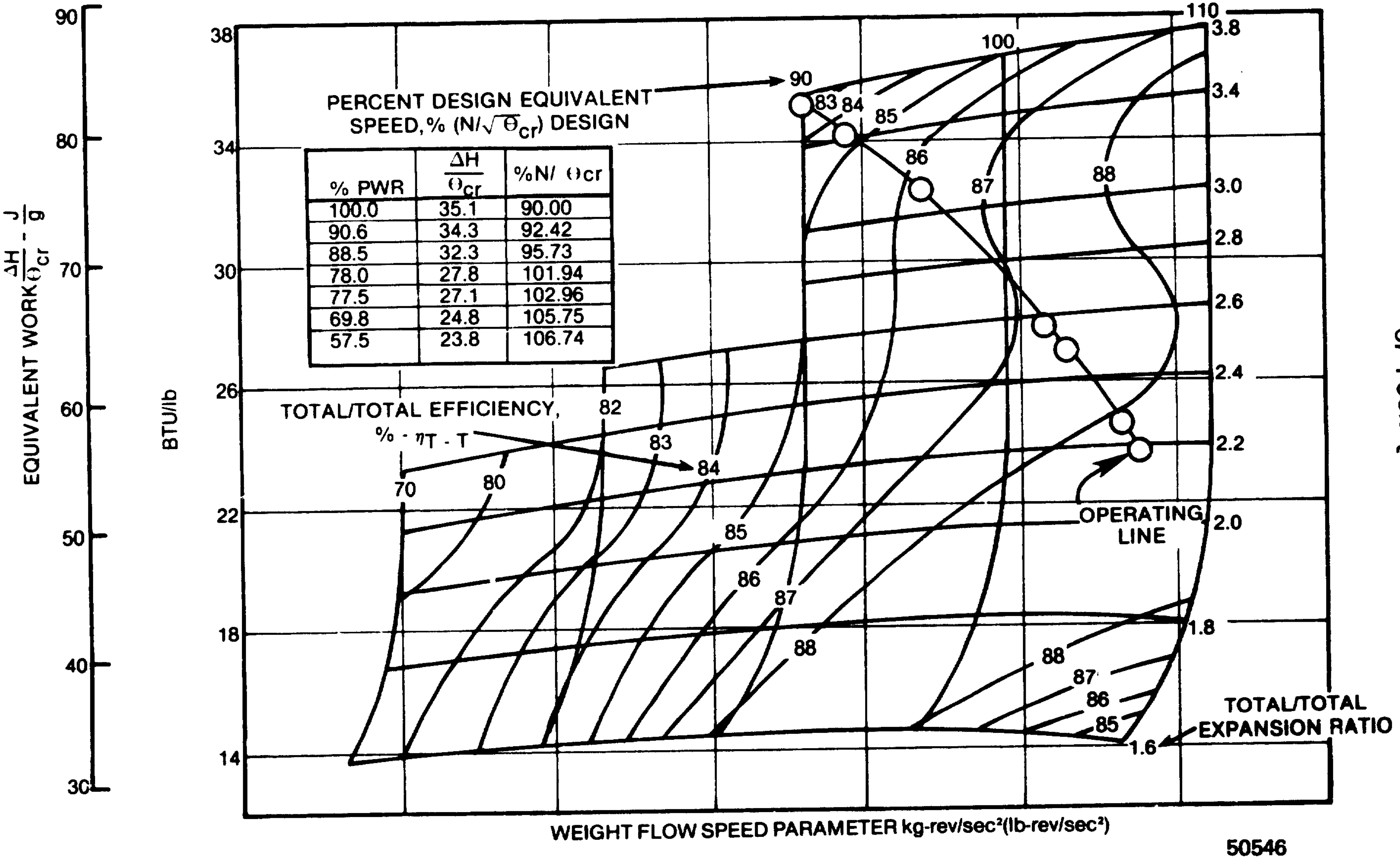

% PWR	$\frac{\Delta H}{\Theta_{cr}}$	%N/ Θcr
100.0	35.1	90.00
90.6	34.3	92.42
88.5	32.3	95.73
78.0	27.8	101.94
77.5	27.1	102.96
69.8	24.8	105.75
57.5	23.8	106.74

Figure 43. SIMPLE CYCLE WITH VARIABLE POWER TURBINE - POWER TURBINE OPERATING LINE.

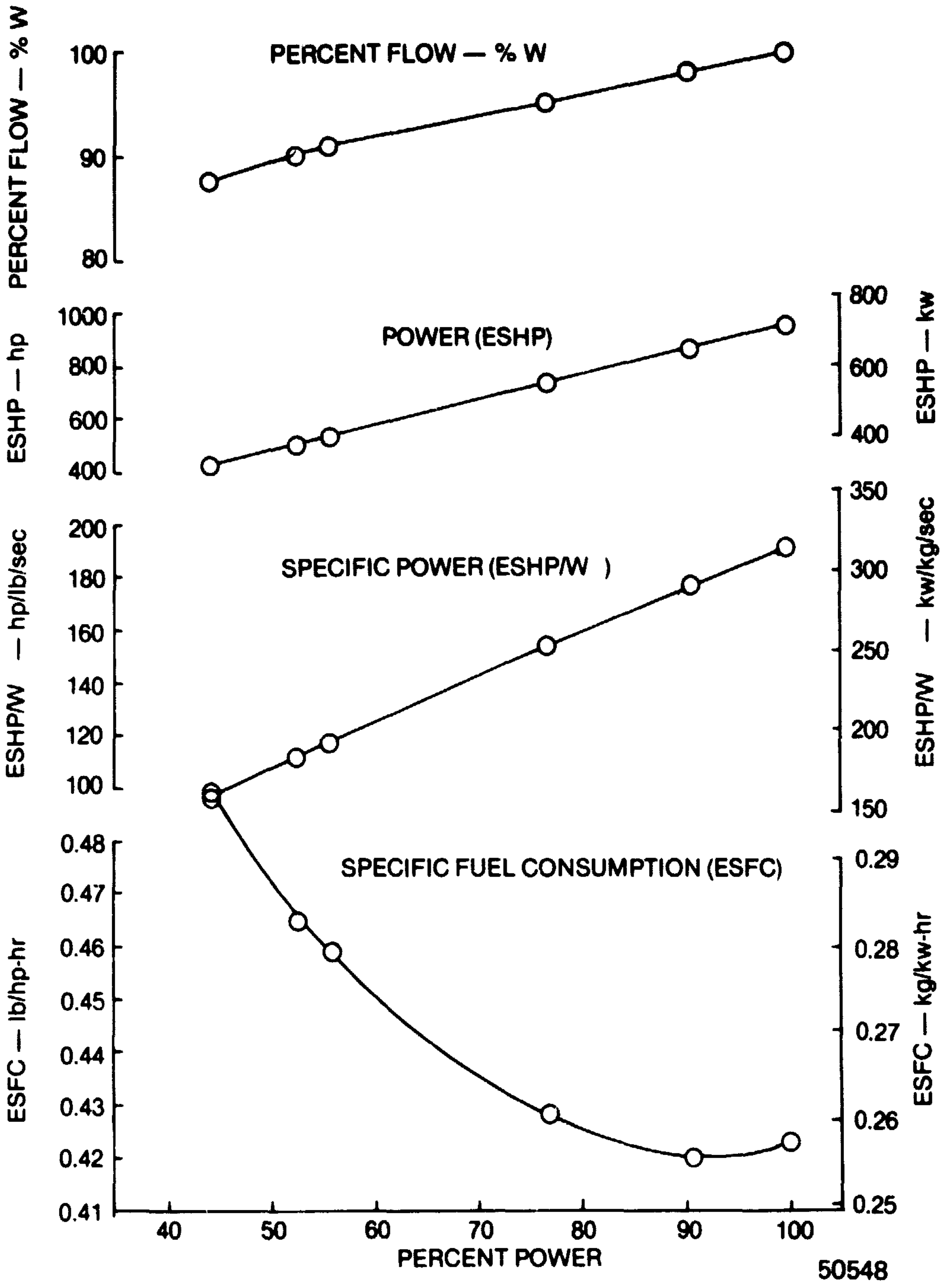

Figure 44. SIMPLE CYCLE PERFORMANCE WITH VARIABLE POWER TURBINE MAX. CPR = 16, TRIT = 1477K (2200°F), UNCOOLED, S. L., STD. DAY.

3.4 ADVANCED TURBINE MATERIALS SELECTION

Metals which are projected to be available in 1988 for advanced technology small gas turbine engine components will evolve primarily from the metals systems currently developed and which will be improved through innovative processing techiques currently under development. Many of these metals/processing methods have reached the level of component feasibility but have not yet gained industry acceptance as production-ready. It is anticipated that the materials property improvements gained from these processes will be well enough developed to support the analysis of radial turbine technology development in the 1988 time frame.

Powder metal technology shows considerable promise with nickel base alloys serving as the major candidate for axial and radial turbines. Since near net shape components can be produced, the advancement in manufacturing will be to provide net shape airfoils with thin sections. The present development of rapid solidification rate (RSR) powders will allow for higher strength materials, Reference 20. The utilization of hot isostatic pressing will enable the quality of these powder metal components to be improved further so as to provide the necessary level of mechanical strength for these critical components.

The continuing requirement for higher turbine rotor operating temperatures demands that the material considerations for the 1988 time frame be directed at metals having the highest potential of strength retention at temperatures of 1367K (2000°F). Turbine rotor metals with this capability include columbium alloys, molybdenum alloys, RSR powder alloys, and nickel base alloys by both directionally solidified casting and single crystal casting.

Columbium is a ductile material which has excellent high temperature strength for application to 1589K (2400°F). This material requires an oxidation protection coating, but at these temperatures any metal requires protection from rapid oxidation. An excellent ductility (10 percent) makes it tolerant of localized stress concentrations.

Cast airfoils produced by directional solidification and single crystal techniques will provide stress-rupture capabilities of 297K-325K (75°F - 125°F) above the conventional equiaxed cast blades.

Molybdenum alloys offer higher stength at temperature than columbium alloys, with the sacrifice of density, but with continued development, and coating protection offer a strong potential for a 1988 candidate turbine material.

A properties comparison of the various material forms is shown in Figure 45. With the material variations presented, fabrication techniques can include casting, forging, or the use of powder metal with hot isostatic pressing (HIP) and dual property rotor fabrication approaches.

The previously mentioned development of RSR powder metals provides one of the best possibilities for replacing cooled turbine blades with a powder metal for operating temperatures of 1367K - 1477K (2000°F - 2200°F). Development efforts are currently in progress by Universal Cyclops and TRW to use a commercial rapid solidification process (CRS) to provide equivalent properties to the RSR material, Reference 21. The use of CRS material having the same properties as shown for RSR 185 in Figure 46 would be a significant improvement over current and equiaxed IN-100 turbine materials. The RSR 185 properties shown were therefore selected as a base for rotor structural life predictions.

ORIGINAL PAGE IS
OF POOR QUALITY

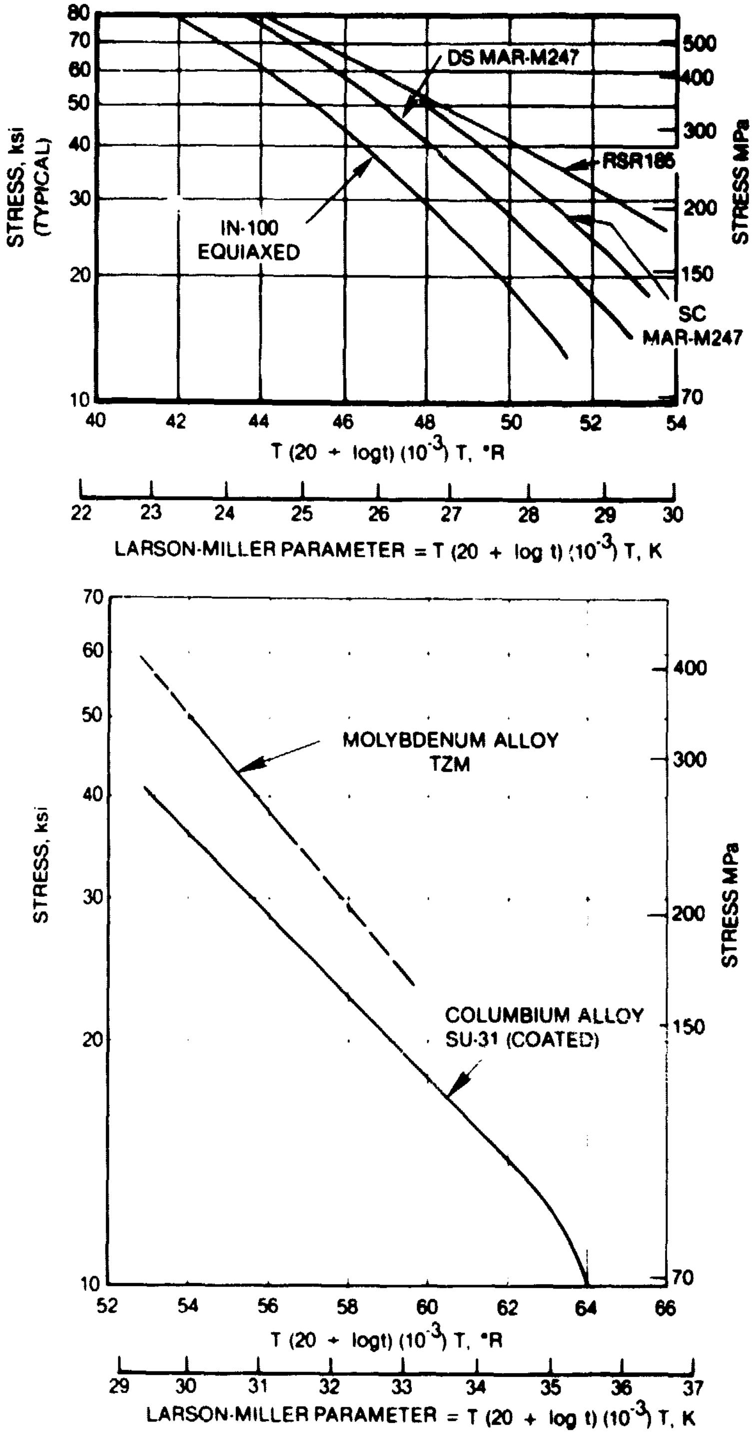

50535

Figure 45. MATERIAL PROPERTY DATA COMPARISON FOR APPLICATION IN ADVANCED TECHNOLOGY TURBINES.

ORIGINAL PAGE IS
OF POOR QUALITY

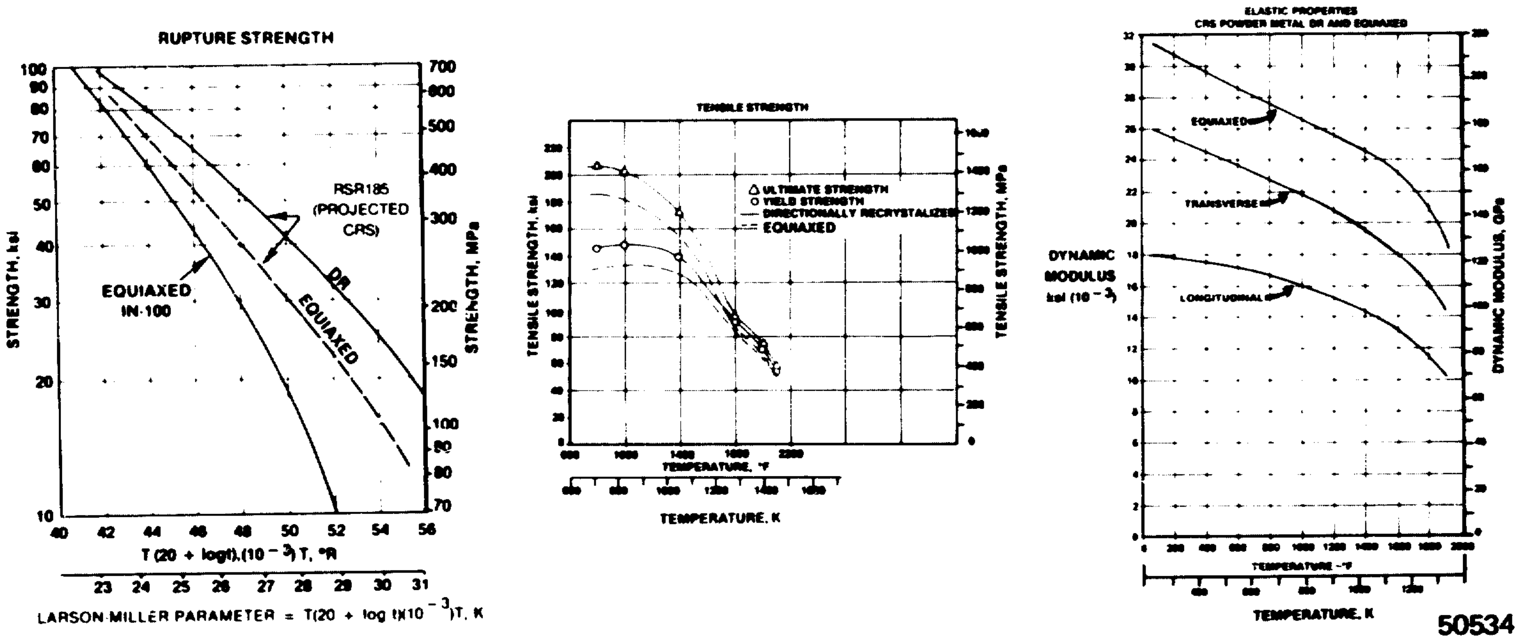

Figure 46. RSR 185 MATERIAL PROPERTIES PROJECTED FOR CRS POWDER METAL.

3.5 STRUCTURAL LIFE FEASIBILITY

In order to quantify the amounts of cooling flows associated with the concept study, a preliminary feasibility study was performed on both the cooled and uncooled rotors. The main thrust was aimed at sizing the rotor blade thickness distribution to a stress rupture life of 4,000 hours and the following duty cycle:

Percent Rated Power	Percent Time
100	20
60	50
55	20
35	5
IDLE	5

Initial temperature distributions in the turbine blade were approximated by adiabatic wall temperatures obtained from local gas temperatures calculated from flowpath analysis of the preliminary geometry. Subsequently, the metal temperatures for the preliminary blade were predicted from heat transfer analysis of blade and disk. The simplified structural blading analysis consisted of distributing the thickness of the blade in a radial direction such that the average stress rupture life was achieved. This simple analysis is representative of life in a one dimensional stress field variation.

The material chosen for the simplified analysis was a CRS (commercial rapid solidification) nickel-based alloy. Section 3.4 gives details of the rotor material selection. Figure 47 gives an iso-life plot for the 1477K (2200°F) uncooled rotor with an 8:1 blade thickness taper ratio. The initial crude analysis shows that most of the blading of the preliminary design has the desired life of 3600 hours at maximum temperature. The feasibility was considered to be adequately defined at this stage of the design definition.

ORIGINAL PAGE IS
OF POOR QUALITY

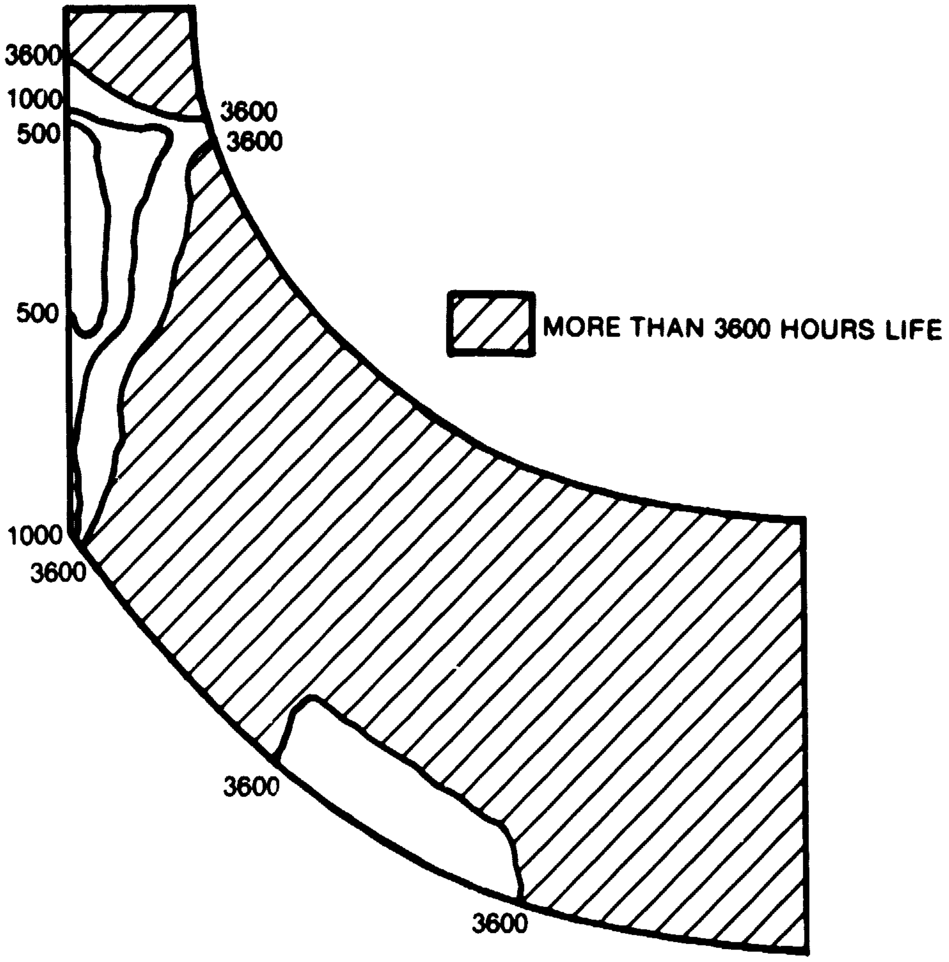

Figure 47. PRELIMINARY LIFE ANALYSIS BASED ON FINITE ELEMENT ANALYSIS AND PROJECTED MATERIAL STRENGTHS OF CRS ALLOY.

PRECEDING PAGE BLANK NOT FILMED

SECTION 4

PRELIMINARY DESIGN DEFINITION (TASK II)

4.1 TURBINE PARAMETRIC EVALUATION

The TASK II preliminary turbine design evaluation focused on parametric optimization of nozzle and rotor design variables. The basic task objective was the selection of design point geometry and flow parameter values to optimize the turbine configuration prior to detailed flow analysis in TASK III. Optimization of the following design parameter variables was addressed as shown in Figure 48:

- Rotor-inlet to Rotor-exit-tip Radius Ratio
- Rotor-exit Axial Velocity Ratio
- Design Point Stator Exit Angle
- Rotor Exit Swirl
- Rotor Tip Speed
- Stator Vane Number
- Rotor Blade Number

Non-radial rotor inlet tip blading was evaluated to be impractical for application in a high tip speed turbine design application with inlet temperatures above 1367K (2000°F). The optimum aerodynamic blade design would include zero incidence with a +32° inlet relative air angle. It was determined in Task I (Figure 47) that some regions of the preliminary radial blade tip exhibited a life expectation at maximum temperature below 3600 hours. Non-radial inlet blade angles would further aggravate tip bending stresses in this region and further limit anticipated rotor life. The rotor and nozzle vane numbers were optimized for constant Zweifel load coefficient during evaluation of the above listed parameters. Optimization trends were later checked for the selected blade and vane numbers with no change in optimum parameter values.

The rotor-tip to rotor-exducer-tip radius ratio (ϵ) was optimized using the radial turbine preliminary design computer code, Radial Flow Turbine - Design Point Program. Values of rotor exit axial velocity ratio, nozzle and rotor exit swirl, stator inlet and exit radius ratios, and rotor incidence were fixed as shown in Figure 48 for this study. Results of the analysis are shown in Figure 49. Though predicted efficiency continues to rise for higher values, a limiting radius ratio (ϵ) value of 1.63 was selected for further analysis. This radius ratio corresponds to an exducer hub radius of 2.54cm (1.0 in.), which is the minimum to allow for a concentric front drive free-turbine shaft. The performance penalty associated with this constraint compared with a 2.0 radius ratio, where blade roots begin to merge, is less than one efficiency point. The effect of an extended and a reduced rotor tip radius was also investigated, as shown in Figure 49.

VARIABLES PARAMETRIC STUDY	STATOR INLET-TO-STATOR EXIT RADIUS RATIO	STATOR VANE NUMBER	STATOR EXIT ANGLE	STATOR EXIT-TO-ROTOR INLET RADIUS RATIO	ROTOR TIP RADIUS	ROTOR RELATIVE INLET ANGLE	ROTOR BLADE NUMBER	ROTOR EXIT AXIAL VELOCITY RATIO	ROTOR EXIT SWIRL	EXDUCER TIP RADIUS	EXDUCER HUB RADIUS
ROTOR-TIP TO EXDUCER-TIP RADIUS RATIO	1.18	O	79.3°	1.16	3.52	0°	O	0.35	0°	V	V
ROTOR EXIT AXIAL VELOCITY RATIO	1.18	O	79.3°	1.16	3.52	0°	O	V	0°	2.16	V
DESIGN POINT STATOR EXIT ANGLE	1.18	O	V	1.16	3.52	0°	O	0.32	0°	2.25	1.00
ROTOR EXIT SWIRL	1.18	O	80°	1.16	V	0°	O	0.32	V	2.25	1.00
ROTOR TIP SPEED	1.18	O	80°	1.16	V	V	O	0.35	V	2.25	1.00
STATOR VANE NO.	1.18	V	80°	1.16	3.52	0°	O	0.32	0°	2.25	1.00
ROTOR BLADE NO.	1.18	O	80°	1.16	3.48	0°	V	0.32	-10°	2.25	1.00

V-VARIABLE O-OPTIMUM SELECTED

Figure 48. TURBINE PRELIMINARY DESIGN OPTIMIZATION.

ORIGINAL PAGE IS
OF POOR QUALITY

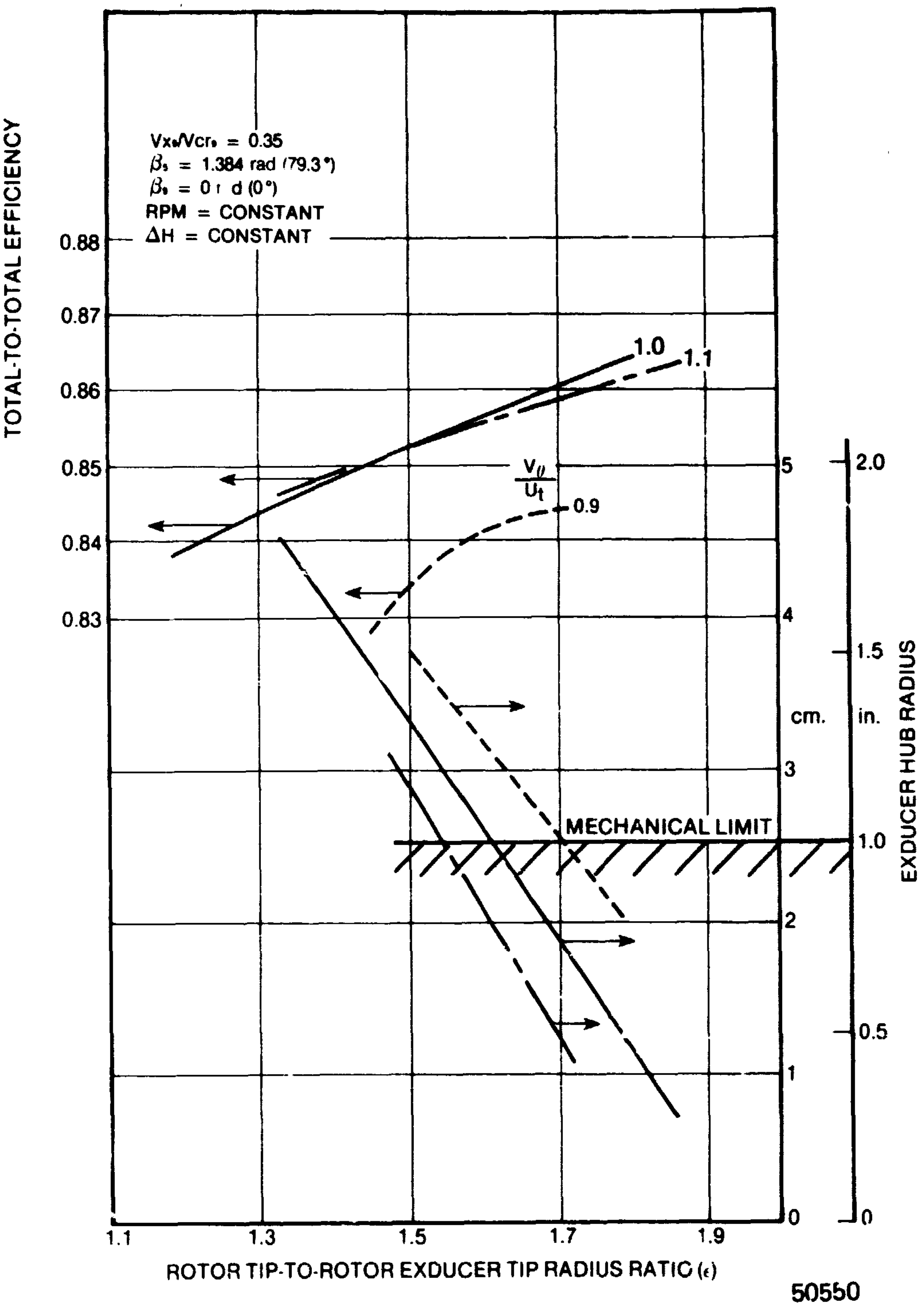

Figure 49. ROTOR-TO-EXDUCER TIP RADIUS RATIO EFFECTS.

Note that, while efficiency continues to rise with increased radius ratio for a rotor work coefficient $(V\ /U_t)$ equal to 1.0 and 1.1 (zero and positive incidence respectively), efficiency peaks for $V_\theta\ /U_t$ of 0.9 at a radius ratio of 1.7 and stage efficiency drops markedly for additional negative rotor incidence increase. Efficiency levels are essentially equivalent for 1.0 and 1.1 work coefficient levels with efficiency estimates for negative rotor incidence $(V_\theta\ /U_t = 0.9)$ about 1.7 points lower.

The rotor exit axial velocity ratio was varied in a similar manner as indicated in Figure 48. Rotor-tip to exducer-tip-radius ratio and nozzle and rotor exit swirl values were fixed for this analysis. Parametric study results are presented in Figure 50. The same exducer hub radius limitation applies as for the previous study. A final rotor exit axial velocity ratio value of 0.35 was selected from the parametric study. Although slightly higher efficiency can be achieved for greater exit velocity ratios (increased hub radius), off-design analysis indicates limit load would occur near or before maximum (100%) flow for these configurations.

The effect of design point nozzle exit angle on overall turbine efficiency is shown in Figure 51. Nozzle axial width was varied with nozzle exit angle to maintain nozzle throat area and fixed angular momentum at the rotor leading edge. The primary contributors to higher efficiency with increased nozzle exit angle, based on the correlations in the preliminary design computer code (Reference 13), are reduced total velocity in the free vortex space and decreased rotor tip clearance-to-width ratio. As a matter of practical consideration, as the nozzle exit angle approaches 90°, free vortex friction loss due to swirl path length becomes predominant and blockage due to trailing edge thickness becomes unacceptable. A variation of stagger angle of only ±0.5° on the vane of an 80° nozzle would change flow capacity by ±5 percent. A nozzle exit angle of 80°, set as an upper limit based on physical manufacturing tolerance limitations, was selected as the final parametric design value for TASK II. It was later determined during Task III analysis, based on the loss correlations of Reference 12 in the design point program, that nozzle exit swirl optimizes at 77° for the final configuration.

A design point rotor exit swirl analysis was conducted as shown in Figure 52. Exducer hub and shroud radii were fixed as were nozzle exit angle and rotor exit axial velocity ratio. The rotor tip radius and exducer relative flow angle were varied to maintain constant turbine work level. For a rotor inlet work factor, (V_θ/U_t) of 1.0, initial examination of Figure 52 would indicate selection of positive exit swirl (with rotation) at design point for optimum efficiency. Off design characteristics were calculated with a fixed geometry and exit swirl, rotor incidence and exducer exit velocities as a function of flow are given in Figure 53. Rotor incidence values are shown for a station immediately at the rotor inlet radius. Using the general trend in exit swirl over the operating range shown in Figure 53 and the duty cycle, a time weighted average exit swirl can be determined as shown in Figure 54. This indicates that 10° positive swirl at design point would result in a time weighted average swirl of positive 30°. A design point exit swirl of -10° will result in a time weighted average exit swirl of +10° and lower exit duct losses. Reduced exit swirl also provides a more manageable entrance condition to the power turbine nozzle inlet station. A design point exit swirl of -10° was selected as the best compromise to allow optimization of overall cycle efficiency with reasonable extremes over the flow range.

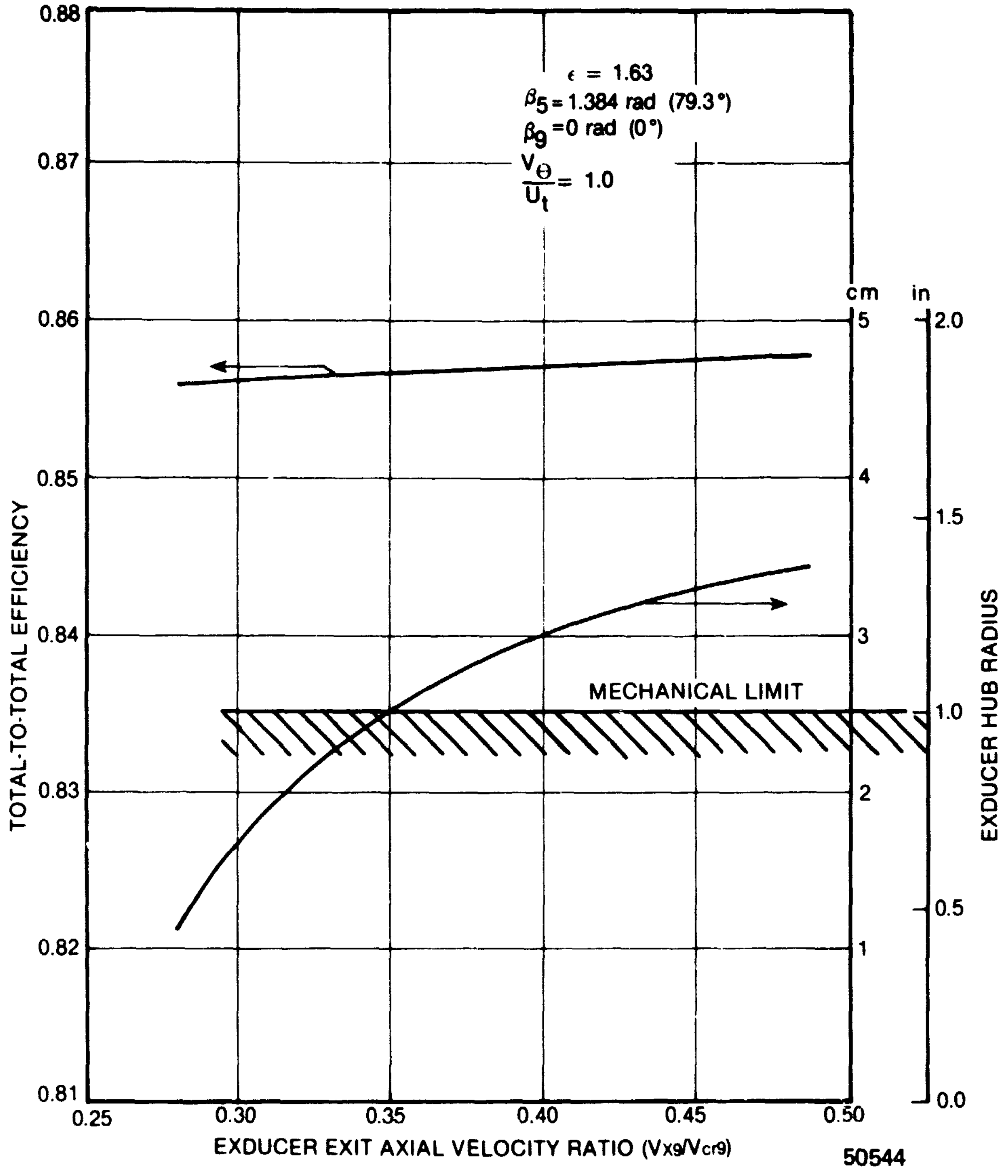

Figure 50. PERFORMANCE EFFECTS OF ROTOR EXIT AXIAL VELOCITY RATIO.

ORIGINAL PAGE IS
OF POOR QUALITY

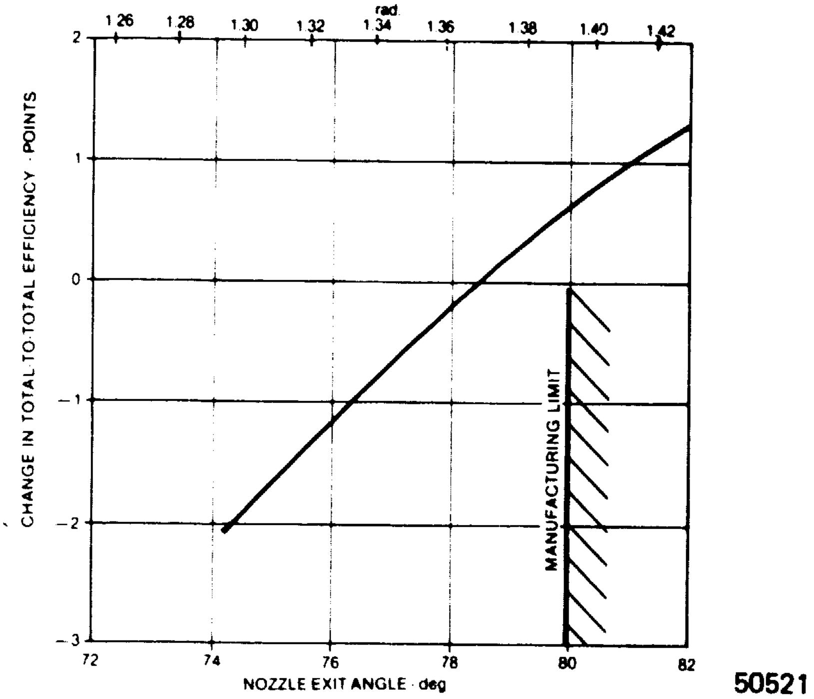

Figure 51. EFFICIENCY CHANGE DUE TO NOZZLE EXIT ANGLE.

Figure 52 also illustrates rotor tip speed effects due to variation of inlet work factor at constant design rotational speed. At a inlet work factor of V_θ/U_t of 1.0 the efficiency change is only 0.5 points over a range of enducer swirl from -0.35 rad. to 0.17 rad. (-20° to +10°) and less than 0.1 points for a work factor of 1.1.

An alternate representation for zero exit swirl is shown in Figure 55. Little or no performance advantage is predicted for rotor tip radius extension or reduction from the nominal value of 8.94 cm (3.52 in.) for inlet work factor of 1.0. In the last iterations on the flowpath for vane and blade optimization, the exducer exit radii were held constant. An exit swirl of -0.17 rad. (-10°), against rotation, and a tip work factor of 1.0 results in a final selected tip radius of 8.834 cm (3.478) or a radius ratio ϵ of 1.54.

The influence of stator vane number on turbine stage efficiency is illustrated in Figure 56. A 17 vane nozzle was selected for the final TASK II configuration based on previous Teledyne CAE radial turbine design and development experience. The final determination of 14 stator vanes was made in reference to TASKS III and IV results, based on aerodynamic vane loading and structural resonance analyses.

The optimum rotor blade number was selected through matching of geometry and aerodynamic conditions for two high efficiency radial turbines, References 22 and 23, using the preliminary design computer program. A Zweifel load coefficient value of about 1.3 was required to match rotor blade number for these turbines as shown in Figure 57. Eleven (11) rotor blades were selected for the TASK II preliminary design based on the same reference value of Zweifel coefficient. The final rotor blade number was selected to satisfy TASK III blade loading analysis requirements. The preliminary design aerodynamic flowpath, with optimum design parameter values selected in Task II, is shown in Figure 58.

A preliminary design point rotor blade flow analysis was conducted using the Northern Research ANALS axisymmetric streamline analysis computer code (Reference 13). The predicted blade-to-blade surface relative velocity loading diagrams are shown in Figure 59 and 60 for design point and maximum flow actuated sidewall nozzle conditions.

ORIGINAL PAGE IS
OF POOR QUALITY

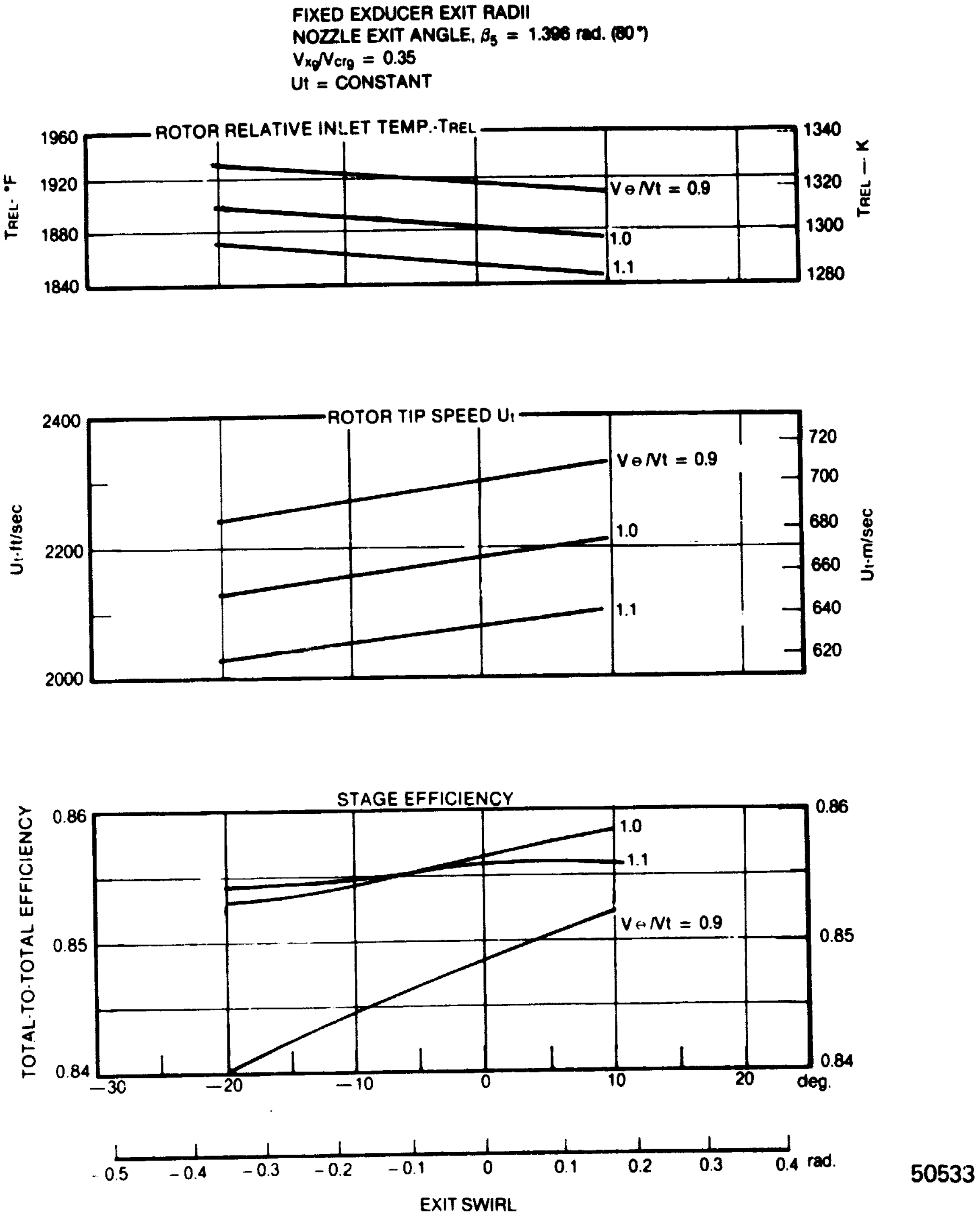

Figure 52. EFFECTS OF EXDUCER EXIT SWIRL AND ROTOR TIP SPEED ON PERFORMANCE AND ROTOR INLET TEMPERATURE.

ORIGINAL PAGE IS
OF POOR QUALITY

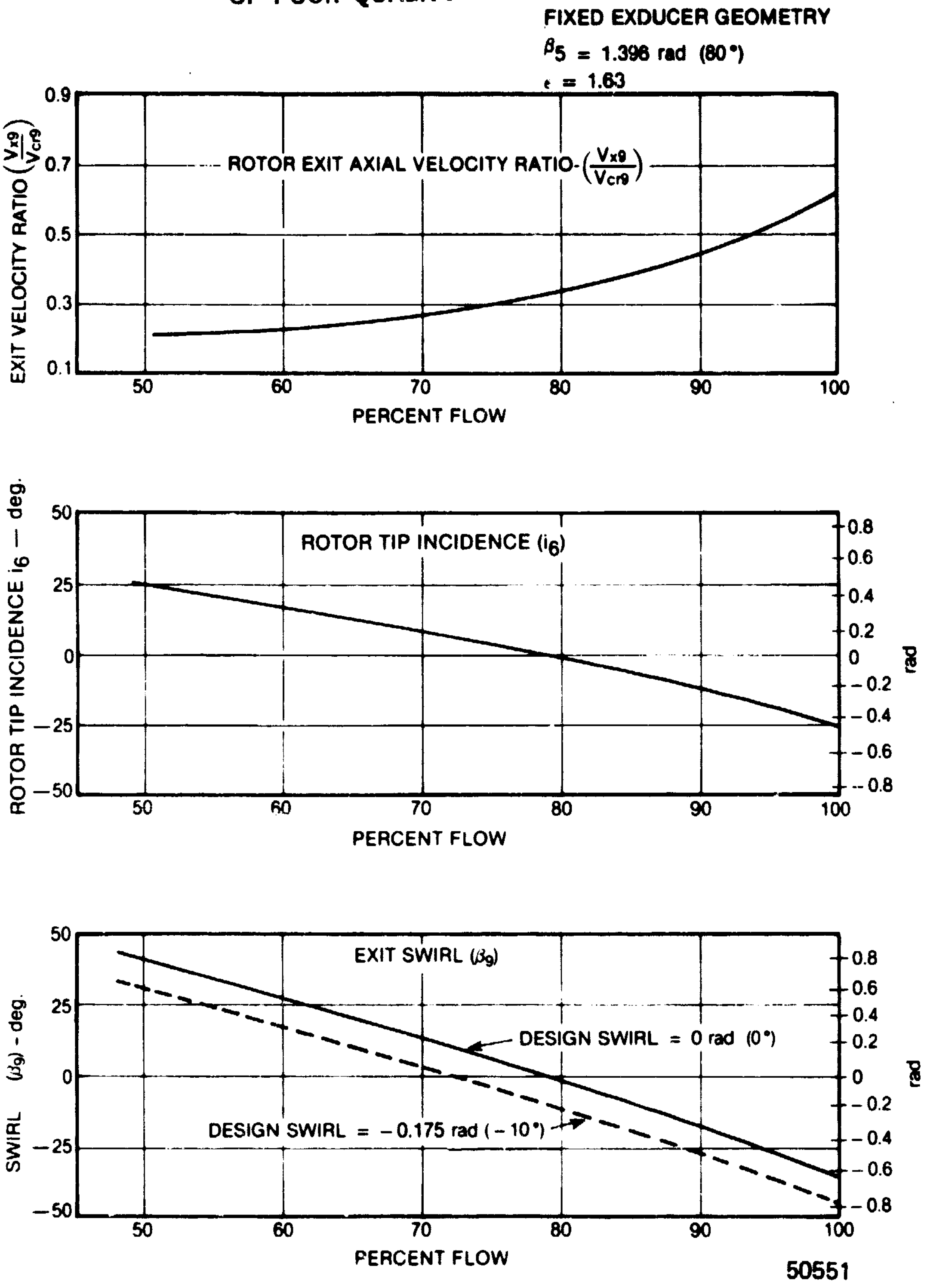

Figure 53. EFFECTS OF OFF-DESIGN FLOW ON ROTOR INLET AND EXIT CONDITIONS.

ORIGINAL PAGE IS
OF POOR QUALITY

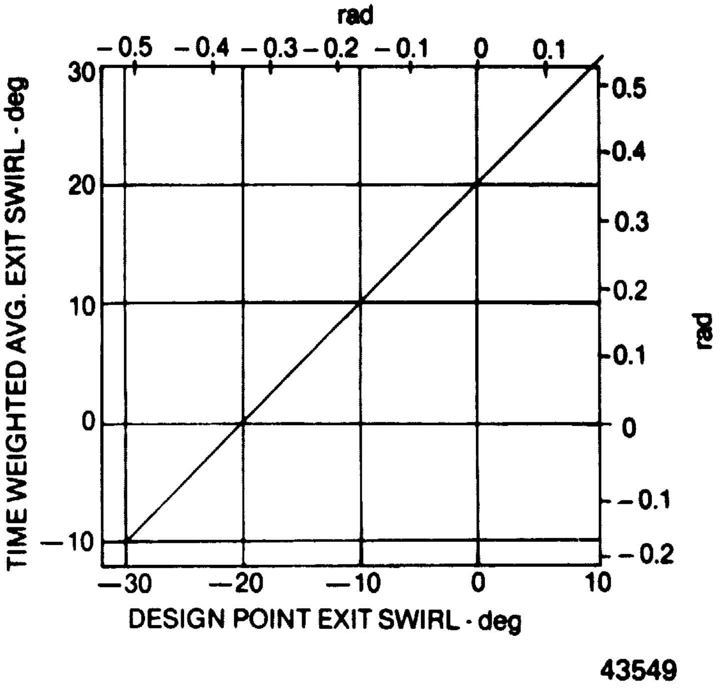

Figure 54. EFFECT OF DESIGN POINT EXDUCER SWIRL ON TIME WEIGHTED SWIRL OVER MISSION DUTY CYCLE.

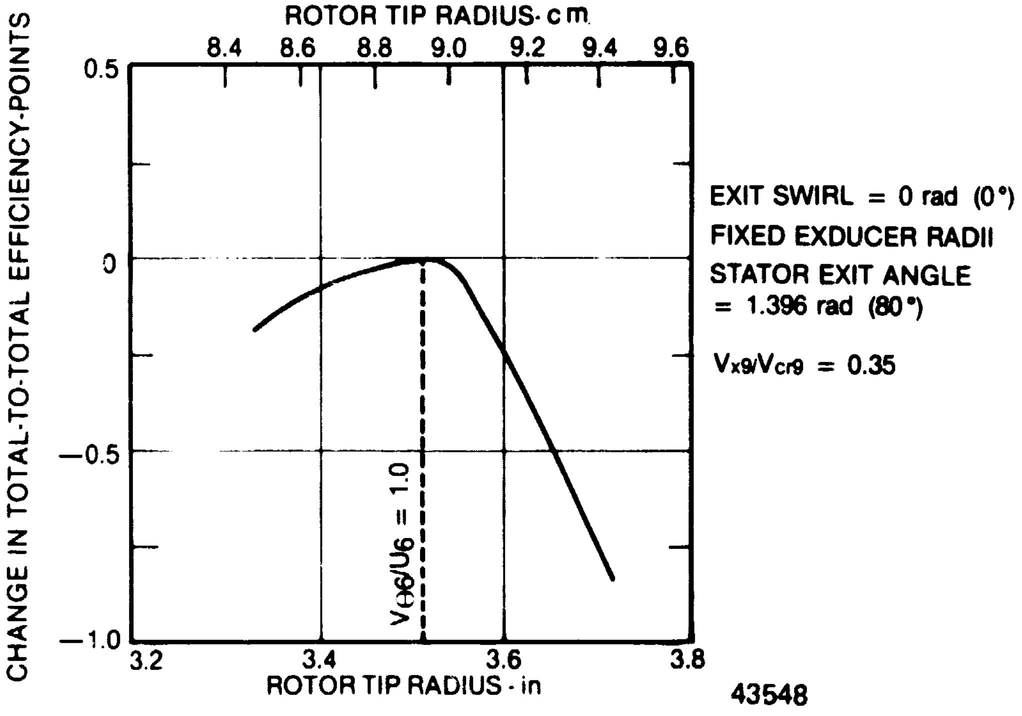

Figure 55. EFFECT OF ROTOR TIP RADIUS CHANGE ON EFFICIENCY.

ORIGINAL PAGE IS
OF POOR QUALITY

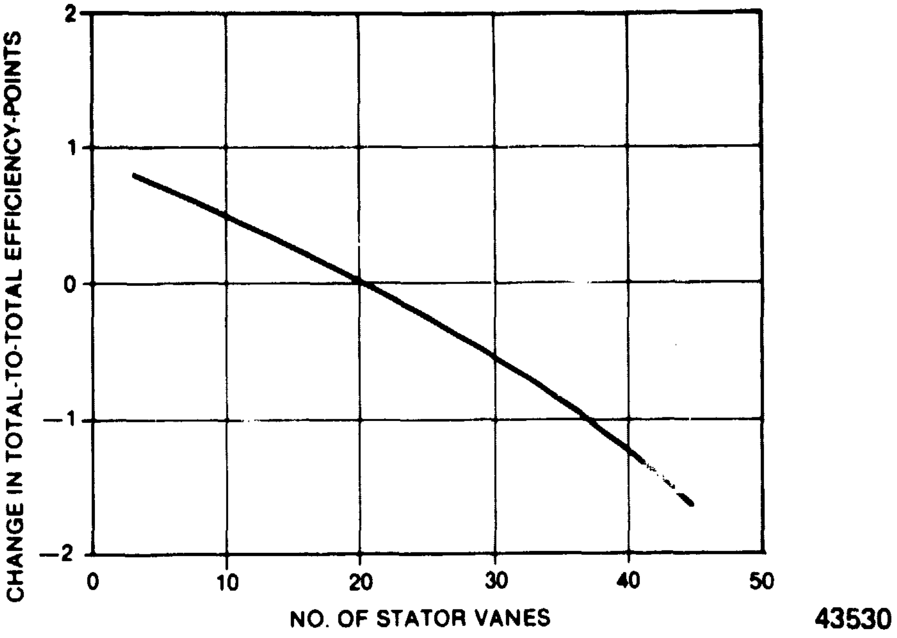

Figure 56. EFFECT OF NOZZLE VANE NUMBER ON OVERALL EFFICIENCY OF FIXED FLOWPATH TURBINE.

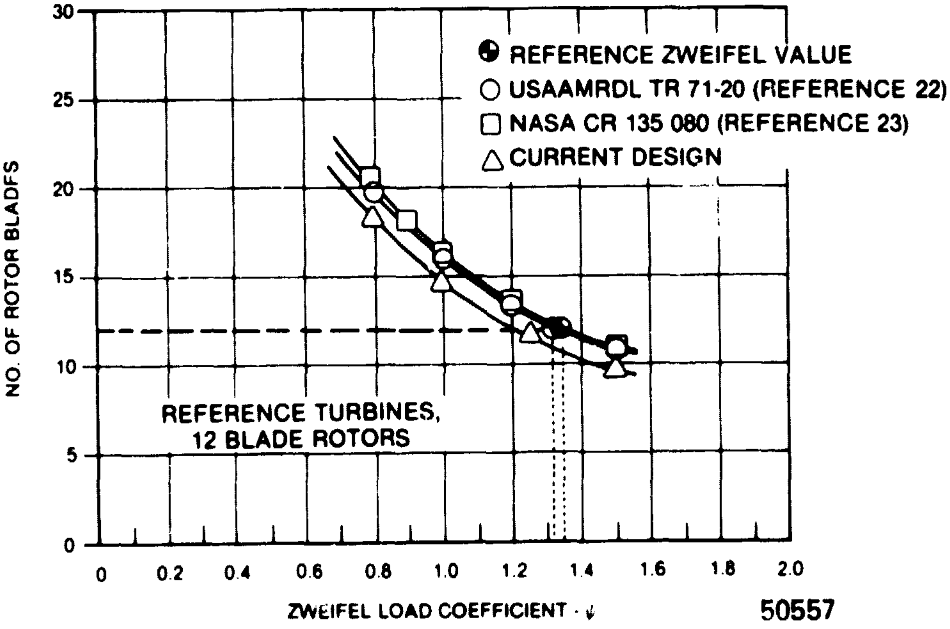

Figure 57. RADIAL TURBINE ROTOR LOADING STUDY.

ORIGINAL PAGE IS
OF POOR QUALITY

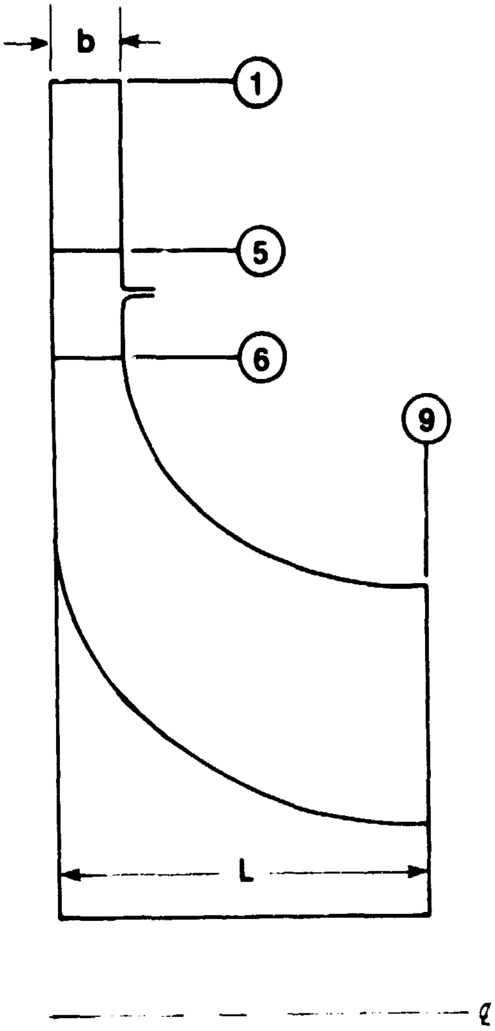

T_1	1506K (2710°R)
P_1	1.602×10^6 Pa (232.4 psia)
W	3.9 lbm/sec
N	71000 RPM
ΔH	190.3 BTU/lbm
$\frac{V_{x9}}{V_{cr9}}$	0.35
R_1	12.543 cm (4.938 in)
R_5	10.284 cm (4.049 in)
R_6	8.834 cm (3.478 in)
R_9 hub	2.540 cm (1.000 in)
R_9 tip	5.720 cm (2.252 in)
$b_{1,5,6}$	0.958 cm (0.377 in)
L	5.334 cm (2.100 in)
Stator Exit Angle	1.40 rad (80°)
Exit Swirl	−0.175 rad (−10°)
No. of Stators	17
No. of Rotor Blades	11

50552

Figure 58. TASK II PRELIMINARY DESIGN TURBINE FLOWPATH.

ORIGINAL PAGE IS
OF POOR QUALITY

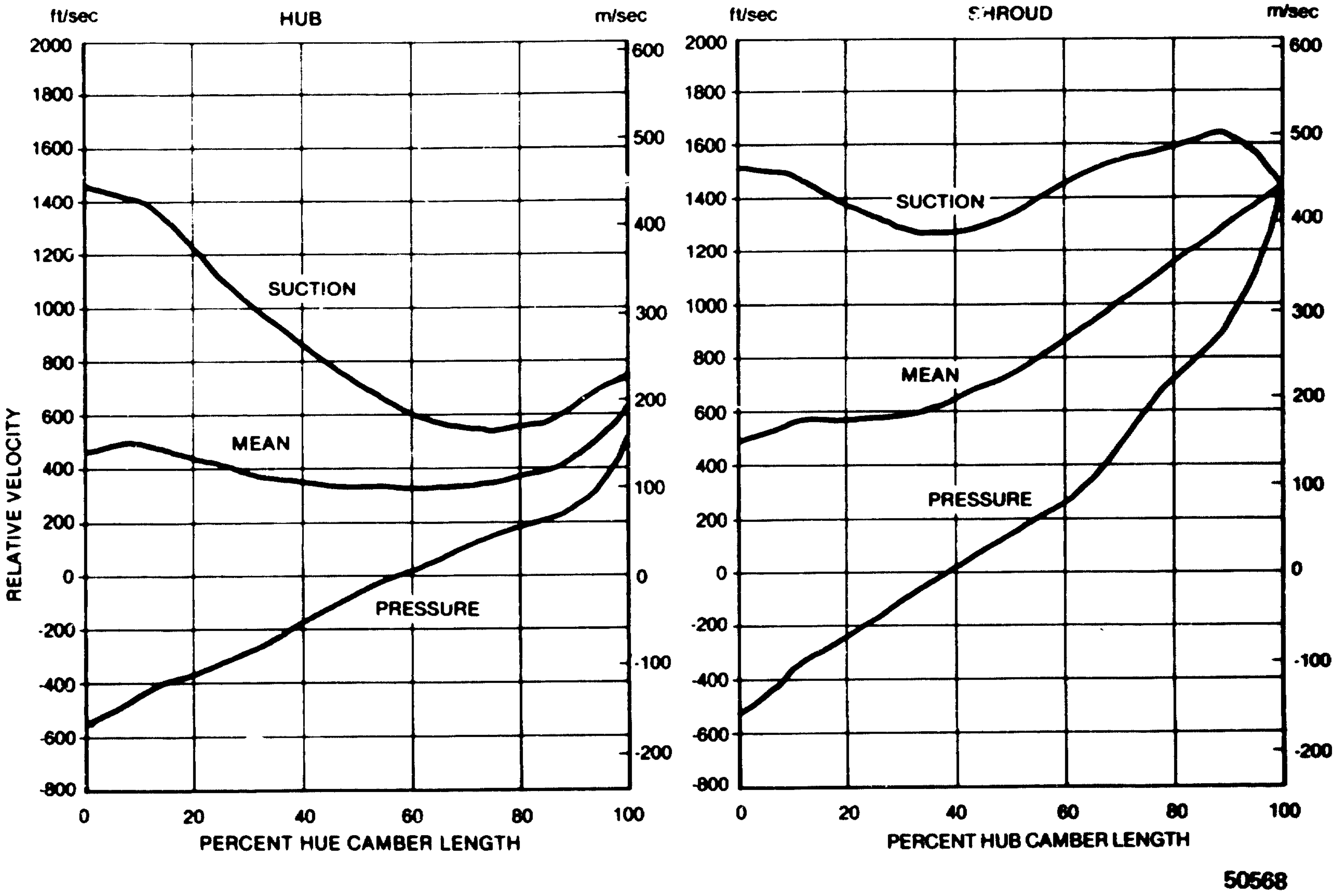

Figure 59. PRELIMINARY ROTOR BLADE LOADINGS, 78% FLOW DESIGN POINT.

ORIGINAL PAGE IS
OF POOR QUALITY

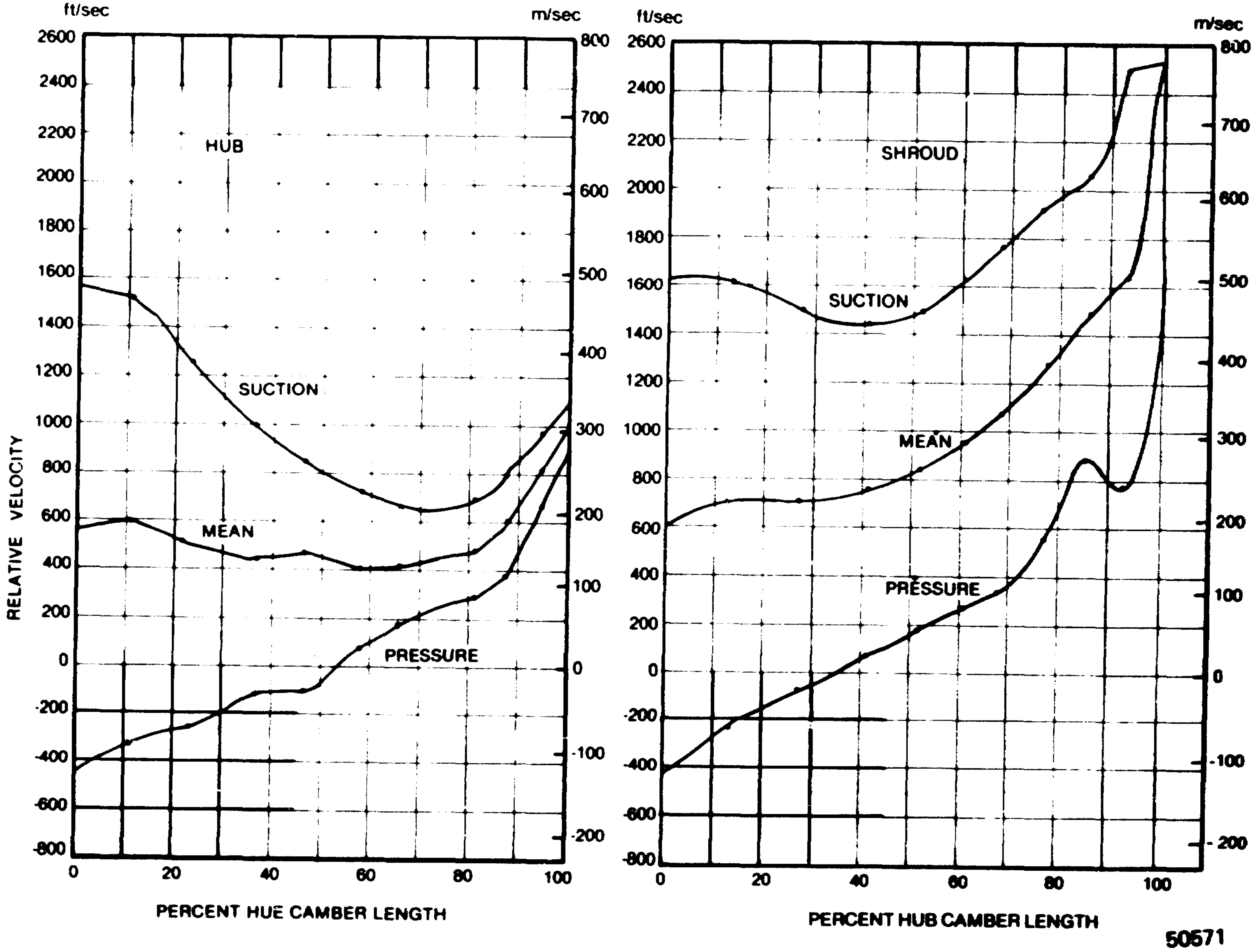

Figure 60. PRELIMINARY ROTOR BLADE LOADINGS, 100% FLOW.

4.2 DESIGN LIFE ANALYSIS

4.2.1 Preliminary Rotor Temperatures

In order to quantify the thermal performance of the uncooled turbine rotor blades a three-step thermal analysis was conducted:

<u>Step 1</u> Adiabatic Wall Temperature Estimate

The effect of gas temperature distribution was calculated for the three gas temperature profiles, shown in Figure 61. These distributions are characterized as follows:

1. Standard Profile - Peak temperature 53K (95°F) above average occurs at 60% blade span. Minimum temperature 134K (242°F) below average occurs at 0% span.

2. Inverted Profile - Peak temperature of 53K (95°F) above average occurs at 40% blade span. Minimum temperature of 134K (242°F) below average occurs at 100% span.

3. Flat Profile - Temperature curve has zero slope from 20% span to 80% span, 17K (30°F) above average. This is deemed the flattest profile attainable.

For the design point, adiabatic wall temperatures were calculated based on the local blade surface gas temperatures and Mach numbers. This adiabatic thermal analysis assumes that conduction within the blade and conduction from the blade to the disk is small with respect to the convection from the hot gas to the blade. Additional metal temperature estimates were made for the high gas flow cases. The results of these calculations are shown in Figures 62 through 64.

Figure 62 shows the blade temperature distribution with a standard (peak at 60% span from the hub) gas temperature profile at design point conditions. Peak temperatures are propogated along streamtube 3 (40 percent flow streamtube) as a consequence of the profile peak at 60% span. A maximum temperature of 1366K (2000°F) occurs at the tip and the minimum temperature of 1033K (1400°F) occurs at the exducer hub.

ORIGINAL PAGE IS
OF POOR QUALITY

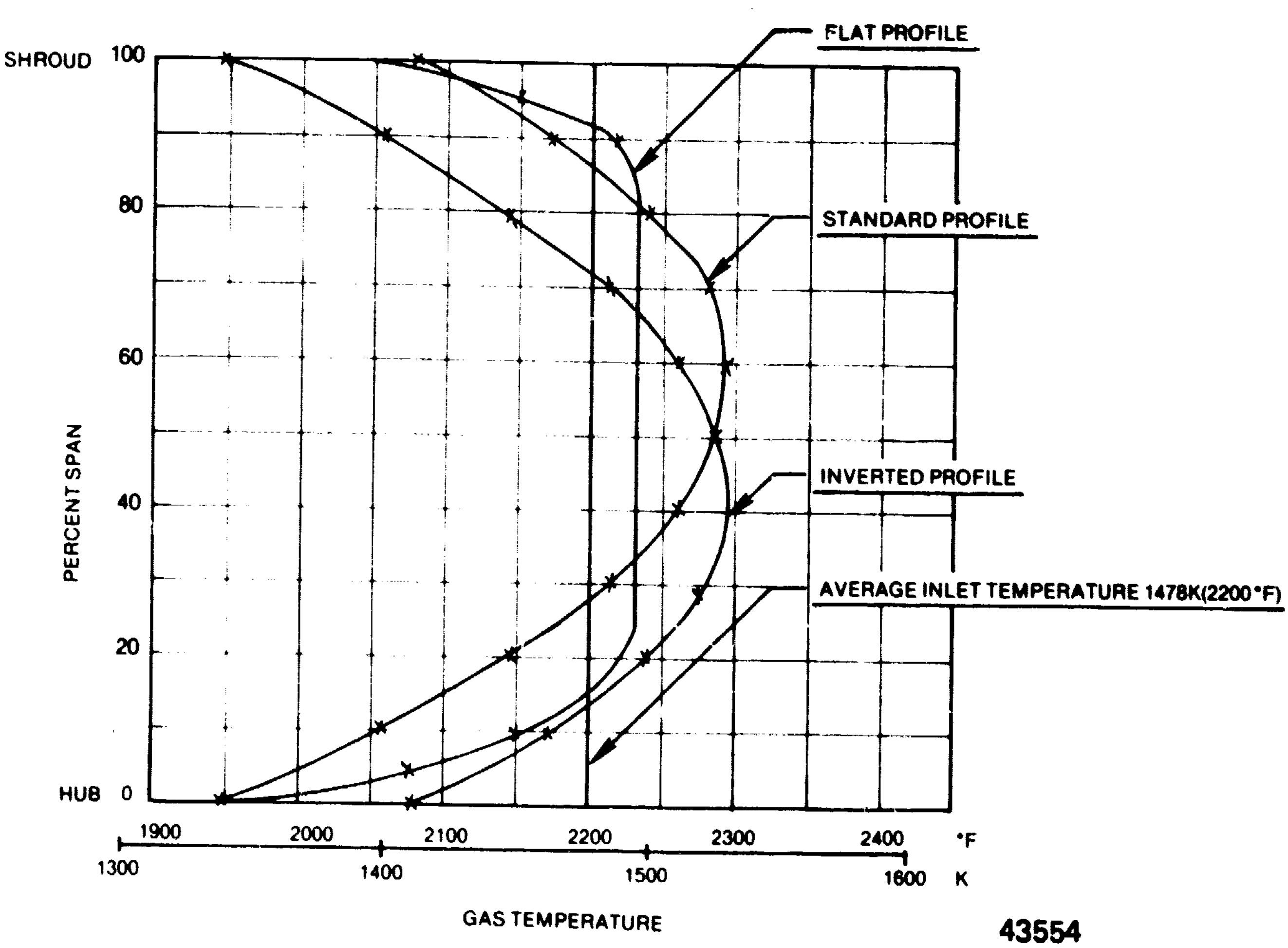

Figure 61. TURBINE INLET GAS TEMPERATURE PROFILES.

ORIGINAL PAGE IS
OF POOR QUALITY

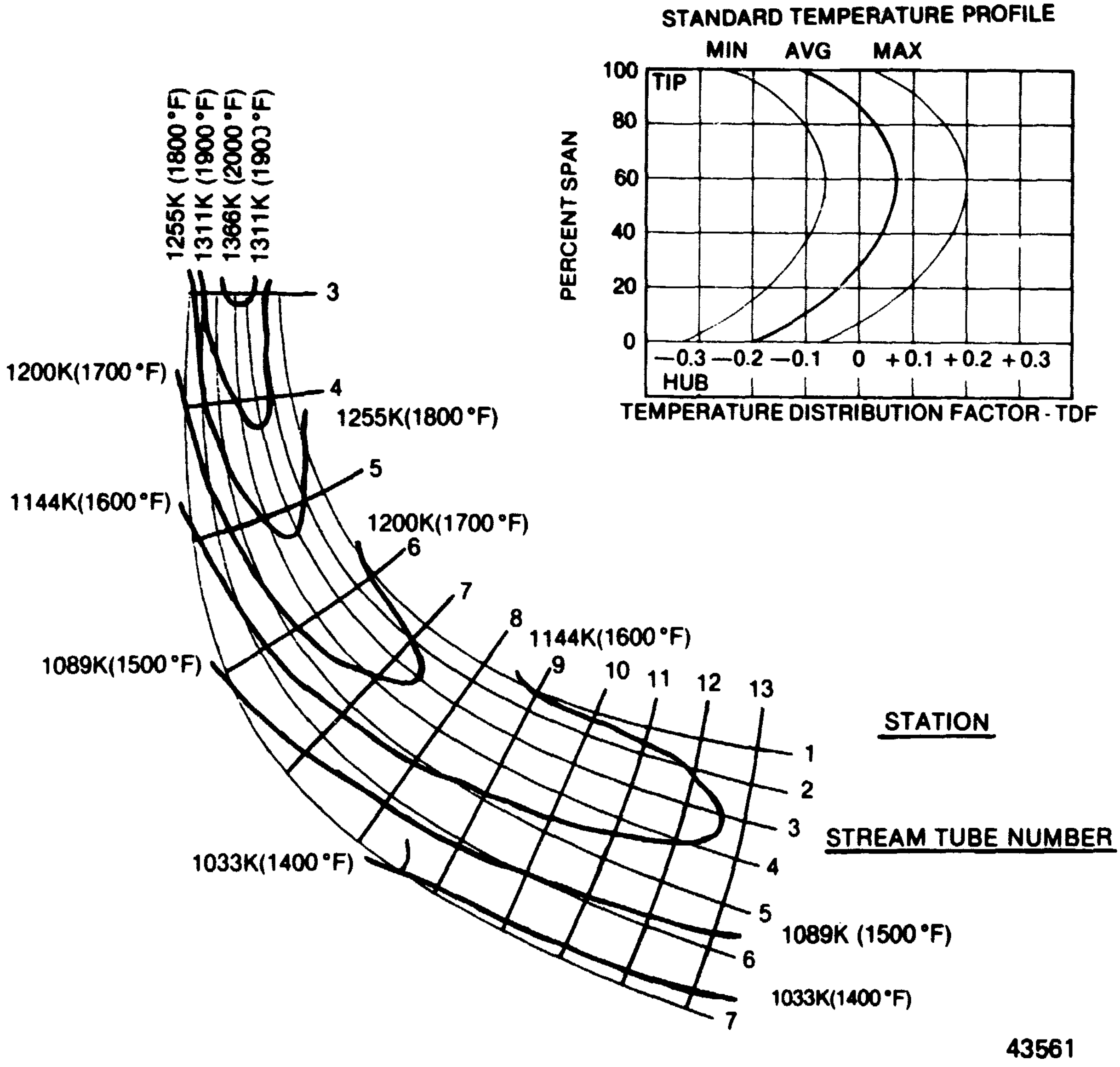

Figure 62. ROTOR DESIGN POINT TEMPERATURE DISTRIBUTION WITH STANDARD TEMPERATURE INLET PROFILE.

Blade temperature distributions with the inverted gas temperature profile (peak at 40% span from the hub) at design point are illustrated in Figure 63. Peak temperatures are propogated along streamtube 4 (60 percent streamtube) as a consequence of the profile peak at the 40% span position. A maximum temperature of 1366°K (2000°F) occurs again at the tip and the minimum temperature of 1089°K (1500°F) occurs at the exducer hub.

In order to further illustrate the change in blade thermal properties due to assumed inlet conditions, the temperature distribution with the flat gas temperature profile is shown in Figure 64 under the conditions of maximum flow. The metal temperature profiles are quite flat. The maximum temperature of 1366°K (2000°F) occurs at the tip and the minimum temperature of 1089°K (1500°F) occurs at the exducer hub. The local temperatures are related to the gas flow rate and to the radius. The gas temperature profile is distorted as it propagates through the rotor resulting in higher local metal temperatures corresponding to higher local gas temperatures.

Step 2 Coarse Grid Two Dimensional (2-D) Thermal Analysis

To evaluate the blade conduction effects with respect to the hot gas convection, a course grid two-dimensional thermal network analysis including the rotor disk was conducted using CINDA (Reference 24). The flat gas temperature profile was applied to a 20 node representation of the rotor, and heat transfer coefficients were evaluated at the design flow condition. Figure 65 is the calculated temperature distribution. The temperature pattern within the blades is nearly the same as for the adiabatic wall case. This demonstrates that intrablade conduction is small with respect to the convection between gas and blade. The maximum temperature of 1355°K (1980°F) occurs at the tip and the minimum temperature of 1116°K (1550°F) occurs at the exducer hub. Significant thermal gradients are developed on the disk front face near the rim. This indicates that care in applying the seal leakage and windage cooling to the disk will be required. Only small differences from Step 1 analysis in the blade temperature distribution are found. It is concluded that the adiabatic assumption is confirmed for preliminary analysis.

ORIGINAL PAGE IS OF POOR QUALITY

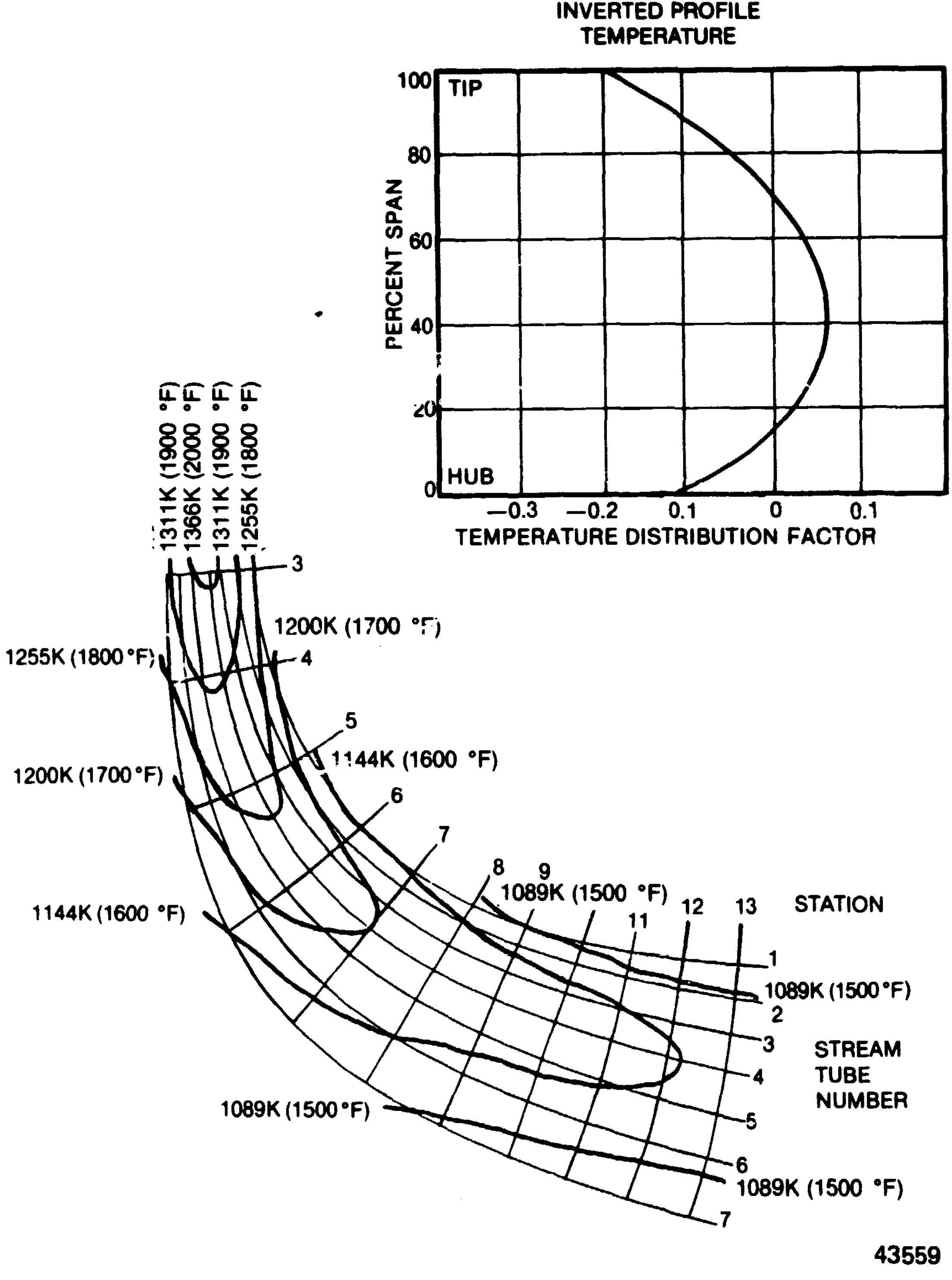

Figure 63. ROTOR DESIGN FLOW TEMPERATURE DISTRIBUTION WITH INVERTED INLET TEMPERATURE PROFILE.

ORIGINAL PAGE IS
OF POOR QUALITY

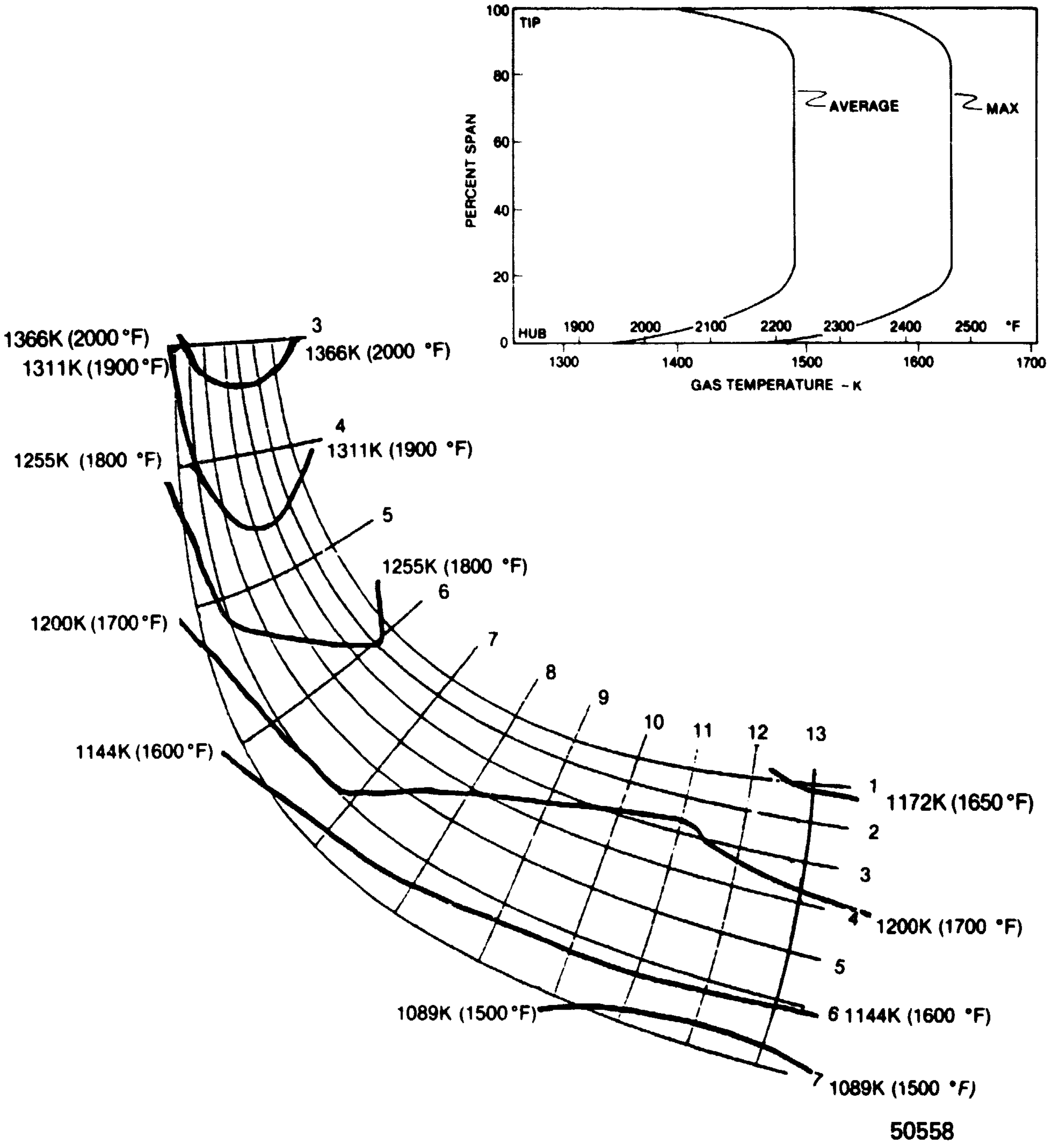

Figure 64. ROTOR MAXIMUM FLOW TEMPERATURE DISTRIBUTION WITH FLAT INLET TEMPERATURE PROFILE.

ORIGINAL PAGE IS
OF POOR QUALITY

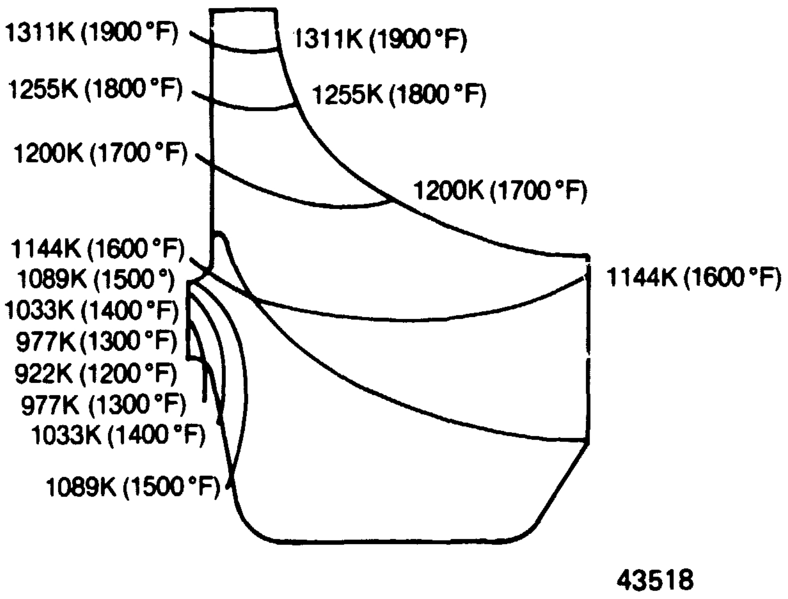

Figure 65. PRELIMINARY 2 DIMENSIONAL ROTOR TEMPERATURE DISTRIBUTION AT DESIGN FLOW.

Step 3 Fine Grid Three Dimensional (3-D) Thermal Analysis

A fine grid CINDA network analysis was conducted to provide a temperature distribution sufficiently detailed to enable a rotor structural life estimate. Gas boundary temperature conditions were compensated for nozzle cooling, leakage flow injection, and mixing effects. For the uncooled rotor configuration a back face labyrinth leakage flow rate of 0.45 percent was assumed to be injected at the bottom of the scalloped rotor backface.

For the flat gas profile, a thermal network was set up in one-to-one correspondence with the aerodynamic streamtube network. This correspondence allowed immediate calculation of the gas temperature, the gas side heat transfer coefficient, and the blade conduction parameters. The analysis was extended to the disk to show the effect of cooling due to labyrinth backface seal leakage and veil cooling due to nozzle sidewall cooling flow injection at the rotor tip. The hub represents a thermal boundary for this analysis with disk temperatures used as a boundary condition for blade analysis. The results of this fine grid analysis are shown in Figure 66. A key result of this analysis is the revelation of a steep temperature gradient at the disk front face near the rim. A cold spot at this location, due primarily to the cold leakage flow injection, extends into the nearby blade and produces high temperature gradients. This analysis thus confirms the results of the coarse grid analysis. It was concluded that, for the final CINDA analysis, greater care would have to be taken in the design of the leakage flow path and an accurate treatment of leading edge velocity loading would be needed from the aerodynamic analysis.

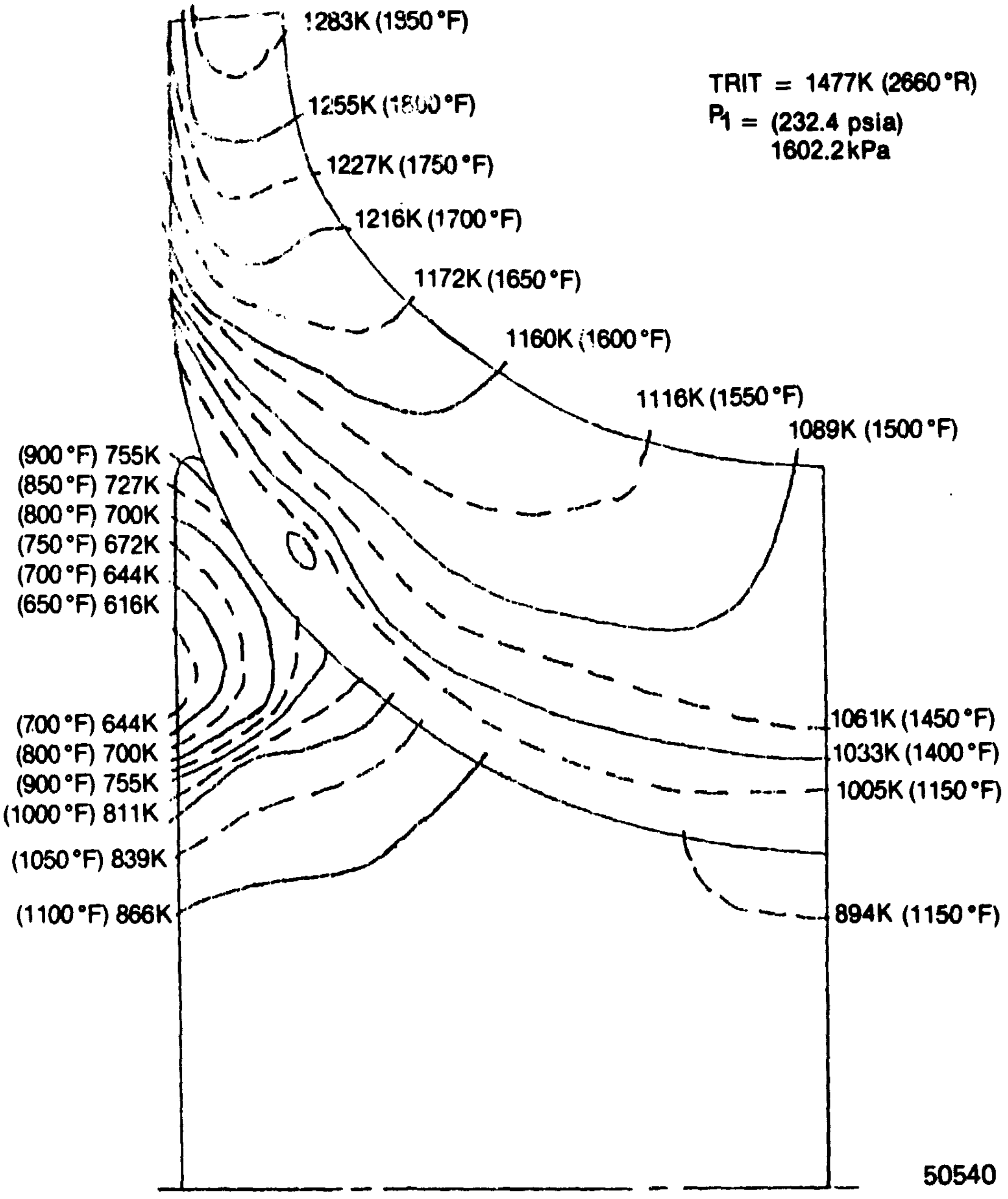

Figure 66. FINE GRID 3-D THERMAL ANALYSIS, ROTOR TEMPERATURE DISTRIBUTION - DESIGN FLOW CONDITIONS.

4.2.2 Rotor Structural Analysis

The structural analysis used the results of the refined thermal analysis to generate a thickness distribution which would provide the design life. Blade and disk stresses were calculated with an axisymetric finite element model which has the capability of representing blade structures as plane stress elements in a meridional plane (Figure 67). Since the blade elements are all radial, minimal inertial bending will be induced from the rotation. This provides a very accurate representation of the stresses. Thickness distributions were generated by preprocessors and input on an iterative basis to achieve a rotor structure with adequate rupture life. The results of the analysis are presented in Figure 68. The maximum stress is the tangential stress in the hub bore. The average tangential stress is 524MPa (76 ksi) providing a burst margin of over 40% on maximum rotor speed. Blade stresses are shown as effective stress (Von Mises equivalent stress). The rupture life is indicated in the blade based on the material properties discussed earlier. The preliminary design presented has been exercised to the point of having acceptable rupture life in all but a few locations for the life specification of Figure 69. At this stage of preliminary analysis it was concluded that the blading of the configuration demonstrated the capability of reaching design goals in the detailed design phase and that further iteration would be unwarranted until the final design thermal conditions were determined.

ORIGINAL PAGE IS
OF POOR QUALITY

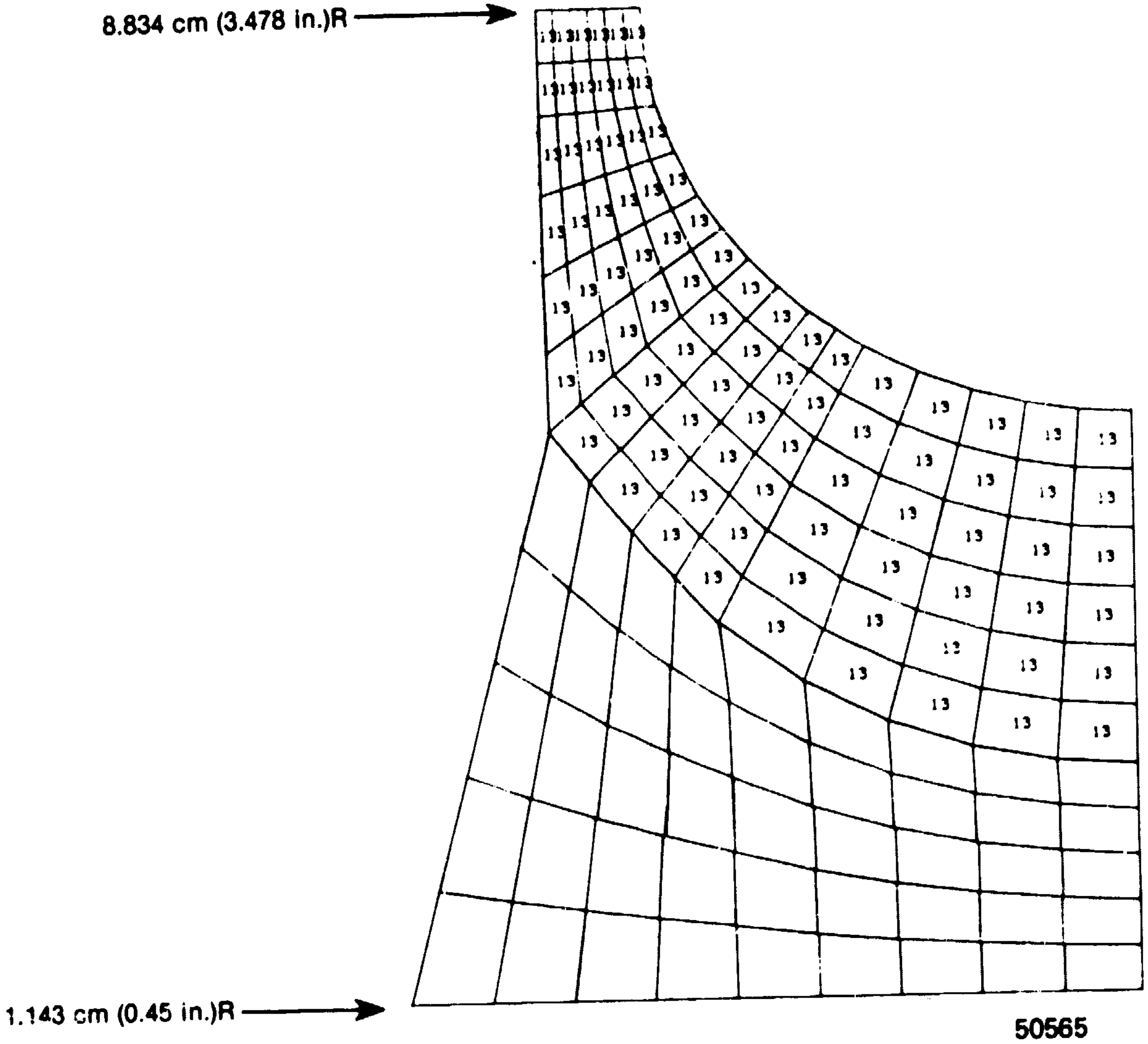

Figure 67. REFINED STRUCTURAL ANALYSIS MODEL.

ORIGINAL PAGE IS
OF POOR QUALITY

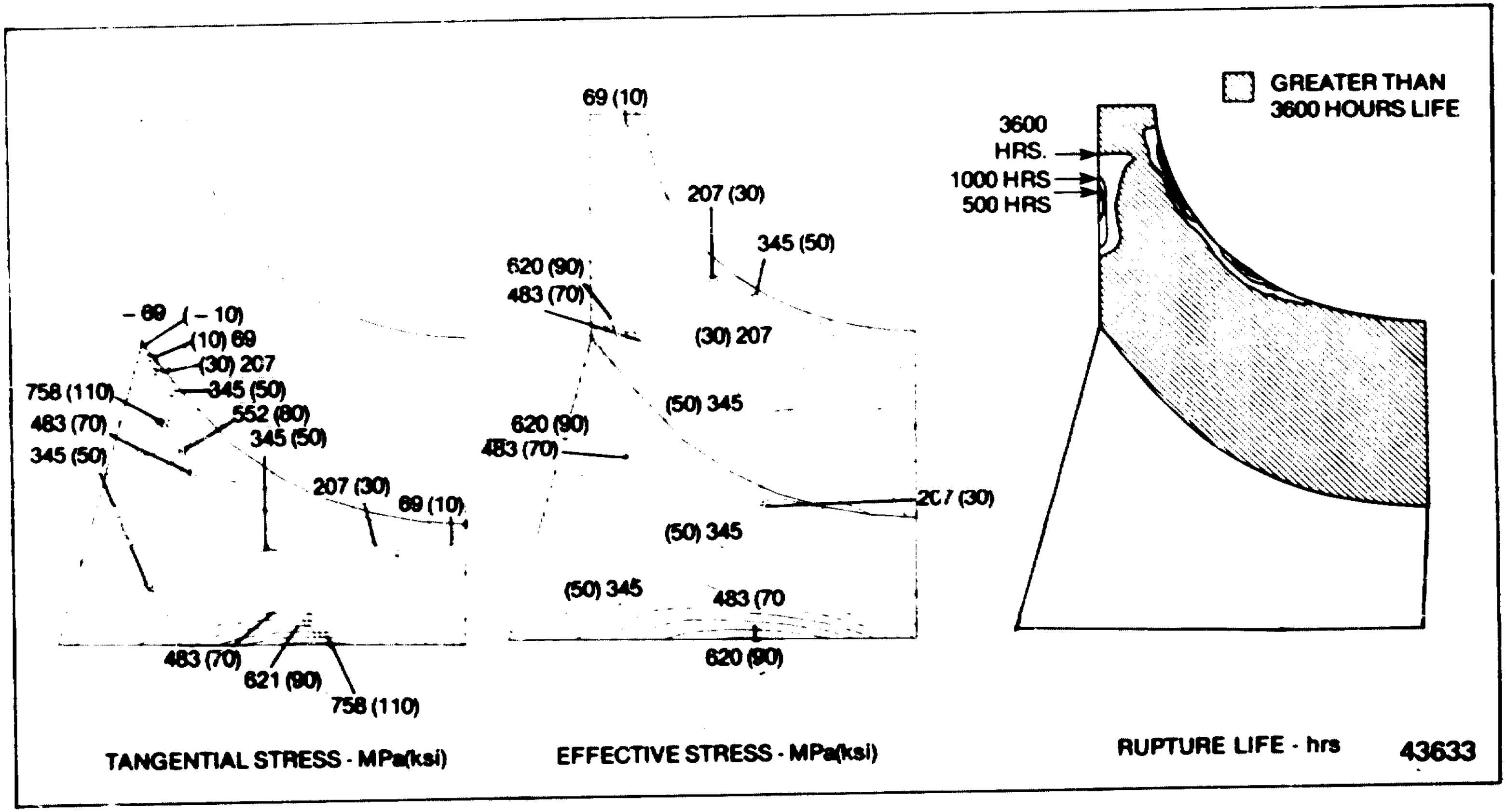

Figure 68. RADIAL TURBINE STRESS AND LIFE ASSESSMENT.

(a) TIME LIMITED LIFE SPECIFICATION

% POWER	% TIME
100	20
60	50
55	20
35	5
IDLE	5

*4000 HOUR TOTAL LIFE: 90% AT MAXIMUM SPEED & TEMPERATURE

(b) EVENT LIMITED LIFE SPECIFICATION

- START AND ACCELERATE TO IDLE
- IDLE FOR 5 MINUTES
- ACCELERATE TO MAXIMUM POWER
- RUN AT MAXIMUM POWER, 5 MINUTES
- SHUTDOWN
- COOL 60 MINUTES
  - 5000 START/STOP CYCLES
  - NO INTERMEDIATE EXCURSIONS

50529

Figure 69. TIME AND EVENT LIMITED LIFE SPECIFICATIONS.

A segment model of the backface including the blade tip was set up to estimate the maximum concentrated stress in the fillet to gain an assessment of the cyclic life capability (Figure 70). The results of the analysis are presented in Figure 71 and indicate a maximum fillet stress of 717MPa(104 ksi). The bore stress is shown as 1034 MPa (150 ksi) which is somewhat higher than the bore stress indicated in Figure 68. The back face will have the support of the less highly loaded disk structures and the peak fillet stress would likely be lower than the 717 MPa (104 ksi) indicated. Even this stress level (which is quite conservative) is well below the yield point of the material. The cyclic stress curve in Figure 72 indicates that directionally recrystallized (DR) RSR185 with minimum property characteristics will withstand approximately 30,000 cycles of peak alternating stress up to 944 MPa (137 KSI) at 867K (1100°F). On this basis the cyclic life would exceed 10,000 cycles of the simple cycle specified in Figure 69. It appears from this analysis that the disk bore will be the LCF limited area of the rotor.

The most common source of distress in turbo-machinery is high cycle fatigue caused by stage vibration (resonance or instability). A preliminary design must address the stage dynamics to insure that the design will operate in a favorable resonant environment. Figure 73 shows the NASTRAN plate model used to analyze the vibratory mode characteristics of the stage. The analysis is a 3-pass solution to account for rotational stiffening effects. The results are presented in Figure 74 which shows the blade frequency and mode shapes (constant deflection) of the first three modes. The model includes the proper thickness distribution and representative blade curvature which will provide an accurate assessment of the vibration characteristics. The resonance diagram in Figure 75 indicates that the first mode (exducer bending mode) has a significant margin on the low order engine excitation (1e-4e). This excitation is caused by inlet or exhaust pressure distributions (circumferential distortion), and has been avoided entirely. The exhaust duct can have up to 7 struts without exciting the rotor. The preliminary choice of 17 stators shows a resonance free condition near maximum speed for that excitation. The resonance situation on a preliminary basis is exceptionally favorable. The final design will determine the idle speed and 35% power speed which should also have a favorable resonance condition. Final tuning includes selection of strut and nozzle counts and thickness distributions to tune the modes.

ORIGINAL PAGE IS
OF POOR QUALITY

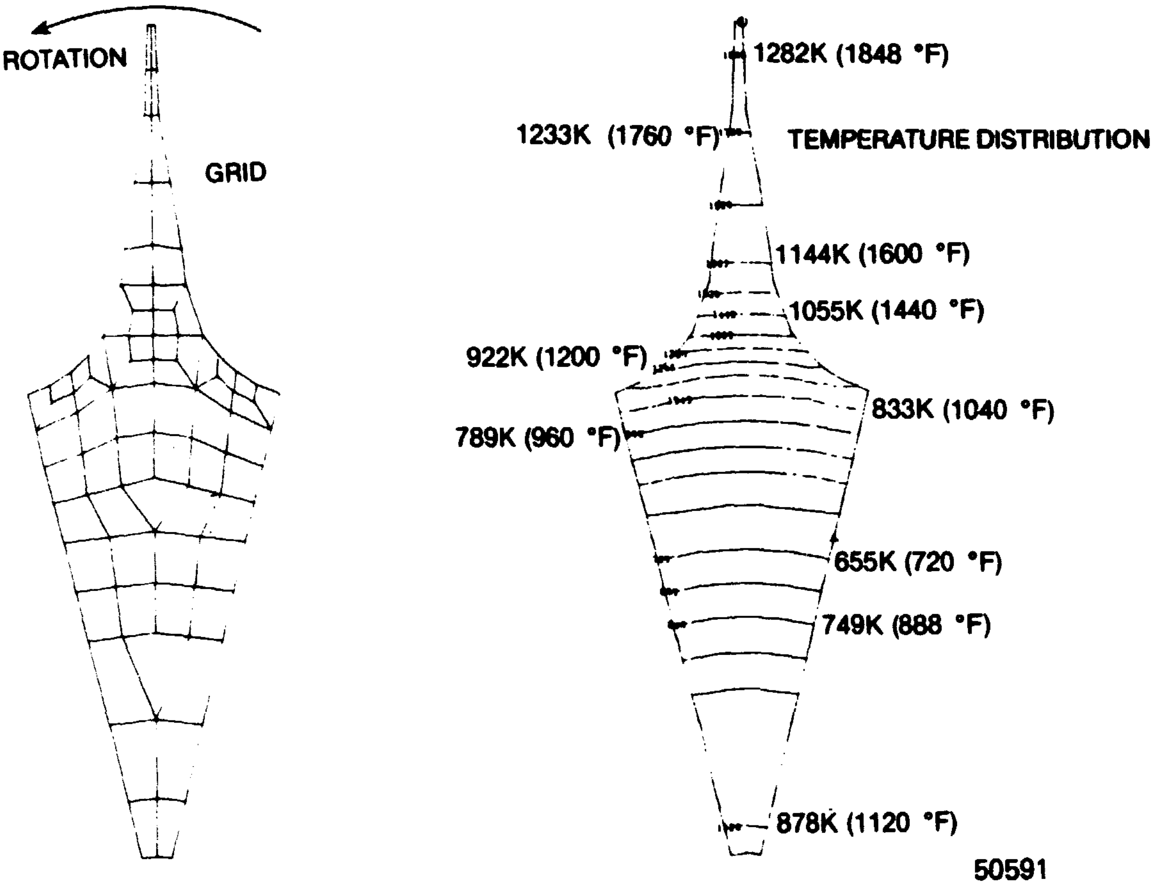

Figure 70. REFINED STRUCTURAL ANALYSIS MODEL OF BACKFACE SEGMENT.

ORIGINAL PAGE IS
OF POOR QUALITY

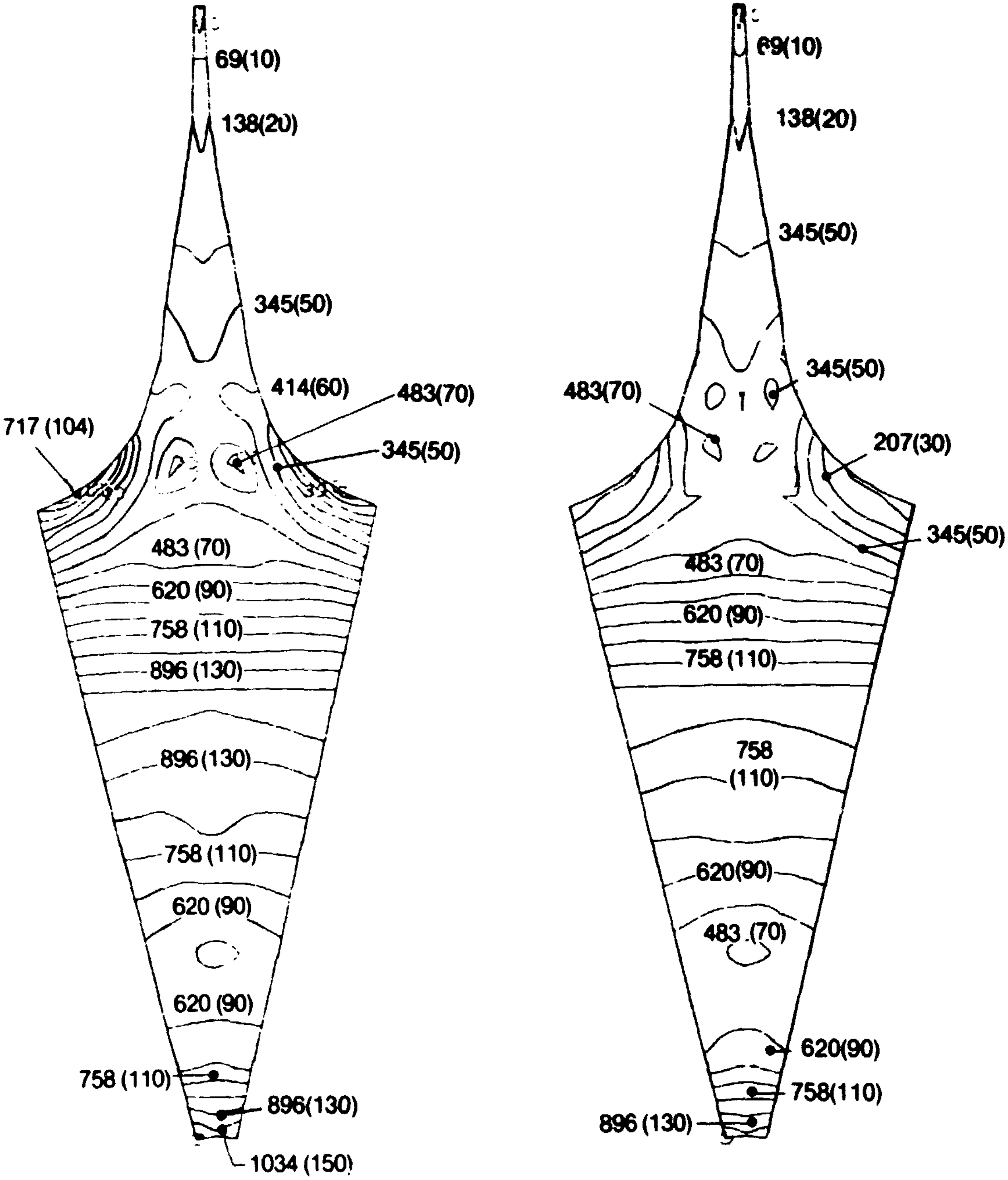

PRINCIPAL STRESS, MPa(ksi)

EFFECTIVE STRESS, MPa(ksi)

Figure 71. RADIAL INFLOW TURBINE CYCLIC LIFE ASSESSMENT.

ORIGINAL PAGE IS
OF POOR QUALITY

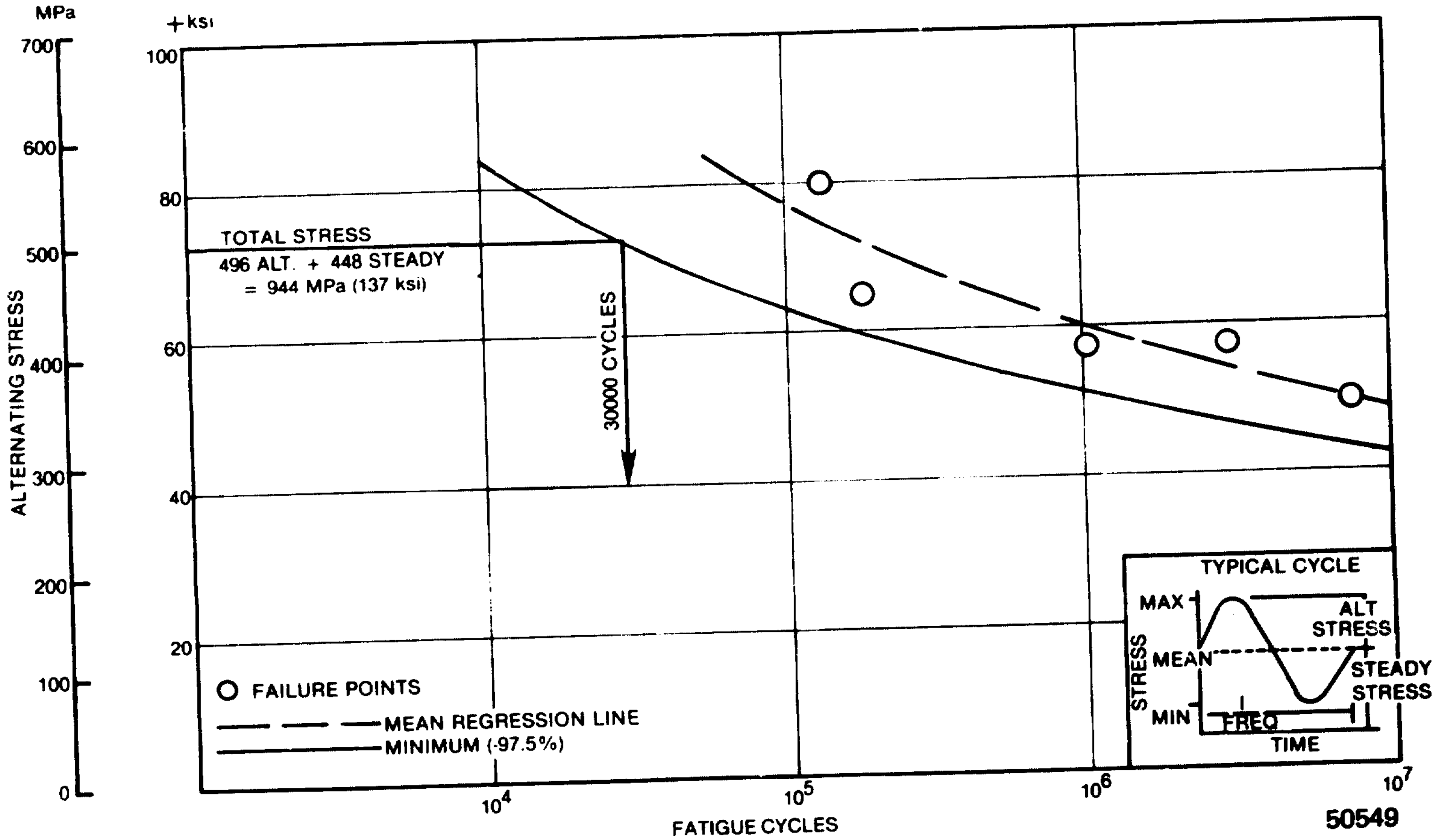

Figure 72. RSR 185 DIRECTIONALLY RECRYSTALIZED MATERIAL CHARACTERIZATION.

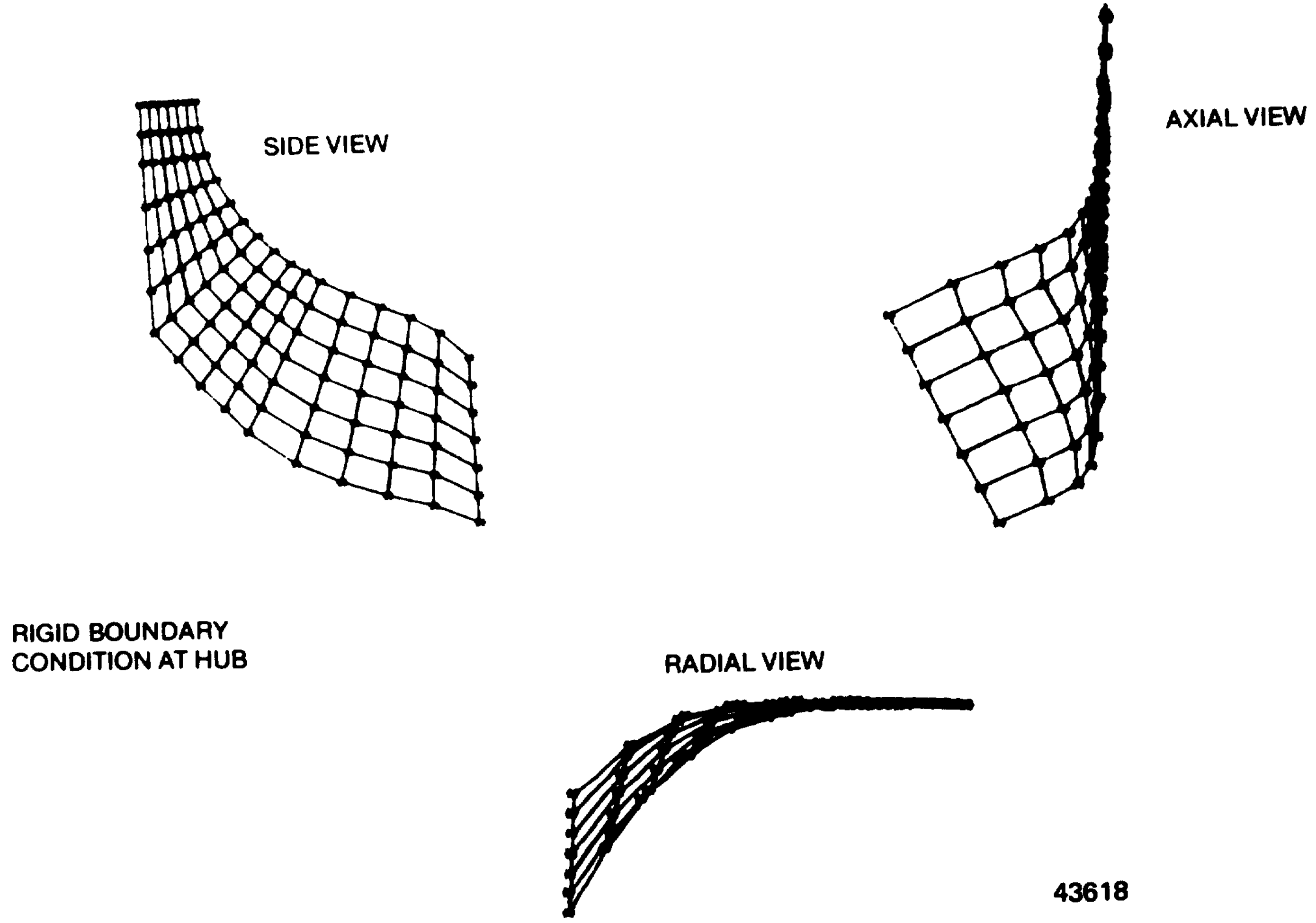

ORIGINAL PAGE IS
OF POOR QUALITY

Figure 73. PRELIMINARY NASTRAN VIBRATION ANALYSIS MODEL.

ORIGINAL [illegible]
OF POOR QUALITY

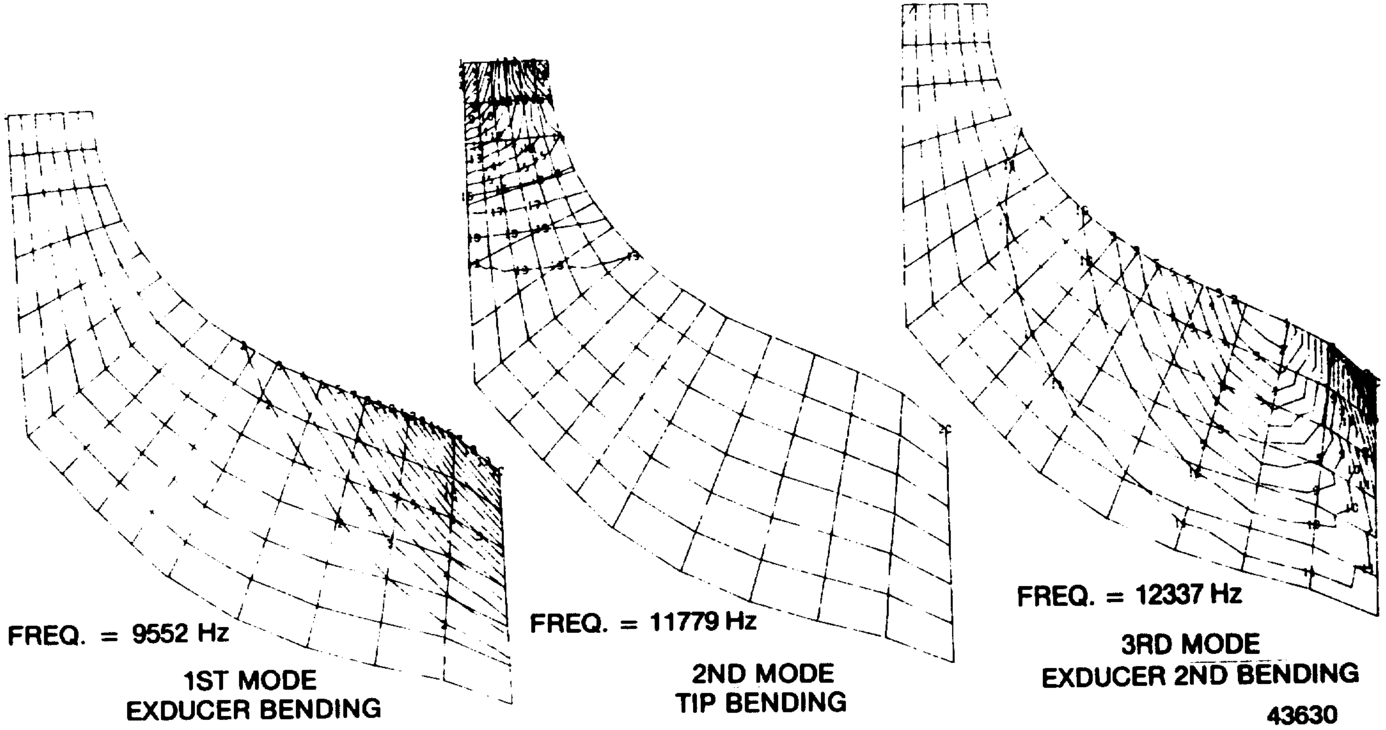

FREQ. = 9552 Hz

1ST MODE
EXDUCER BENDING

FREQ. = 11779 Hz

2ND MODE
TIP BENDING

FREQ. = 12337 Hz

3RD MODE
EXDUCER 2ND BENDING

43630

Figure 74. NASTRAN MODAL ANALYSIS, DEFLECTED MODE SHAPES.

ORIGINAL PAGE IS
OF POOR QUALITY

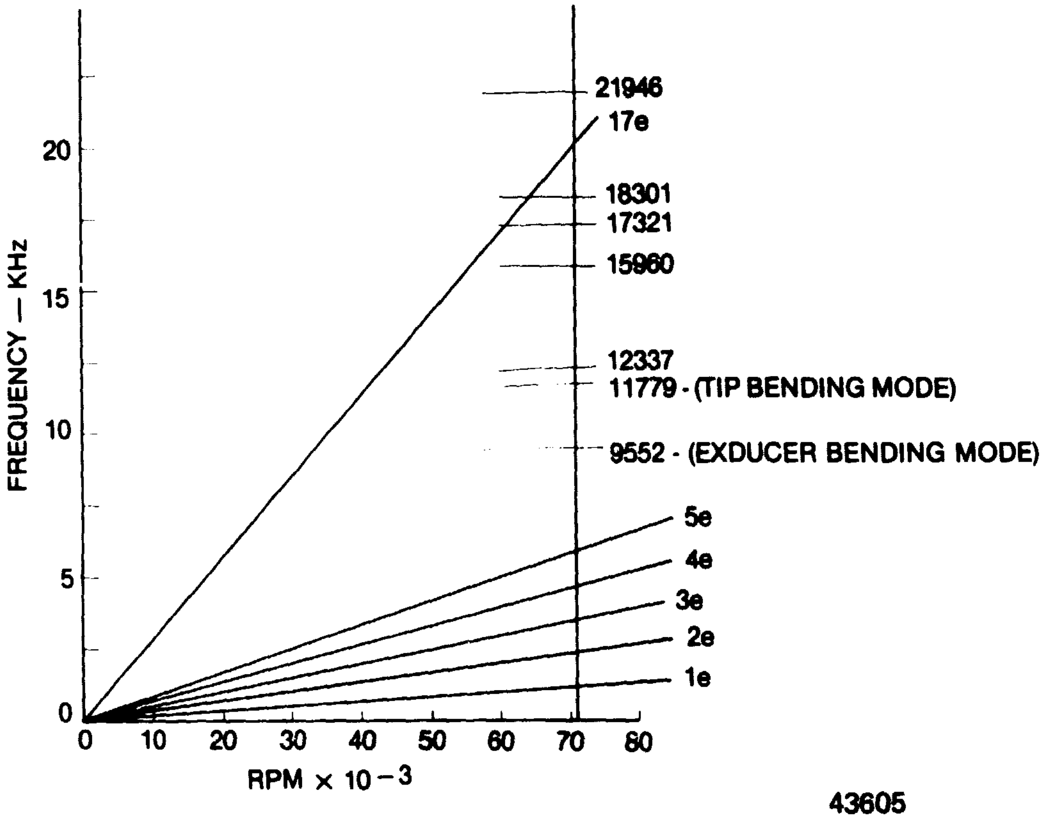

Figure 75. PRELIMINARY RESONANCE DIAGRAM.

As a final element of the preliminary structural assessment, a sensitivity study was undertaken to determine the flexibility which will be possible in the final design. The study was intended to determine the tip and hub thickness combinations necessary to meet the blade life goals. It was determined that a hub to tip taper ratio of 6.8 or greater is necessary for adequate life. This is based on a one dimensional analysis and is representative of the latitude which would be available for vibration tuning or to provide life margins.

SECTION 5.0

AERODYNAMIC DESIGN (TASK III)

5.1 FINAL FLOWPATH

Following completion of the preliminary turbine design study, the initial selection of nozzle exit angle and free-vortex radius ratio was reviewed. Detailed studies on the rotor loading showed a requirement of increasing the number of blades from 11 to 13 to avoid suction side separation as discussed in Section 5.3.2 and the number of nozzle vanes was reduced from 17 to 15 to avoid rotor blade critical frequencies. It was also determined at the end of Task II that a 0.009 rad. (0.5 degree) error in nozzle vane setting for a 1.4 rad. (80°) nozzle exit angle would result in an error in throat area of about 5.0 percent. In order to provide greater tolerance to nozzle setting error and reduce free-vortex friction loss, as indicated by a parametric stator exit angle study using the new vane and rotor numbers, the nozzle exit angle was reduced. The study results shown in Figure 76 indicate that, based on the loss model of Reference 12, included in the design point computer code, the turbine design point efficiency peaks at 1.34 rad. (77°) nozzle exit angle. A design nozzle exit angle of 1.34 rad. (77°) was selected, as indicated in the final design parameter list in Figure 77.

The free-vortex radius ratio from nozzle exit to rotor inlet was changed from 1.164 to 1.096 to further reduce friction losses in this section. Figure 78 indicates that the free-vortex loss can be substantially reduced by this change in nozzle exit radius ratio. The axial width of the free vortex space was also increased by a small amount, from 0.764 cm. (0.301 in.) at the nozzle trailing edge to 0.787 cm. (0.310 in.) or 0.023 cm. (0.009 in.). This linear increase in width on the outer shroud was sized in direct proportion to the flow increase downstream of the nozzle throat due to nozzle vane cooling flow injection. The split line location of the sidewall and geometry definition is discussed in Section 5.3.2. Stator vane and rotor blade numbers were revised to optimize the initial Task II design configuration. Detailed stress analysis showed that the exducer annulus area could be increased and still meet life requirements. The rotor exit axial critical velocity ratio was, therefore, reduced to 0.310 to lower transition duct losses. A 2.54 cm (1.0 in) hub radius was maintained with -10° exit swirl. The revised flowpath shown in Figure 77 was used as the basis for Task III detailed nozzle and rotor flow analyses.

ORIGINAL PAGE IS
OF POOR QUALITY

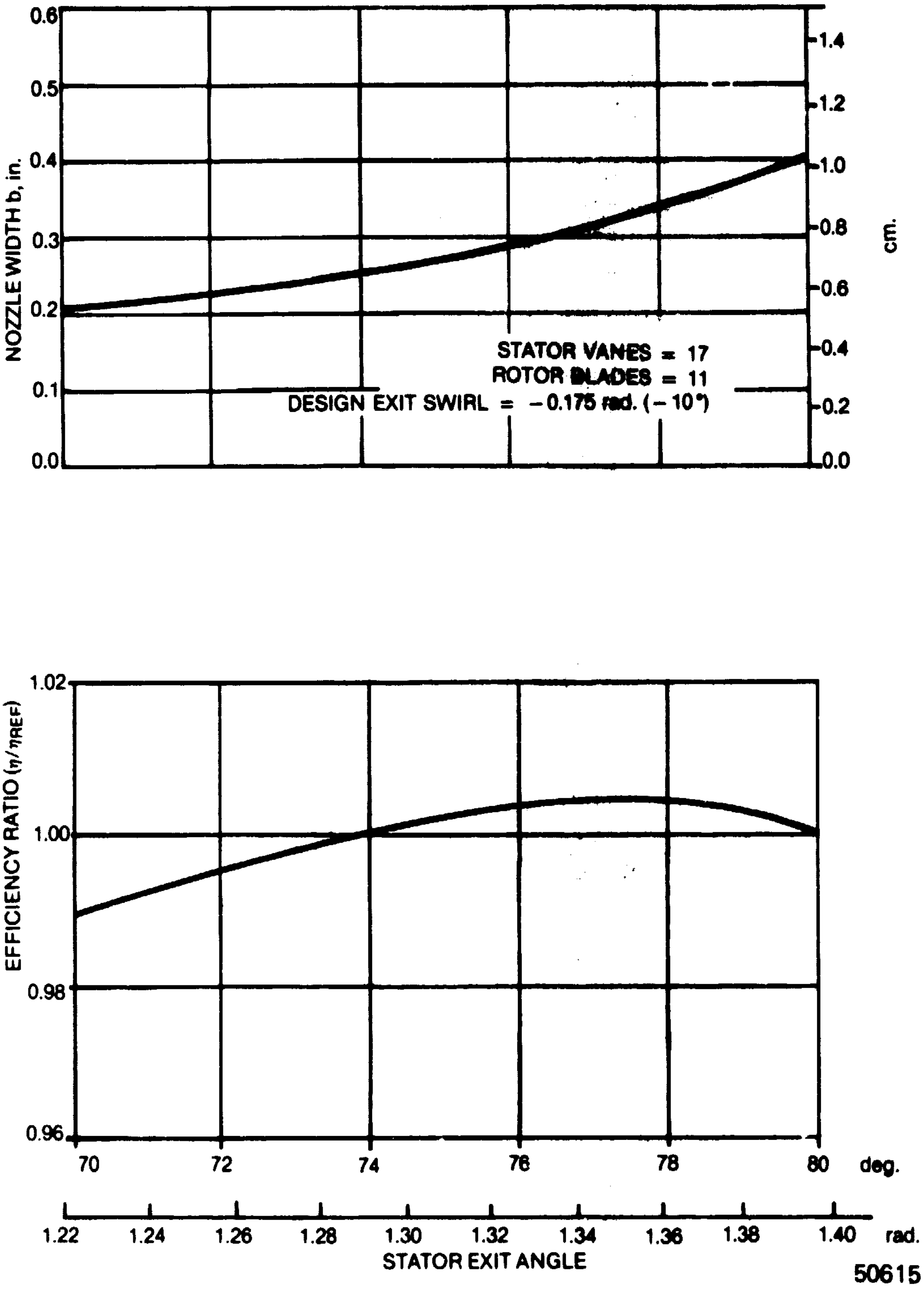

Figure 76. STATOR EXIT ANGLE REVISION.

ORIGINAL PAGE IS
OF POOR QUALITY

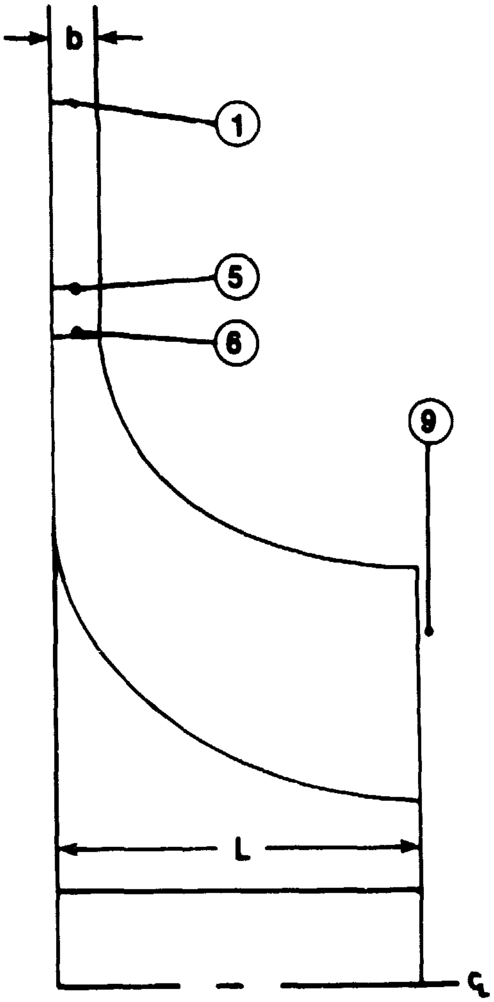

T_1	1506K (2710°R)
P_1	1.602 × 10^6 Pa (232.4 psia)
W	1.77 kg/sec (3.9 lbm/sec)
N	71,000 rpm
ΔH	442.5 kj/kg (190.3 Btu/lbm)
T_9	1477K (2660°R)
$\frac{V_{x9}}{V_{cr9}}$	0.31
R_1	12.573 cm (4.950 in)
R_5	9.680 cm (3.811 in)
R_6	8.834 cm (3.478 in)
R_9 HUB	2.540 cm (1.000 in)
R_9 TIP	5.720 cm (2.252 in)
$b_{1,5}$	0.764 cm (0.301 in)
b_6	0.787 cm (0.310 in)
L	5.334 cm (2.100 in)
STATOR EXIT ANGLE	1.34 rad. (77°)
EXIT SWIRL	−0.175 rad. (−10°)
NO. OF STATORS	15
NO. OF ROTOR BLADES	13

50617

Figure 77. FINAL AERODYNAMIC DESIGN PARAMETER VALUES.

ORIGINAL PAGE IS
OF POOR QUALITY

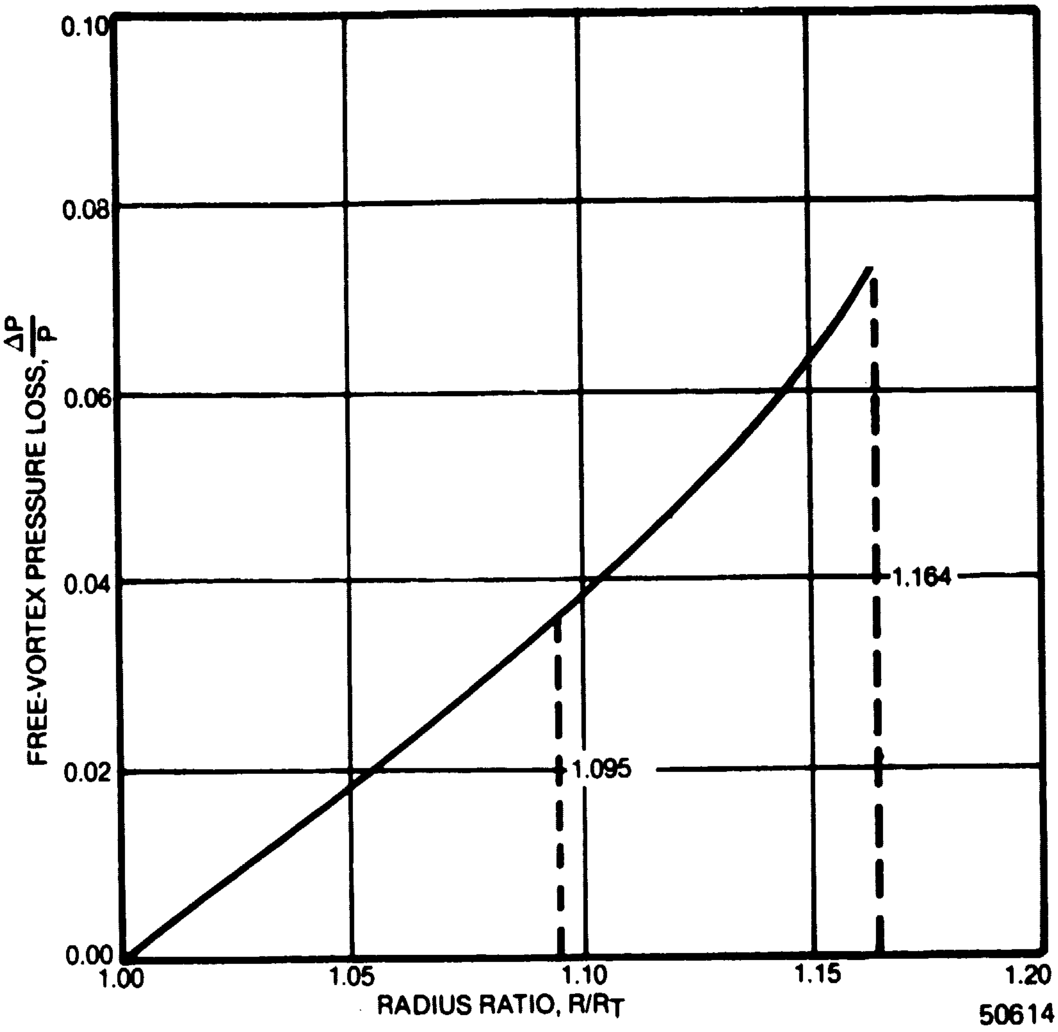

Figure 78. FREE-VORTEX LOSS VARIATION.

5.2 VELOCITY DIAGRAMS

Velocity diagrams were predicted for the final radial turbine design as shown in Figures 79, 80 and 81. The design point diagrams shown in Figure 79 were predicted using the radial turbine design point analysis computer code. The shift in rotor flow requirement as a function of power for the actuated sidewall nozzle configuration is shown in Figure 35, Section 3.3.3.1. The part power velocities were predicted using the turbine off design performance prediction computer code. The nozzle flowrate is approximately proportional to width for this configuration and the nozzle exit angle is fixed so that the nozzle throat conditions are the same as at design point. The rotor leading edge incidence at 100% power is -0.39 rad (-22.4°) (against rotation) with 0.71 rad. (40.6°) negative rotor exit absolute swirl. The turbine work requirement ($\Delta H/\theta_{cr}$) for 100% power is 4.0 percent above the design point level. This is due to compressor efficiency reduction with increasing flow above the design point value. The effect of this turbine work increase is included in the velocity diagrams.

Velocity diagrams for 50% power are shown in Figure 81. For 50% power the rotor inlet incidence is +0.29 rad. (+16.4°) (with rotation) with 0.73 rad. (42.0°) positive rotor exit swirl. The turbine specific work at 50% power is approximately the same as the design point level 89.2 kJ/kg (38.35 Btu/lb).

The estimated turbine efficiency levels for the 50-100% power range are shown in Figure 82 as a function of percent of maximum compressor air flow. The peak turbine efficiency at 78% flow was derated 2.0 points from fixed geometry nozzle performance to account for losses associated with variable sidewall vane recirculation leakage and nozzle cooling. For off-design cycle calculations, an additional 2% loss in total pressure was assigned for transition duct losses between the gas generator and power turbines. A more accurate transition loss penalty evaluation requires a design analysis of the power turbine and transition length trade off losses as a function of inlet swirl, diameter ratio and power turbine efficiency. Since both variable nozzle concepts showed nearly the same rotor variation in exit swirl, and inlet conditions to the transition duct with flow, Figures 80, 81 and 98, 99, Section 5.4.1, the same interturbine loss was assumed for both vane concepts for comparison purposes.

ORIGINAL PAGE IS
OF POOR QUALITY

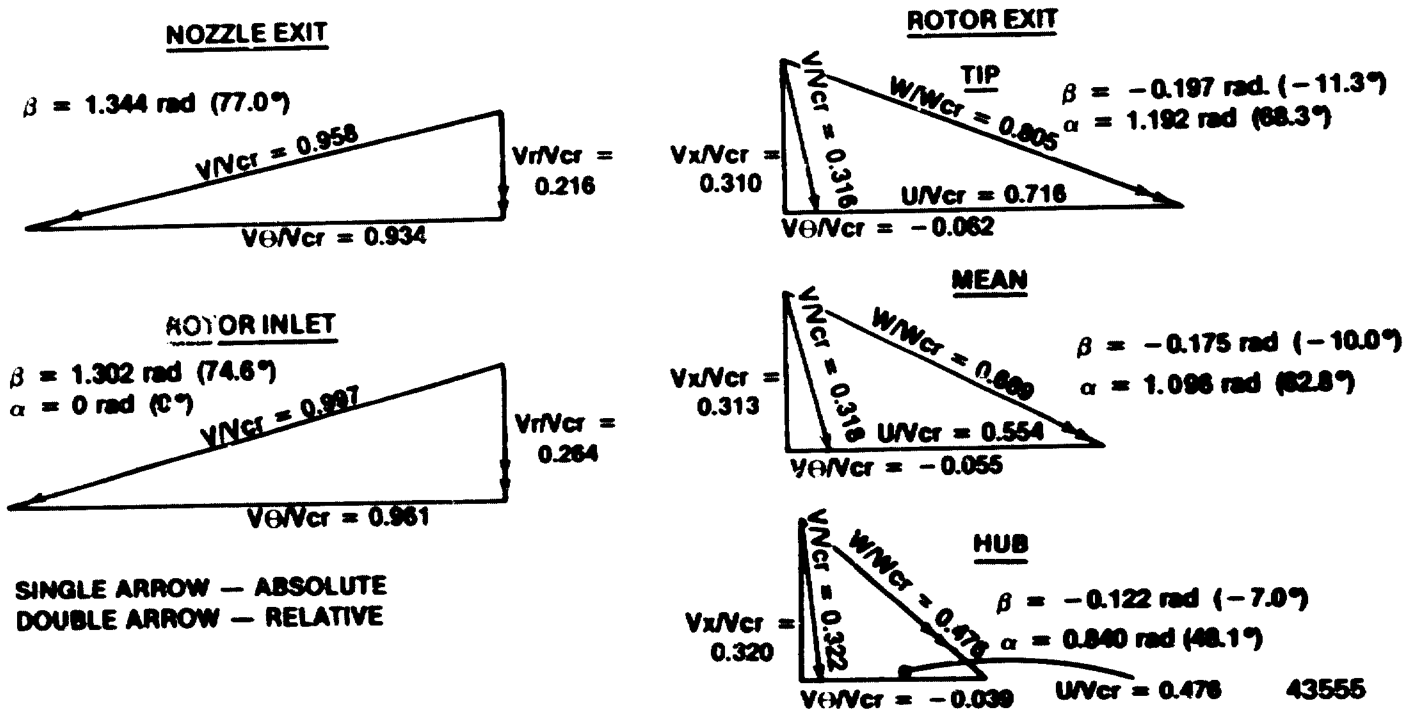

Figure 79. DESIGN POINT VELOCITY DIAGRAMS.

ORIGINAL PAGE IS
OF POOR QUALITY

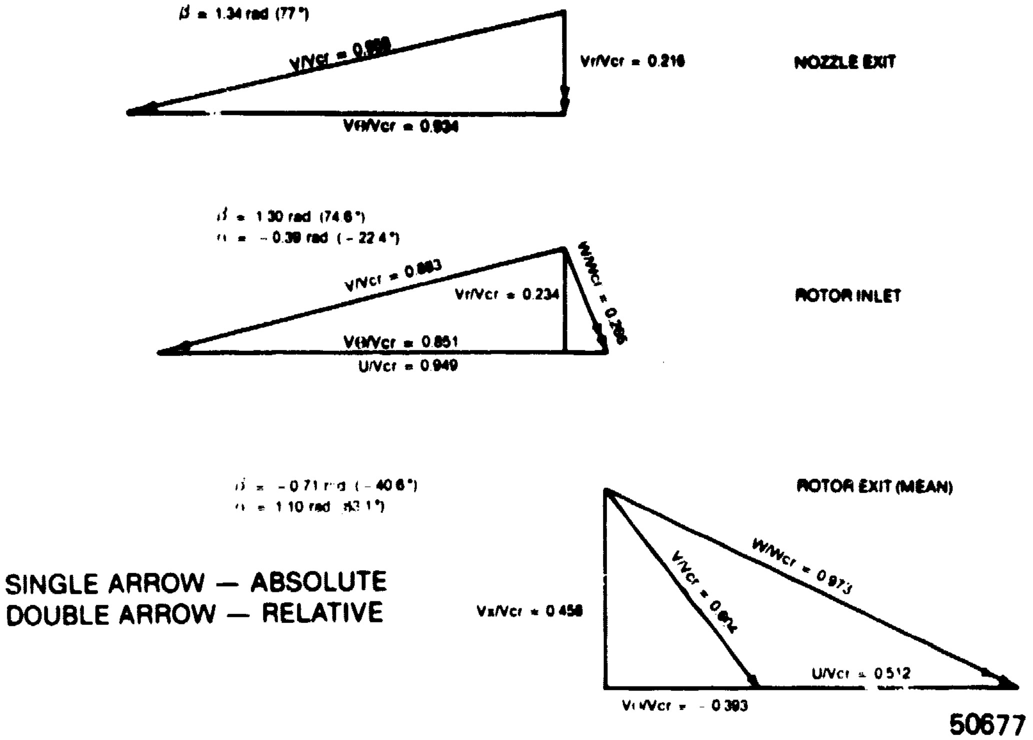

Figure 80. ACTUATED SIDEWALL NOZZLE 100% POWER VELOCITY DIAGRAMS.

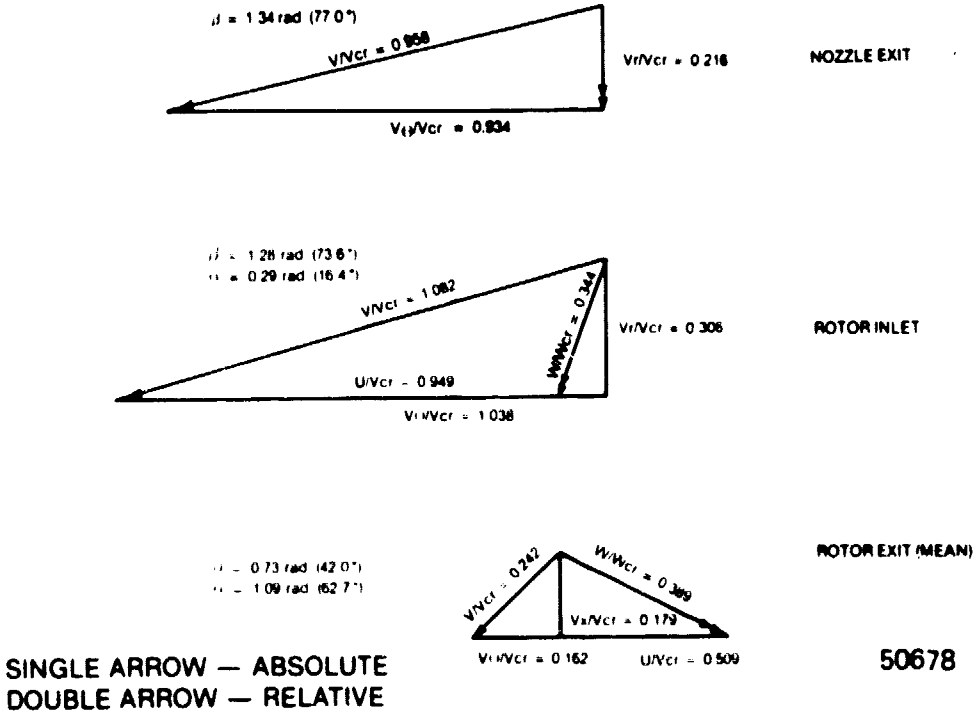

Figure 81. ACTUATED SIDEWALL 50% POWER VELOCITY DIAGRAMS.

ORIGINAL PAGE IS
OF POOR QUALITY

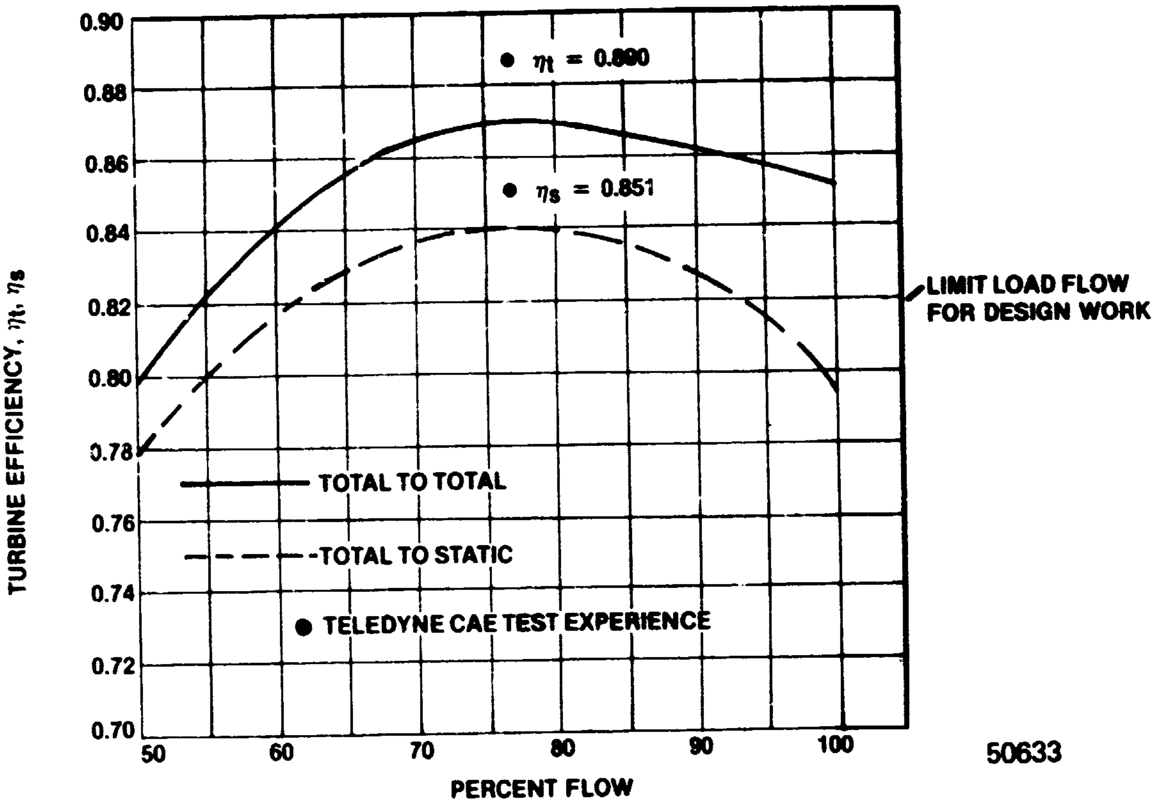

igure 82. PREDICTED VARIATION OF TURBINE EFFICIENCY WITH PERCENT POWER.

5.3 NOZZLE AND ROTOR FLOW ANALYSES

5.3.1 Stator Vane Design

A range of nozzle designs with 14 through 17 vanes was analyzed. The stator vane profiles for the 14 vane and 17 vane configurations are shown in Figures 83 and 84, respectively. A blade-to-blade flow analysis computer code (Reference 25) was used to predict vane surface velocity loadings, shown in Figure 85, for these vane profiles. While the surface velocity differentials are higher (as expected) for the 14 vane nozzle, both stator configurations provide smooth and continuous acceleration to the nozzle throat. Selection of any nozzle vane number between 14 and 17 would provide acceptable aerodynamic characteristics.

The final 15 vane nozzle aerodynamic design configuration is shown in Figure 86. The final nozzle design is a parallel sidewall configuration. The vane chord, selected to provide a well defined throat passage, results in a vane solidity of 1.44 based on exit radius. This value is on the high end of the optimum design range and should provide enhanced off-design operating characteristics. The suction surface ahead of the throat is composed of two elliptical arc sections to provide smoothly accelerating flow to the throat. The nozzle throat area selection was based on a choked throat at design flow with 6% area reduction to account for pressure loss and aerodynamic blockage. A modified log spiral curve to give a near constant velocity was used to define the suction side nozzle vane contour from the throat to the vane trailing edge. Figure 87 shows the vane surface velocity ratio distributions for the final vane profile. The suction surface diffusion downstream of the throat has been minimized. Suction surface boundary layer characteristics were predicted as shown in Figure 88 using the boundary layer analysis computer code of Reference 26. This analysis showed no indication of flow separation for the selected nozzle vane profile based on the incompressible shape factor (H_i) remaining below 2.8 along the suction surface profile for a turbulent boundary layer solution.

Vane surface profile coordinates for the design nozzle configuration are listed in Table VIII. The vane inlet and exit radii and b-width are shown in Figure 86. The leading edge vane thickness is 0.762 cm (0.300 in) and trailing edge normal thickness is 0.152 cm (0.060 in).

ORIGINAL PAGE IS
OF POOR QUALITY

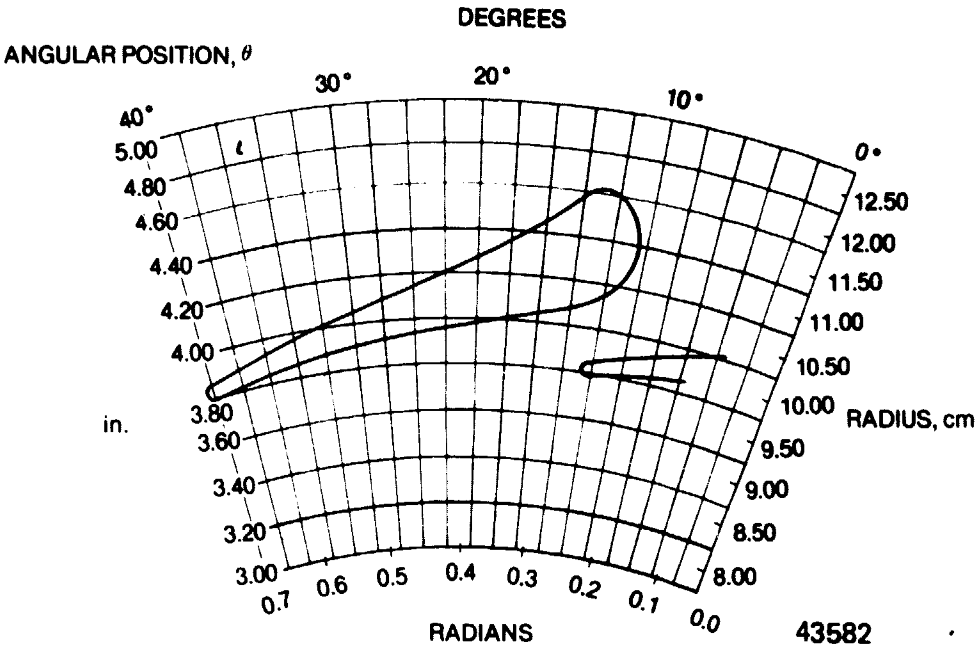

Figure 83. 14 VANE (LONG CHORD) NOZZLE CONFIGURATION.

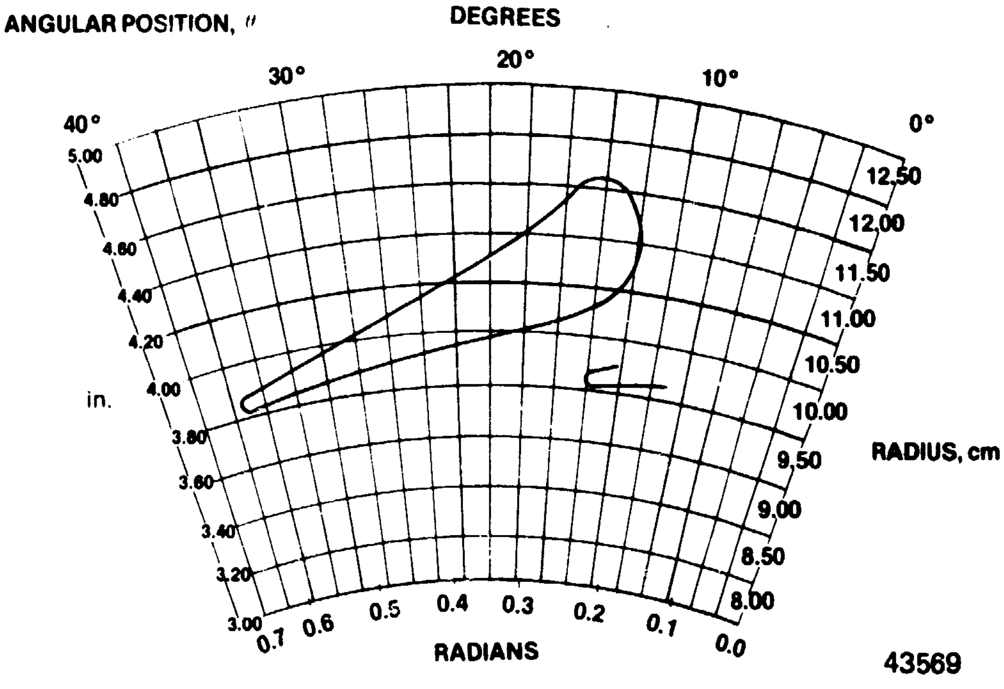

Figure 84. 17 VANE NOZZLE CONFIGURATION.

ORIGINAL PAGE IS
OF POOR QUALITY

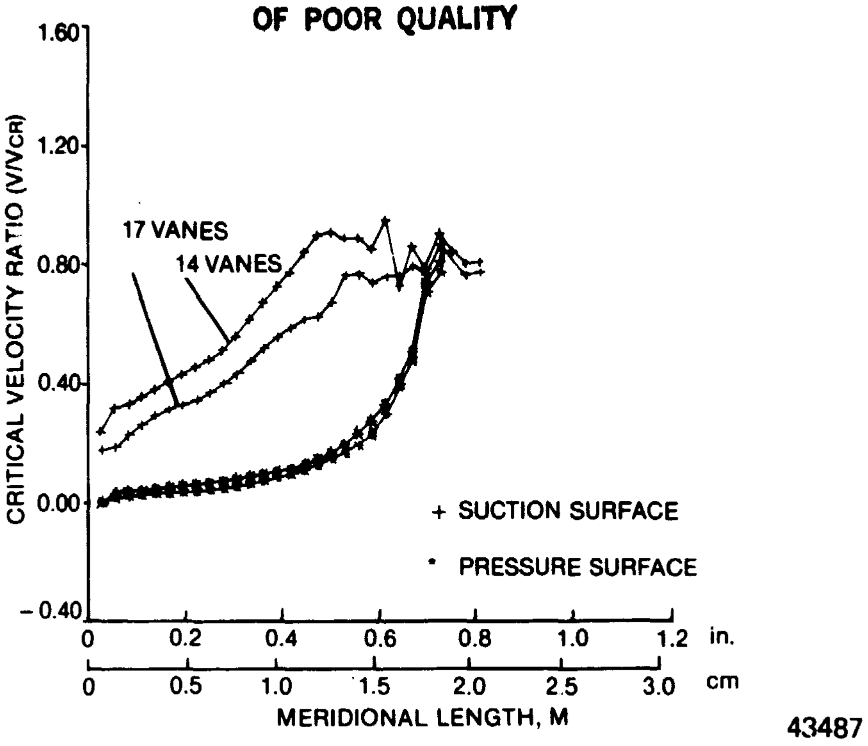

Figure 85. NOZZLE VANE SURFACE VELOCITY RATIO DISTRIBUTIONS.

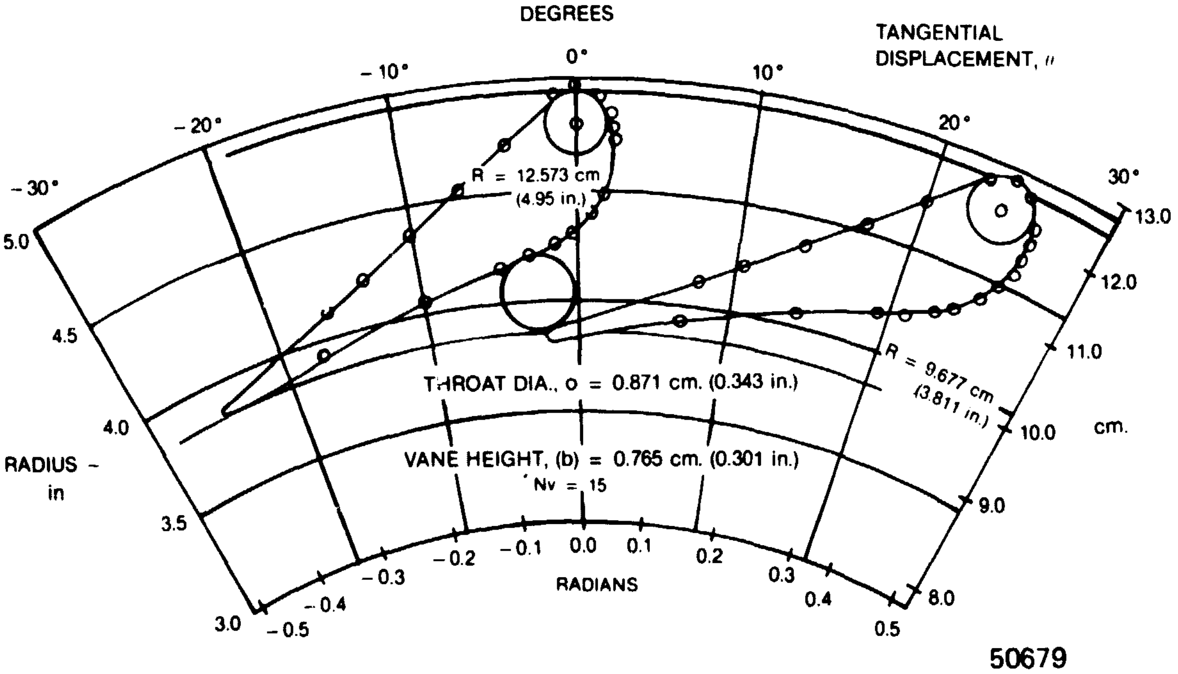

Figure 86. NOZZLE VANE PROFILE, DESIGN SETTING.

ORIGINAL PAGE IS
OF POOR QUALITY

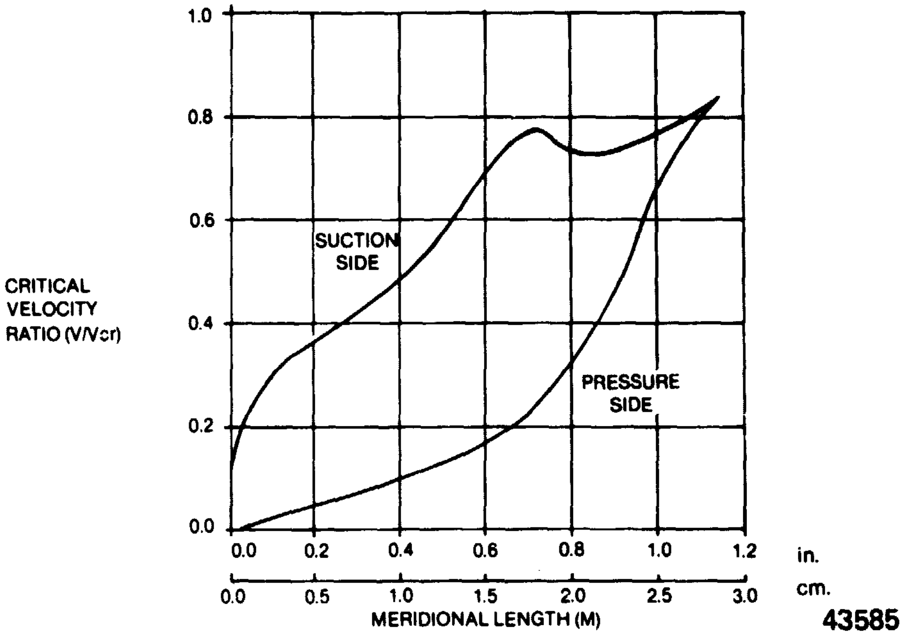

Figure 87. FINAL NOZZLE VANE SURFACE VELOCITY LOADING, 15 VANES.

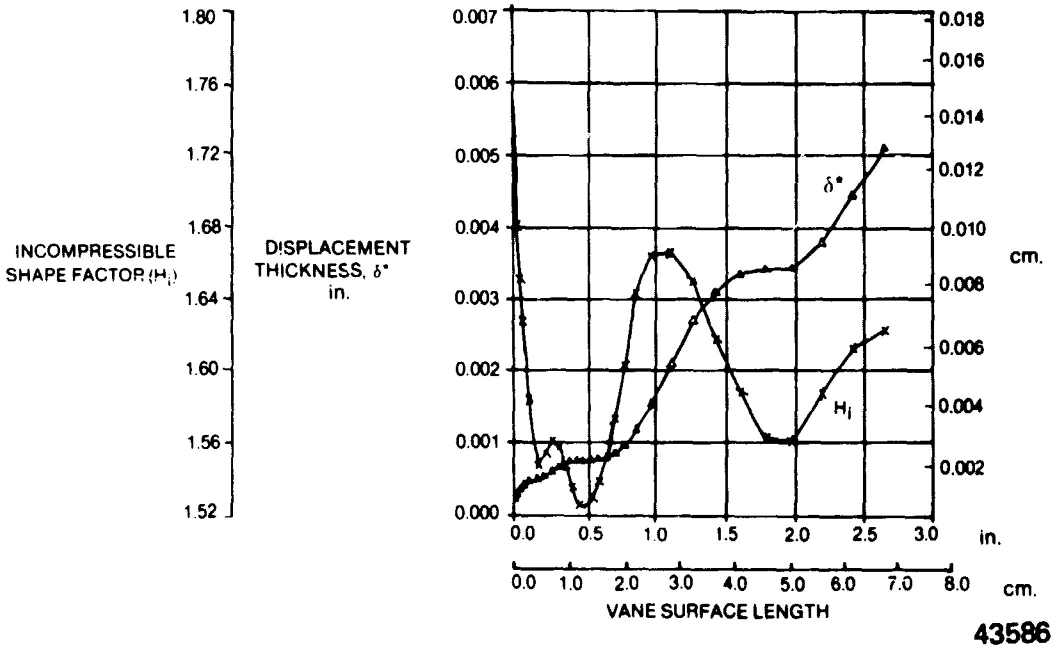

Figure 88. NOZZLE VANE SUCTION SURFACE BOUNDARY LAYER PROFILE

ORIGINAL PAGE IS
OF POOR QUALITY

TABLE VIII

NOZZLE VANE SURFACE COORDINATES

R,cm.	θ, rad.	R, in.	θ, deg.
12.573	0.0000	4.950	0.000
12.474	0.0208	4.911	1.189
12.319	0.0308	4.850	1.766
12.162	0.0363	4.788	2.082
11.999	0.0388	4.724	2.222
11.796	0.0386	4.644	2.214
11.587	0.0354	4.562	2.028
11.379	0.0284	4.480	1.630
11.168	0.0167	4.397	0.954
11.052	0.0074	4.351	0.424
10.937	-0.0048	4.306	-0.277
10.818	-0.0220	4.259	-1.260
10.681	-0.0516	4.205	-2.956
10.577	-0.0819	4.164	-4.695
10.315	-0.1692	4.061	-9.697
9.977	-0.3001	3.928	-17.197
9.797	-0.3874	3.857	-22.199
9.677	-0.4470	3.810	-25.615
9.827	-0.4505	3.869	-25.816
9.957	-0.4066	3.920	-23.301
10.465	-0.2826	4.120	-16.197
10.711	-0.2360	4.217	-13.525
11.092	-0.1754	4.367	-10.054
11.514	-0.1199	4.533	-6.871
11.966	-0.0692	4.711	-3.963
12.474	-0.0208	4.911	-1.189
12.573	0.0000	4.950	0.000

5.3.2 FREE VORTEX SPACE

Consideration was given to several free vortex geometries to minimize losses at off design conditions. Either side wall or both walls could be actuated for variable flow capacity. The double sidewall had higher leakage losses, higher cooling losses and would be heavier and more complicated, mechanically, than a single moveable wall. The outer shroud wall was chosen for actuation as having a higher performance potential than hub wall actuation based on loading considerations. The preliminary rotor loading distributions, Figure 59 and 60, Section 4.1, showed the hub suction side reaction as lowest (negative or diffusing flow) in the flowpath and the diffusion in this region increases with closing of the nozzle area. Any flow disturbances on the hub wall due to variable geometry increases the probability of higher rotor hub losses and flow separation. Conversly, the tip shroud has very high reaction and because of the accelerating flow, this region should be more tolerant to the variable geometry. The flowpath velocity distributions are based on a compressible axisymmetric inviscid quasi-three dimensional flow solution with pressure loss corrections. However, viscous flow solutions are influenced by viscosity, turbulence and vorticity Reference 27 and the most efficient positioning of the wall variable geometry should be determined by experimental research. As a matter of mechanical practicality (Figures 36 and 37, Section 3.3.3.1; for engine layout) and simplified analysis, the outer shroud was selected for the movable wall.

A low radius ratio wall split line was located close to the rotor tip. This provides a uniform flow and incidence over most of the tip and at low flows, transfers the sudden expansion losses to the relative, lower Mach number, plane of the rotor. Figure 89 defines the selected geometry and shows the sidewall positions corresponding to 50%, 82% and 100% power positions.

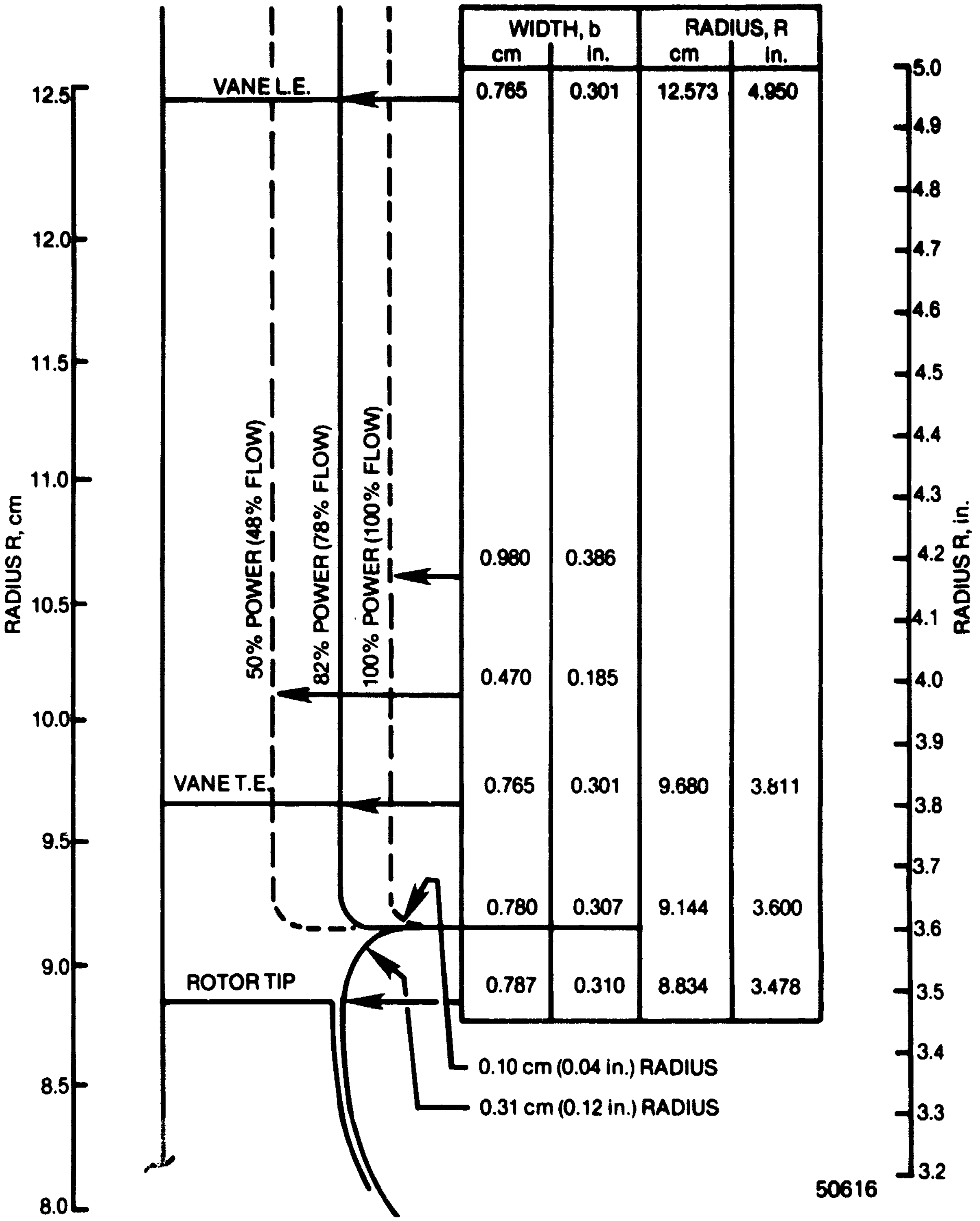

WIDTH, b		RADIUS, R	
cm	in.	cm	in.
0.765	0.301	12.573	4.950
0.980	0.386		
0.470	0.185		
0.765	0.301	9.680	3.811
0.780	0.307	9.144	3.600
0.787	0.310	8.834	3.478

Figure 89. SIDEWALL AND FREE VORTEX GEOMETRY DEFINITION.

5.3.3 Rotor Flowpath And Blade Design

The turbine rotor flowpath and blade contours were designed using the streamtube flow analysis computer code (Reference 13). Sufficient rotor calculation stations were specified to provide flow velocity definition in high curvature regions along the hub and shroud surfaces. The final design flowpath is shown in Figure 90. Hub and shroud contours were adjusted to smooth the mean flow velocity profiles and minimize diffusion losses throughout the rotor flowfield. A rotor polytropic efficiency level of 0.898, corresponding to the rotor adiabatic efficiency prediction from the preliminary design code, was used in the rotor design analysis.

The final distribution of hub and shroud blade angle is shown in Figure 91. Rotor blade camber line sections are comprised of radial elements to enhance structural integrity for operation with the high tip speed and inlet temperature. The blade angle distribution was selected to optimize blade surface velocity loading distributions. The full blade turning was accomplished within the covered blade passage ahead of the exducer throat in order to minimize exit flow deviation and assure the attainment of design turbine work. Figure 92 shows the exducer blade profiles along streamline sections at the hub, mean, and shroud sections. These and other section plots were used to determine the geometric exducer throat area as shown in Figure 93. The integrated geometric throat area is 4.8 percent greater than the analytical throat calculated in the flow analysis computer code. This assures that the actual rotor hardware will have adequate choke flow margin.

Figure 94 shows the final blade surface relative velocity loading diagrams at hub and shroud for the Task III flowpath and blade angle distribution. Blade angles were iterated using the flow analysis code to minimize suction surface velocity diffusion and distribute blade loading as evenly as possible over the rotor flowpath length. Analytical predictions show high loading at the rotor leading edge due to a computer coding constraint for zero incidence that flow follows the blade immediately at the leading edge. The loadings were modified as shown to reflect a lack of perfect flow guidance due to slip for the first 30% of rotor blade length. Blade surface relative velocity profiles were analyzed for possible flow separations using the boundary layer analysis computer code (Reference 26). The initial boundary layer was assumed to be laminar and transition to turbulent flow was predicted with no flow separation occurring on the hub and shroud surface profiles. The predicted distribution of boundary layer displacement thickness and shape factor are shown in Figure 95. For laminar flow, separation is assumed to occur at that station where the skin friction coefficient passes from positive to negative and turbulent separation assumed to occur where the incompressible shape factor (H_i) reaches a value of 2.8, Reference 26. These conditions were avoided in the blading and were used as criteria for completion of the design.

Following completion of the Task III design, a rotor trailing edge cutback was initiated to modify exducer blade resonance and eliminate a region of high stress concentration at the rotor blade exit. The final cutback shown in Figure 95 has the additional effect of reducing blade surface friction losses while reducing rotor work by only 0.3%.

Rotor blade coordinates for the final blade angle and thickness distributions are listed in Table IX. Rotor coordinate radius, R, and axial length, Z, dimensions are defined in the flowpath drawing in Figure 96. The blade meanline polar angle, θ, is the circumferential displacement from a meridional plane through the rotor centerline and intersecting the center of the rotor leading edge tip. Blade thickness, Tn, is the full blade thickness normal to the local blade mean camber line direction. The rotor backface scallop profile and web thickness distribution are shown in Figure 97.

ORIGINAL PAGE IS
OF POOR QUALITY

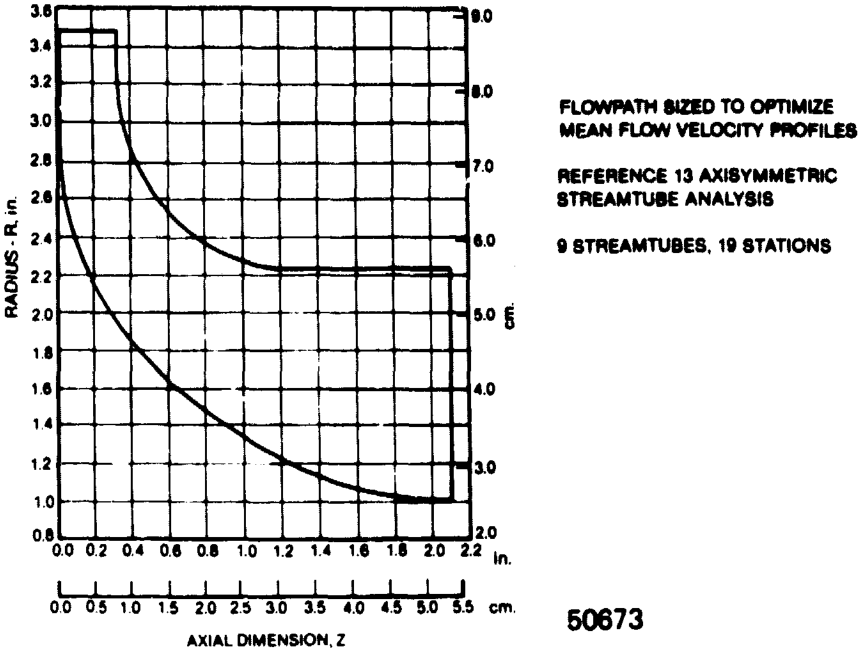

Figure 90. ROTOR FLOWPATH ANALYSIS.

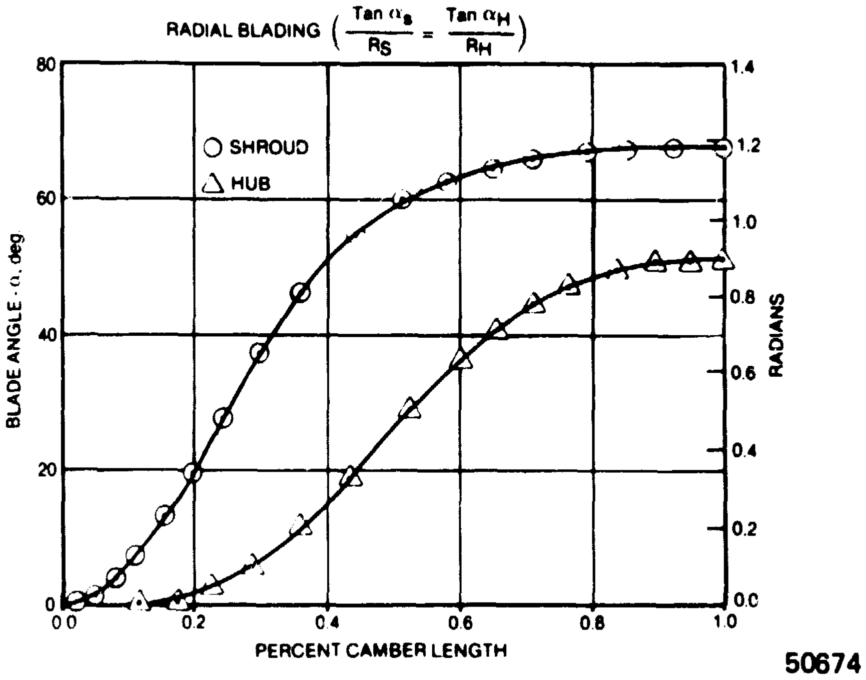

Figure 91. ROTOR AERODYNAMIC BLADE ANGLE DISTRIBUTIONS.

ORIGINAL PAGE IS
OF POOR QUALITY

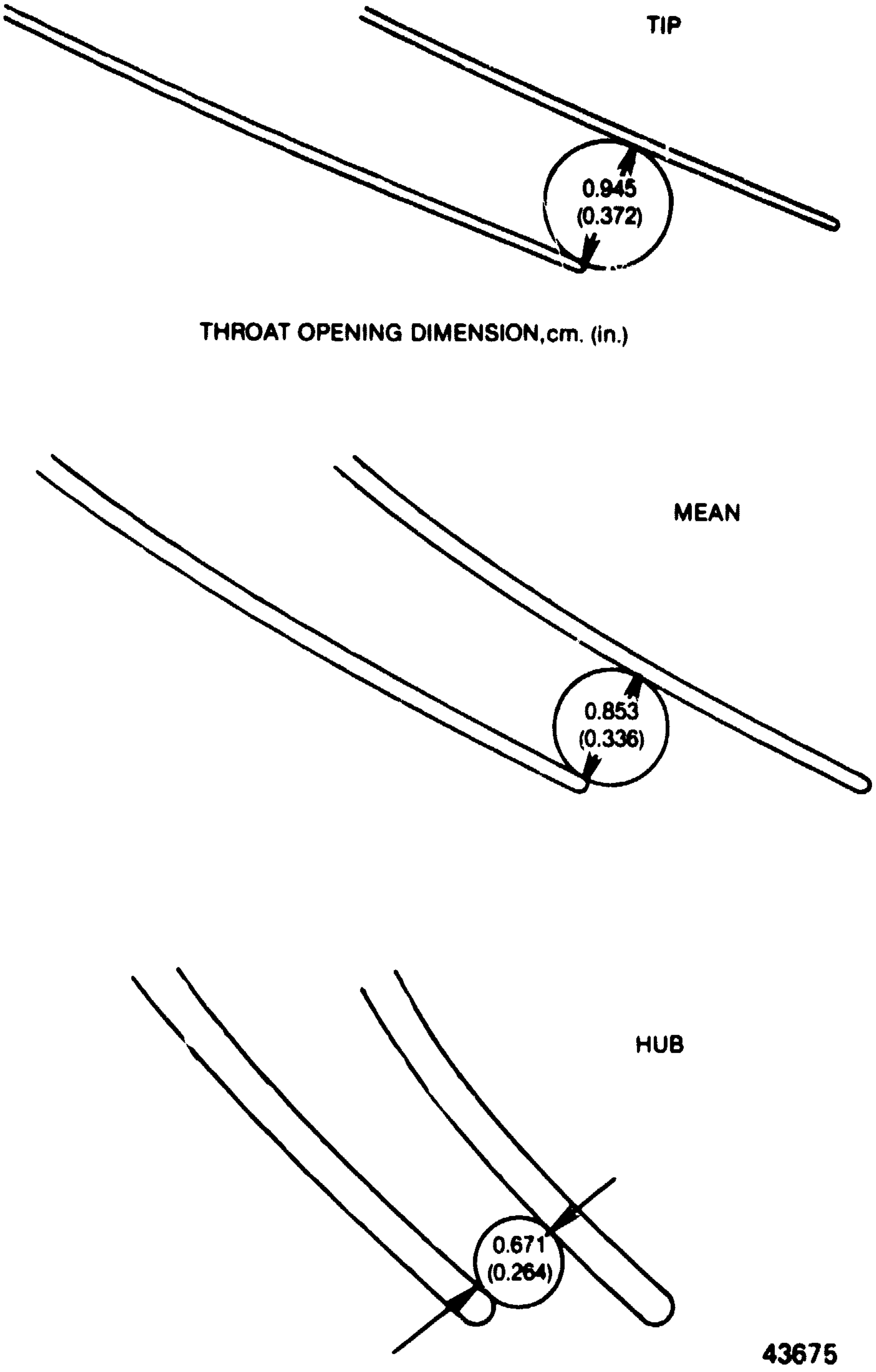

Figure 92. EXDUCER STREAMTUBE THROAT SECTIONS.

ORIGINAL PAGE IS
OF POOR QUALITY

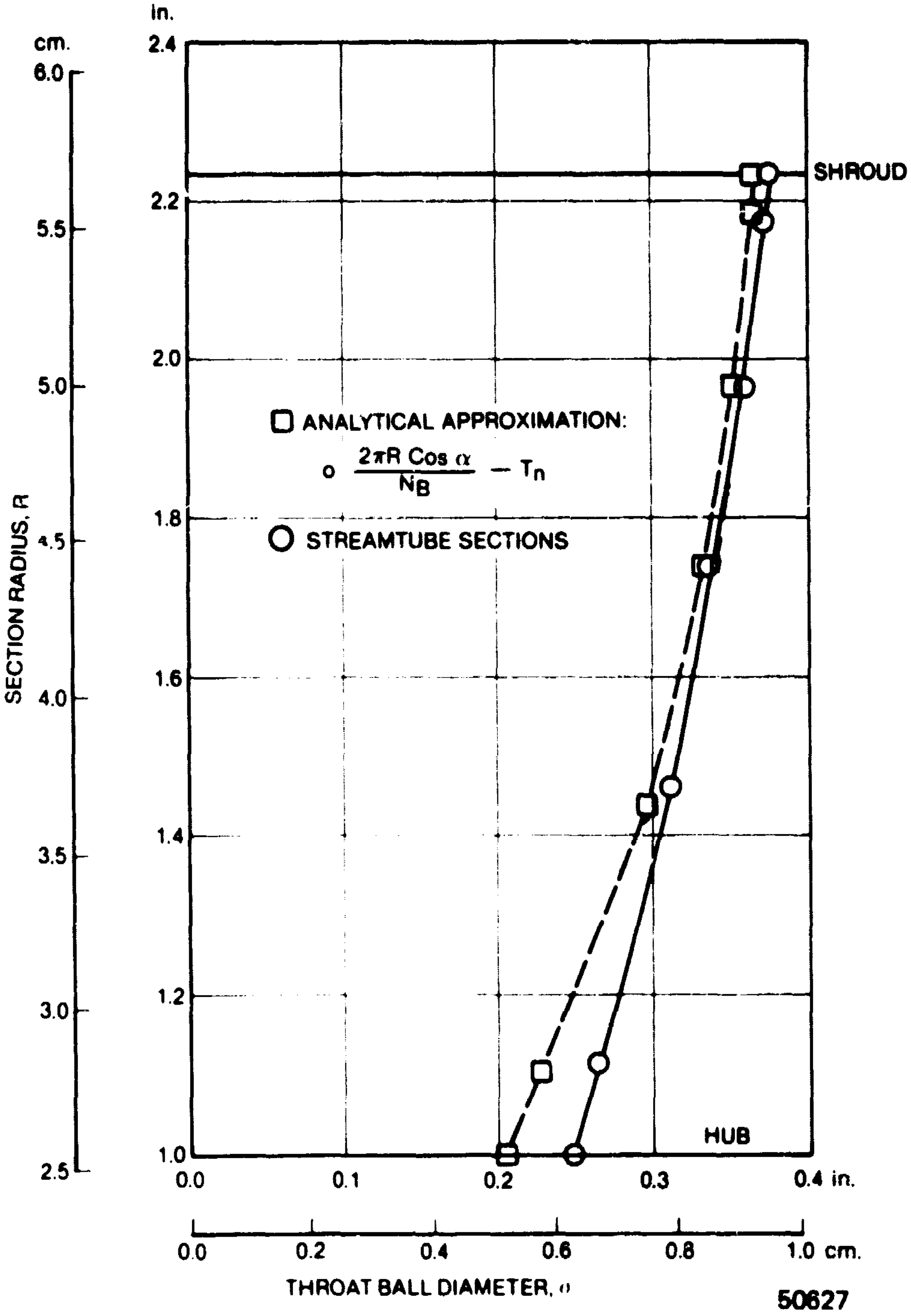

Figure 93. EXDUCER THROAT AREA DISTRIBUTION.

ORIGINAL PAGE IS
OF POOR QUALITY

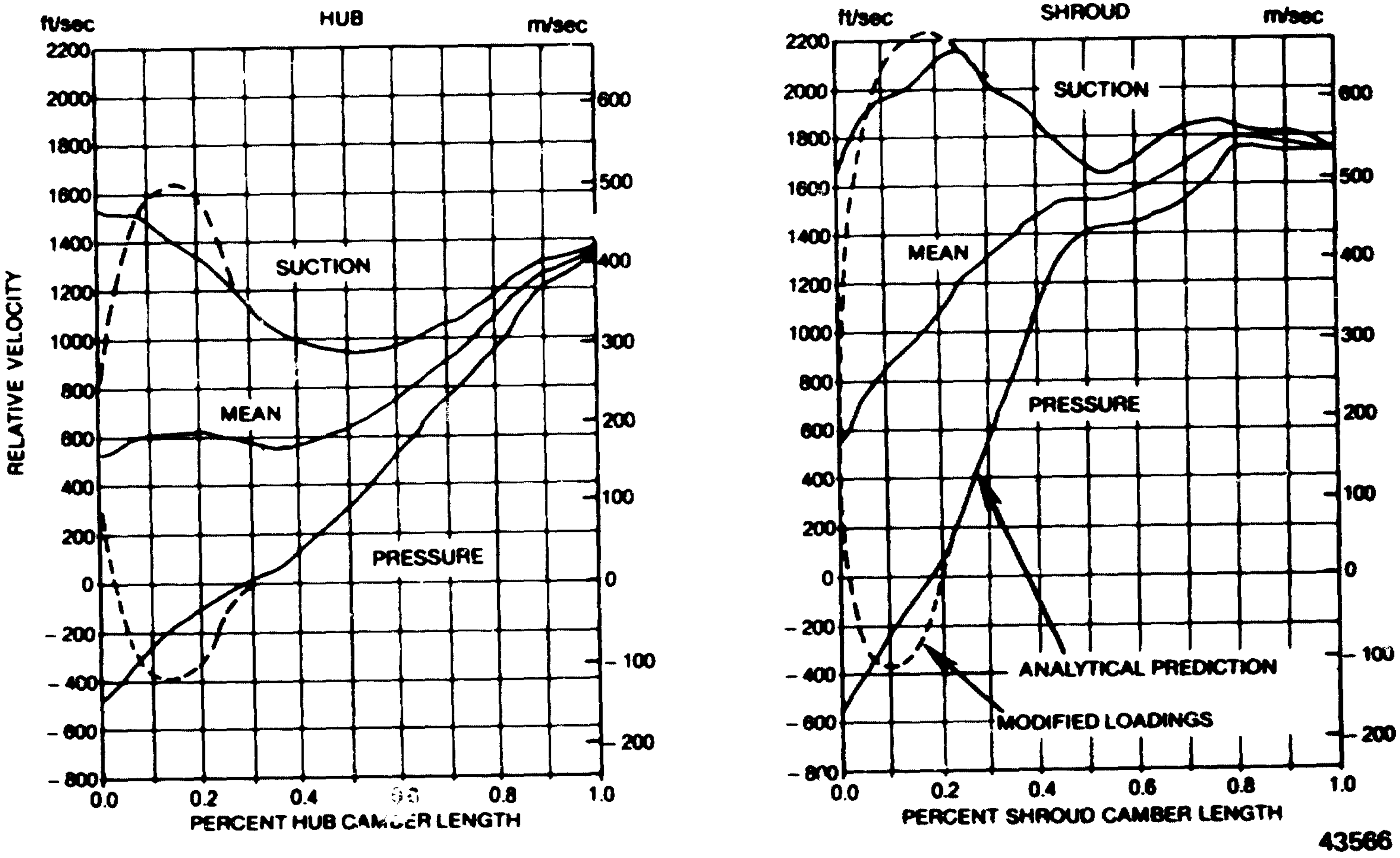

Figure 94. ROTOR BLADE RELATIVE VELOCITY LOADINGS.

ORIGINAL PAGE IS
OF POOR QUALITY

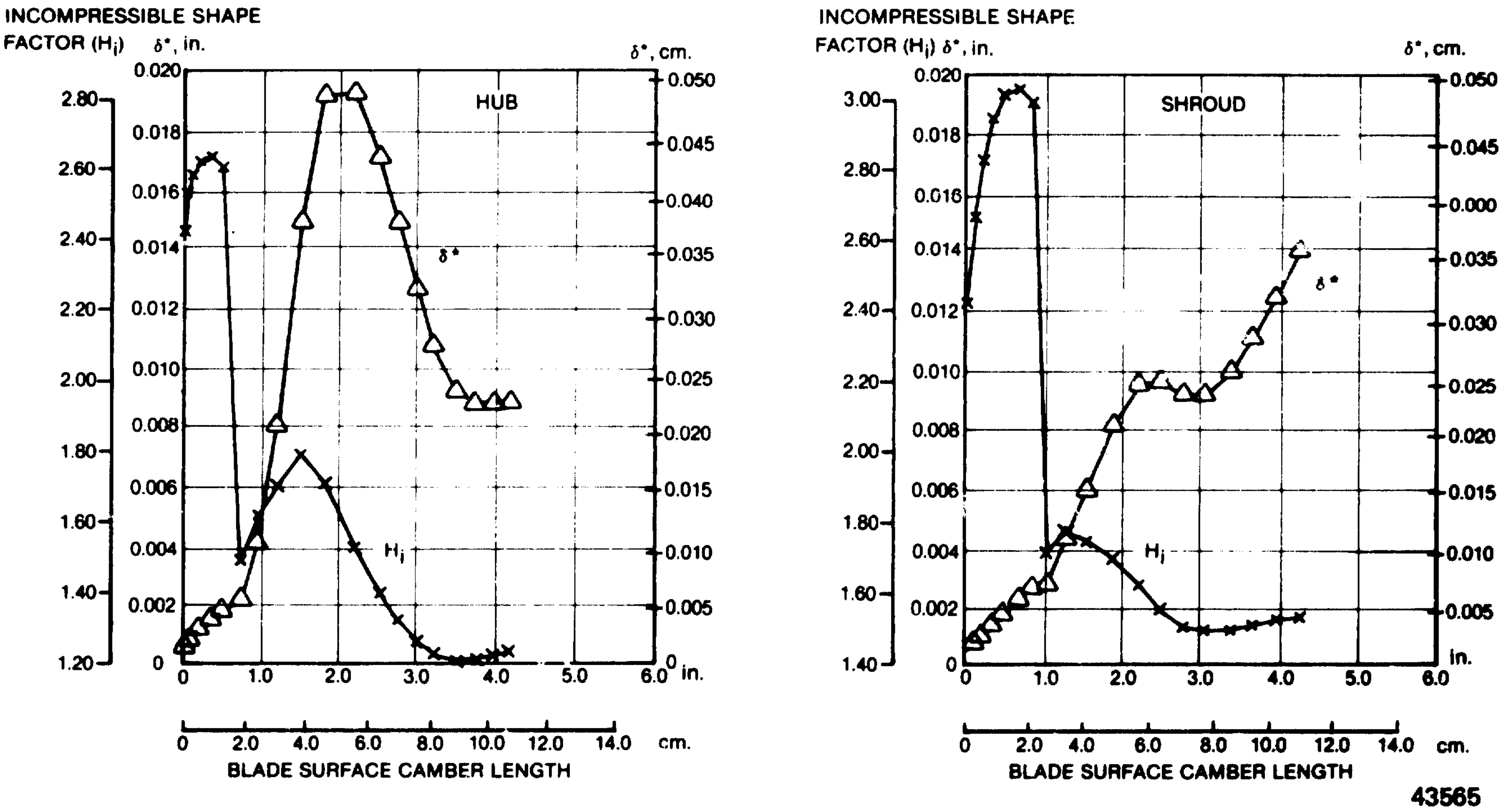

Figure 95. ROTOR BLADE SUCTION SURFACE BOUNDARY LAYER PROFILES.

ORIGINAL PAGE IS
OF POOR QUALITY

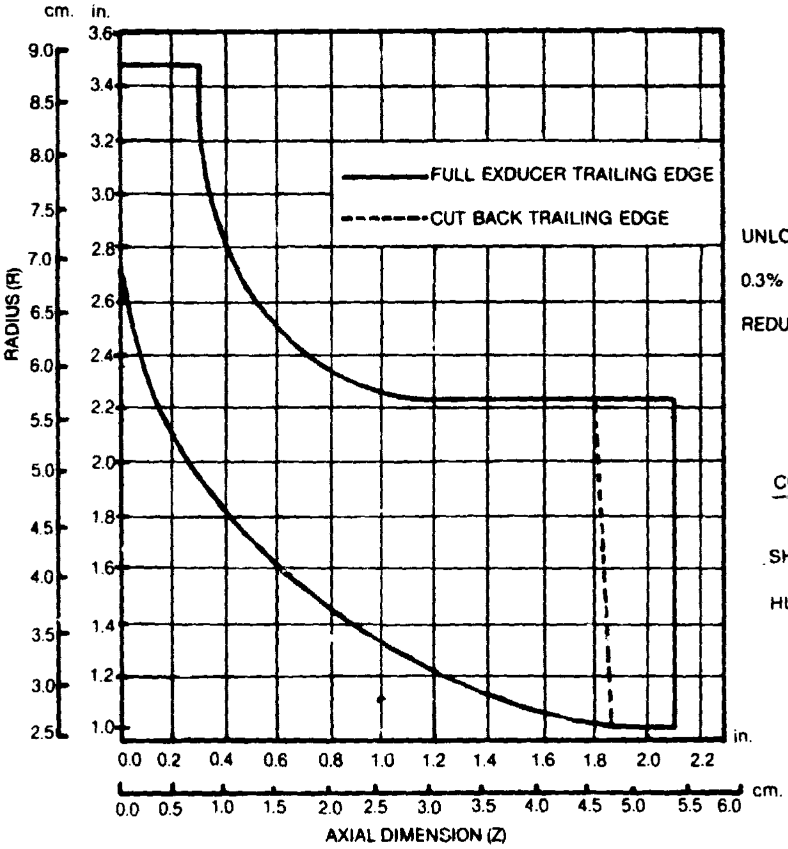

UNLOADED BLADE SECTION REMOVED

0.3% WORK REDUCTION

REDUCED BLADE LENGTH (LOSS, WEIGHT)

CUTBACK COORDINATES

	R, cm (in.)	Z, cm (in.)
SHROUD	5.669 (2.232)	4.572 (1.800)
HUB	2.588 (1.019)	4.724 (1.860)

50670

Figure 96. ROTOR EXDUCER CUTBACK DEFINITION.

TABLE IX

ROTOR BLADE MEANLINE COORDINATES

R,cm.	Z,cm.	θ,rad.	Tn,cm.	R,in.	Z,in.	θ,deg.	Tn,in.
8.839	0.7873	0.0349	0.0762	3.480	0.3100	2.000	0.0300
8.836	0.6593	0.0258	0.0765	3.479	0.2596	1.477	0.0301
8.833	0.4868	0.0154	0.0768	3.478	0.1916	0.884	0.0302
8.827	0.3115	0.0072	0.0777	3.475	0.1226	0.410	0.0306
8.821	0.1335	0.0016	0.0789	3.473	0.0526	0.094	0.0311
8.839	0.0000	0.0000	0.0762	3.480	0.000	0.000	0.0300
8.565	0.7873	0.0349	0.0823	3.372	0.3100	2.000	0.0324
8.562	0.6684	0.0262	0.0860	3.371	0.2632	1.502	0.0338
8.556	0.5014	0.0160	0.0920	3.368	0.1974	0.917	0.0362
8.550	0.3258	0.0076	0.1006	3.366	0.1283	0.433	0.0396
8.544	0.1430	0.0018	0.1097	3.364	0.0563	0.101	0.0432
8.541	0.0000	0.0000	0.1158	3.363	0.0000	0.000	0.0456
8.291	0.7885	0.0349	0.0869	3.264	0.3104	2.000	0.0342
8.284	0.6742	0.0269	0.0975	3.262	0.2654	1.539	0.0384
8.278	0.5108	0.0167	0.1128	3.259	0.2011	0.955	0.0444
8.269	0.3344	0.0080	0.1295	3.256	0.1316	0.459	0.0510
8.263	0.1469	0.0019	0.1490	3.253	0.0578	0.109	0.0587
8.262	0.0000	0.0000	0.1655	3.253	0.0000	0.000	0.0652
7.964	0.8141	0.0383	0.1116	3.136	0.3205	2.200	0.0439
7.949	0.7004	0.0287	0.1308	3.130	0.2758	1.643	0.0515
7.931	0.5355	0.0181	0.1612	3.122	0.2108	1.036	0.0635
7,916	0.3539	0.0089	0.1998	3.116	0.1393	0.508	0.0779
7.903	0.1564	0.0021	0.2402	3.112	0.0616	0.123	0.0946
7.899	0.0000	0.0000	0.2746	3.110	0.0000	0.000	0.1081
7.644	0.8717	0.0419	0.1353	3.010	0.3432	2.400	0.0533
7.617	0.7559	0.0325	0.1646	2.999	0.2976	1.863	0.0648
7.583	0.5852	0.0209	0.2134	2.986	0.2304	1.199	0.0840
7.553	0.3932	0.0106	0.2722	2.974	0.1548	0.607	0.1072
7.529	0.1798	0.0027	0.3414	2.964	0.0708	0.154	0.1344
7.517	0.0000	0.0000	0.4002	2.959	0.0000	0.000	0.1576
7.169	1.026	0.0541	0.2045	2.822	0.4039	3.100	0.0805
7.120	0.9053	0.0440	0.2560	2.803	0.3564	2.523	0.1008
7.056	0.7224	0.0298	0.3359	2.778	0.2844	1.705	0.1322
6.992	0.5121	0.0164	0.4235	2.753	0.2016	0.940	0.1675
6.934	0.2560	0.0052	0.5255	2.730	0.1008	0.297	0.2069
6.891	0.0363	0.0035	0.6089	2.713	0.0143	0.200	0.2400
7.644	1.177	0.0768	0.2496	3.010	0.4632	4.400	0.0983
6.730	1.088	0.0607	0.3210	2.650	0.4284	3.479	0.1264

TABLE IX (Cont'd.)

ROTOR BLADE MEANLINE COORDINATES

R,cm.	Z,cm.	θ,rad.	Tn,cm.	R,in.	Z,in.	θ,deg.	Tn,in.
6.632	0.9022	0.0432	0.4225	2.611	0.3552	2.475	0.1663
6.532	0.6736	0.0260	0.5322	2.572	0.2652	1.492	0.2095
6.428	0.3901	0.0104	0.6507	2.531	0.1536	0.596	0.2562
6.349	0.1302	0.0044	0.9662	2.499	0.0512	0.250	0.3804
6.431	1.477	0.1082	0.3182	2.532	0.5815	6.200	0.1253
6.340	1.341	0.0899	0.3975	2.496	0.5280	5.149	0.1565
6.187	1.158	0.0677	0.4941	2.436	0.4560	3.878	0.1945
6.035	0.9144	0.0450	0.5800	2.376	0.3600	2.577	0.2284
5.883	0.6096	0.0225	0.6520	2.316	0.2400	1.291	0.2567
5.723	0.3155	0.0096	0.9662	2.253	0.1242	0.550	0.3804
6.098	1.829	0.1588	0.2012	2.401	0.7200	9.100	0.0792
5.944	1.707	0.1402	0.2771	2.340	0.6720	8.034	0.1091
5.761	1.524	0.1126	0.3533	2.268	0.6000	6.453	0.1391
5.547	1.280	0.0827	0.4285	2.184	0.5040	4.737	0.1687
5.273	0.9754	0.0506	0.5035	2.076	0.3840	2.900	0.1982
5.043	0.6593	0.0271	0.5590	1.985	0.2596	1.550	0.2201
5.852	2.232	0.2373	0.1646	2.304	0.8788	13.600	0.0648
5.669	2.134	0.2159	0.2082	2.232	0.8400	12.375	0.0820
5.395	1.981	0.1838	0.2691	2.124	0.7800	10.535	0.1060
5.121	1.737	0.1462	0.3237	2.016	0.6840	8.377	0.1274
4.755	1.463	0.1029	0.3944	1.872	0.5760	5.896	0.1553
4.445	1.142	0.0567	0.4532	1.750	0.4498	3.250	0.1784
5.695	2.737	0.3647	0.1149	2.242	1.078	20.900	0.0452
5.456	2.682	0.3439	0.1466	2.148	1.056	19.706	0.0577
5.090	2.560	0.3124	0.1957	2.004	1.008	17.903	0.0770
4.694	2.377	0.2684	0.2569	1.848	0.9360	15.381	0.1012
4.267	2.103	0.2114	0.3347	1.680	0.8280	12.115	0.1318
3.815	1.816	0.1571	0.4145	1.502	0.7151	9.000	0.1632
5.669	3.139	0.4799	0.0853	2.232	1.236	27.500	0.0336
5.364	3.109	0.4717	0.1064	2.112	1.224	27.029	0.0419
4.938	3.048	0.4461	0.1466	1.944	1.200	25.563	0.0577
4.481	2.896	0.4015	0.2021	1.764	1.140	23.007	0.0796
3.962	2.652	0.3363	0.2783	1.560	1.044	19.272	0.1096
3.429	2.386	0.2792	0.3591	1.350	0.9392	16.000	0.1414
5.669	3.475	0.5889	0.0771	2.232	1.368	33.75	0.0304
5.334	3.444	0.5866	0.0930	2.100	1.356	33.62	0.0366
4.877	3.383	0.5641	0.1271	1.920	1.332	32.33	0.0500
4.359	3.261	0.5201	0.1777	1.716	1.284	29.80	0.0700

TABLE IX (Concl'd.)

ROTOR BLADE MEANLINE COORDINATES

R,cm.	Z,cm.	θ,rad.	Tn,cm.	R,in.	Z,in.	θ,deg.	Tn,in.
3.780	3.078	0.4504	0.2536	1.488	1.212	25.81	0.0998
3.193	2.806	0.3857	0.3307	1.257	1.105	22.10	0.1302
5.669	3.816	0.7163	0.0768	2.232	1.502	41.05	0.0302
5.334	3.810	0.7122	0.0866	2.100	1.500	40.81	0.0341
4.816	3.749	0.6914	0.1167	1.896	1.476	39.62	0.0460
4.267	3.658	0.6493	0.1643	1.680	1.440	37.21	0.0647
3.627	3.444	0.5796	0.2347	1.428	1.356	33.22	0.0924
2.987	3.215	0.5043	0.3987	1.176	1.266	28.90	0.1570
5.669	4.100	0.8376	0.0768	2.232	1.614	48.00	0.0302
5.304	4.084	0.8250	0.0832	2.088	1.608	47.28	0.0328
4.785	4.054	0.8069	0.1116	1.884	1.596	46.24	0.0439
4.206	3.962	0.7687	0.1558	1.656	1.560	44.05	0.0613
3.505	3.780	0.7042	0.2256	1.380	1.488	40.36	0.0888
2.842	3.585	0.6282	0.3597	1.119	1.411	36.00	0.1416
5.669	4.459	0.9859	0.0765	2.232	1.756	56.50	0.0301
5.304	4.450	0.9774	0.0817	2.088	1.752	56.01	0.0322
4.755	4.420	0.9660	0.1070	1.872	1.740	55.36	0.0421
4.145	4.359	0.9392	0.1506	1.632	1.716	53.82	0.0593
3.414	4.267	0.8909	0.2210	1.344	1.680	51.06	0.0870
2.685	4.110	0.8420	0.4039	1.057	1.618	48.25	0.1590
5.669	4.734	1.099	0.0765	2.232	1.864	63.00	0.0301
5.273	4.724	1.098	0.0802	2.076	1.860	62.90	0.0316
4.724	4.724	1.091	0.1055	1.860	1.860	62.53	0.0415
4.115	4.663	1.074	0.1491	1.620	1.836	61.53	0.0587
3.353	4.602	1.043	0.2195	1.320	1.812	59.74	0.0864
2.610	4.505	1.002	0.2332	1.027	1.773	57.40	0.1476
5.669	5.026	1.226	0.0762	2.232	1.979	70.25	0.0300
5.273	5.029	1.226	0.0814	2.076	1.980	70.24	0.0320
4.274	4.999	1.221	0.1064	1.860	1.968	69.98	0.0419
4.084	4.968	1.208	0.1500	1.608	1.956	69.23	0.0590
3.322	4.938	1.187	0.2188	1.308	1.944	68.00	0.0862
2.569	4.866	1.156	0.4037	1.011	1.916	66.25	0.1590
5.669	5.334	1.361	0.0762	2.232	2.100	78.00	0.0300
5.273	5.334	1.362	0.0802	2.076	2.100	78.04	0.0316
4.724	5.334	1.358	0.1045	1.860	2.100	77.88	0.0412
3.292	5.334	1.330	0.2179	1.296	2.100	76.22	0.0858
2.540	5.334	1.361	0.3786	1.000	2.100	78.00	0.1490

ORIGINAL PAGE IS
OF POOR QUALITY

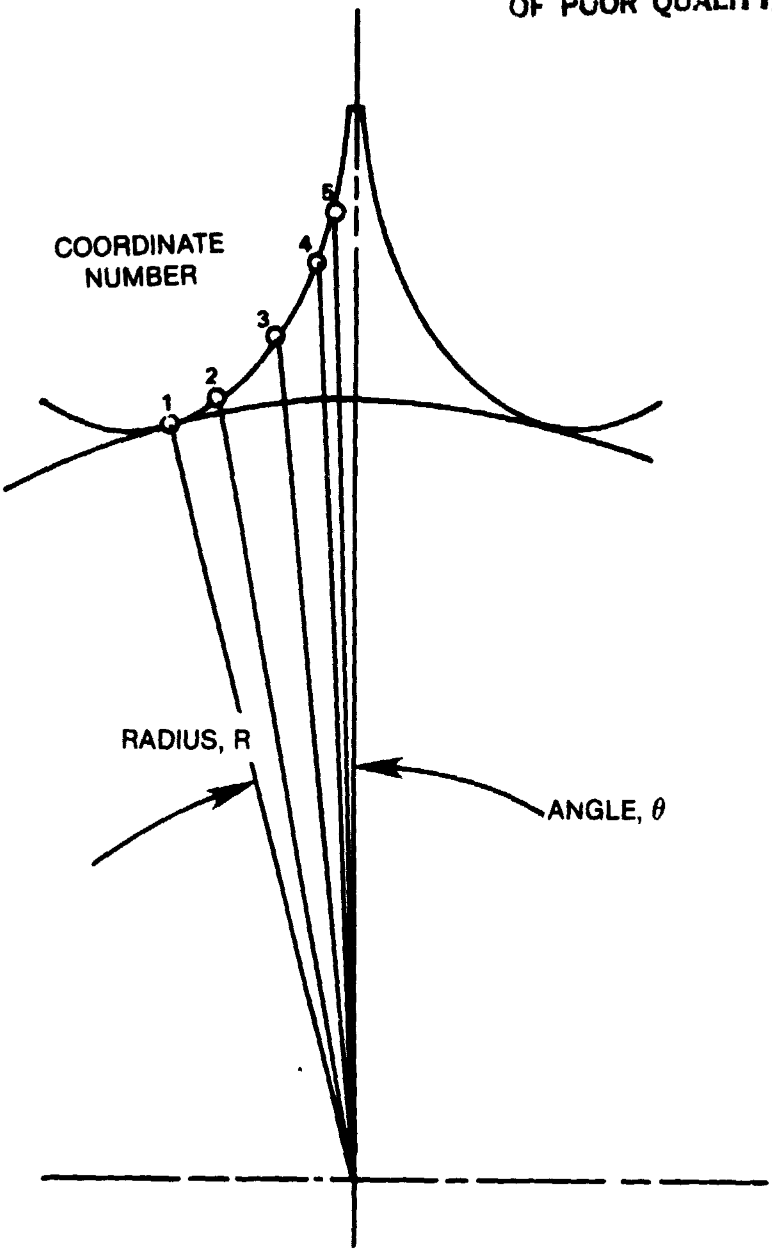

OORDINATE NUMBER	RADIUS R cm	RADIUS R, (in)	θ RADIANS	θ (DEGREES)	THICKNESS Tn cm	THICKNESS Tn, (in.)
1	6.350	2.500	0.242	13.846	0.294	0.116
2	6.452	2.540	0.175	10.000	0.277	0.109
3	6.883	2.710	0.096	5.500	0.229	0.090
4	7.518	2.960	0.041	2.324	0.178	0.070
5	7.899	3.110	0.017	1.000	0.178	0.070

50613

Figure 97. TURBINE ROTOR BACKFACE SCALLOP COORDINATES.

5.4 PIVOTED NOZZLE ADDENDUM

5.4.1 Velocity Diagrams

As an addendum to the work scope, a design and analysis of an alternate, pivoted nozzle configuration for the variable area radial turbine was investigated. The pivoted vane nozzle design is used as a basis of performance comparison for the actuated sidewall nozzle design discussed in section 5.3.1. The stator vane profile and solidity selected for the actuated sidewall design were found to be suitable for the pivoted vane nozzle configuration. This dual application allows direct comparison of the two nozzle area variation concepts by providing the same design performance base for both designs. Performance variations throughout the power range can be directly attributed to differences in the method of stator throat area variation. The pivoted nozzle design point velocity diagrams, vane surface velocity loadings, and boundary layer profiles are the same as for the actuated sidewall nozzle.

The pivoted nozzle velocity diagrams for 100% power are shown in Figure 98. The nozzle vane angle was pivoted open 0.044 rad. (2.5°) from the nominal setting of 1.34 rad. (77°), to open the nozzle throat area by the 28 percent required to pass the maximum flow rate of 2.2 kg/sec (5.0 lb/sec). The rotor with a pivoted vane nozzle has a leading edge incidence of 0.41 rad. (23.4°) which is comparable to the incidence for the actuated sidewall nozzle design at the same 100% power, Figure 80.

An indication of the rotor mean reaction and diffusion losses is given by a DeHall number, De, defined as:

$$De = \left[\frac{W_9 - W_6}{W_6}\right] \quad \text{where}$$

W_9 = rotor exit mean relative velocity

W_6 = rotor inlet mean relative velocity

The mean value increases from 0.08 at 78% flow (Figure 79) to 2.50 at 100% flow (Figure 80) for the actuated wall nozzle concept whereas the pivoted vane concept increase is 22% lower (Figures 79 and 98). This is further aggravated on the rotor suction side hub where the De Hall number decreases to negative values (diffusion).

Velocity diagrams for the 50% power pivoted vane configuration are shown in Figure 99. The nozzle vanes were pivoted closed 0.10 rad. (5.5°) to 1.44 rad. (82.5°) trailing edge angle to reduce throat area and flow rate 38.5 percent for the 50% power point. The rotor leading edge incidence is 0.18 rad. (10.1°) greater than the incidence angle for the actuated sidewall design at 50% power operating conditions, Figure 81.

Higher losses at off design conditions on the pivoted vane turbine concept are attributable to increased vane leading edge incidences and greater rotor tip incidences due to the variable stagger settings required to change power (flow). Additional losses are incurred due to rotor reaction changes and resulting non-optimum vane loadings with stagger, whereas the actuated sidewall concept maintains near constant vane loading.

The estimated variation of turbine efficiency with flow for the pivoted nozzle configuration is shown in Figure 100. Off design characteristics are compared to the actuated sidewall nozzle in Section 3.3.2, Figure 29 where the duty cycle time weighted efficiency was found to favor the sidewall concept.

ORIGINAL PAGE IS
OF POOR QUALITY

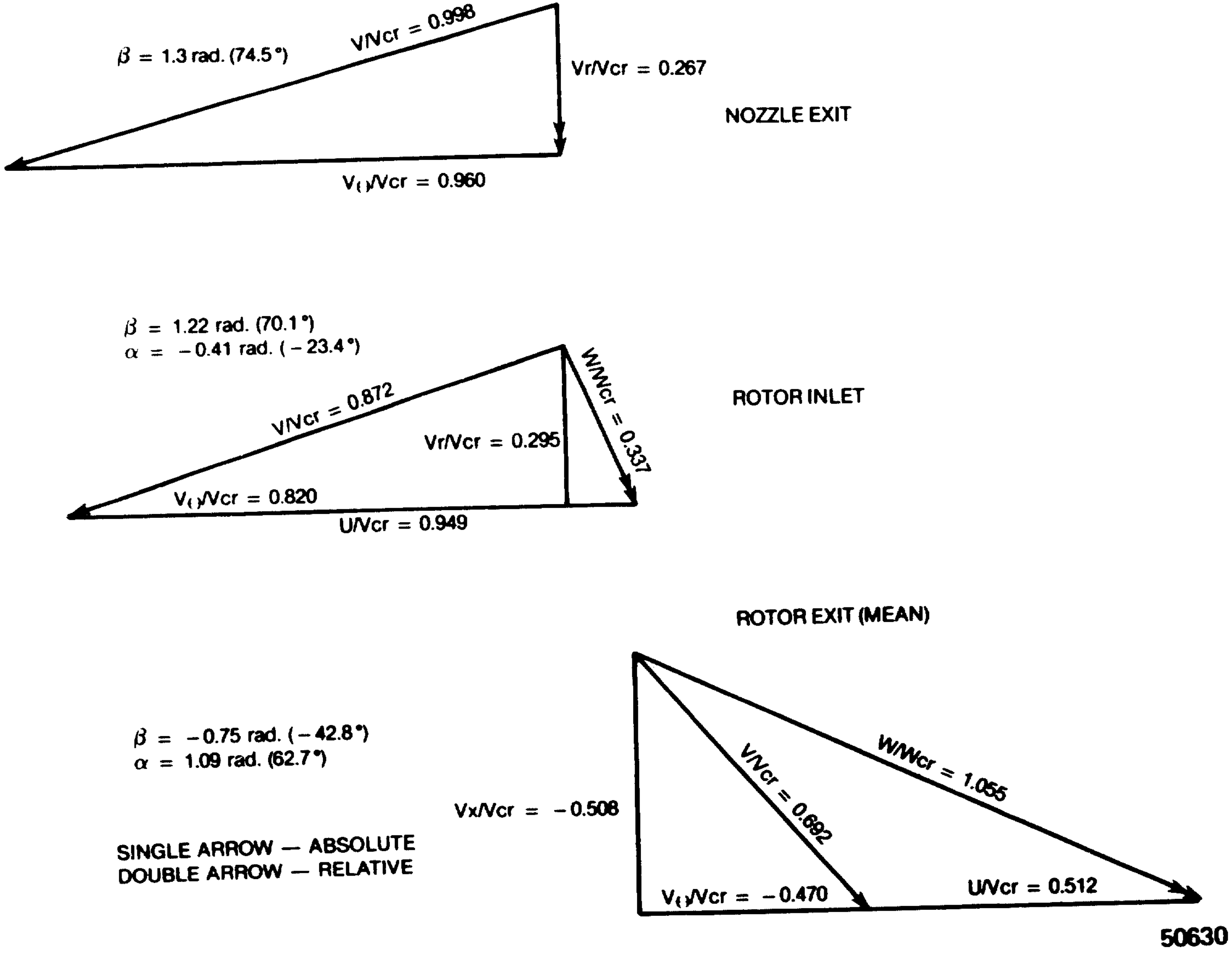

Figure 98. PIVOTED NOZZLE, 100% POWER VELOCITY DIAGRAMS.

ORIGINAL PAGE IS
OF POOR QUALITY

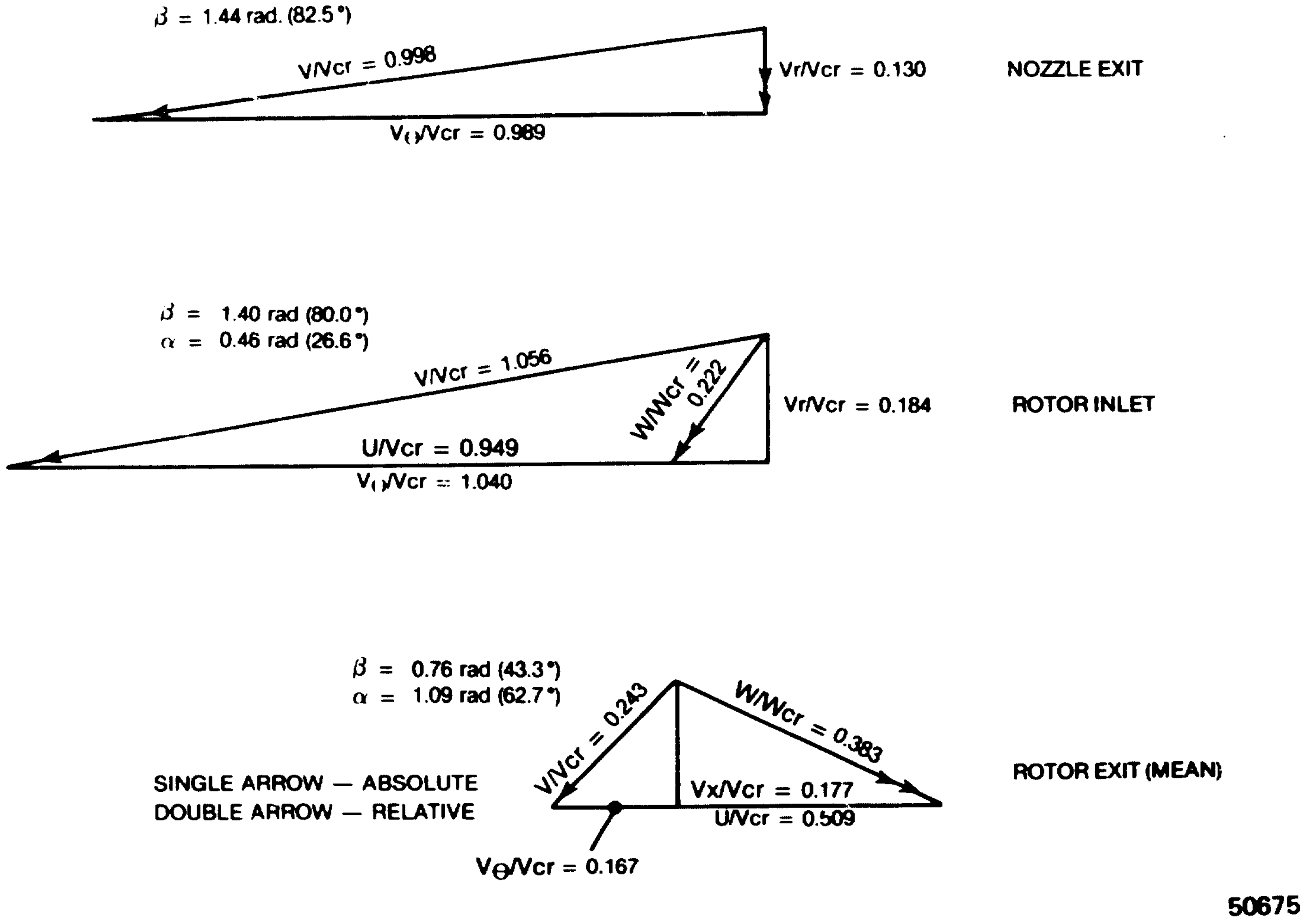

Figure 99. PIVOTED VANE, 50% POWER VELOCITY DIAGRAMS.

ORIGINAL PAGE IS
OF POOR QUALITY

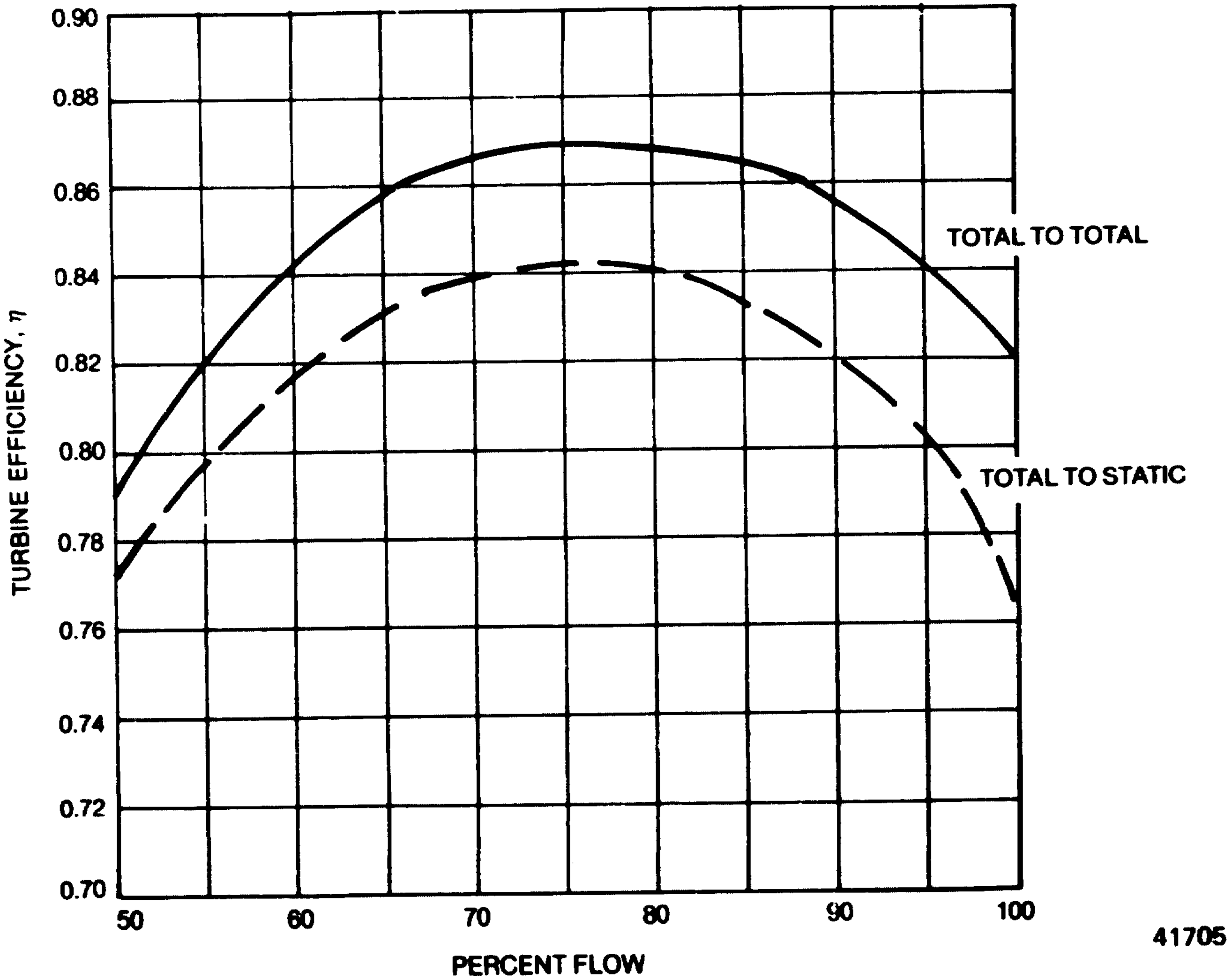

Figure 100. PREDICTED EFFICIENCY LEVELS (TASK III) PIVOTED VANE NOZZLE ADDENDUM.

5.4.2 STATOR FLOW ANALYSIS

Figure 101 shows the pivoted nozzle vane at the design flow setting and indicates the position of the vane pivot point. The pivoted nozzle vane setting for operation at 100% power is pivoted open 0.04 rad. (2.5°) as shown in Figure 102. Blade-to-blade vane surface velocity ratio loadings for this configuration are shown in Figure 103. Surface velocity loadings from vane leading edge to the nozzle throat average 19 percent higher than design point levels. Suction surface diffusion in the uncovered section between the nozzle throat and trailing edge is also increased for the 100% flow. The suction surface boundary layer shape factor distribution for turbulent flow analysis is shown in Figure 104. Boundary layer analysis indicated full flow attachment along the nozzle vane surfaces for the 100% power velocity profiles shown in Figure 103.

The nozzle vane position for operation at 50% power is pivoted closed 0.10 rad. (5.5°) as shown in Figure 105. Vane surface velocity loadings for this flow setting are shown in Figure 106. Surface velocity loadings average 30 percent less than design point levels. The suction surface boundary layer shape factor distribution is shown in Figure 107. No vane surface separation is predicted for the 50% power velocity profiles shown in Figure 106. The pivoted nozzle vane design should provide satisfactory performance for operation throughout the design power and flow operating range.

ORIGINAL PAGE IS
OF POOR QUALITY

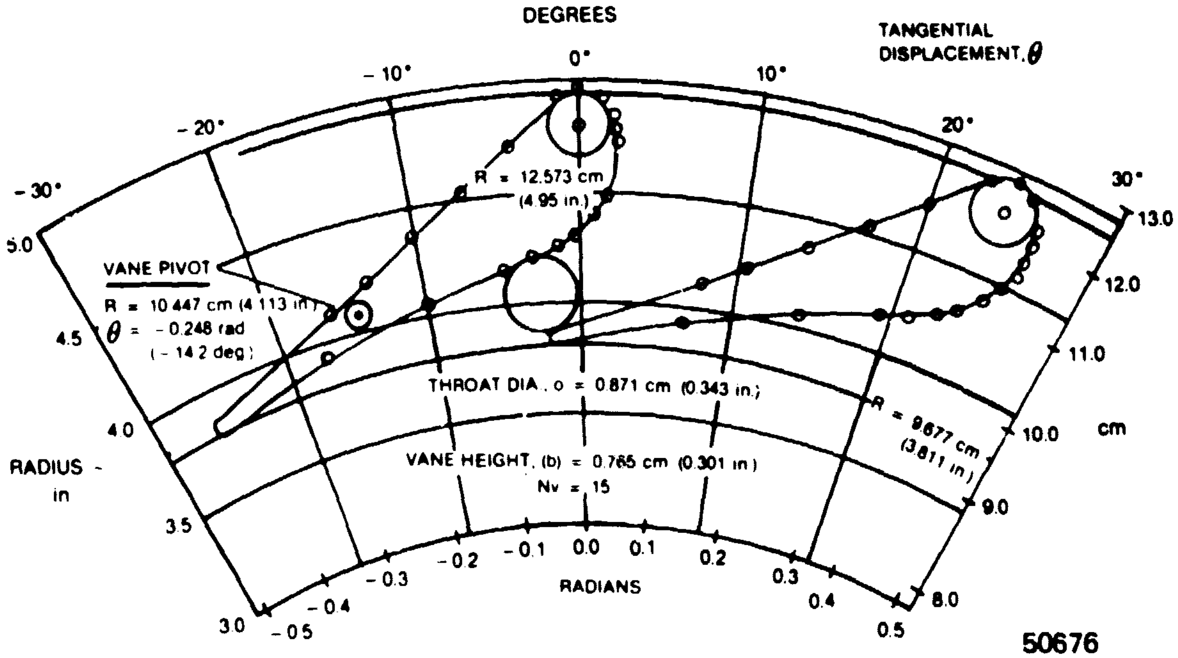

Figure 101. PIVOTED NOZZLE VANE PROFILE, DESIGN SETTING.

ORIGINAL PAGE IS
OF POOR QUALITY

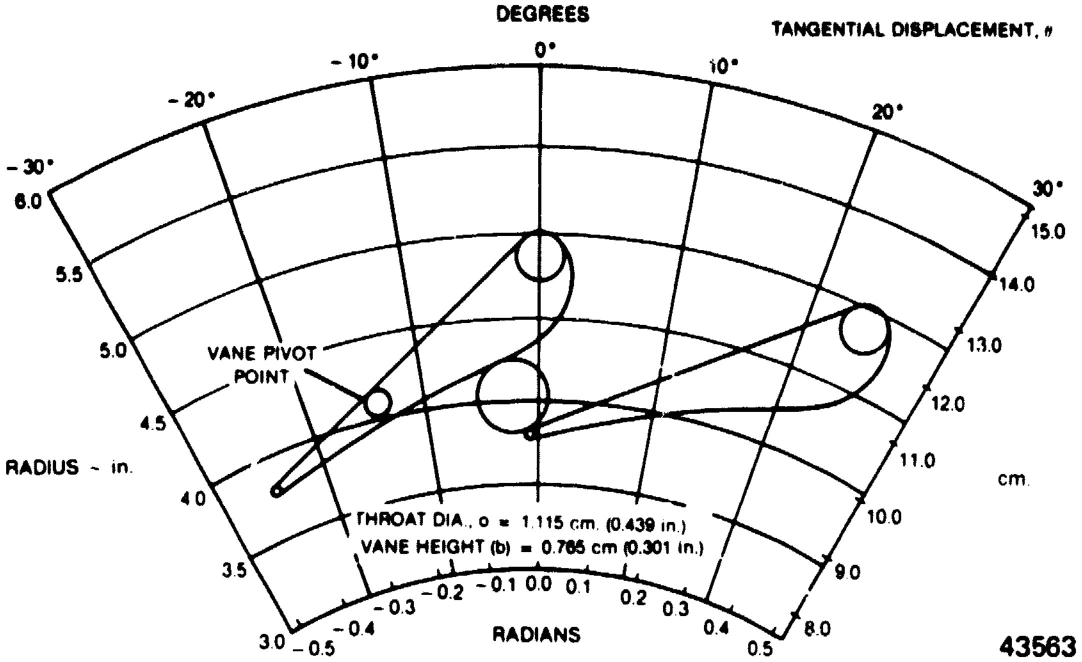

Figure 102. PIVOTED NOZZLE VANE CONFIGURATION, 100% POWER.

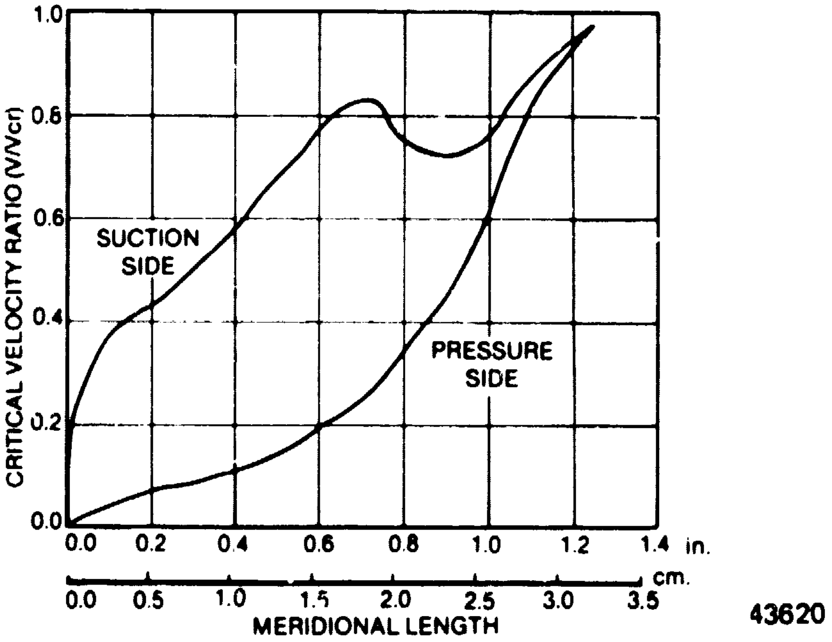

Figure 103. PIVOTED NOZZLE VANE, SURFACE VELOCITY LOADING, 100% POWER.

ORIGINAL PAGE IS
OF POOR QUALITY

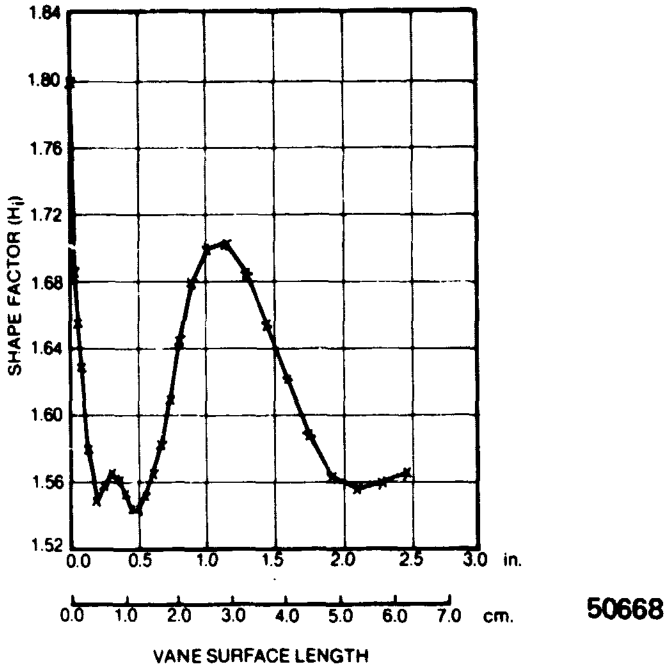

gure 104. PIVOTED NOZZLE VANE, SUCTION SURFACE BOUNDARY LAYER, 100% POWER.

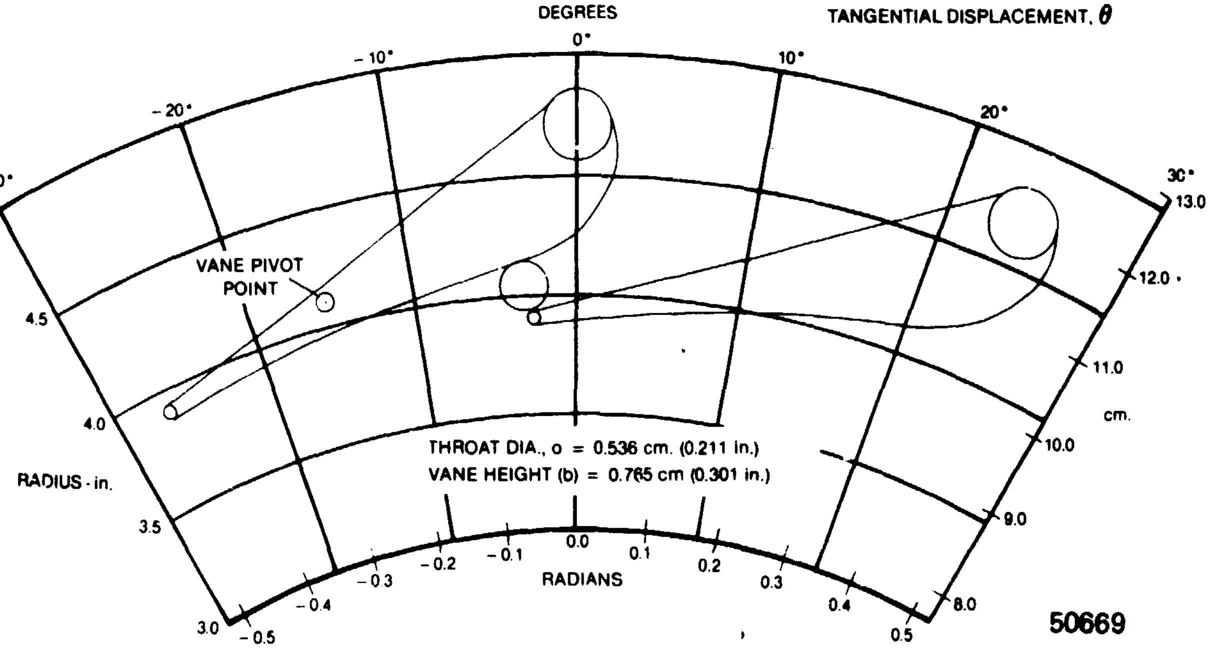

Figure 105. PIVOTED NOZZLE VANE CONFIGURATION, 50% POWER.

ORIGINAL PAGE IS
OF POOR QUALITY

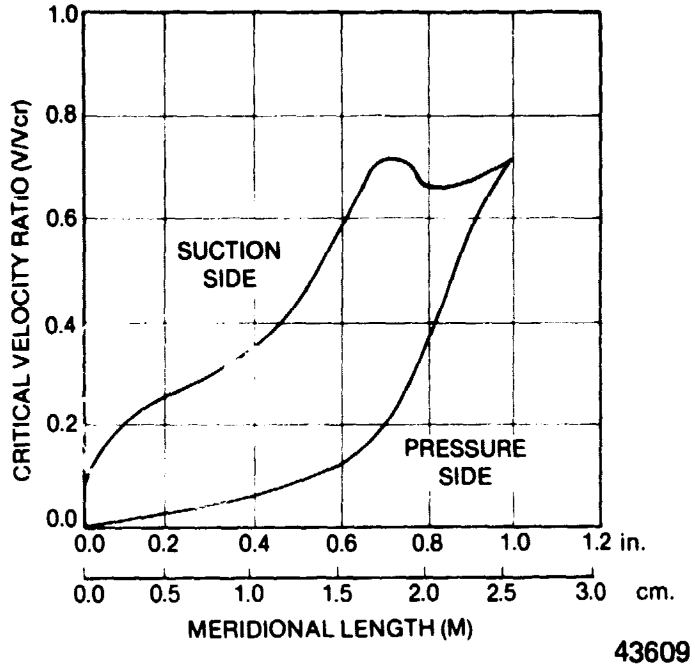

Figure 106. PIVOTED NOZZLE, VANE SURFACE LOADING, 50% POWER.

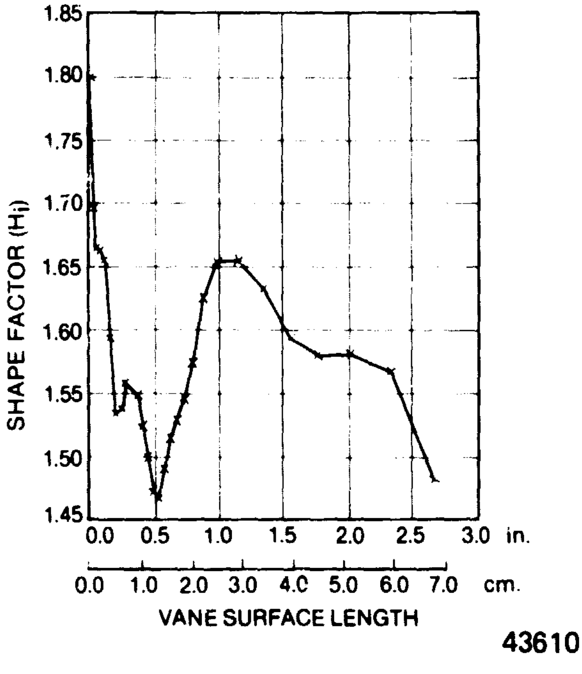

Figure 107. PIVOTED VANE, SUCTION SURFACE BOUNDARY LAYER, 50% POWER.

PRECEDING PAGE BLANK NOT FILMED

SECTION 6.0

HEAT TRANSFER/MECHANICAL DESIGN ANALYSES (TASK IV)

6.1 NOZZLE THERMAL ANALYSIS

6.1.1 Stator Vane Design

The cooling configuration was designed for the maximum power position of the actuated sidewall configuration with a nozzle passage width of 0.764 cm. (0.301 in.) and an engine airflow of 2.268 kg/sec (5.0 lb/sec). The design turbine nozzle inlet gas temperature (TNIT) is 1506 K (2250°F). The nozzle inlet temperature results from cooling flow iterations and the requirement of a mixed rotor inlet temperature (TRIT) of 1477 K (2200°F). A cooling supply temperature of 722 K (841°F) and pressure of 1.652×10^6 N/m^2 (239.6 psia), from the design point cycle analysis were assumed for this design. A variable vane wall thickness tapering from 0.762 mm (0.030 in.) at the leading edge and mid-chord section to a thickness of 0.508 mm (0.020 in.) at the trailing edge was chosen to satisfy structural and heat transfer requirements.

The nozzle heat transfer model was developed using TACT I, Reference 28, a NASA computer program for the transient thermal analysis of a cooled turbine blade or vane equipped with a coolant insert. Figure 108 defines the impingement cooling hole geometry and specifies the trailing edge pin fin configurations determined by TACT I. The cooling hole pattern was designed to distribute impingement air according to local cooling needs so that uniform vane temperatures were achieved.

The vane temperatures are affected by the pattern factor of the combustor and the temperature profile across the axial channel. The temperature profile is normally selected from the best profile dictated by the rotor configuration as discussed in Section 4.2.1. The vane was designed for the maximum local hot spot temperature of 1591 K (2404°F) which occurs as a result of a combustor pattern or temperature difference factor, TDF, of 0.11.

The combustor was sized for a large volume to accommodate the flow changes over the power spectrum without variable geometry mechanisms. The heat release rate, consequently, is low, 0.226 kw/m^3-Pa (2.21×10^6 Btu/hr - ft^3 atm) at 100% power, and the TDF of 0.11 with a flat type of gradient was considered a realistic goal.

ORIGINAL PAGE IS
OF POOR QUALITY

LOCATION	IMPINGEMENT HOLE CONFIGURATION HOLE DIA. in	cm	NO. OF HOLES
A	0.012	0.030	6
B	0.012	0.030	8
C	0.010	0.025	8
D	0.010	0.025	8
E	0.010	0.025	6
F	0.010	0.025	6
G	0.010	0.025	5
H	0.010	0.025	4
I	0.012	0.030	4
J	0.012	0.030	7
K	0.012	0.030	7
L	0.012	0.030	7
M	0.012	0.030	6
N	0.012	0.030	6
O	0.012	0.030	7
P	0.012	0.030	7
Q	0.012	0.030	9
R	0.012	0.030	8
S	0.012	0.030	7
T	0.012	0.030	7
U	0.012	0.030	6
V	0.012	0.030	6
W	0.012	0.030	6
X	0.012	0.030	7
Y	0.012	0.030	8
Z	0.012	0.030	8

	PIN FIN CONFIGURATION PIN FIN DIA. in	cm	NO OF PINS
PF 1	0.040	0.012	5
PF 2	0.040	0.102	5
PF 3	0.030	0.102	4
PF 4	0.030	0.076	4
PF 5	0.030	0.076	3

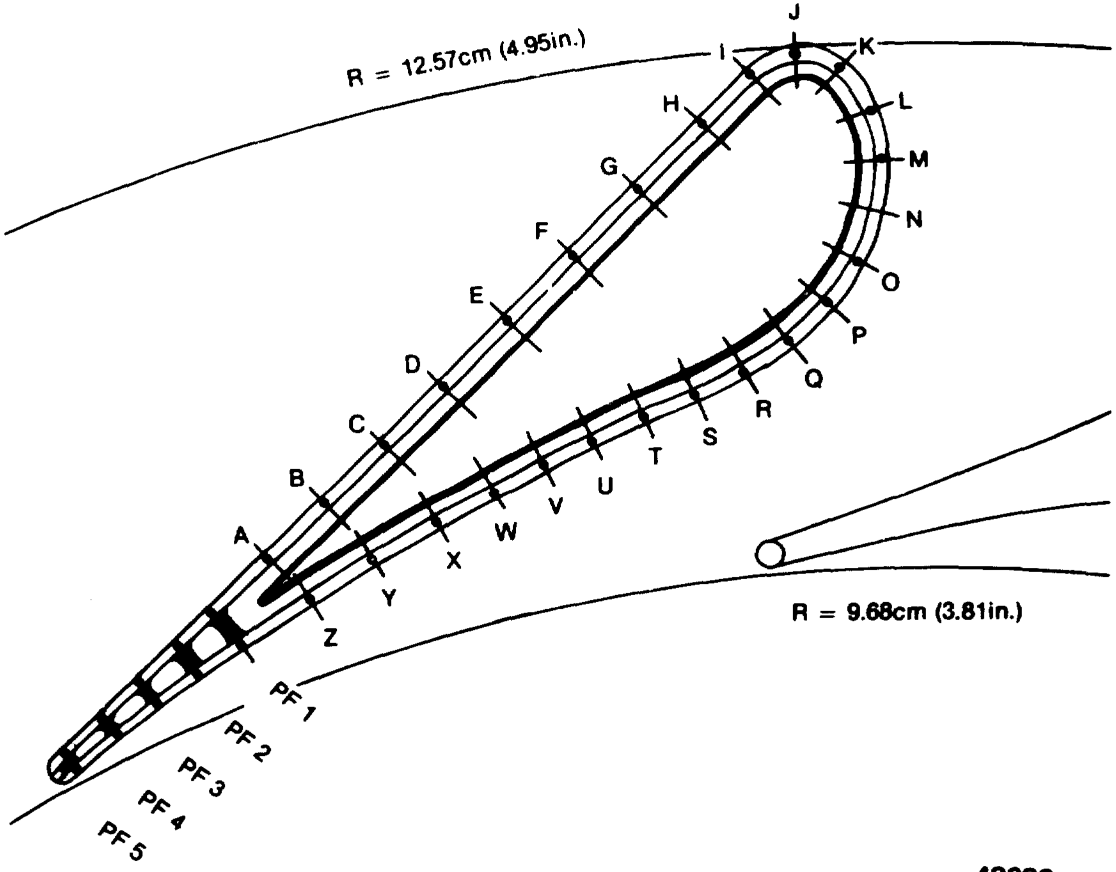

Figure 108. NOZZLE VANE COOLING CONFIGURATION.

The cooling airflow requirement for the nozzle vane is calculated to be 3.0% of engine air flow, slightly increased from the preliminary design estimates. The increase was necessary due to the greater vane surface area of a longer chord airfoil. Figure 109 shows the calculated vane metal temperatures. The calculated maximum surface temperature is 1302 K (1885°F). The calculated cooling exit temperature is 994 K (1330°F) with an average cooling effectiveness of 0.374 and an average coolant heat transfer coefficient of 3421 watts/m^2K (603 Btu/hr-ft^2 °F).

6.1.2 Nozzle Shroud Analysis

The cooling configuration for the radial nozzle shrouds was also designed for the maximum power condition and engine air flow of 2.268 kg/sec. (5.0 lb/sec). A heat transfer model was established for the shrouds using the CINDA numerical differencing analyzer computer code for general 3-dimensional thermal networks (Reference 24).

The required coolant flows for both the front and the rear shrouds are calculated to be 1.5% of engine airflow as shown in Figure 110. These coolant flows increased from the preliminary design value of 1.1% due to an increase in the shroud surface areas. The shroud surface areas increased primarily due to increased nozzle leading edge radius for the final aerodynamic design.

Figure 111 defines the impingement cooling hole geometry for the front shroud. The impingement hole geometry for the rear or outer shroud should be similar and will be precisely defined during detailed design for a specific application. Figure 112 shows the shroud isotherm distribution. The calculated maximum metal temperature is 1278 K (1840°F). The calculated coolant exit temperature is 1052 K (1434°F) with an average cooling effectiveness of 0.30.

All of the 1.5% cooling air for the front shroud will discharge into the mainstream in the space between the nozzle trailing edge and rotor leading edge as shown in Figure 110. Forty-five (45) 0.457 mm (0.018 in.) diameter holes oriented at the nozzle exit angle are required to allow mainstream cooling injection with minimum loss to the cycle. Only 1.1% of the 1.5% cooling air for the rear or outer shroud discharges into the mainstream space between nozzle trailing edge and rotor leading edge. Forty-five (45) 0.356mm - 0.432 mm (0.014 in - 0.017 in) diameter holes with orientation similar to those on the front

ORIGINAL PAGE IS
OF POOR QUALITY

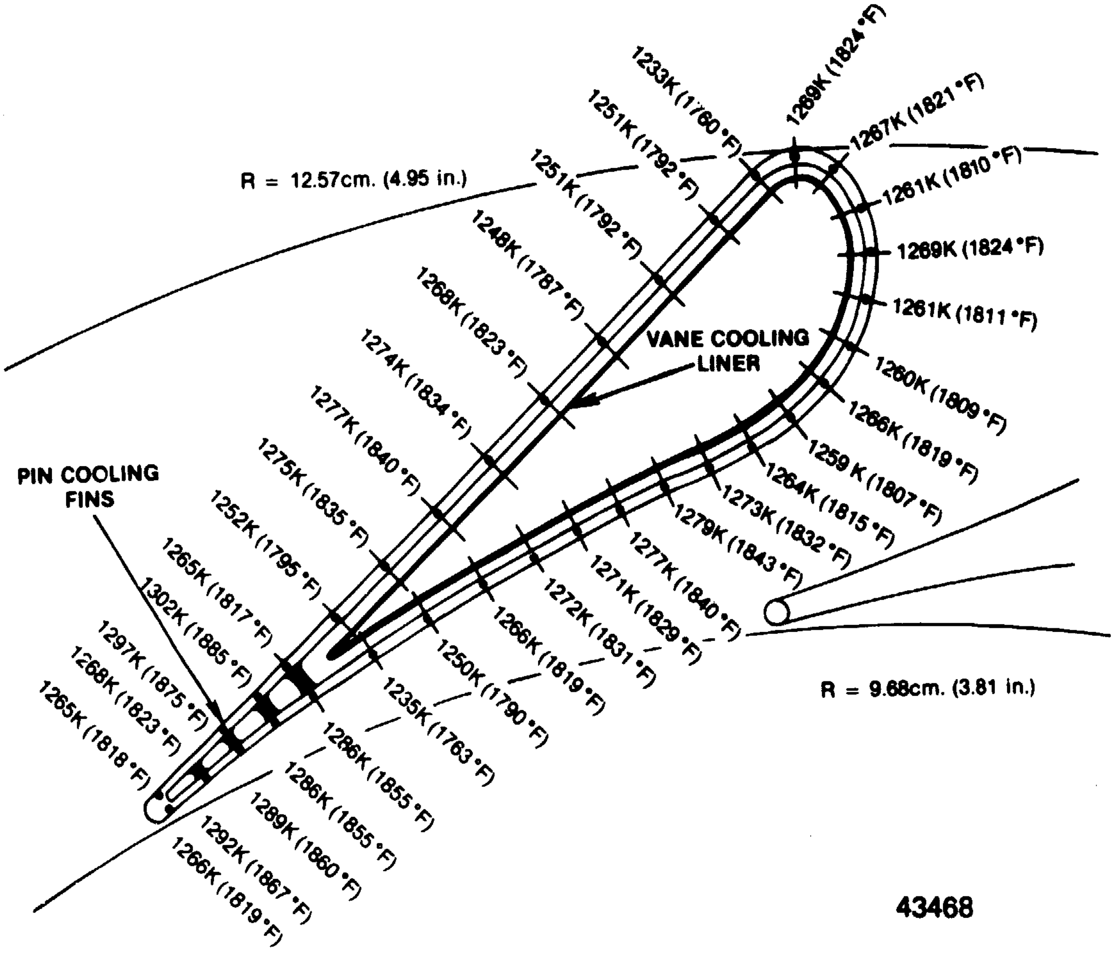

Figure 109. NOZZLE VANE TEMPERATURE DISTRIBUTION.

ORIGINAL PAGE IS
OF POOR QUALITY

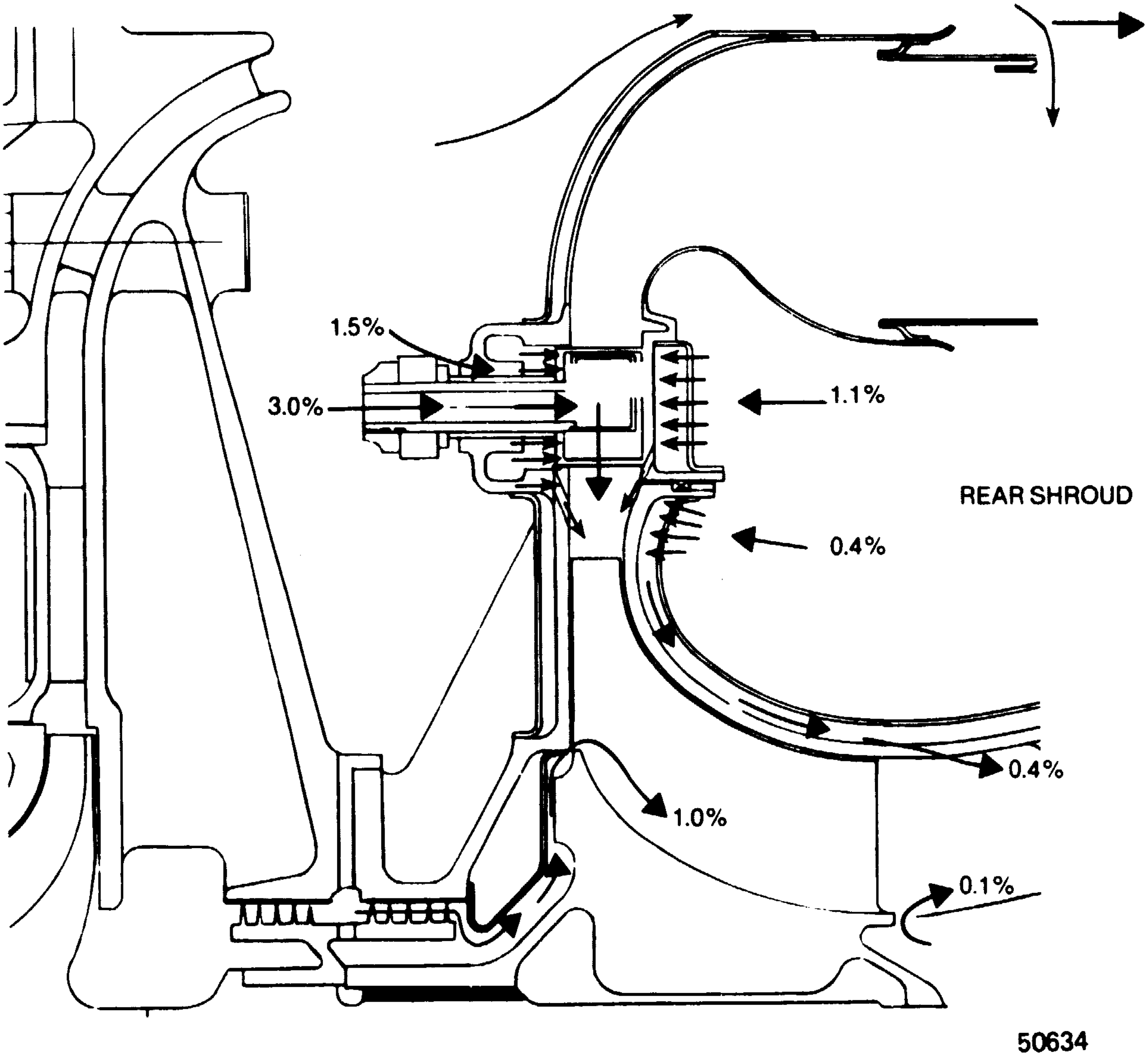

Figure 110. TURBINE COOLING FLOW RATES.

ORIGINAL PAGE IS
OF POOR QUALITY

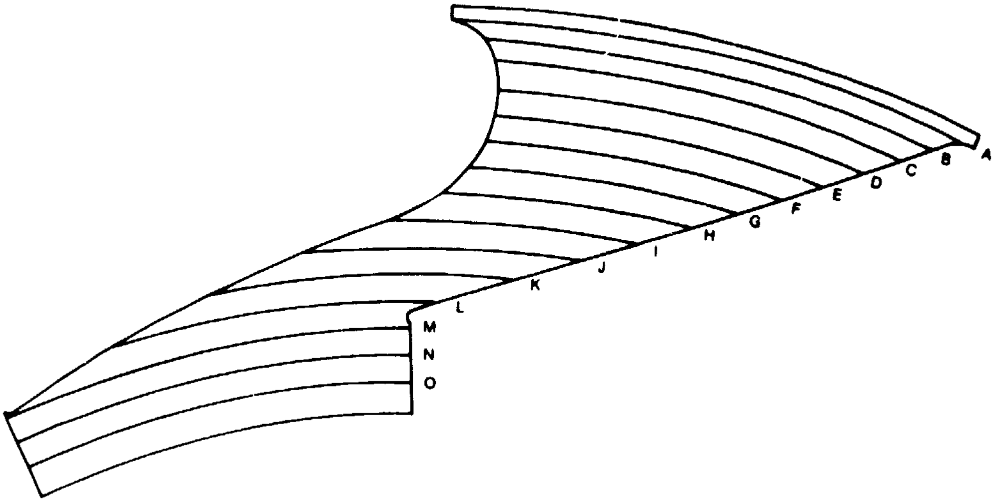

IMPINGEMENT HOLE CONFIGURATION

	RADIAL POSITION		HOLE DIAMETER		NO. OF HOLES
	cm	in	cm	in	
A	12.57	4.95	0.0254	0.010	9
B	12.40	4.88	0.0254	0.010	8
C	12.19	4.80	0.0254	0.010	8
D	11.94	4.70	0.0254	0.010	7
E	11.68	4.60	0.0254	0.010	7
F	11.43	4.50	0.0254	0.010	7
G	11.18	4.40	0.0254	0.010	6
H	10.92	4.30	0.0254	0.010	6
I	10.67	4.20	0.0254	0.010	6
J	10.41	4.10	0.0254	0.010	7
K	10.16	4.00	0.0254	0.010	7
L	9.91	3.90	0.0254	0.010	8
M	9.65	3.80	0.0254	0.010	10
N	9.40	3.70	0.0254	0.010	10
O	9.14	3.60	0.0254	0.010	10

43479

Figure 111. NOZZLE SHROUD COOLING CONFIGURATION.

ORIGINAL PAGE IS
OF POOR QUALITY

shroud are required. The remaining 0.4% cooling air for the rear shroud discharges into the mainstream from the space behind the rotor blade to cool the rotor shroud. There are 15 cooling exit holes of 0.392 mm (0.016 in.) nominal diameter. All the cooling exit holes are orientated to be in line with the local mainstream flow direction.

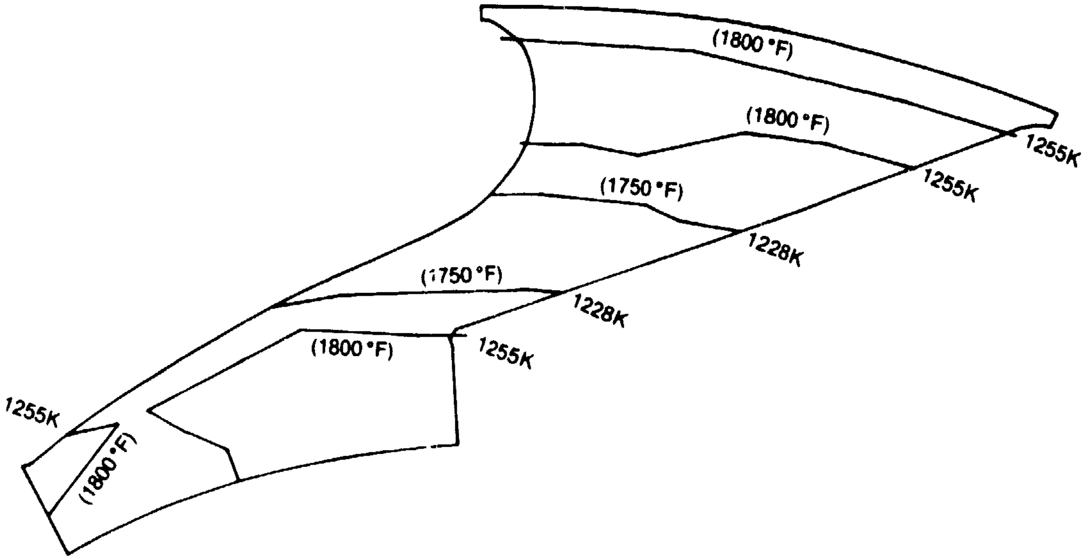

43581

Figure 112. NOZZLE SHROUD TEMPERATURE DISTRIBUTION.

6.2 STATOR STRUCTURAL ANALYSIS

The detail mechanical design of the stator was not completed since an actual engine configuration design was not part of the investigation. The end conditions on the vane, therefore, were not specified. It was assumed that the ends of the stator vane remained planar and were constrained from sloping so that the thermal growth was constant over the vane cross section. The chordwise thermal gradient was assumed to be constant over the width of the vane. The above assumptions were simulated by modeling the vane cross section with finite elements perpendicular to the vane walls. This vane stress model is shown in Figure 113.

The thermal gradient shown in Figure 109 was applied to the stator vane finite element model. The resulting thermal stresses, shown in Figure 114, were quite low with a maximum longitudinal tensile stress of 102.1 MPa (14.8 ksi), occurring near the trailing edge on the suction surface and a maximum equivalent Von Mises thermal stress of 98 MPa (14.2 ksi). This is only about 17% of the 0.2% yield strength at 1172 K (1650°F) for the family of cast materials projected for the 1988 time frame, as shown in Figure 115. Gas bending stresses are also quite low due to the relatively low aspect ratio, producing very high safety margins on the vane.

ORIGINAL PAGE IS
OF POOR QUALITY

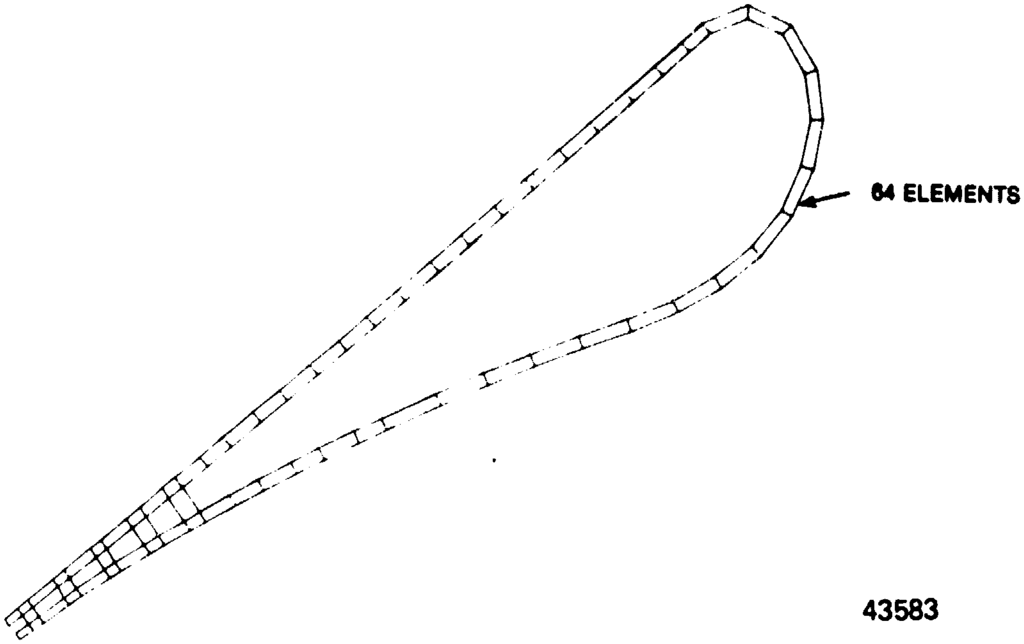

Figure 113. VANE FINITE ELEMENT MODEL.

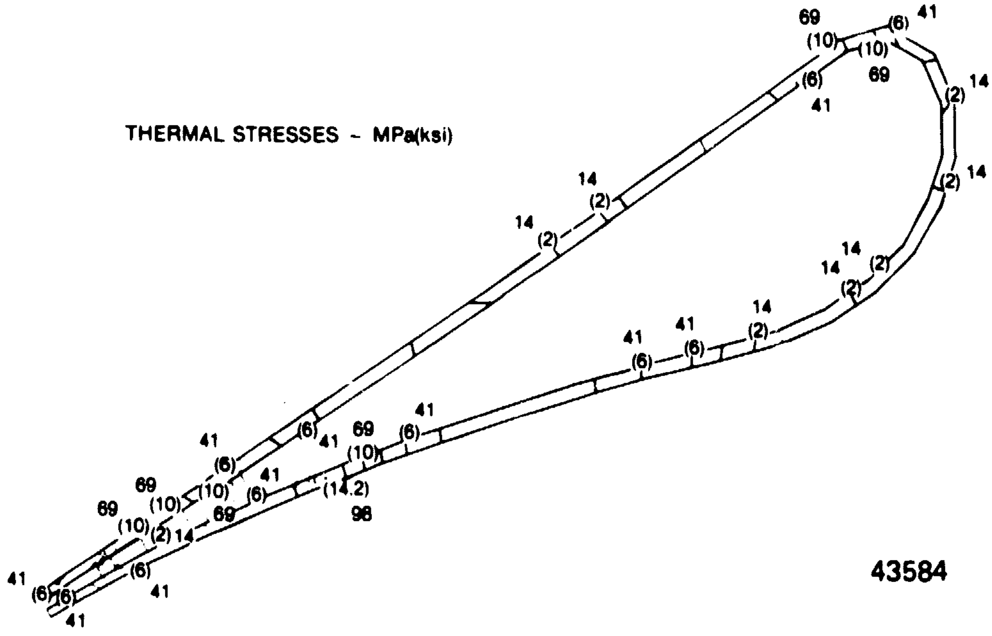

Figure 114. NOZZLE VANE VON-MISES EQUIVALENT THERMAL STRESSES.

ORIGINAL PAGE IS
OF POOR QUALITY

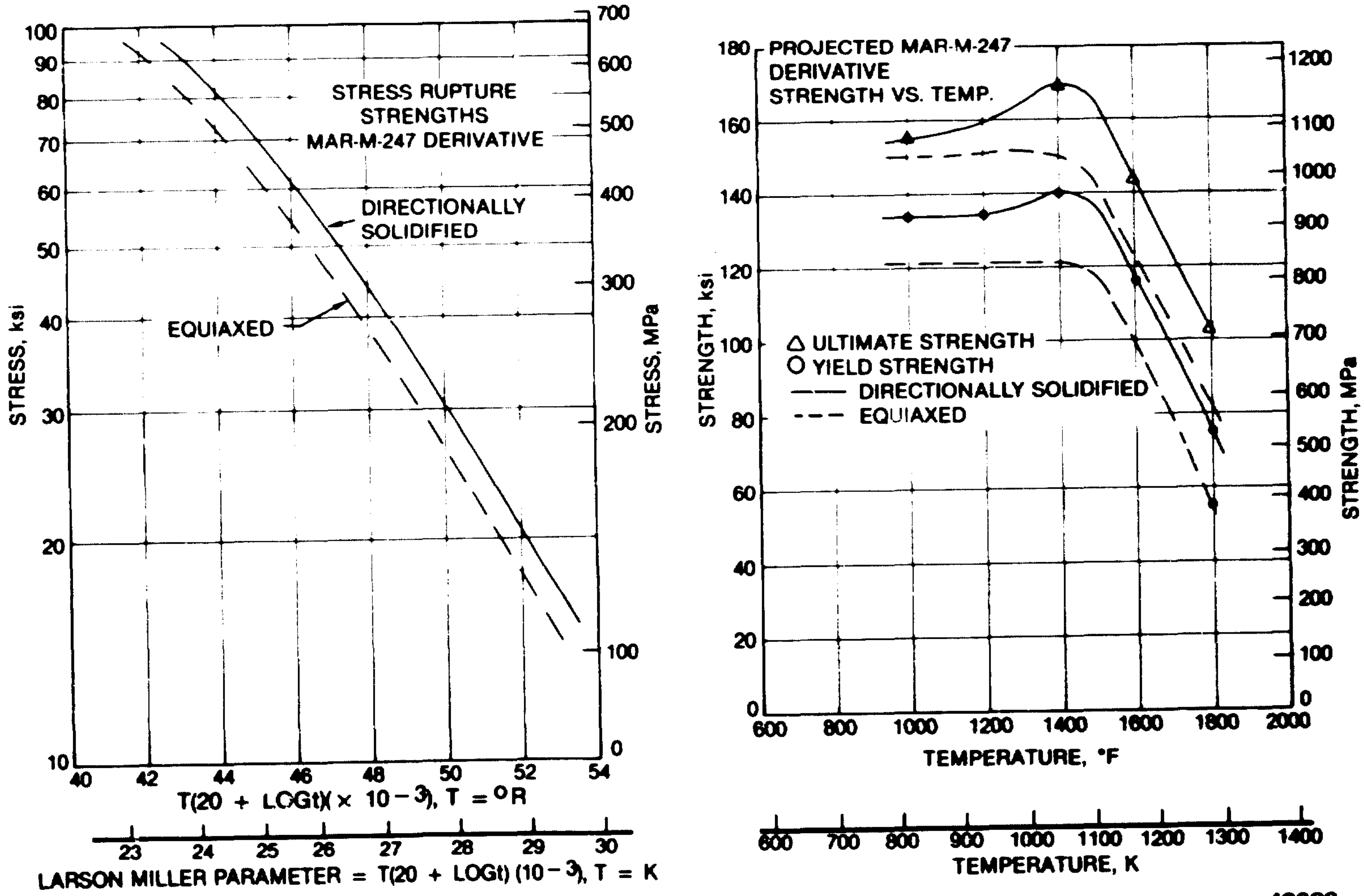

43626

Figure 115. TURBINE STATOR MATERIAL DESIGN CURVES.

6.3 ROTOR THERMAL ANALYSIS

6.3.1 Design Point Analysis

The CINDA computer code used for calculation of component temperature distributions is outlined in Reference 24. The heat transfer system is broken up into small discrete lumped-parameter volumes called nodes. All geometric data is known at these discrete points for calculation of nodal capacitances and nodal conductances. In addition, gas temperature is known at these points, together with sufficient flow data to calculate a heat transfer coefficient using a turbulent flat plate algorithm. The nodal pattern is extrapolated into the disk by extending the station lines radially inward. Figure 116 shows the nodal diagram used for the analysis.

The disk is thermally inseparable from the blades. After the first step preliminary analysis (Section 4.2), blades and disk were treated as a unit. The results of the preliminary analyses indicated that the introduction of seal leakage, windage, and cooling effects would have to be handled carefully to avoid steep temperature gradients which tend to penetrate into the blade. In the final analysis, the seal leakage was introduced parallel to the disk front face so that the temperature gradient was confined to the disk. One percent seal leakage cooling flows radially outward along the disk front face as shown in Figure 110. This leakage slips over the disk edge into the flowpath and film cools the disk rim. Another 1.5% nozzle shroud film cooling flow is injected from the nozzle front (left) sidewall and also cools the rotor in the hub region at the outer radius. The film thickness representing 2.5% cooling flow is less than two percent of the blade span and the cooling effect of the film is confined to the disk along the rotor flowpath.

Figure 117 shows an isothermal representation of the temperature distribution at design point. The disk is nearly isothermal except in the immediate vicinity of the flowpath and in the vicinity of the front face near the rim, where both sides are cooled. The majority of the disk lies between 977 K (1300°F) and 1016 K (1370°F). The exception is the small triangular volume at the front face rim. This area is effectively cooled on all sides by leakage windage and by veil cooling to reduce the minimum temperature to 894 K (1150°F).

The calculated maximum blade temperature was reduced over the preliminary analyses values to 1227 K (1750°F) at the tip as a consequence of the more realistic tip velocity distribution

ORIGINAL PAGE IS
OF POOR QUALITY

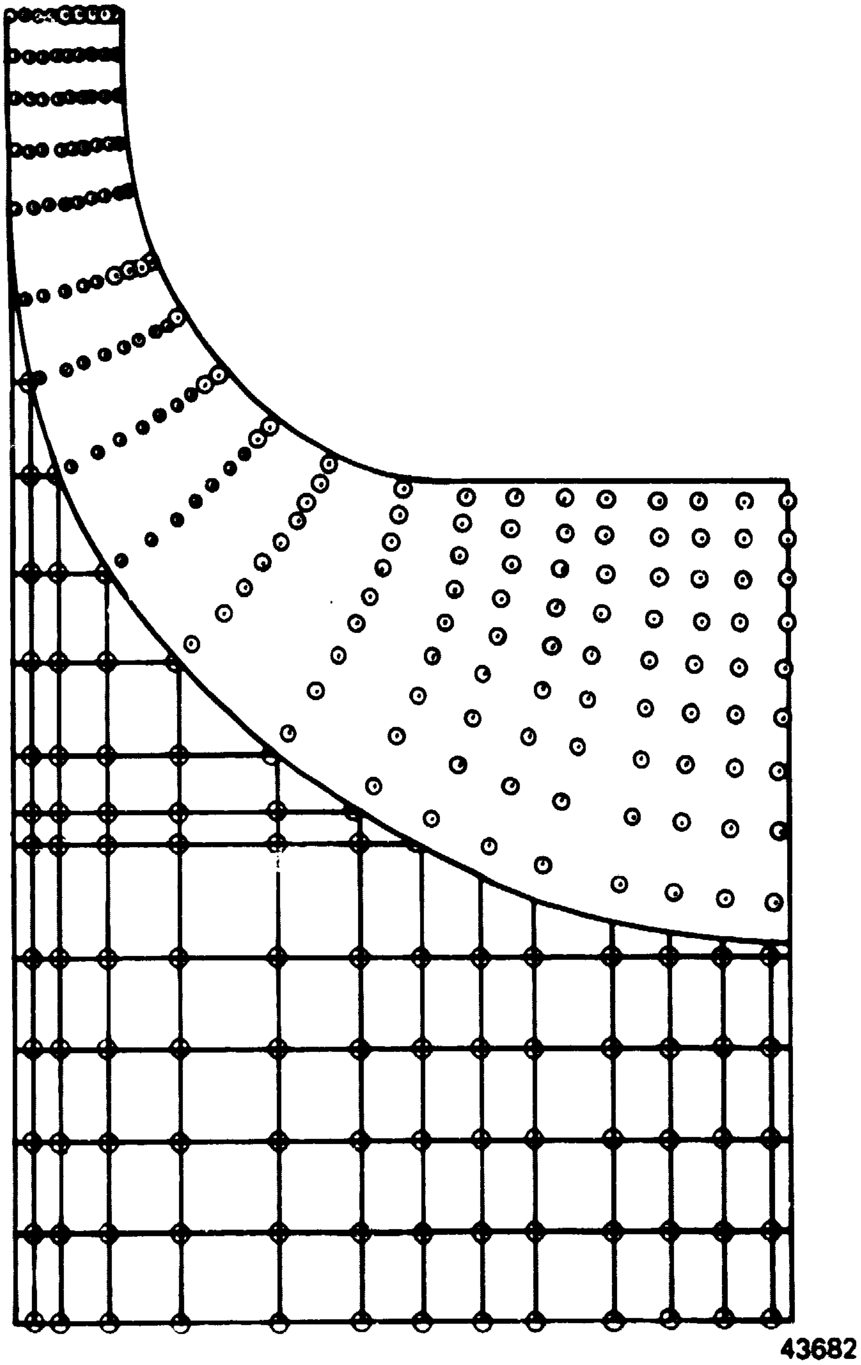

Figure 116. ROTOR THERMAL NODE DIAGRAM.

ORIGINAL PAGE IS
OF POOR QUALITY

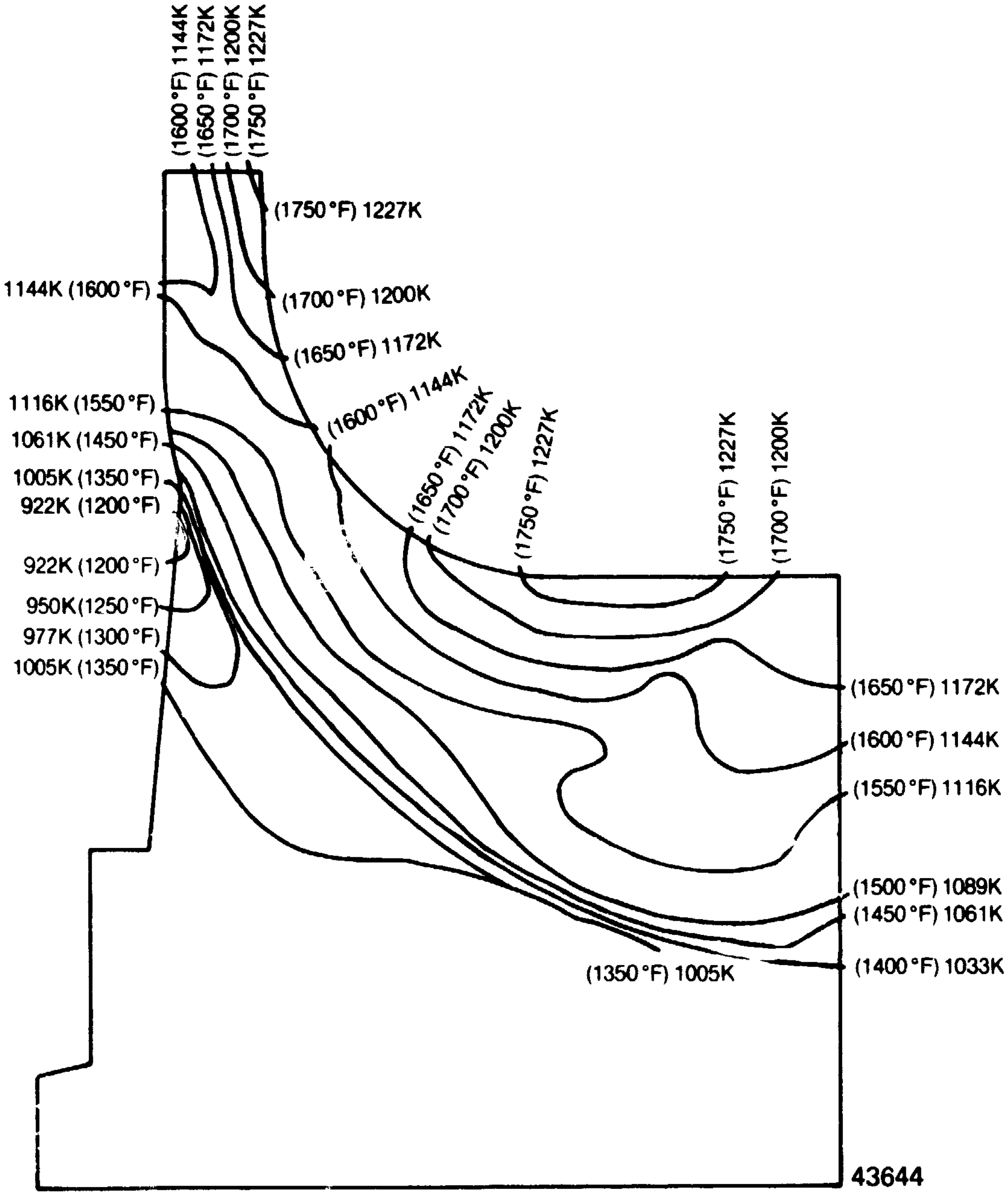

Figure 117. ROTOR HEAT TRANSFER ANALYSIS.

calculated during TASK III aerodynamic analysis. The blade root temperature is nearly constant at 1033 K (1400°F). The blade, where thin, creates little resistance to circumferential input of heat, a typical surface-to-surface temperature gradient is 3 K (6°F). The calculated blade and disk temperatures meet requirements for life at the maximum rated gas temperature, as discussed in Section 6.4.3.

6.3.2 Transient Predictions

The CINDA computer code described in Section 6.3.1 was run for a 12 second acceleration/deceleration cycle as specified in MIL-E-8593A. Elapsed time was extended to 15 seconds to allow the final temperatures to asymptote to the steady state conditions. The transient schedule was assumed to consist of 1) a linear change from idle operating conditions to 100% speed, no-load in 8 seconds and 2) a linear change from no-load to design point in 4 seconds. Engine flow and temperature were structured into non-dimensional difference ratios at these three points (design point =1), and these ramps were used to recalculate the thermal boundary conditions within CINDA as a function of time. The deceleration schedule was assumed to be a reverse trace of this acceleration schedule.

The CINDA program was configured to calculate the distribution of metal temperature for:

1. Design point steady state.
2. Ramp transient - design point to idle
3. Idle steady state
4. Ramp transient - idle to design point

The steady state points, in addition to generating useful data, provide a stable starting point for the transient calculations. The ramp transient calculations require iterations on the boundary temperatures and heat transfer coefficients at each time tep in the transient calculation.

Figure 118 is a histogram of three typical nodes and the gas relative temperature. The nodes more remote from the hot gas, such as 421, change most slowly and the nodes most intimate with the gas stream, such as 19, change most rapidly. Node 209 is near the region of most cooling. This node is changing at nearly the same rate as the buried node 421, indicating little effect of the transient on disk thermal distribution. Neither node exhibits significant time lag. Node 19 is one of the nodes most exposed to the hot gas. This node changes most rapidly and exhibits negligible time lag.

ORIGINAL PAGE IS
OF POOR QUALITY

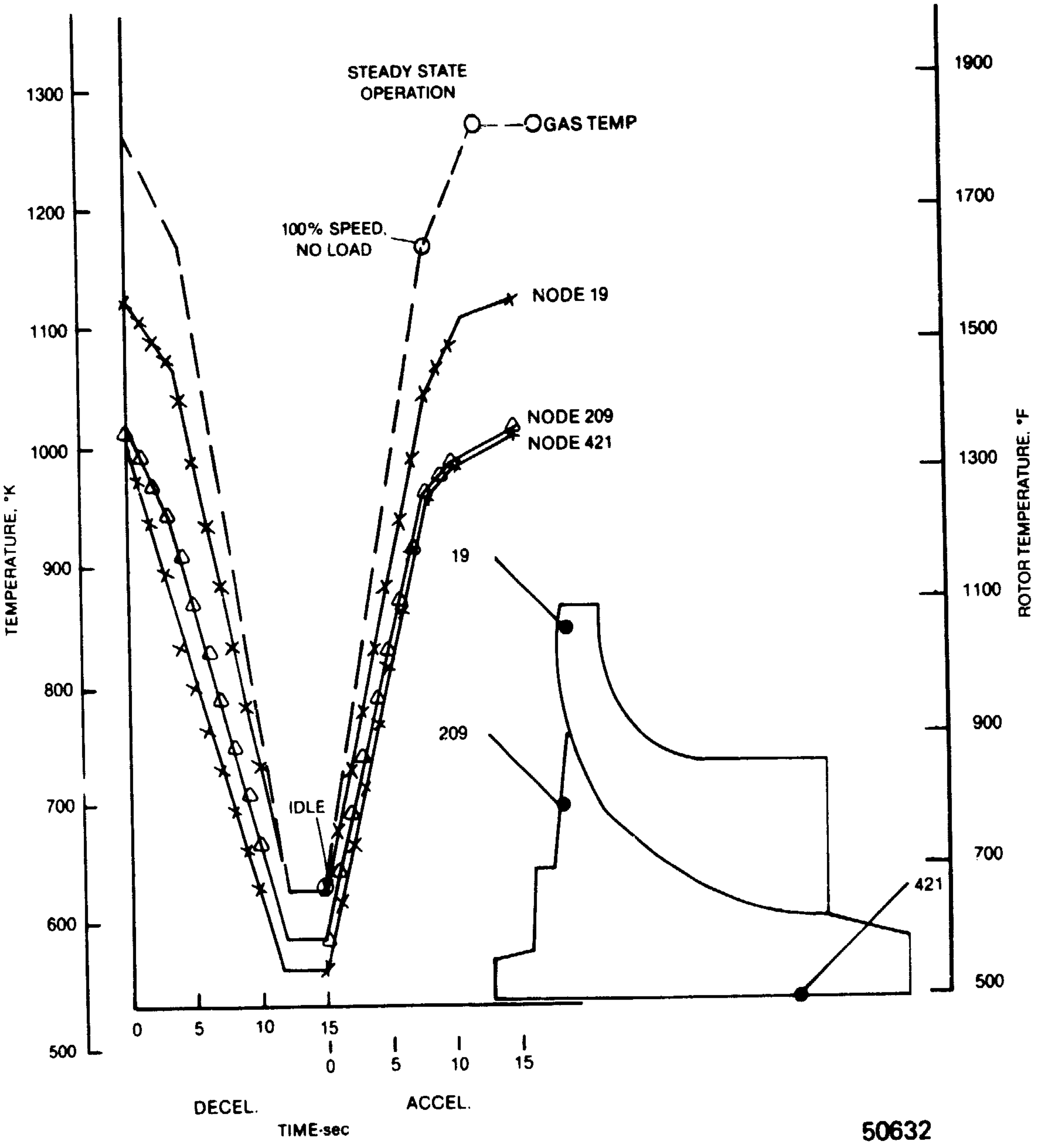

Figure 118. TRANSIENT TEMPERATURE HISTOGRAM, TYPICAL NODES.

6.4 ROTOR STRUCTURAL ANALYSIS

6.4.1 Design Methodology

The feasibility of meeting the structural life goals of the radial turbine was demonstrated in the Task II preliminary structural analysis. The Task IV structural analysis was performed to analytically demonstrate that the life goals are still met with the final design configuration established in Task III. The rotor centrifugal and thermal stresses were calculated with a finite element model which represents the blades as plane stress elements in the meridional plane and the disk as axisymmetric elements, Figure 119. The blade gas bending and centrifugal stresses and natural frequencies were calculated with a NASTRAN plate model shown in Figure 120. Emphasis was placed on the centrifugal blade stresses which are the primary stresses that govern the blade creep rupture life for a given temperature.

The blade stress rupture lives were calculated using the direct centrifugal effective Von Mises stress at the midplane of each element from the NASTRAN plate model. The Larson-Miller parameters for the calculated element stresses were obtained from the material stress rupture curves and then the life was calculated from the Larson-Miller parameters and element temperature. Stress redistribution due to creep was not considered in the analysis.

ORIGINAL PAGE IS
OF POOR QUALITY

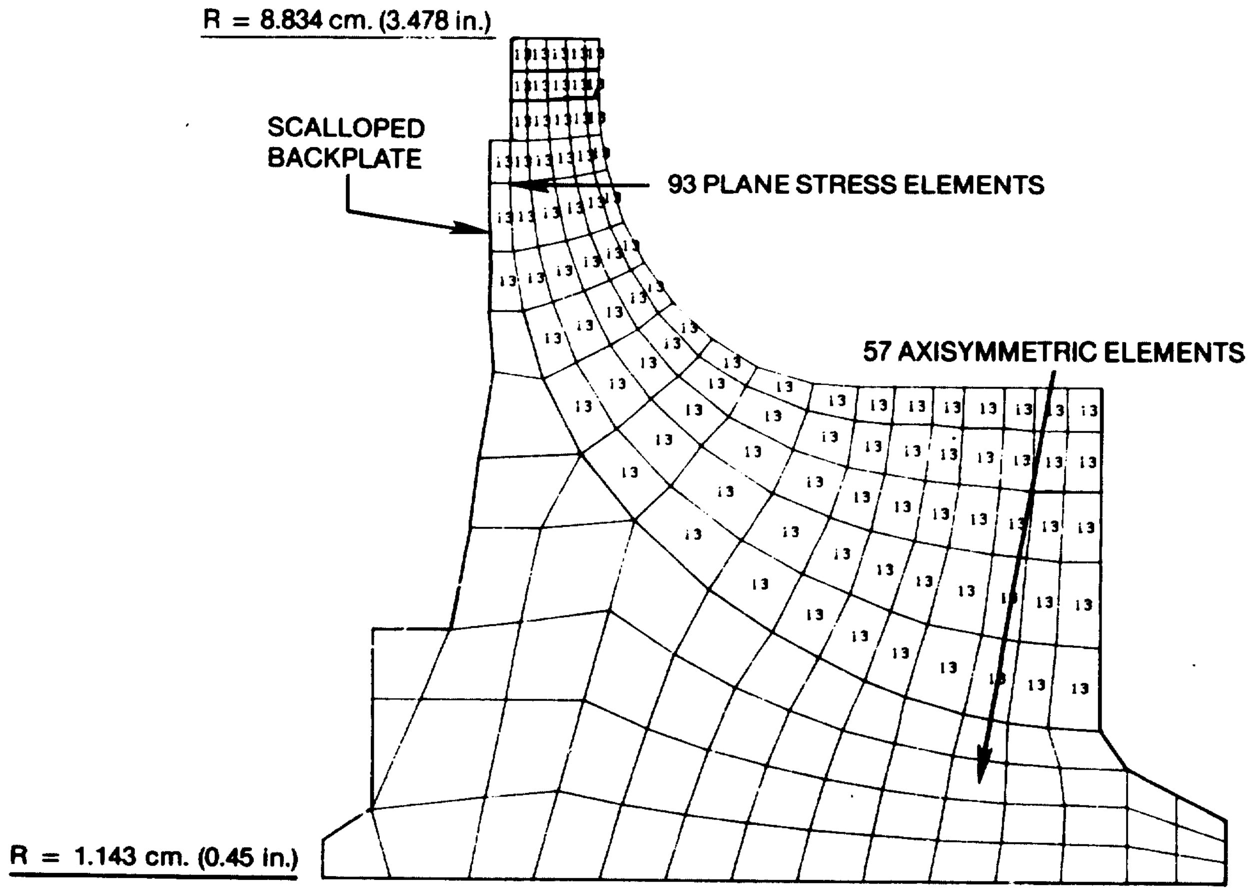

Figure 119. RADIAL TURBINE ROTOR FINITE ELEMENT MODEL.

41700

ORIGINAL PAGE IS
OF POOR QUALITY

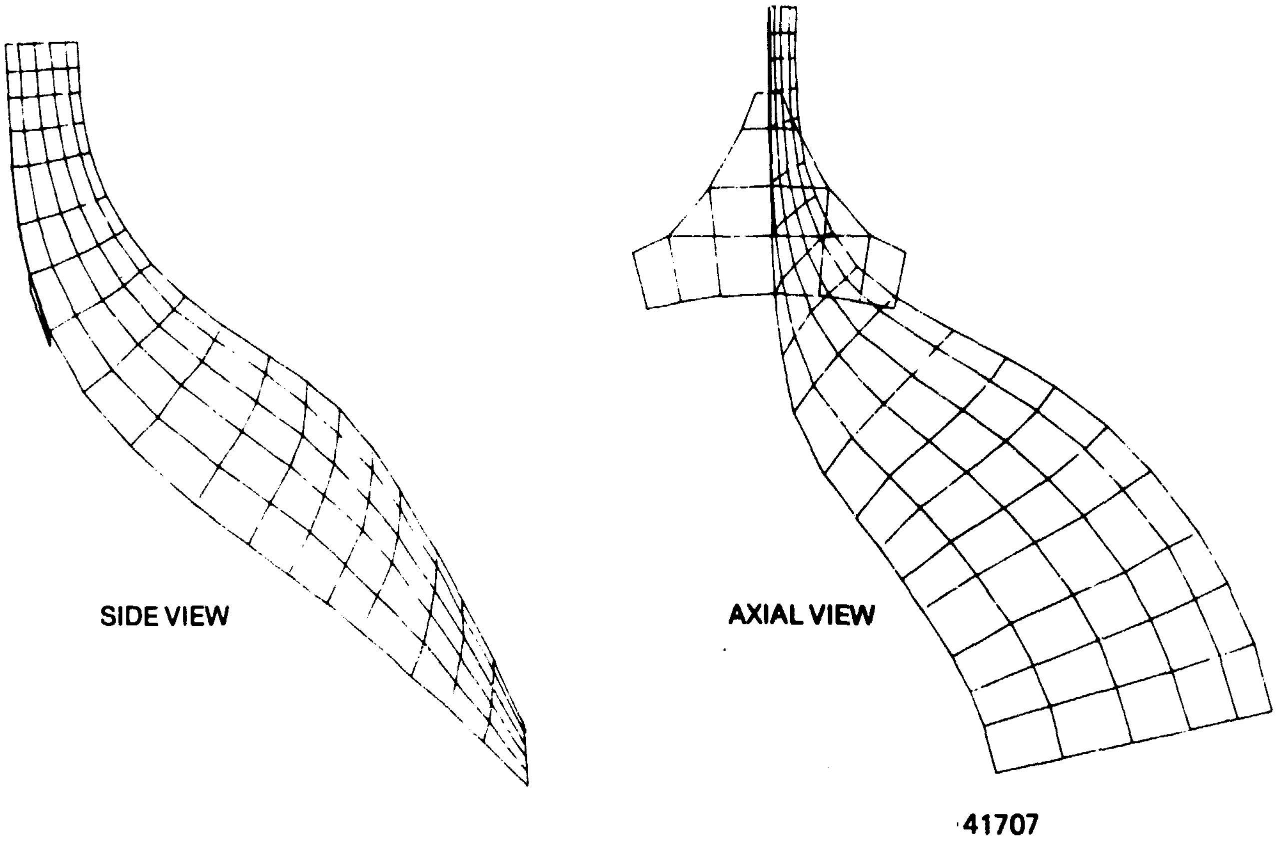

Figure 120. RADIAL TURBINE BLADE PLATE MODEL.

The material selected for the rotor during Task II was a CRS powder metal with directionally recrystallized (DR) blade tips. The anisotropic properties of the DR material in the blade tips which were included in the NASTRAN plate model are shown in Figure 46, Section 3.4.

The life goals were 3600 hours at maximum temperature and speed, based on 90% of the 4000 hour design life, and 5000 single start-stop cycles as discussed in the Task II structural Section 4.2.2.

6.4.2 Disk Stresses And Life

The rotor centrifugal stresses were calculated for the maximum steady state speed of 71,000 RPM and the final steady state thermal gradient. The average tangential stress in the disk was 487 MPa (70.6 ksi) which yields a burst speed margin of approximately 34% for a CRS powder metal disk at an average temperature of 1016 K (1370°F). The rotor Von-Mises equivalent stresses are shown in Figure 121. The maximum stress of 986 MPa (143 ksi) occurs in the bore but is only slightly above the 0.2% yield strength which means only a small central portion of the bore will be subjected to yielding.

Disk stresses were also calculated for a deceleration transient from maximum to idle speed. This condition represented the maximum thermal gradient between the disk backplate and bore. The calculated Von-Mises equivalent stresses are shown in Figure 122. The bore stresses were within the range of stresses from the steady state analysis and the same will be true for the acceleration transient because the gradients were lower. Therefore, the maximum strain is assumed to occur at maximum speed in the disk bore. For a maximum equivalent bore stress of 986 MPa (143 ksi), and Rene' 95 LCF properties, which is considered typical of equiaxed powder metals, a LCF life of approximately 8×10^4 startup and shutdown cycles was determined based on a single mission cycle as described in the Task II structural analysis summary (Section 4.2.2.)

6.4.3 Blade Stresses And Life

The blade thickness distribution generated during Task II was used initially and refined during the Task IV analysis. The blade combined thermal and centrifugal stresses at maximum speed calculated from the plane stress model, are shown in Figure 121. Stresses were well below the 0.2% yield strength of the CRS powder metal. The gas bending stresses at maximum conditions, calculated using the plate model, were generally below 6.9 MPa (1 ksi) and are of no significance.

Centrifugal stresses were calculated for the blade using the 3D plate model. Creep rupture lives were then calculated using the powder metal Larson-Miller parameter curves introduced during Task I. The initial blade lives did not meet the 3600 hour life goal at maximum conditions. The backface labyrinth leakage air of 1.0% reduced the temperatures along the blade hub. In addition, the blade hub was thickened to reduce centrifugal stresses. The resulting blade life contours are shown in Figure 123. The 3600 hour life goal was not met in the exducer portion of the blade, however, the final aerodynamic analysis has indicated

ORIGINAL PAGE IS
OF POOR QUALITY

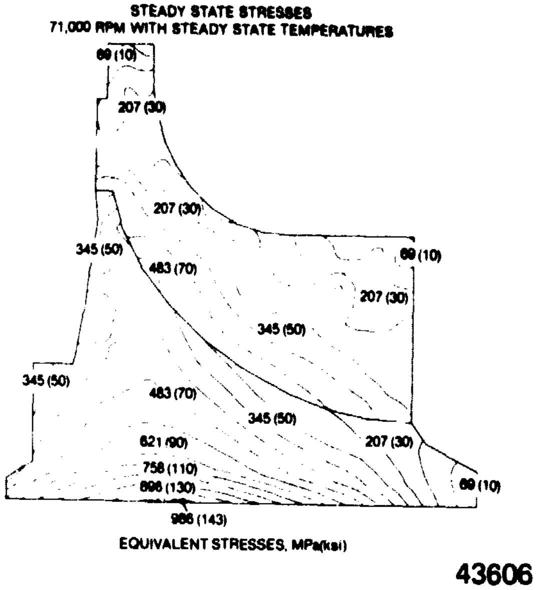

Figure 121. COMBINED CENTRIFUGAL AND THERMAL VON-MISES EQUIVALENT STRESSES AT 71,000 RPM, STEADY STATE MAXIMUM POWER CONDITIONS.

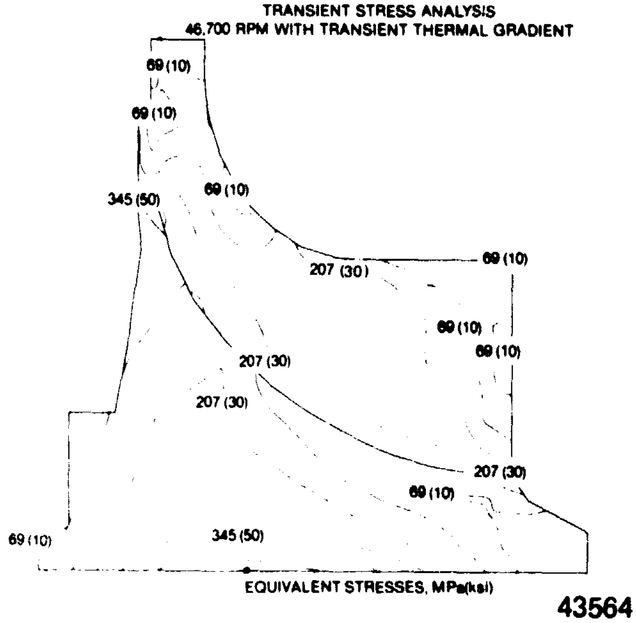

Figure 122. COMBINED CENTRIFUGAL AND THERMAL VON-MISES EQUIVALENT STRESSES DURING DECELERATION FROM MAXIMUM POWER TO IDLE.

ORIGINAL PAGE IS
OF POOR QUALITY

that this portion of the blade can be trimmed back since loadings are very low in this portion of the blade. Therefore, there was no attempt at decreasing stresses in the exducer region any further.

The calculated creep rupture life of the blade, in a small local region near the backplate, did not meet the 3600 hour life goal. However, the surrounding material in the backplate and blade has a very high life and as creep occurs in the local area, the stresses will redistribute so that the creep life will be much greater than calculated with the current linear analysis. Therefore, no further attempts were made to increase regional lives and it is concluded that the overall blade life will exceed the 3600 hours creep rupture life goal at the maximum speed and temperature condition.

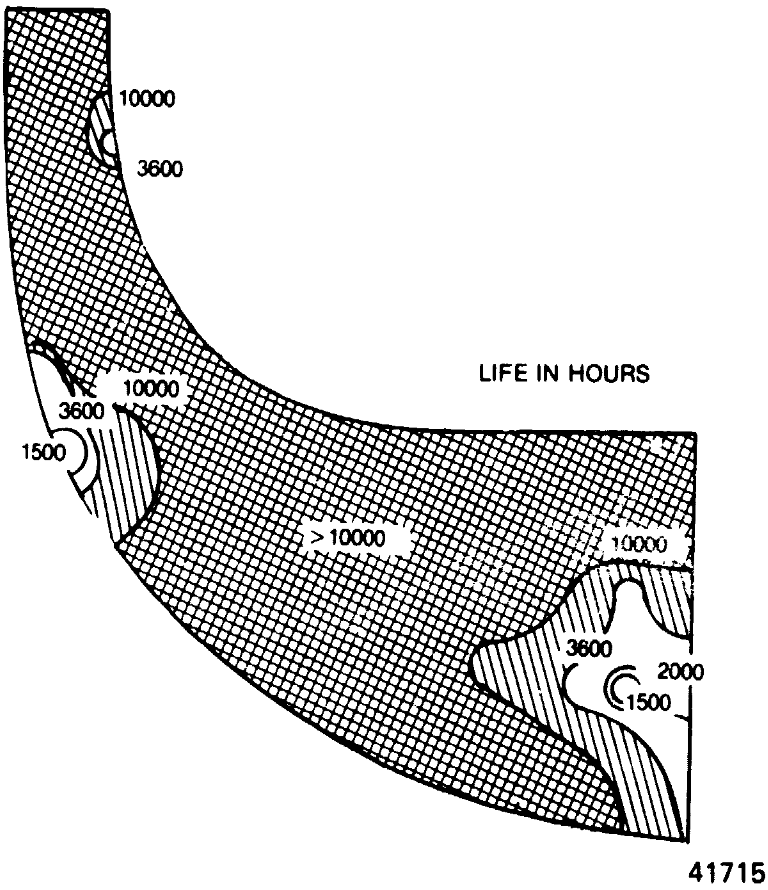

Figure 123 RADIAL TURBINE BLADE CREEP RUPTURE LIFE CONTOURS FOR MAXIMUM SPEED AND TEMPERATURE CONDITIONS (71,000 RPM AT MAXIMUM TEMPERATURE).

ORIGINAL PAGE IS
OF POOR QUALITY

6.4.4 Blade Vibration Analysis

The blade plate model with backplate was used to determine natural frequencies and mode shapes at room temperature and zero speed and at maximum power conditions with temperature and speed effects included. The resonance diagram is shown in Figure 124. The analysis shows a potential resonance of the 12th mode with 15 inlet stators at maximum speed where the 50%-100% power range occurs. It was therefore recommended that 14 stator vanes be used, which is acceptable aerodynamically. The mode shape of the 12th mode shown in Figure 125, indicates that the maximum deflection occurs in the inducer portion of the blade.

The 7th and 9th modes are predicted to be near resonance in the low speed range. Problems are not anticipated because of the low power conditions and because these modes show very little activity in the inducer portion of the blade. The 11th and 12th modes show considerable activity in the inducer portion and steady state operation at these resonances should be avoided. The 11th mode resonance is in the transient speed range while the 12th mode resonance will be above the maximum speed for 14 stator vanes, so that no vibration problems are anticipated with this blade design.

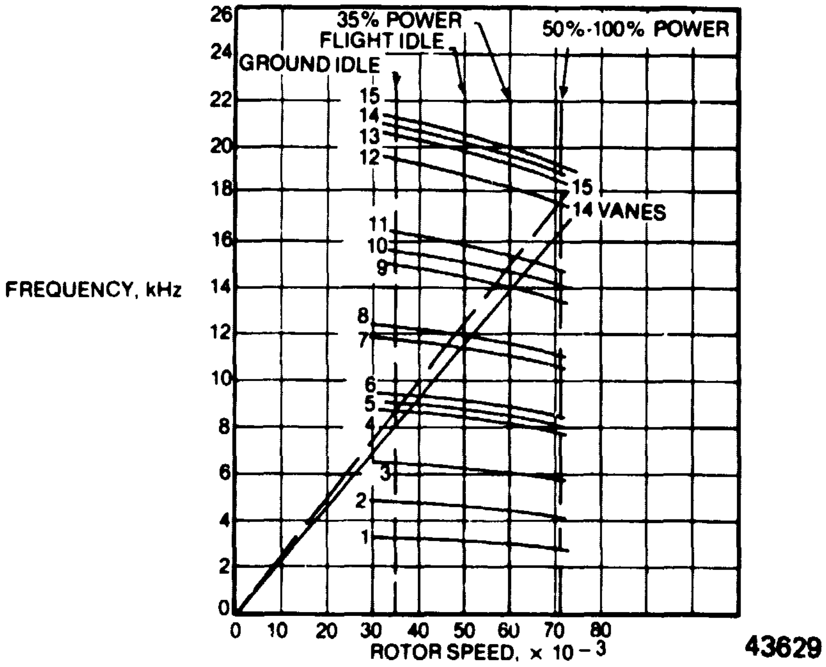

Figure 124. BLADE RESONANCE DIAGRAM.

ORIGINAL PAGE IS
OF POOR QUALITY

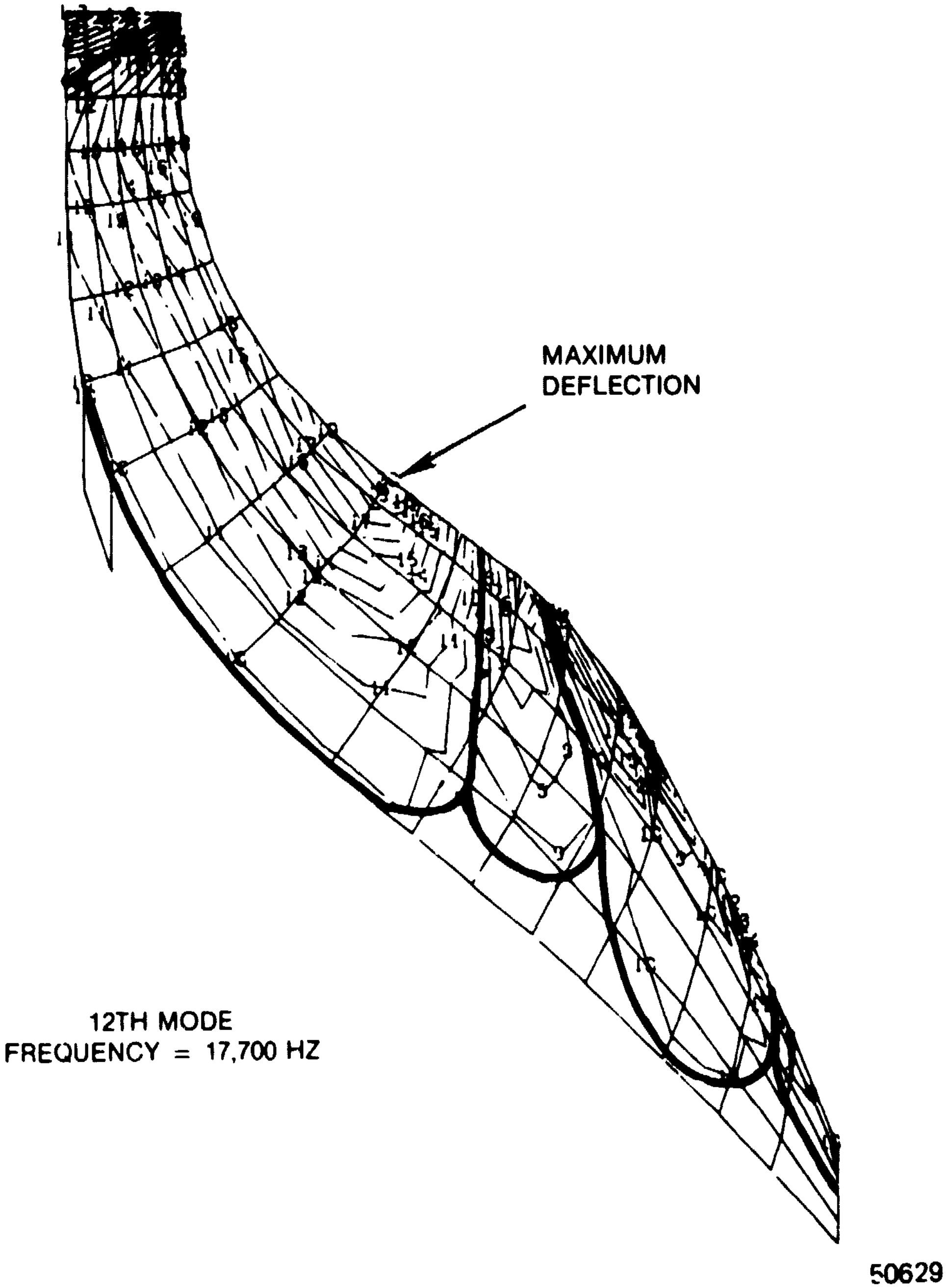

12TH MODE
FREQUENCY = 17,700 HZ

Figure 125. BLADE MODE SHAPE, MODE 12.

PRECEDING PAGE BLANK NOT FILMED

SECTION 7.0

TEST PROGRAM PLAN (TASK V)

The objective of the Task V effort is to establish a test plan for a follow on program consisting of completion of detailed design, preparation of fabrication drawings, fabrication and aerodynamic testing of the turbine. The primary emphasis is the measurement of overall efficiency and identification of the flow field, leading to aerodynamic improvements and improvements in the cooling scheme. Variable geometry loss mechanism details will be investigated. Design and off design characteristics and performance degradations due to nozzle cooling flow rotor leakage injections are to be identified.

The primary geometric configuration to be investigated is the actuated sidewall concept. Because of the unique configuration and variable geometry losses of the pivoted vane concept, the recommended test program plan also encompasses comparative testing with actuation of pivoted vanes.

The following parameters have been identified as requirements to be measured during the test;

Turbine total to total pressure ratio

Turbine total to static pressure ratio

Equivalent mass flow, $\frac{W\sqrt{\theta_{cr}}}{\delta}$,

Equivalent specific work $\frac{\Delta H}{\theta cr}$

Total to total and total to static efficiencies

Equivalent speed $\frac{N}{\sqrt{\theta cr}}$

Exit total pressure, total temperature and flow angle versus percent span at exit from the nozzle, exit from the exducer, and exit from the exhaust diffuser.

Flow field surveys of the vanes and the vaneless space.

Flow field surveys of the rotor.

To assure that realistic conditions are imposed on the turbine stage it is also recommended that an exhaust diffuser follow the rotor. This diffuser should be of a geometry of a real and practical application of the turbine stage.

The turbine test plan consists of five basic tasks as follows:

Task I - Design
Task II - Fabrication and Assembly
Task III - Actuated Sidewall Evaluation
Task IV - Pivoted Vane Evaluation
Task V - Reports

The overall turbine test program outline is given in Figure 126 along with a schedule.

7.1 DESIGN AND TEST EVALUATION

7.1.1 TASK I - Rig Design

The first item under this Task is to conduct a rig layout of the turbine to be tested. A preliminary layout is shown in Figure 127. The expansion ratio across the turbine is generated by flowing air at approximately 1.6 atmospheres and an inlet temperature of 250°F to the turbine and ducting the discharge to a vacuum system. The power produced by the turbine is absorbed by a water dynamometer. Torque is measured by a dynamic torque measuring device connected between the water dynamometer and the turbine rotor. The geometry of the turbine is configured to include cooling flows. This cooling flow will be adjusted to duplicate design percentages of the flow and momemtum ratios of the mainstream to primary flows. Provision is made in the turbine housings for Laser Doppler Velocimeter (LDV) survey windows on the nozzle and the rotor. Adapters will be designed to an existing turbine rig. A structural analysis and design will be conducted to the extent to verify integrity and freedom from blade resonant frequencies during operations. A shaft dynamics analysis will also be conducted to avoid shaft critical frequencies during testing. Detailed drawings of the adapters and the turbine hardware are scheduled for completion at the end of the fifth month of the Task I effort.

ORIGINAL PAGE IS
OF POOR QUALITY

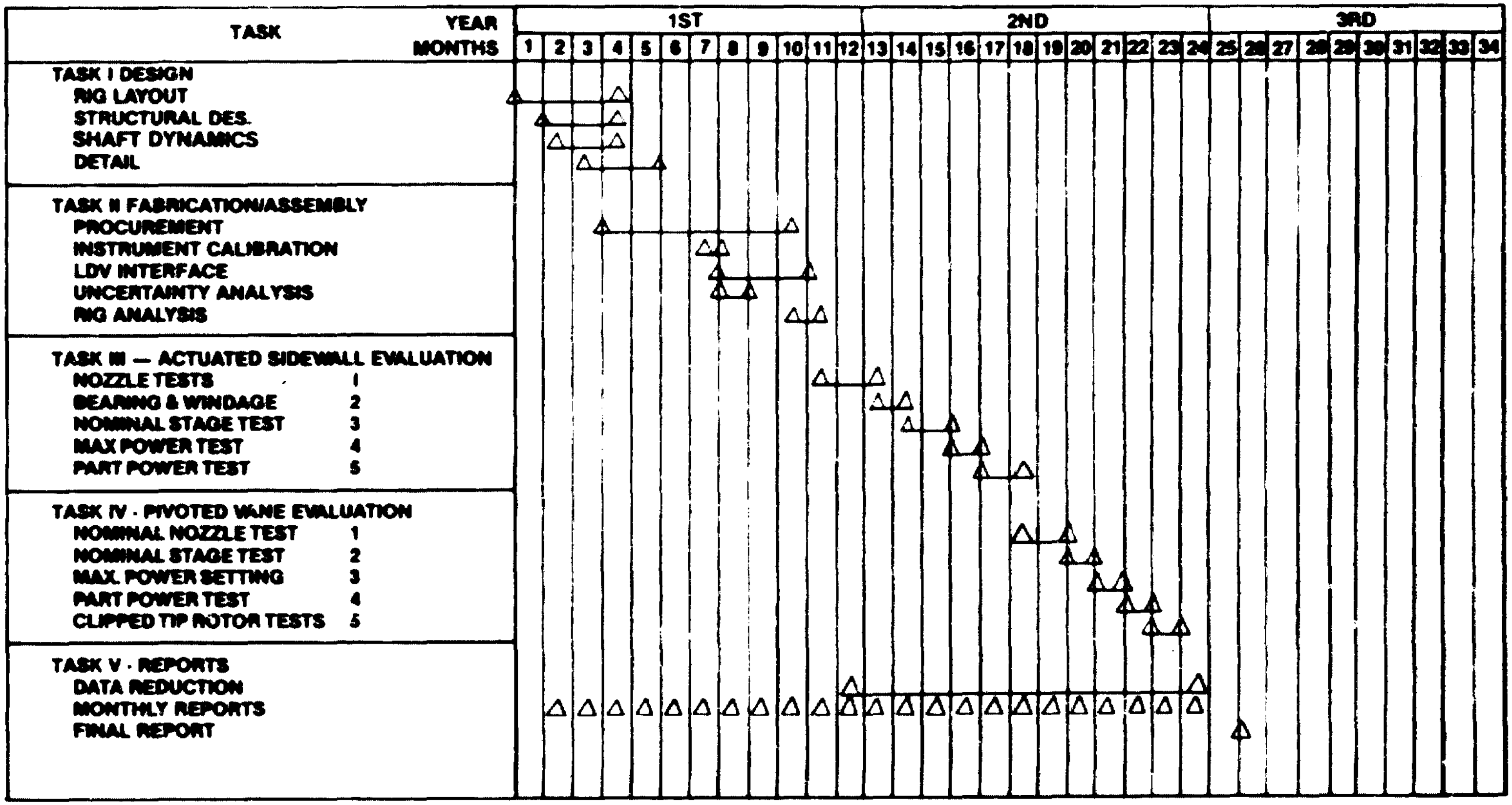

43674

Figure 126. COOLED VARIABLE NOZZLE RADIAL TURBINE TEST PROGRAM.

ORIGINAL PAGE IS
OF POOR QUALITY

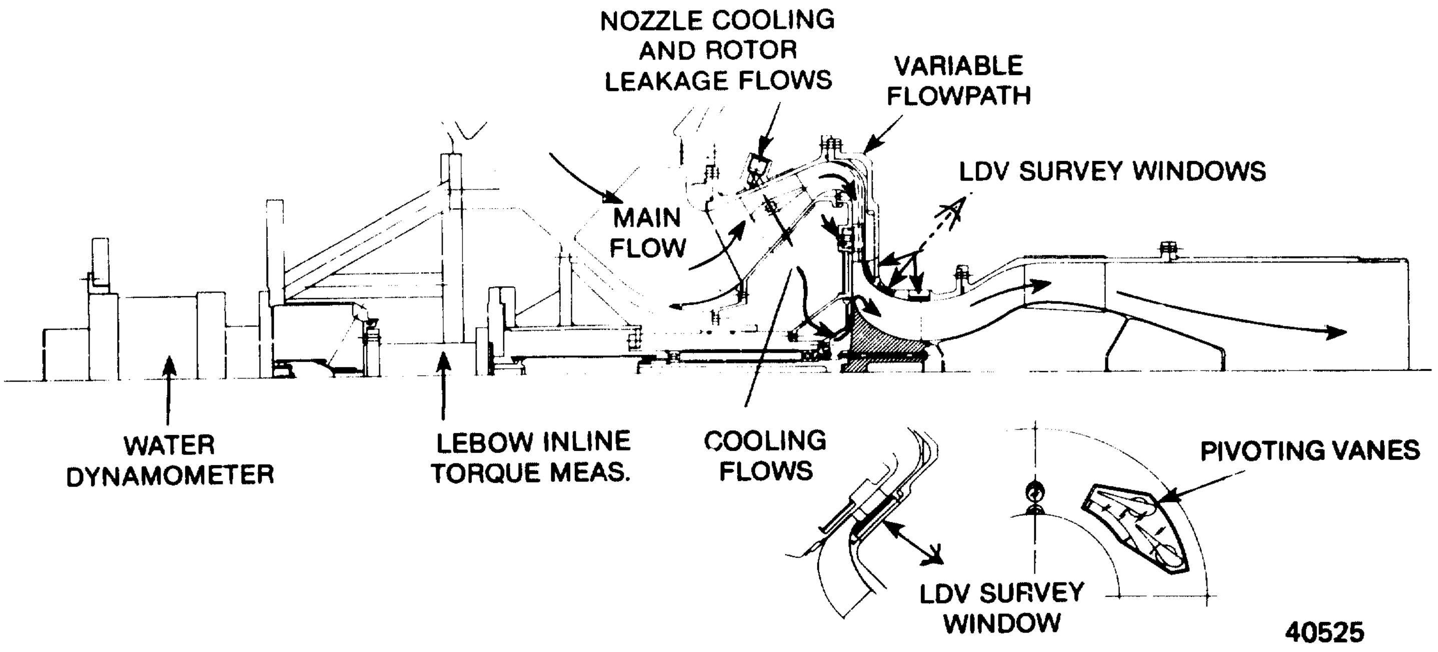

Figure 127. COOLED VARIABLE NOZZLE RADIAL TURBINE PRELIMINARY RIG LAYOUT.

ORIGINAL PAGE IS
OF POOR QUALITY

7.1.2 Task II Fabrication And Assembly

Parts will be released for procurement and fabrication as drawing details are completed and checked. As instrumentation is acquired, it will be calibrated for accuracy. The accuracy of the instrumentation and data acquisition will be identified by an uncertainty analysis. The precision index, bias, uncertainty, and uncertainty in percent of the nominal value will be quantified for the main turbine performance parameters.

Sufficient instrumentation will be provided to allow calculation of the turbine performance parameters previously described. The principal turbine instrumentation locations are given in Figure 128. Instrumentation to be used is described as follows:

a. Flow Rate - Total airflow through the turbine will be measured by an orfice or venture within plus or minus 1% accuracy. Cooling flow rates will be similarly measured.

b. Inlet Total Pressure And Temperature - Turbine inlet total pressure and temperature will be measured using four combination total pressure temperature probes equally spaced around the circumference. The probe element will be located at gas passage heights corresponding to the same percentage heights of the exducer, that is, centers of equal areas.

c. Inlet Total Pressure And Temperature Surveys - Total pressure and temperature will be surveyed from wall to wall using a combined survey probe, at the same location as total pressure and temperature rakes are located. The total pressure entering the turbine will be found by mass averaging the recorded data.

d. Stator Inlet Static Pressure - Stator inlet static pressure will be measured with four static pressure taps equally spaced around the circumference on each of the sidewalls.

ORIGINAL PAGE IS
OF POOR QUALITY

e. Stator Exit Static Pressure - Stator exit static pressure will be measured with four static pressure taps equally spaced around the circumference, on each of the sidewalls at the rotor leading edge.

f. Static Pressure On Outer Rotor Shroud - The static pressure distribution along the outer rotor shroud will be measured by eight static taps equally spaced as shown in Figure 128.

g. Turbine Exit Static Pressure - Turbine exit static pressure will be measured with four static pressure taps equally spaced around the circumference on both hub and tip.

h. Turbine Exit Total Pressure Angle And Temperature Surveys - The rotor exit conditions will be measured by two probes located 90° apart at two locations as shown in Figure 128.

i. Local Velocity And Flow Angle - The local velocity and flow angle will be surveyed with a LDV in the nozzle and vaneless nozzle exit space. Surveys will be conducted from pressure side to the suction side of the nozzle vanes in planes corresponding to 5%, increments of 10% to 90%, and also 95% of the vane span. The rotor will have provision for surveys at three locations as shown in Figure 128. Surveys will be conducted at each of these locations and at 5% increments of 10% to 90% and 95% of the blade span.

j Angular Position Of Rotor - The rotor position will be located by a lamp or light emitting diode and light transmitting fibroptics located at the exducer trailing edge. A commercial "Skan-a-Matic" fibroptic scanner can be used for this purpose.

k. Turbine Torque And Speed - Torque and rotational speed will be measured using an in-line LeBow Torque sensor. Torque measuement corrections will be made for bearing and friction losses. A computerized automatic data acquisition system will be used to reduce data. As part of the Task II effort the LDV will be interfaced with the computer acquisition system.

ORIGINAL PAGE IS
OF POOR QUALITY

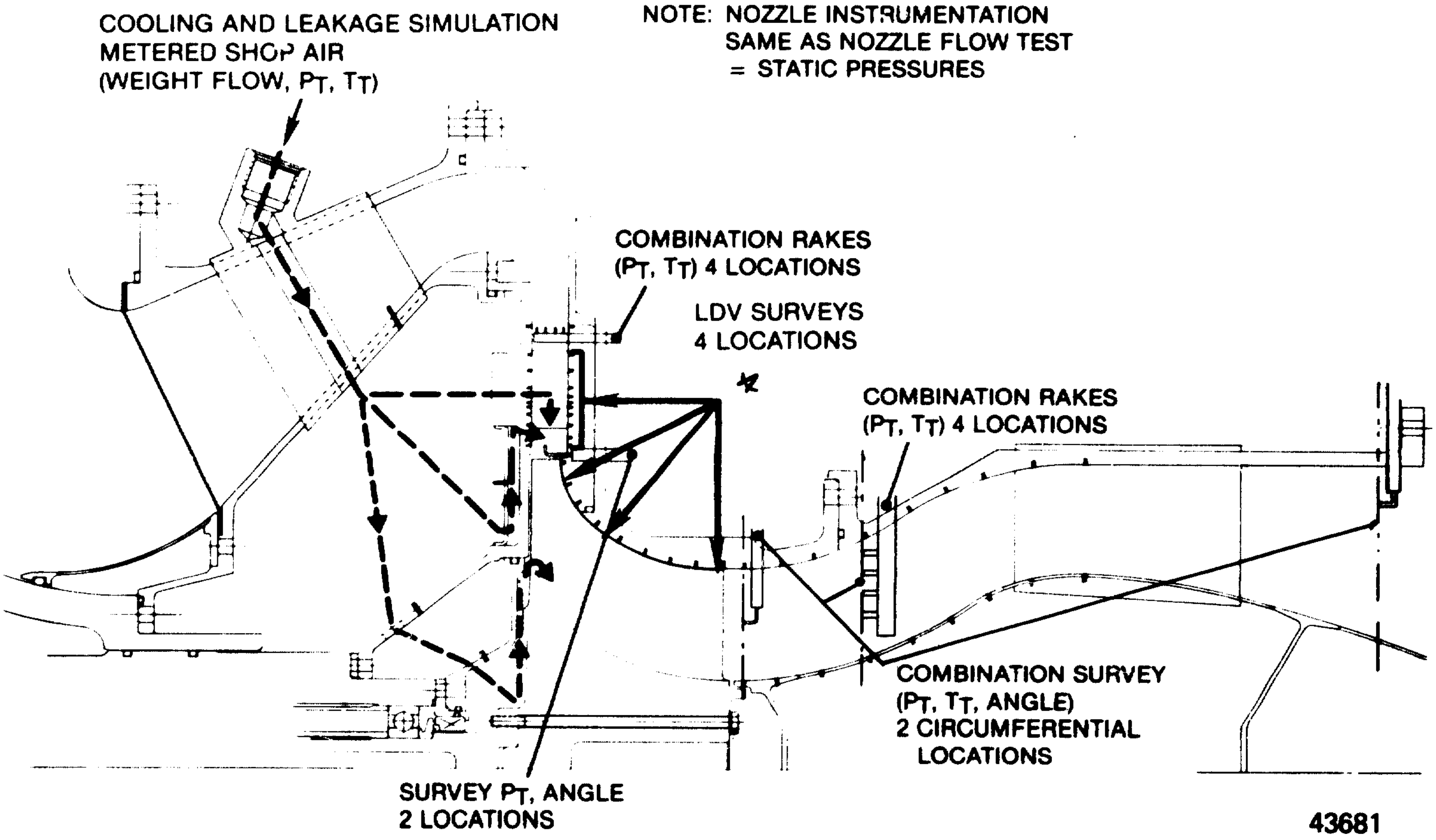

Figure 128. RADIAL TURBINE RIG INSTRUMENTATION.

7.1.3 Task III Actuated Sidewall Evaluation

A total of five tests are planned to evaluate performance of the actuated sidewall nozzle turbine. The recommended tests are as follows:

Nozzle Test

The nozzle characteristics will be identified by testing with the nozzle in the nominal position with the rotor removed. A flow calibration curve will be generated of corrected flow versus pressure ratio with a minimum of five data points. The vanes and the nozzle exit vaneless space will be surveyed by a LDV to characterize velocity angle and turbulence intensity. This data will identify endwall leakage loss mechanisms. Surveys will be made from blade to blade and at planer locations of 5%, 10% increments to 90% and 95% of height.

Bearing And Windage Test

A test will be conducted on a rotorless spindle to characterize torque as a function of speed. This will identify the corrections to be made for the bearing spindle and windage losses to the overall turbine performance. This enables the data reduction and comparison of efficiency from torque and temperature measurements.

Stage Characteristics - (78% Flow Nozzle Setting)

The turbine will be run over a range of speeds and pressure ratios at design nozzle setting to produce an overall turbine map similar to the one shown in Figure 129. Approximately forty test points will be required to characterize a map. Rotor exit surveys will be conducted at several points at 100% speed. At the design point flow, static tap data on the rotor and exhaust diffuser ducting will be recorded. Surveys will also be made on the nozzle, rotor and at the exhaust diffuser exit. A performance matrix will be identified with variable nozzle cooling and rotor leakage flows similar to the curve of Figure 130. At the design point a complete LDV survey of the rotor will also be made to obtain plots of internal velocity and angle. Average turbulence intensity will also be measured at the four LDV locations.

ORIGINAL PAGE IS
OF POOR QUALITY

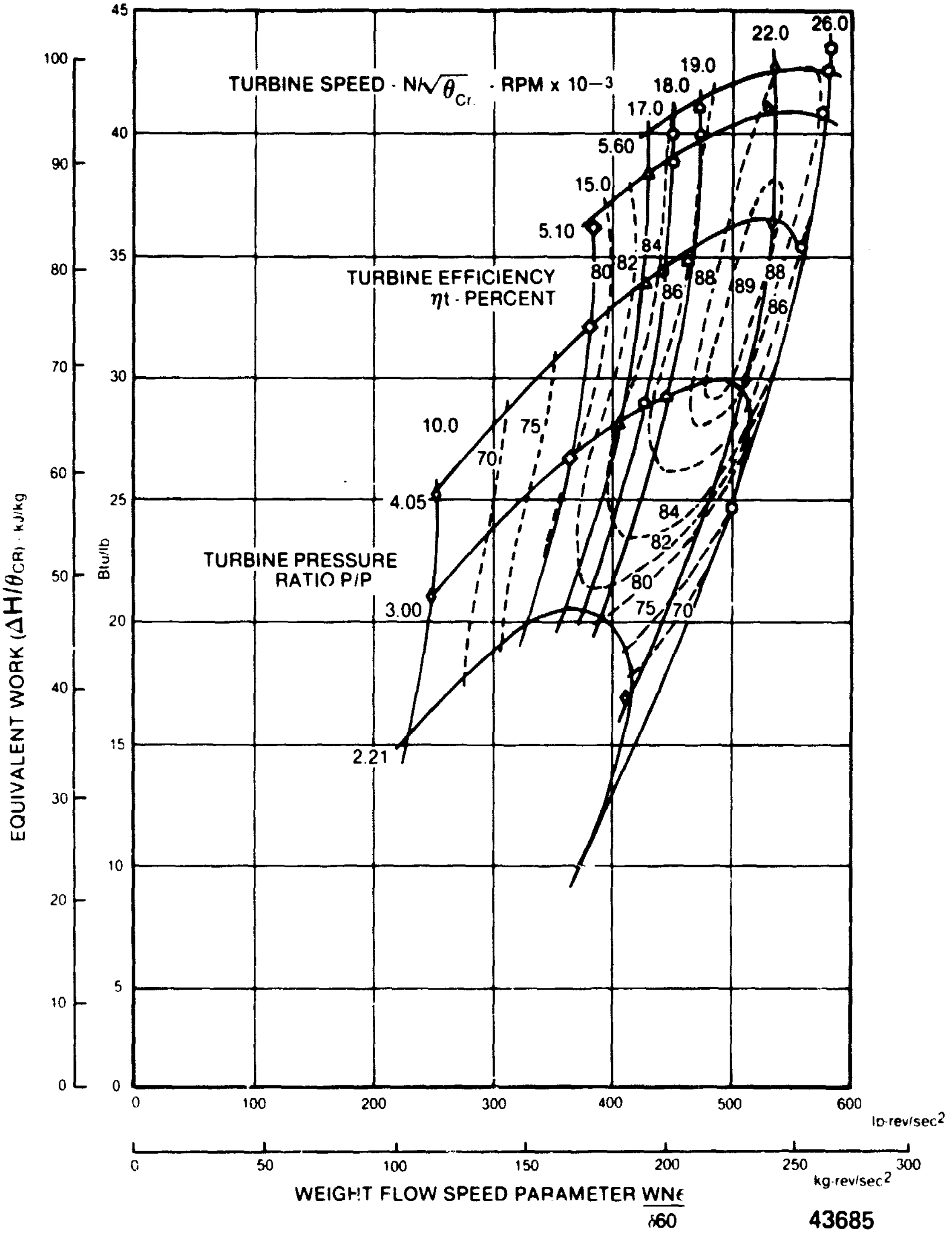

Figure 129. TYPICAL RADIAL TURBINE PERFORMANCE MAP.

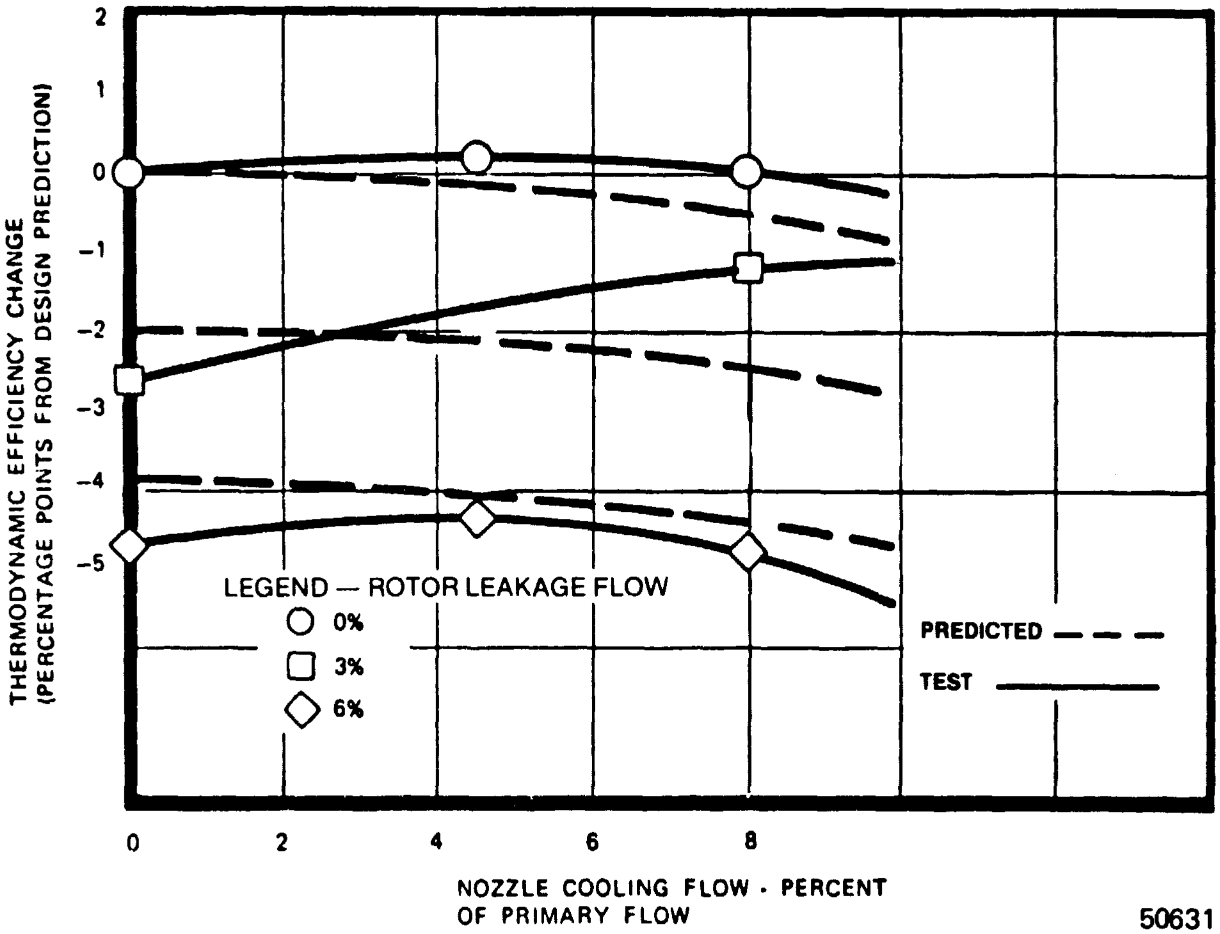

Figure 130. EFFECT OF COOLING AND LEAKAGE FLOW ON TURBINE PERFORMANCE.

100% Maximum Power Setting - (100% Flow Nozzle Setting)

At the maximum power, or wide open nozzle setting, data will be obtained for a partial map. Fifteen points consisting of five speed points each of three pressure ratios will be tested. At the design work and 100% speed, the nozzle and rotor will be surveyed with LDV. Sidewall sudden contraction losses will be quantified from this data. Rotor exit swirl and entrance conditions to the exhaust diffuser will also be measured.

50% Intermediate Power Setting - (48% Flow Nozzle Setting)

Test data for a partial map and stage characteristics as described for 100% power will also be measured at the 50% power rating.

65% and 90% Flow Nozzle Setting

Tests at two additional nozzle flow settings at 100% speed and design work will provide data for a five point performance curve; 48%, 65%, 78%, 90% and 100% flow, of efficiency versus flow capacity. Total pressure and angle surveys at rotor discharge will also define inlet conditions to the exhaust diffuser as a function of nozzle flow setting.

The variable-capacity cycle analysis assumed that the cooling flow to the nozzle would be monitored to a fixed percentage of mainstream flow. To quantify the severity of the penalty, two nozzle cooling flows and two rotor labyrinth leakage injection flows will be imposed at the 100% speed, design work point at each of the nozzle capacity flow settings. This data will quantify the cooling and labyrinth leakage penalties over the 50% to 100% power range. The type of data to be obtained and the test descriptions are summarized in Table X.

ORIGINAL PAGE IS
OF POOR QUALITY

TABLE X

TEST CONFIGURATION SUMMARY

TYPE OF TEST	GEOMETRY	DATA TO BE OBTAINED	TEST POINTS
NOZZLE CALIBRATION	NOMINAL AND 3 INTERMEDIATE	FLOW $\frac{W\sqrt{\theta_{cr}}}{\delta}$ VS $\frac{P}{P}$	5 PER SETTING
NOZZLE SURVEYS	DESIGN POINT	LDV SURVEY VANES AND VANELESS SPACE V, β, T = $\frac{u'}{U}$, LOCAL VELOCITY, ANGLE, AVERAGE TURBULENCE INTENSITY	5, 20, 40, 60, 80, 95 PERCENT PASSAGE HEIGHT
BEARING AND WINDAGE	SPINDLE WITH DUMMY ROTOR	TORQUE, SPEED	14 POINTS
STAGE CHARACTERISTICS & SURVEY	~~MAXIMUM~~ POWER SETTING — COMPLETE STAGE	PARTIAL MAP $\frac{WN}{\delta 60}$, ϵ, $\frac{N}{\sqrt{\theta_{cr}}}$, $\frac{\Delta H}{\theta_{cr}}$, η NOZZLE AND ROTOR LDV SURVEY	5 SPEED POINTS AT EACH OF 3 PRESSURE RATIOS 5, 20, 40, 60, 80, 95 PERCENT PASSAGE HEIGHT
EFFICIENCY CHANGE DUE TO COOLING INJECTION	NOZZLE AT DESIGN SETTING — COMPLETE STAGE	EFFICIENCY CHANGE VS NOZZLE AND ROTOR COOLING FLOW	3 ROTOR LEAKAGE AND 3 NOZZLE COOLING FLOW RATES
EFFICIENCY CHANGE DUE TO NOZZLE AREA, COOLING, AND LEAKAGE INJECTION	NOZZLE AT INTERMEDIATE SETTING — DESIGN PRESSURE RATIO	EFFICIENCY CHANGE VS. % NOZZLE FLOW, COOLING FLOW AND ROTOR LEAKAGE INJECTION	65%, 90% NOZZLE FLOW 2 NOZZLE COOLING AND 2 ROTOR LEAKAGE FLOWS
OVERALL STAGE CHARACTERISTICS	COMPLETE STAGE DESIGN POINT NOZZLE SETTING	OVERALL STAGE MAP, $\frac{WN}{\delta 60}$, ϵ, $\frac{N}{\sqrt{\theta_{cr}}}$, $\frac{\Delta H}{\theta_{cr}}$, η ROTOR EXIT SURVEYS, TOTAL AND STATIC EFFICIENCIES DESIGN POINT STATIC TAP AND LOSS DATA ON ROTOR AND DUCTING SURVEYS-NOZZLE ROTOR AND EXHAUST DIFFUSER EXIT PERFORMANCE WITH MATRIX OF COOLING FLOWS COMPLETE LDV SURVEY OF ROTOR - V, β, $\frac{u}{V}$	40 POINTS FOR MAP LDV SURVEYS AT 5, 20, 40, 60, 80, 95 PERCENT PASSAGE HEIGHT
PART POWER STAGE CHARACTERISTICS	NOZZLE AT INTERMEDIATE SETTING	PARTIAL MAP $\frac{WN}{\delta 60}$, ϵ, $\frac{N}{\sqrt{\theta_{cr}}}$, $\frac{\Delta H}{\theta_{cr}}$, η	5 SPEED POINTS AT EACH OF 3 PRESSURE RATIOS
STAGE CHARACTERISTICS	ROTOR TIP RADIUS REDUCED 10 PERCENT DESIGN NOZZLE SETTING	PARTIAL MAP $\frac{WN}{\delta 60}$, ϵ, $\frac{N}{\sqrt{\theta_{cr}}}$, $\frac{\Delta H}{\theta_{cr}}$, η	5 SPEED POINTS AT EACH OF 3 PRESSURE RATIOS

50672

7.1.4 Task IV - Pivoted Vane Evaluation

A Total of five tests are recommended to be conducted on the pivoted vane configuration so that a direct comparison can be made to the data of the actuated sidewall turbine. These tests would be the same as the tests outlined for Task III except for duplication testing. As a final test, it is recommended that the rotor be clipped at the tip by 10%. The Task II parametric evaluation showed no aerodynamic advantage to reduce the rotor tip diameter, however, material removal at the tip would reduce stresses and improve the life in the critical rotor backface region. The reduced rotor tip test would provide additional test data on the free fortex losses and performance trade-off data for improved rotor durability. A partial turbine map would also be generated to demonstrate the effects of reducing the tip diameter on overall efficiency.

7.1.5 Task V - Data Reduction and Reporting

Test data will be analyzed for both nozzle configurations and recommendations will be made on the basis of the results of the testing. The Task V effort consisting of reporting will present monthly progress reports to be followed by a final report. The above described five task turbine test program will provide comparative data of two variable nozzle area radial turbine configurations. Direct comparisons can be made between the two concepts for overall performance efficiency changes. Conditions entering the exhaust diffuser can be identified and performance including the exhaust diffuser can also be evaluated and compared. Efficiency change as a function of cooling flow through the nozzle and rotor will be quantified for both configurations. Part power and max power conditions will show advantages or disadvantages of the turbine concepts. The LDV surveys of the nozzle and the rotor will provide data to identify areas of high loss. Detailed measurements of this internal flow field then can be used to improve the design. An extensive data base will be provided for computer modeling and design and improvement techniques.

SECTION 8.0

CONCLUSIONS AND RECOMMENDATIONS

The design of an advanced centripetal radial turbine with a variable geometry nozzle has been carried out in adequate detail to show structural feasibility for a rotor-craft application. Engine cycle optimization and matching studies were conducted with cooling and parisitic losses to define performance requirements and environmental conditions. The final cycle selection was based on the minimum integrated fuel consumption over the duty cycle of a typical helicopter.

Rotor cooling losses and the geometry compromises necessary to accommodate cooling were predominate sources of inefficiency and led to a selection of an uncooled engine cycle with a design point inlet temperature of 1477K (2200°F) and a compressor pressure ratio of 16:1. With the stipulated maximum airflow of 2.27 kg/sec (5.0 lbs/sec), the engine maximum and design point performance is predicted as:

	Max. Power	Intermediate Rated Power (78% Flow)
ESHP kw(hp)	685 (918)	563 (755)
ESFC kg/hr-kw (lbs/hr-hp)	0.261 (0.429)	0.251 (0.413)

The variable geometry nozzle showing the higher potential performance was determined to be the moveable sidewall concept. The cooling flow requirement on the nozzle vane was 2.0% with a minimum loss trailing edge dump geometry. The stage efficiency of the turbine was predicted to be in excess of 87 percent at design with cooling and variable geometry losses included.

The conclusions drawn are based on the best test data and correlation models at hand. Since there was no data available on the moveable sidewall concept, a conservative assumption of a sudden expansion or contraction loss was assumed in addition to incidence losses on the rotor where off-design conditions were encountered. Test data and modeling could show where improvements in design should be made.

PRECEDING PAGE BLANK NOT FILMED

A test program has been identified to isolate major sources of losses including cooling and leakage flow losses. This program would entail the testing of the variable sidewall in several positions with variable amounts of cooling and leakage flows. Laser Doppler Velocimetry is recommended for non-intrusive survey of the nozzle, vaneless space and rotor. Because both the pivoted vane and moveable sidewall variable area concepts have individual desirable characteristics it is recommended that each be tested with the same rotor. Direct comparisons can then be made between the two concepts for overall efficency changes.

Overall and some local deficiencies can be identified by conventional instrumentation. The LDV non-intrusive surveys can provide benchmark data for more sophisticated computational fluid mechanics procedures to pinpoint loss sources. Computer modeling followed by modification and test should lead to higher performance of the present design and an improvement in design tools.

SECTION 9

LIST OF SYMBOLS

Symbols	Definition
A	area, cm^2; in^2
b	nozzle vane height; cm, in
C	single stage centrifugal compressor
cc	two stage centrifugal compressor
C_o	isentropic velocity corresponding to total head, m/sec; ft/sec
CPR	compressor pressure ratio
CRS	commercial rapid solidification
DR	directionally recrystallized blade material
e	engine order (rotational frequency), Hz
ESFC	equivalent specific fuel consumption, kg/kw-hr; lb/hp-hr
ESHP	equivalent shaft power, kw; hp
$f(AN^2)$	annulus area - speed stress parameter, $\frac{cm\ 2-rev^2}{sec^2}$; $\frac{in^2-rev^2}{sec^2}$
H	boundary layer shape factor, $H = \frac{\delta *}{\theta_{cr}}$
H	enthalpy, J/g; B/lb
H_{ad}	total to static adiabatic head, m; ft
HIP	hot isostatic pressing
i	incidence angle, rad; deg
L	rotor axial blade length, cm; in
LCF	low cycle fatigue

LIST OF SYMBOLS (Cont'd.)

Symbols	Definition
LDV	laser doppler velocimeter
M	meridonial length, cm; in
N	rotational speed, rev/sec
N_B	blade number
N_s	specific speed $= \dfrac{N\sqrt{Q}}{H_{ad}^{\;3/4}}$
N_V	vane number
o	throat ball diameter, cm; in.
P	stagnation pressure, kPa; psia
P/P	total pressure ratio
ΔP	total pressure loss kPa; psia
PF	pin fin
Q	volume flow from exit of turbine, m^3/sec; ft^3/sec
q	dynamic head=1/2 (ρV^2), kPa; psia
R	radius, cm; in
RSR	rapid solidification rate (powder metal process)
s	blade pitch spacing, cm; in
SC	single crystal blade material
T	stagnation temperature, K; ^oR

LIST OF SYMBOLS (Cont'd.)

Symbols	Definition
T	turbulence intensity, $T = \frac{u'}{U}$
t	time in Larsen-Miller stress parameter, Hr
TDF	combustor pattern factor, $TDF = \frac{T_L - T_{av}}{T_{av} - T_{CDT}}$
Tn	normal thickness, cm; in
TNIT	turbine nozzle inlet temperature, K; ^{o}F
TRIT	turbine rotor inlet temperature, K; ^{o}F
U	blade velocity, m/sec; ft/sec
U	mean through flow velocity (in turbulence intensity), m/sec; ft/sec
u	velocity parallel to boundary-layer surface in x-direction, m/sec; ft/sec
u'	root mean squared turbulent velocity component in through flow direction, m/sec; ft/sec
V	absolute gas velocity, m/sec; ft/sec
V_o	flight velocity, kts
W	relative gas velocity, m/sec; ft/sec
W	gas air flow, kg/sec; lbs/sec
Z	axial dimension, cm; in
α	relative gas flow angle measured from meridional plane, rad; deg
β	absolute gas flow angle measured from meridional plane, rad; deg
γ	ratio of specific heats

LIST OF SYMBOLS (Cont'd.)

Symbols	Definition
δ	boundary layer thickness, m; ft
δ	ratio of inlet stagnation pressure to sea level standard
δ^*	boundary layer displacement thickness, $\int_0^\delta \left(1-\frac{\rho u}{\rho_e u_e}\right)dy$, , cm; in
ϵ	rotor inlet tip-to-exducer tip radius ratio
ϵ	function of δ defined as $\frac{\gamma_{sl}}{\gamma}\left[\left(\frac{\gamma+1}{2}\right)^{\frac{\gamma-1}{\gamma}}\left(\frac{\gamma_{sl}+1}{2}\right)^{\frac{\gamma_{sl}}{\gamma_{sl}-1}}\right]$
η	efficiency
η_t	total-to-total adiabatic efficiency, percent
$\Delta\eta_t$	change in total-to-total efficiency, points
θ	coordinate angular position in plane perpendicular to axis of rotation, rad; deg
θ	boundary layer momentum thickness, $\int_0^\delta \frac{\rho u}{\rho_e u_e}\left(1-\frac{u}{u_e}\right)dy$, cm, in
θ_{cr}	squared ratio of critical velocity at turbine inlet temperature to critical velocity at standard sea level temperature.
ρ	density, kg/m^3; slugs/ft^3
ψ	Zweifel coefficient
ω	rotational speed,rad/sec

LIST OF SYMBOLS (Cont'd)

Subscripts

AV	average
CD	compressor discharge
CDT	compressor discharge temperature
cr	condition at Mach number of 1.0
e	value external to boundary layer
FT	free-turbine
H	hub
HPC	high pressure compressor
HPT	high pressure turbine
L	local
LE	leading edge
MAX	maximum value
MECH	mechanical
n	normal direction
ov	overall
r	radial direction
REF	reference value
REL	relative to blade
S	shroud
sl	standard sea level conditions
T	total condition
T	throat
t	tip
T-T	total-to-total
TE	trailing edge
x	axial direction
x,y	coordinate system parallel to and perpendicular to the wall
θ	tangential direction

APPENDIX

STATION LOCATIONS

The following numerical station identification is used throughout this report.

1. Nozzle vane entrance just ahead of the leading edge
2. Nozzle vane entrance just inside the leading edge
3. Nozzle vane throat station
4. Station just ahead of the nozzle trailing edge
5. Station immediately downstream of the nozzle vane
6. Station immediately ahead of the rotor tip
7. Exducer throat station
8. Rotor exducer station immediately ahead of the trailing edge
9. Rotor exducer station immediately downstream of the trailing edge

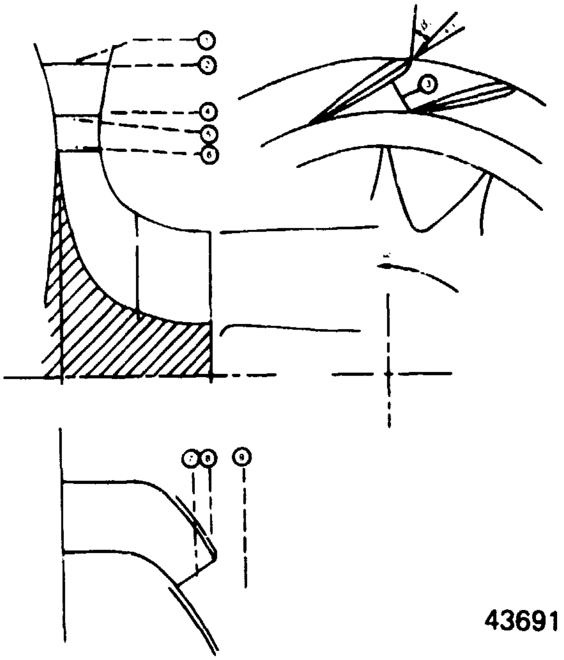

SECTION 10.0

REFERENCES

1. "Advancements in Turbopropulsion Combustion", AIAA/SAE 14th Propulsion Conference, July, 1978.

2. Benstein, E., "Small Flying Gas Turbine Engines are Different", AIAA/SAE Paper, 1974.

3. Easterling, Albert E., "A Comparative Study of Simple, Regenerative, and Variable Capacity Cycles for Gas Turbine Engines", USAAVRADCOM TR 81-D-1, October, 1980.

4. Pratt and Whitney - Florida, "Centrifugal Compressor Technology Study for Air Force Missions", AFAPL TR70-86, 1972.

5. Pampreen, R.C., "The Use of Variable Inlet Guide Vanes for Automotive Gas Turbine Engine Augmentation and Load Control", SAE 760285, February 1976.

6. Harp, James L., and Oatway, Thomas P., "Centrifugal Compressor Development for a Variable Area Turbocharger", SAE SP-79/442, 1979.

7. Bryce, C.A., et al, "Advanced Two-Stage Compressor Program, Design of Inlet Stage", NASA CR-120943, August 1973, p. 40.

8. Smith, R., and Benstein, E.H., "Advanced General Aviation Turbine Engine Study (GATE)", NASA CR-159624, June 1979.

9. Hartsel, J. E., "Prediction of Effects of Mass-Transfer Cooling on the Blade Row Efficiency of Turbine Airfoils", AIAA Paper No. 72-11, January 1972.

10. Anderson, L. R., Heiser, W. H., and Jackson, J. C., "Axisymmetric One-Dimensional Compressible Flow-Theory and Applications:, ASME Paper 70-GT-82, May, 1970.

11. Tipton, D. L., and Monson, D. S., "High-Temperature Radial Turbine Aero-Test", U.S. Army Research and Technology Laboratories Report No. USAAVRADCOM-TR-81-D-19, 18 Sept. 1979 - 18 February 1981.

12. Rodgers, C., "Efficiency and Performance Characteristics of Radial Turbines", Society of Automotive Engineers Paper No. 660754.

13. Northern Research and Engineering Corp., "A Computing System for the Design and Analysis of Radial Turbomachinery," NREC Report No. 1000B, 1967.

14. Balje, O.E., "A Study on Design Criteria and Matching of Turbomachines, Parts A and B", American Society of Mechanical Engineers, Papers 60-WA-230 and 60-WA-231.

15. Theododorsen, T., and Regier, A., "Experiments on Drag of Revolving Disks, Cylinders, and Streamline Rods at High Speeds", NACA Report No. 793.

16. Rogo, Casimir, "Development of a High Tip Speed Radial Turbine System for a Small Turboalternator", Society of Automotive Engineers Paper 710552, 1971.

17. Tseka, J., and Letton, G.C., Jr., "Variable Geometry Air Cycle Machine, "ASME Paper No. 77ENAs-7, 1977.

18. McCormick, Barnes W., Jr., Aerodynamics of V/STOL Flight, Academic Press, New York, London, 1967, p. 157.

19. Helton, D. J., Lueders, H. G., and Arvin, J. R., "An Experimental Investigation of a Subscale Variable Pressure Ratio High Thru Flow Turbine", Air Force Aero-Propulsion Laboratory Report AFAPL-TR-77-7, February, 1977.

20. "RSR Powder Processed Blades and Vanes", Air Force Contract No. F33615-80-C-5005.

21. "Advanced Powder Metal Superalloys for Rotating Components", Air Force Contract No. F33615-80-C-5096.

22. Calvert, Glenn S., Beck, Stephen C., Okapuu, Ulo, "Design and Experimental Evaluation of a High-Temperature Radial Turbine", USAAMRDL TR71-20, May 1971.

23. Rodgers, C., "Advanced Radial Inflow Turbine Rotor Program - Design and Dynamic Testing", NASA CR-135080, September 1976.

24. Lewis, D.R., Gaski, J.D., Thompson, C.R., "Chrysler Improved Numerical Differencing Analyzer for 3rd Generation Computers", TN-AP-67-287, 1967.

25. Katsanis, Theodore, "Fortran Program for Calculating Transonic Velocities on a Blade-To-Blade Stream Surface of a Turbomachine", NASA TN D-5427, September 1969.

26. McNally, William D., "Fortran Program for Calculating Compressible Laminar and, Turbulent Boundary Layers in Arbitrary Pressure Gradients", NASA TN D-5681, May 1970.

27. Khalil, I., and Tabakoff, W., "A Study of the Viscous and Nonadiabatic Flow in Radial Turbines", Journal of Engineering for Power, July 1981, Vol. 103, pp. 481-489.

28. Gaugler, Raymond E., "TACT 1, A Computer Program for Transient Thermal Analysis of a Cooled Turbine Blade or Vane Equipped with a Coolant Insert", NASA TP-1271, 1978.